TRAKYA UNIVERSITY
JOURNAL OF NATURAL SCIENCES

27 Volume 1 Number April 2026

TRAKYA UNIVERSITY JOURNAL OF NATURAL SCIENCES

TUJNS

Trakya Univ J Nat Sci
ISSN 2528-9691

Trakya University Journal of Natural Sciences
www.tujns.org
Volume: 27, Number: 1, April 2026

ISSN 2528-9691

Trakya University Journal of Natural Sciences

Volume: 27 **Number: 1** **April** **2026**

Trakya Univ J Nat Sci

www.tujns.org
e-mail: tujns@trakya.edu.tr

Correspondence Address
Trakya Üniversitesi Fen Bilimleri Enstitüsü Binası, Balkan Yerleşkesi – 22030 Edirne / TÜRKİYE
e-mail: tujns@trakya.edu.tr
Tel: +90 284 2358230
Fax: +90 284 2358237

This journal is a peer-reviewed publication and is indexed in Biological Sciences, BIOSIS Previews, CAB Abstracts, the Directory of Open Access Journals (DOAJ), the Emerging Sources Citation Index (ESCI), Scopus, TÜBİTAK-ULAKBİM Life Sciences Database (Turkish Journal Index), and Zoological Record.

Publisher: www.galenos.com.tr • Publisher Certificate Number: 14521

ISSN 2528-9691

Trakya University Journal of Natural Sciences
www.tujns.org
Volume: 27, Number: 1, April 2026

ISSN 2528-9691

Trakya University Journal of Natural Sciences
www.tujns.org
Volume: 27, Number: 1, April 2026

ISSN 2528-9691

Trakya University Journal of Natural Sciences
www.tujns.org
Volume: 27, Number: 1, April 2026

ISSN 2528-9691

Trakya University Journal of Natural Sciences
www.tujns.org
Volume: 27, Number: 1, April 2026

ISSN 2528-9691

Trakya University Journal of Natural Sciences
www.tujns.org
Volume: 27, Number: 1, April 2026

ISSN 2528-9691

Trakya University Journal of Natural Sciences
www.tujns.org
Volume: 27, Number: 1, April 2026

Prof. Dr. Seray TÖZ
E-mail: seray.toz@gmail.com

Ege University, School of Medicine, Department of Basic Medical Sciences, Division of Parasitology, İzmir, Türkiye

Medical Parasitology

Prof. Dr. Tuğba ONGUN SEVİNDİK
E-mail: tsevindik@sakarya.edu.tr

Sakarya University, Faculty of Science, Department of Biology, Division of Botany, Sakarya, Türkiye

Algology, Hydrobiology, Community Ecology, Limnology

Prof. Dr. Yerlan TURUSPEKOV
E-mail: yerlant@yahoo.com

Institute of Plant Biology and Biotechnology, Laboratory of Molecular Genetics, Almaty, Kazakhstan

Biological Sciences, Plant Biotechnology in Agriculture

Prof. Dr. Yeşim SAĞ AÇIKEL
E-mail: yesims@hacettepe.edu.tr

Hacettepe University, Faculty of Engineering, Department of Chemical Engineering, Division of Process and Reactor Design, Ankara, Türkiye

Industrial Biotechnology, Chemical Engineering, Separation Processes, Environmental and Sustainable Processes, Materials Science and Technologies, Nanotechnology

Prof. Dr. Yıldız AYDIN
E-mail: ayildiz@marmara.edu.tr

Marmara University, Faculty of Science, Department of Biology, Division of Molecular Biology, İstanbul, Türkiye

Plant Biotechnology, Plant Tissue and Cell Culture

Assoc. Prof. Dr. Albena LAPEVA-GJONOVA
E-mail: gjonova@gmail.com

Sofia University, Faculty of Biology, Department of Zoology and Anthropology, Sofia, Bulgaria

Entomology

ISSN 2528-9691

Trakya University Journal of Natural Sciences
www.tujns.org
Volume: 27, Number: 1, April 2026

Assoc. Prof. Dr. Beata ZİMOWSKA
E-mail: beata.zimowska@up.lublin.pl

University of Life Sciences in Lublin, Department of Plant Protection, Subdepartment of Phytopathology and Mycology, Lublin, Poland

Biological Sciences, Plant and Fungus Systematics and Taxonomy, Microbiology, Mycology

Assoc. Prof. Dr. Boris ASSYOV
E-mail: contact@boletales.com

Bulgarian Academy of Sciences, Institute of Biodiversity and Ecosystem Research, Sofia, Bulgaria

Mycology

Assoc. Prof. Dr. Fatih EKİNCİ
E-mail: fatihekinci@ankara.edu.tr

TED University, Rectorate, Department of Common Courses, Ankara, Türkiye

Machine Vision, Natural Language Processing, Modelling and Simulation, Artificial Intelligence (Other), Physical Sciences, Nuclear Physics, Health Physics

Assoc. Prof. Dr. Güray DOĞAN
E-mail: gdogan@akdeniz.edu.tr

Akdeniz University, Faculty of Engineering, Department of Environmental Engineering, Division of Environmental Technologies, Antalya, Türkiye

Climate Change Impact and Adaptation, Air Pollution Modelling and Control, Air Pollution Processes and Air Quality Measurement

Assoc. Prof. Dr. Melike SAPMAZ METİN
E-mail: melikesapmaz@yahoo.com

Trakya University, School of Medicine, Department of Basic Medical Sciences, Division of Histology and Embryology, Edirne, Türkiye

Cell Development, Proliferation and Death, Toxicology, Histology and Embryology

Assoc. Prof. Dr. Pınar YILMAZ
E-mail: pinar.yilmaz@marmara.edu.tr

Marmara University, Faculty of Science, Department of Biology, Division of Plant Diseases and Microbiology, İstanbul, Türkiye

Microbiology, Bacteriology

ISSN 2528-9691

Trakya University Journal of Natural Sciences
www.tujns.org
Volume: 27, Number: 1, April 2026

ISSN 2528-9691

Trakya University Journal of Natural Sciences
www.tujns.org
Volume: 27, Number: 1, April 2026

ISSN 2528-9691

Trakya University Journal of Natural Sciences
www.tujns.org
Volume: 27, Number: 1, April 2026

Contents

Editorial

Research Articles

ISSN 2528-9691

Trakya University Journal of Natural Sciences
www.tujns.org
Volume: 27, Number: 1, April 2026

Trakya University Journal of Natural Sciences, 27(1), 1–2, 2026
DOI: 10.23902/trkjnat.202631
www.tujns.org

Editorial

A new era for TUJNS: quality, transparency, and visibility through professional publishing

Kadri Kiran[1,2]

[1]*Trakya University, Faculty of Sciences, Department of Biology, Edirne, Türkiye*
[2]*Editor-in-Chief, Trakya University Journal of Natural Sciences*

Cite this article as: Kiran, K. (2026). A new era for TUJNS: quality, transparency, and visibility through professional publishing. *Trakya University Journal of Natural Sciences, 27*(1), 1–2. https://doi.org/10.23902/trkjnat.202631

In June 2025, the Trakya University Journal of Natural Sciences (TUJNS) reached an important milestone: by partnering with Galenos Publishing House, the journal entered a new phase of professional publishing and began restructuring its editorial and production processes within a more systematic framework. The rationale for this decision was clear. As TUJNS expanded in thematic range and methodological depth, aligning the journal with a publishing environment that is more standardized, more traceable, more ethically transparent, and more discoverable became essential. Galenos is an independent academic publisher founded in 1997 that strongly emphasizes editorial ethics, scientific integrity, digital infrastructure, and international visibility.

In this new period, we strengthened our workflows so that readers can access high-quality science more rapidly and clearly, while authors can benefit from a more predictable editorial experience. At the same time, the journal's website was updated and given the domain name www.tujns.org. The journal's scope, policies, author and reviewer guidance, and archive access were reorganized in a more integrated and accessible manner. The redesigned website aims to improve the visibility of TUJNS through clearer archive navigation, more consistent article metadata, and more transparent policy pages. As a result, archive browsing and topic-based discovery have become more practical for readers, while key publishing components, including the journal's scope, ethical principles, data availability policy, peer review procedures, and appeal and complaint mechanisms, are now more clearly presented for authors.

One of the most visible outcomes of the professional publishing model launched with Galenos is the standardization of article layout and page design. The journal's typography and page hierarchy now follow a more consistent template, and the resulting uniformity in headings, section flow, figure and table placement, and reference presentation has significantly improved both the readability and the traceability of scientific content, as can already be seen in recent articles published under the new model (Kumru et al., 2025). The active use of the Manuscript Manager online system for submissions and peer review has helped support a more orderly, traceable, and transparent interaction among authors, editors, and reviewers. Therefore, TUJNS has moved toward a structure that not only preserves content quality but also makes its publishing processes more institutionalized and measurable.

As shown in Table 1, although the transition to a professional publisher, the renewed web infrastructure, and the Manuscript Manager submission system took effect only in the second half of 2025, their impact began to be felt almost immediately. Compared with 2024, the total number of submissions increased in 2025; the number of submitting countries increased from 9 to 17; and submissions from outside Türkiye strengthened markedly in both absolute number and proportional share. Notably, the number of submissions from Türkiye remained broadly stable, while its share of total submissions decreased substantially. At the same time, manuscripts began to arrive from a much wider range of countries. Together, these patterns indicate that TUJNS has already begun to gain broader international visibility and appeal. We believe that

E-mail: *kadrikiran@trakya.edu.tr*
ORCID iDs of the author(s): *KK. 0000-0001-7983-0194*

Epub: 1 April 2026, **Published:** 24 April 2026

Table 1. Geographic diversification of manuscript submissions to TUJNS (2024 vs. 2025).

Year	Total submissions	Türkiye (n)	Türkiye (%)	Other countries (n)	Other countries (%)	Submitting countries
2024	62	44	71.0%	18	29.0%	9
2025	103	41	39.8%	62	60.2%	17

this trend will become even more pronounced in the coming years, enabling the journal to move more decisively toward becoming a truly global journal and allowing this internationalization to contribute positively to its scientific quality, selectivity, and overall publishing standards.

The rise in total submissions to TUJNS in 2025, the marked increase in the number of countries submitting to the journal, and especially the strengthening of submissions from outside Türkiye show that the journal's growing international visibility has already begun to produce tangible outcomes. This development is also clearly reflected in the content we publish. In 2024, the journal established a strong thematic foundation ranging from basic biology studies, such as yeast metabolism (Yilmazer & Karaer Uzuner, 2024), to ecological research, such as benthic habitat classification (Tekeli & Aslan, 2024). In 2025, this foundation deepened in a biomedical direction through *in silico* cancer analyses (Tokcaer Keskin, 2025), and in the second issue of 2025, it broadened even further through work in natural product chemistry and biological activity, environmental health, and applied biotechnology (Awad et al., 2025; Ozojiofor et al., 2025; Servi et al., 2025). Taken together, these developments show that TUJNS has not only grown in volume but is also moving toward a more mature publication profile in terms of subject range, methodology, and international reach. As this trend continues, we believe that both the journal's scientific impact and publication quality will be elevated, further consolidating TUJNS's position as a more visible natural sciences journal on the global stage.

References

Awad, A. H., El-Gendy, S., Saeed, Y., & Kamal, S. (2025). Indoor air quality of academia-related workshops based on health complaints. *Trakya University Journal of Natural Sciences, 26*(2), 156–173. https://doi.org/10.23902/trkjnat.565464764

Kumru, E., Edis, G., Sahin, E., Keskin, E., & Akata, I. (2025). Expanding the diversity of *Genea* Vittad. (Ascomycota, Pezizales) in Türkiye: Morphological and molecular insights into newly recorded species. *Trakya University Journal of Natural Sciences, 26*(2), 106–117. https://doi.org/10.23902/trkjnat.1640957

Ozojiofor, O. U., Abdulsalami, M. S., Egbe, N. E., & Haroun, A. A. (2025). Marine-derived *Penicillium oxalicum* M6A as a halotolerant biocatalyst for enzymatic biodegradation and detoxification of the azo dye Direct Red 75. *Trakya University Journal of Natural Sciences, 26*(2), 143–155. https://doi.org/10.23902/trkjnat.5877563254657

Servi, H., Barak, T. H., Sen, A., Kara Ertekin, S., Turker, H., Turkyilmaz Unal, B., & Islek, C. (2025). Chemical composition of endemic *Hypericum bilgehan-bilgilii* Baskose & Savran essential oil and its alpha-glucosidase antidiabetic, anti-inflammatory, cytotoxic and antioxidant potentials. *Trakya University Journal of Natural Sciences, 26*(2), 127–134. https://doi.org/10.23902/trkjnat.5767632345

Tekeli, Z., & Aslan, H. (2024). Identification of benthic habitat types of the Canakkale Strait coast using the European Nature Information System and the Barcelona Convention habitat classification schemes. *Trakya University Journal of Natural Sciences, 25*(2), 133–150. https://doi.org/10.23902/trkjnat.1471425

Tokcaer Keskin, Z. (2025). *In silico* analysis of IL7RA missense mutations in lung, breast and skin cancers. *Trakya University Journal of Natural Sciences, 26*(1), 9–17. https://doi.org/10.23902/trkjnat.1545678

Yilmazer, M., & Karaer Uzuner, S. (2024). Effects of glucose on the cellular respiration in fission yeast expressing human GSK3B gene. *Trakya University Journal of Natural Sciences, 25*(1), 1–10. https://doi.org/10.23902/trkjnat.1339397

Trakya University Journal of Natural Sciences, 27(1), 3–13, 2026
DOI: 10.23902/trkjnat.2025716
www.tujns.org

Research Article

Mitogenome characterization and phylogenetic relationships of Turkish horses (*Equus caballus*)

Saffet Teber[1,2]*

[1]*Erciyes University Faculty of Agriculture, Department of Agricultural Biotechnology, Kayseri, Türkiye*
[2]*Erciyes University, Genome and Stem Cell Center (GenKök), Kayseri, Türkiye*

Cite this article as: Teber, S. (2025). Mitogenome characterization and phylogenetic relationships of Turkish horses (*Equus caballus). Trakya University Journal of Natural Sciences, 27*(1), 3–13. https://doi.org/10.23902/trkjnat.2025716

Abstract

Background: Horses (*Equus caballus*) have been selectively bred for numerous purposes since their domestication, leading to various breeds and increased genetic diversity within the species.

Aims: This study focused on the mitogenome characterization and phylogenetic relationships of Turkish feral (yılkı) and domestic horse breeds.

Methods: In this study, the whole mitogenomes of Turkish feral (yılkı) and domestic horse breeds were first amplified using long-range polymerase chain reaction, sequenced with ~4000× coverage on the Illumina MiSeq platform, and their phylogenetic relationships were subsequently analyzed.

Results: The mitogenomes of Turkish horses were 16657 base pairs in length, encompassing 13 protein-coding genes (PCGs), 22 transfer RNA (tRNA) genes, two ribosomal RNA (rRNA) genes, one origin of replication (O_L), and one non-coding control region (displacement-loop). In the mitogenomes, the *ND6* gene and eight tRNAs ($tRNA^{Gln}$, $tRNA^{Ala}$, $tRNA^{Asn}$, $tRNA^{Cys}$, $tRNA^{Tyr}$, $tRNA^{Ser(UCN)}$, $tRNA^{Glu}$, and $tRNA^{Pro}$) were encoded on the light strand (L), while the origin of replication (O_L), 12 PCGs, 14 tRNAs, and two rRNA genes were encoded on the heavy strand (H). A total of 45 gaps and 68 overlaps were identified in the intergenic regions of the assembled mitogenomes. In the Maximum Likelihood phylogenetic tree, the feral (yılkı) horse clustered within haplogroup A together with breeds from North America, the Middle East, Southern Europe, and Central Asia, while the domestic horse was clustered in haplogroup B together with breeds from Southern Europe and Central Europe.

Özet

Dayanak: Atlar (*Equus caballus*), evcilleştirmenin bir sonucu olarak birçok farklı görev için yetiştirilmiş ve bununla birlikte çeşitli ırklar elde edilerek tür içi genetik çeşitlilik artmıştır.

Amaçlar: Bu çalışma, Türk yılkı ve evcil at ırklarının mitogenom karakterizasyonu ve filogenetik ilişkilerine odaklanmıştır.

Yöntemler: Bu çalışmada Türkiye yılkı ve yerli at ırklarının tüm mitogenomu ilk kez uzun parçalı polimeraz zincir reaksiyonu ile çoğaltılmış, Illumina MiSeq platformu ile ~4000× kapsamla dizilenerek karakterize edilmiş ve filogenetik ilişkileri incelenmiştir.

Bulgular: Türk atlarına ait mitogenomlar 16.657 baz çifti uzunluğunda olup 13 protein kodlayan gen (PCG), 22 transfer RNA (tRNA) geni, iki ribozomal RNA (rRNA) geni, bir replikasyon başlangıç bölgesi (O_L) ve bir kodlamayan kontrol bölgesi (displacement-loop) içermektedir. Mitogenomlarda *ND6* geni ile sekiz tRNA ($tRNA^{Gln}$, $tRNA^{Ala}$, $tRNA^{Asn}$, $tRNA^{Cys}$, $tRNA^{Tyr}$, $tRNA^{Ser(UCN)}$, $tRNA^{Glu}$ ve $tRNA^{Pro}$) hafif iplik (L) üzerinde kodlanırken; replikasyon başlangıç bölgesi (O_L), 12 PCG, 14 tRNA ve iki rRNA geni ağır iplik (H) üzerinde kodlanmıştır. Dizilenmiş mitogenomların intergenik bölgelerinde toplam 45 boşluk (gap) ve 68 bindirme (overlap) belirlenmiştir. Maksimum Olabilirlik filogenetik ağacında yılkı atı; Kuzey Amerika, Orta Doğu, Güney Avrupa ve Orta Asya'dan ırklarla birlikte A haplogrubunda, evcil at ise Güney Avrupa ve Orta Avrupa'dan ırklarla birlikte B haplogrubunda kümelenmiştir.

Sonuç: Bu çalışma, Türk atları için ilk kapsamlı mitogenom verilerini sunarak evrimsel biyoloji, genetik çeşitlilik ve koruma

Edited by: *Coşkun Tez*
***Corresponding Author:** Saffet Teber, **E-mail:** saffetteber@gmail.com*
***ORCID iDs of the author(s):** ST. 0000-0002-9987-3287*

Received: 07 August 2025, **Accepted:** 03 November 2025, **Epub:** 26 November 2025 **Published:** 24 April 2026

Conclusion: This study significantly contributes to evolutionary biology, genetic diversity, and conservation by providing the first comprehensive mitogenome data for Turkish horses, establishing a foundational resource for future comparative and evolutionary genomic research.

çalışmalarına önemli katkı sağlamaktadır. Ayrıca gelecekte yapılacak karşılaştırmalı ve evrimsel genomik araştırmalar için temel bir kaynak oluşturmaktadır.

Keywords: *Equus caballus*, horse, mitogenome, next-generation sequencing, Türkiye

Introduction

Horses, belonging to the genus *Equus* (Mammalia: Perissodactyla: Equidae), were domesticated later than many other mammals. Although not definitive, archaeological and genetic evidence suggests that domestication occurred on the Eurasian steppes approximately 5,000–6,000 years ago (Lippold et al., 2011; Outram et al., 2009). Throughout history, horses have been primarily utilized for agriculture, transportation, sports, and military purposes, thereby enhancing mobility and trade, influencing warfare, and profoundly transforming human civilization (Levine, 2005; Outram et al., 2009). Selective breeding for traits such as strength, size, appearance, temperament, and endurance has driven intraspecific genetic differentiation and increased phenotypic variation among modern breeds (Lippold et al., 2011).

Due to its unique geographical position, Anatolia has served as a critical center for species domestication, animal migration, and transportation routes (MacHugh & Bradley, 2001; Naderi et al., 2008; Rezaei et al., 2010; Zeder, 2008). In Türkiye, the principal horse breeds include Arabian, Anatolian Native, Ayvacık Pony, Canik, Çamardı Kula, Cirit, Çukurova, Eastern Anatolian, Hınıs, Karacabey, Karakacan, Malakan, Thrace (Rumelia), Rahvan, Turkish-Arab, Turkish Nonius, and Uzunyayla (Bayram, 2005; Ozbeyaz & Akcapinar, 2010). In addition to these, there are also horses known as "*yılkı,*" which have been released into the wild, with their use declining due to increased mechanization in Anatolia (Hacan et al., 2018). Despite the rich diversity of native horse populations, the genetic variability of Anatolian horses remains insufficiently explored, and comprehensive studies are needed to uncover their evolutionary and historical contributions to global horse diversity.

Although numerous studies have analyzed complete mitochondrial DNA (mitogenomes) to investigate genetic diversity and population history in horses (Achilli et al., 2012; Ahlawat et al., 2025; Lippold et al., 2011; Sheikh et al., 2019; 2023), complete mitogenome data for horses in Türkiye are still lacking. Previous research on Turkish horses has mainly focused on morphological traits (Celik et al., 2015; Yilmaz, 2013), partial mtDNA regions (particularly the D-loop) (Koban et al., 2012; Köseman et al., 2019), and SSR-based analyses (Aksu et al., 2010; Koban et al., 2012; Koseman et al., 2020). Within the scope of the TURKHAYGEN-1 project, designated to genotype Anatolian domestic animals in Türkiye, 21 SSR markers and mtDNA D-loop sequences were analyzed across four horse breeds. This study revealed high allelic diversity and significant sequence variation (Koban et al., 2012). Similarly, a partial mtDNA (D-loop) study of 28 Turkish horses identified 42 polymorphic sites and 10 haplogroups (Köseman et al., 2019). The presence of repeat sequences in the mitochondrial D-loop region can affect the topology of phylogenetic trees; therefore, whole mitogenome sequencing provides a more reliable and comprehensive approach for assessing genetic diversity and elucidating phylogenetic relationships (Achilli et al., 2012). Sixteen mitogenome haplogroups (A–R) have been identified among 83 horse individuals distributed across Asia, Europe, the Middle East, and the Americas (Achilli et al., 2012).

The advent of next-generation sequencing technologies has enabled rapid and accurate characterization of mitochondrial genomes, which, being smaller and less complex than nuclear genomes, serves as highly effective molecular markers (Brankovics et al., 2017; Yong et al., 2015). The mitochondrial genome is widely employed in studies involving evolutionary analysis, genetic diversity, phylogeny, population structure, and taxonomy (Carpi et al., 2016; Delsuc et al., 2003; Hassanin et al., 2013; Olivieri et al., 2017; Ramos et al., 2018). Moreover, mitochondrial genomes provide critical insights for comparative and evolutionary genomic research (Carpi et al., 2016; Du et al., 2025; Olivieri et al., 2017; Ramos et al., 2018). In mammals, mitochondrial DNA typically ranges from 15 to 18 kilobases in length (Galtier et al., 2009; Jenuth et al., 1996; Saccone et al., 1999) and contains 37 genes, including 22 tRNAs, 2 rRNAs, and 13 protein-coding genes (PCGs), and 1 non-coding control region (Galtier et al., 2009; Iborra et al., 2004).

Accordingly, the objectives of this study were to i) characterize the mitogenomes of Turkish domestic and feral (yılkı) horses, ii) establish a reference mitogenome database for Turkish horse populations, and iii) elucidate phylogenetic relationships among Turkish horses.

Materials and Methods

Sample Collection and Genomic DNA (gDNA) Isolation

Hair samples from one female feral (yılkı) and one domestic horse from Kayseri, Türkiye, were collected and preserved in absolute alcohol at −20 °C until genomic DNA extraction. gDNA was isolated using the DNeasy Blood and Tissue Kit (Cat. No: 69504, QIAGEN) following the manufacturer's protocol. The concentration of extracted gDNA was quantified using the dsDNA Quantification Broad Range kit (Cat. No: Q32850, Thermo Fisher Scientific). DNA purity and integrity were assessed by electrophoresis on a 1% agarose gel and spectrophotometric absorbance measurements. The extracted gDNA samples were subsequently used to amplify the entire mitochondrial genome in two overlapping fragments via long-range polymerase chain reaction (PCR).

PCR, Library Preparation, and Sequencing

The complete mitochondrial genome was amplified in two overlapping fragments using the long-range PCR method with NEB LongAmp® Taq 2X Master Mix (Cat. No: M0287S, NEB). Primer pairs AL1_2024L–BH1_13002H (~11,000 base pairs [bp]) and LuLu_12690L–LuLu_2503H (~6,500 bp) were used, as described by Ibis (2019). PCR reactions and cycling conditions were performed according to Ibis (2019). The concentration of the resulting amplicons was determined using the QuBit dsDNA HS Kit (Cat. No: Q32851, Thermo Fisher Scientific) and diluted to 0.2 ng/μL for sequencing library preparation. Sequencing libraries were prepared using the Illumina Nextera XT DNA Library Preparation Kit (Cat. No: FC-131-1096) and the Nextera XT Index Kit (Cat. No: FC-131-1002) (Illumina), according to the manufacturer's instructions. Library normalization was performed using a bead-based approach, and sequencing was conducted on the Illumina MiSeq platform (Genom and Stem Cell Center, GENKOK, Erciyes University, Kayseri, Türkiye) with the MiSeq Reagent Kit v2.

Bioinformatics Analyses

The raw sequencing reads were imported into Geneious Prime (https://www.geneious.com) for quality assessment, filtering, and subsequent analyses. Adapter sequences were removed from the raw reads, and both low-quality reads (quality score <25) and short reads (<50 bp) were discarded using the BBDuk trimming tool within Geneious Prime. The remaining high-quality reads were mapped against the reference mitochondrial genome (GenBank accession number NC_001640) using the Geneious Mapper algorithm, configured with highest sensitivity/medium parameters and fine-tuning for up to 25 iterations. Annotation information was transferred from the reference mitogenome and applied through Geneious Prime. To further validate the data, the raw reads were also subjected to *de novo* assembly using GetOrganelle software (Jin et al., 2020). Annotation boundaries were manually inspected and confirmed with MITOS2 (Donath et al., 2019) and tRNAscan-SE 2.0 Web Server (Lowe & Chan, 2016). Visualization of tRNA secondary structures was performed using the VARNA Java program (Darty et al., 2009), and circular representations of the mitogenome were generated with CG View web software (Grant & Stothard, 2008). The base composition of the mitogenomes was analyzed using Geneious Prime. Strand asymmetries were determined according to the following formulas: AT skew = [A-T]/[A + T] and GC skew = [G-C]/[G + C].

Phylogenetic Analyses

In addition to the newly obtained mitogenomes, a comparative dataset was assembled, comprising 31 horse mitogenomes and two outgroup mitogenomes from the genus *Equus*, all obtained from the GenBank database (*National Center for Biotechnology Information)* (Table 1). Sequence alignments were generated using the MAFFT algorithm (Katoh et al., 2002) implemented in Geneious Prime with default settings. Following alignment, the D-loop region characterized by a high mutation rate, repetitive motifs, and alignment ambiguities in mammals, was excluded from subsequent phylogenetic reconstruction. Ambiguous regions that introduced uncertainty into the dataset were further removed using the GBlocks v.0.91b program (Castresana, 2000) with default parameters. The optimal base substitution model was identified using jModelTest 2.1.10 (Darriba et al., 2012) based on the AIC criterion. Phylogenetic inference was performed using the Maximum Likelihood (ML) method in MEGA11 (Tamura et al., 2021) with 10,000 bootstrap replicates to assess node support.

Table 1. List of horse mitogenomes used in phylogenetic analyses, including two outgroups.

Name	Species	Accession number	Haplogroup	Reference
Feral-TR	*E. caballus*	PQ573015	A	In this study
JN398377_Efc-m_A	*E. caballus*	JN398377	A	Achilli et al. (2012)
JN398378_Efc-m_A	*E. caballus*	JN398378	A	Achilli et al. (2012)
JN398382_Efc-m_A	*E. caballus*	JN398382	A	Achilli et al. (2012)
JN398384_Efc-m_A	*E. caballus*	JN398384	A	Achilli et al. (2012)
JN398380_Efc-m_A	*E. caballus*	JN398380	A	Achilli et al. (2012)
JN398385_Efc-m_A	*E. caballus*	JN398385	A	Achilli et al. (2012)
JN398381_Efc-m_A	*E. caballus*	JN398381	A	Achilli et al. (2012)
JN398383_Efc-m_A	*E. caballus*	JN398383	A	Achilli et al. (2012)
JN398379_Efc-m_A	*E. caballus*	JN398379	A	Achilli et al. (2012)
Domestic-TR	*E. caballus*	PQ573014	B	In this study
JN398391_Efc-m_B	*E. caballus*	JN398391	B	Achilli et al. (2012)
JN398390_Efc-m_B	*E. caballus*	JN398390	B	Achilli et al. (2012)
JN398386_Efc-m_B	*E. caballus*	JN398386	B	Achilli et al. (2012)
JN398388_Efc-m_B	*E. caballus*	JN398388	B	Achilli et al. (2012)

Table 1. Continued.

Name	Species	Accession number	Haplogroup	Reference
JN398387_Efc-m_B	*E. caballus*	JN398387	B	Achilli et al. (2012)
JN398389_Efc-m_B	*E. caballus*	JN398389	B	Achilli et al. (2012)
JN398398_Efc-m_D	*E. caballus*	JN398398	D	Achilli et al. (2012)
JN398392_Efc-m_C	*E. caballus*	JN398392	C	Achilli et al. (2012)
JN398414_Efc-m_I	*E. caballus*	JN398414	I	Achilli et al. (2012)
JN398413_Efc-m_H	*E. caballus*	JN398413	H	Achilli et al. (2012)
JN398421_Efc-m_L	*E. caballus*	JN398421	L	Achilli et al. (2012)
JN398404_Efc-m_G	*E. caballus*	JN398404	G	Achilli et al. (2012)
JN398401_Efc-m_E	*E. caballus*	JN398401	E	Achilli et al. (2012)
JN398402_Efp-m_F	*E. przewalskii*	JN398402	F	Achilli et al. (2012)
JN398419_Efc-m_J	*E. caballus*	JN398419	J	Achilli et al. (2012)
JN398420_Efc-m_K	*E. caballus*	JN398420	K	Achilli et al. (2012)
JN398449_Efc-m_Q	*E. caballus*	JN398449	Q	Achilli et al. (2012)
JN398446_Efc-m_P	*E. caballus*	JN398446	P	Achilli et al. (2012)
JN398445_Efc-m_O	*E. caballus*	JN398445	O	Achilli et al. (2012)
JN398439_Efc-m_M	*E. caballus*	JN398439	M	Achilli et al. (2012)
JN398440_Efc-m_N	*E. caballus*	JN398440	N	Achilli et al. (2012)
JN398456_Efc-m_R	*E. caballus*	JN398456	R	Achilli et al. (2012)
MK982180_Ea_Tr	*E. asinus*	MK982180		Ibis (2019)
NC_001788_Eaa-m	*E. asinus*	NC_001788		Xu et al. (1996)

Results

Characterization of Mitochondrial Genomes

Complete mitochondrial genomes (mitogenomes) of Turkish horses, each with a total length of 16,657 bp, were obtained at approximately 4000× coverage (Table 2) and deposited in the GenBank database under accession numbers PQ573014 and PQ573015 (Figure 1, Table 2). The mitogenomes obtained for both Turkish horses were identical in overall structure, including the lengths of regions and tRNA sequences, with variations restricted limited to mutations within gene regions. No insertion or deletion (*InDel*) sites were detected between the two mitogenomes. In the mitogenomes of Turkish horses, the *ND6* and eight tRNAs ($tRNA^{Gln}$, $tRNA^{Ala}$, $tRNA^{Asn}$, $tRNA^{Cys}$, $tRNA^{Tyr}$, $tRNA^{Ser(UCN)}$, $tRNA^{Glu}$, and $tRNA^{Pro}$) were encoded on the light strand (L), while the O_L origin, 12 *PCGs*, 14 *tRNAs*, and two rRNA genes were located on the heavy strand (H) (Figure 1, Table 3). The nucleotide composition results revealed that the mitogenomes of the feral (yılkı) and domestic horses were highly similar. In the feral (yılkı) horse, the nucleotide composition comprised 32.20% adenine (A), 25.90% thymine (T), 13.40% guanine (G), and 28.60% cytosine (C), while in the domestic horse, it consisted of 32.20% adenine (A), 25.80% thymine (T), 13.40% guanine (G), and 28.60% cytosine (C). Both mitogenomes exhibited identical A + T (58%) and G + C (42%) ratios (Table 4).

A total of 45 gaps and 68 overlaps were identified within the intergenic regions of the domestic and feral horse mitogenomes. The longest overlap, spanning 43 bp, was located between *ATP8* and *ATP6*, whereas the longest gap, 8 bp in length, occurred between $tRNA^{Ser}$ and $tRNA^{Asp}$ (Table 3).

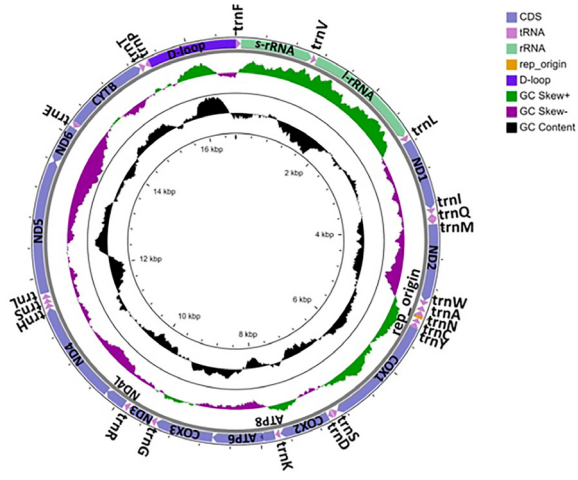

Figure 1. Circular map of the mitochondrial genome obtained from a Turkish horse.

Table 2. Sequencing read statistics for Turkish horse mitogenomes.

Isolate	Location	Raw sequences		Filtered sequences		Coverage (X)	Mitogenome length (bp)
		Read count	Average sequence length (bp)	Read count	Average sequence length (bp)		
EqCabTR1 *(PQ573014)*	Kayseri	495458	224.5	357324	195.9	4183.4	16657
EqCabTR2 *(PQ573015)*	Kayseri	487640	219.4	357336	191.4	4019.1	16657

Table 3. Annotation of genomic regions in the mitogenomes of Turkish horses.

Region	Start–stop		Length	Direction	Intergenic region	Start codon	Stop codon	Anti-codon
$tRNA^{Phe}$	1	70	70	H	0			GAA
s-rRNA	71	1046	976	H	0			
$tRNA^{Val}$	1047	1113	67	H	0			TAC
l-rRNA	1114	2693	1580	H	0			
$tRNA^{Leu}$	2694	2768	75	H	2			TAA
ND1	2771	3727	957	H	−1	ATG	TAG	
$tRNA^{Ile}$	3727	3795	69	H	−3			GAT
$tRNA^{Gln}$	3793	3865	73	L	2			TTG
$tRNA^{Met}$	3868	3936	69	H	0			CAT
ND2	3937	4977	1041	H	−2	ATA	TAG	
$tRNA^{Trp}$	4976	5045	70	H	5			TCA
$tRNA^{Ala}$	5051	5119	69	L	1			TGC
$tRNA^{Asn}$	5121	5193	73	L	0			GTT
rep origin	5195	5227	33	H	−2			
$tRNA^{Cys}$	5226	5291	66	L	0			GCA
$tRNA^{Tyr}$	5292	5358	67	L	1			GTA
COX1	5360	6904	1545	H	−3	ATG	TAA	
$tRNA^{Ser}$	6902	6970	69	L	8			TGA
$tRNA^{Asp}$	6979	7045	67	H	0			GTC
COX2	7046	7729	684	H	3	ATG	TAA	
$tRNA^{Lys}$	7733	7800	68	H	1			TTT
ATP8	7802	8005	204	H	−43	ATG	TAG	
ATP6	7963	8643	681	H	−1	ATG	TAA	
COX3	8643	9426	784	H	0	ATG	T--	
$tRNA^{Gly}$	9427	9495	69	H	0			TCC
ND3	9496	9842	347	H	0	ATA	TA-	
$tRNA^{Arg}$	9843	9911	69	H	1			TCG
ND4L	9913	10209	297	H	−7	ATG	TAA	
ND4	10203	11580	1378	H	0	ATG	T--	

Table 3. Continued.

Region	Start–stop		Length	Direction	Intergenic region	Start codon	Stop codon	Anti-codon
$tRNA^{His}$	11581	11649	69	H	0			GTG
$tRNA^{Ser}$	11650	11709	60	H	1			GCT
$tRNA^{Leu}$	11711	11780	70	H	6			TAG
ND5	11787	13601	1815	H	−17	ATG	TAA	
ND6	13585	14112	528	L	0	ATG	TAA	
$tRNA^{Glu}$	14113	14181	69	L	4			TTC
CYTB	14186	15325	1140	H	0	ATG	AGA	
$tRNA^{Thr}$	15326	15398	73	H	1			TGT
$tRNA^{Pro}$	15400	15465	66	L	0			TGG
D-loop	15466	16657	1192	H	0			

Table 4. Nucleotide compositions of the mitogenomes of Turkish horses.

Feral (domestic)	Length	%	A%	T%	G%	C%	A + T%	G + C%	AT skew	GC skew
Total length	16657	100	32.20	25.90 (25.80)	13.40	28.60	58	42	0.10	-0.36
PCGs	11401	68.42	31.30 (31.40)	26.10	12.10	30.40	57.50	42.50	0.09	-0.43
rRNAs	2556	15.34	36.70	23.80 (27.70)	16.90	22.60 (22.70)	60.50 (60.40)	39.50 (39.60)	0.21	-0.14
tRNAs	1517	9.10	34.70	27.20	15.60	22.50	62	38	0.12	-0.18
D-loop	1192	7.15	27.10 (27.30)	26.30 (26.20)	15.70 (15.50)	30.90 (31.00)	53.40	46.60	0.01	-0.32

PCG = protein-coding gene.

The combined length of the 13 PCG in the Turkish horses mitogenomes was 11401 bp, representing 68.42% of the total mitogenome length. These genes encoded 3,799 amino acids. Among the encoded amino acids, 4.3% were acidic, 6.9% basic, 11.2% charged, 29.3% polar uncharged, and 61.9% hydrophobic. Of the PCGs, 11 genes initiated with the "ATG" codon, whereas *ND2* and *ND3* began with 'ATA'. The stop codon "TAA" was present in six genes, while "TAG" appeared in *ND1*, *ND2*, and *ATP8*, and "AGA" was found in *CYTB*. Incomplete stop codons were detected as "T—" in *COX3* and *ND4*, and "TA-" n *ND3* (Table 3). Codon usage frequencies in the Turkish horse mitogenomes are provided in Table 5. The most frequently used codons were "CUA" (285), "AUC" (208), "AUA" (186), and "UUC" (160), while the least frequent codon was "CGG" (3).

The total length of rRNA genes was 2556 bp comprising the 12S-rRNA (s-rRNA) was 976 bp and the 16S-rRNA (l-rRNA) was 1580 bp, located between $tRNA^{Phe}$ and $tRNA^{Leu}$(UUR), and separated by $tRNA^{Val}$. The tRNA genes ranged in length from 60 to 75 bp. All tRNAs exhibited the typical cloverleaf secondary structure, except for $tRNA^{Ser}$(AGY), which lacked a dihydrouridine (DHU) arm (Figure 2). The replication origin, 32 bp in length, was situated within the WANCY tRNA cluster. The control region (D-loop) measured 1,192 bp, making it the longest non-coding sequence in the mitogenome.

Phylogenetic Analyses

The mitogenomes of Turkish horses, together with those representing other horse haplogroups available in the GenBank database, were analyzed using the GTR + I substitution model under the ML method with 10,000 bootstrap replications (Table 1, Figure 3). In the resulting phylogenetic tree, the Turkish feral horse (yılkı) clustered with strong bootstrap support within Haplogroup A, grouping with other A haplogroup horses from various geographic regions, including North America (Chincoteague Pony, JN398377), the Middle East (Caspian Pony, Arab, and unidentified Syrian and Iranian breeds, JN398378, JN398384, JN398380, and JN398383), Southern Europe (Maremmano breed, JN398379, JN398381, and JN398382), and Central Asia (Akhal-Teke breed, JN398385). In contrast, the domestic Turkish horse was positioned with high bootstrap support within Haplogroup B, together with undefined Syrian breeds from the Middle East (JN398391 and JN398389), Maremmano and undefined Italian breeds from Southern Europe (JN398390, JN398387, and JN398388), and the Westphalian breed from Central Europe (JN398386).

Table 5. Codon usage in the mitogenomes of Turkish horses.

		Domestic horse		Feral horse	
Amino acid	**Codon**	**Count**	**Fraction**	**Count**	**Fraction**
Ala	GCG	5.00	0.02	5.00	0.02
	GCA	76.00	0.32	76.00	0.32
	GCT	51.00	0.22	51.00	0.22
	GCC	103.00	0.44	103.00	0.44
Cys	TGT	5.00	0.22	5.00	0.22
	TGC	18.00	0.78	18.00	0.78
Asp	GAT	26.00	0.40	26.00	0.39
	GAC	39.00	0.60	40.00	0.61
Glu	GAG	19.00	0.20	20.00	0.21
	GAA	78.00	0.80	77.00	0.79
Phe	TTT	78.00	0.33	77.00	0.32
	TTC	160.00	0.67	161.00	0.68
Gly	GGG	30.00	0.14	30.00	0.14
	GGA	99.00	0.46	99.00	0.46
	GGT	21.00	0.10	22.00	0.10
	GGC	64.00	0.30	63.00	0.29
His	CAT	22.00	0.21	22.00	0.21
	CAC	81.00	0.79	81.00	0.79
Ile	ATT	131.00	0.39	132.00	0.39
	ATC	208.00	0.61	207.00	0.61
Lys	AAG	10.00	0.10	10.00	0.10
	AAA	87.00	0.90	87.00	0.90
Leu	TTG	21.00	0.03	21.00	0.03
	TTA	61.00	0.10	61.00	0.10
	CTG	38.00	0.06	38.00	0.06
	CTA	285.00	0.46	285.00	0.46
	CTT	68.00	0.11	68.00	0.11
	CTC	140.00	0.23	140.00	0.23
Met	ATG	45.00	0.19	45.00	0.20
	ATA	186.00	0.81	185.00	0.80
Asn	AAT	40.00	0.27	40.00	0.27
	AAC	110.00	0.73	109.00	0.73
Pro	CCG	7.00	0.04	7.00	0.04
	CCA	76.00	0.40	76.00	0.40
	CCT	36.00	0.19	36.00	0.19
	CCC	72.00	0.38	72.00	0.38
Gln	CAG	8.00	0.09	8.00	0.09
	CAA	83.00	0.91	83.00	0.91
Arg	CGG	3.00	0.05	3.00	0.05
	CGA	37.00	0.58	37.00	0.58
	CGT	8.00	0.13	7.00	0.11

Table 5. Continued.

		Domestic horse		Feral horse	
Amino acid	**Codon**	**Count**	**Fraction**	**Count**	**Fraction**
	CGC	16.00	0.25	17.00	0.27
Ser	AGT	12.00	0.04	12.00	0.04
	AGC	53.00	0.17	53.00	0.17
	TCG	9.00	0.03	9.00	0.03
	TCA	121.00	0.40	121.00	0.40
	TCT	36.00	0.12	36.00	0.12
	TCC	73.00	0.24	73.00	0.24
Thr	ACG	11.00	0.03	11.00	0.03
	ACA	144.00	0.46	144.00	0.46
	ACT	57.00	0.18	57.00	0.18
	ACC	103.00	0.33	103.00	0.33
Val	GTG	25.00	0.13	25.00	0.13
	GTA	78.00	0.42	79.00	0.42
	GTT	31.00	0.17	31.00	0.16
	GTC	53.00	0.28	53.00	0.28
Trp	TGG	8.00	0.08	8.00	0.08
	TGA	96.00	0.92	96.00	0.92
Tyr	TAT	47.00	0.37	47.00	0.37
	TAC	81.00	0.63	81.00	0.63

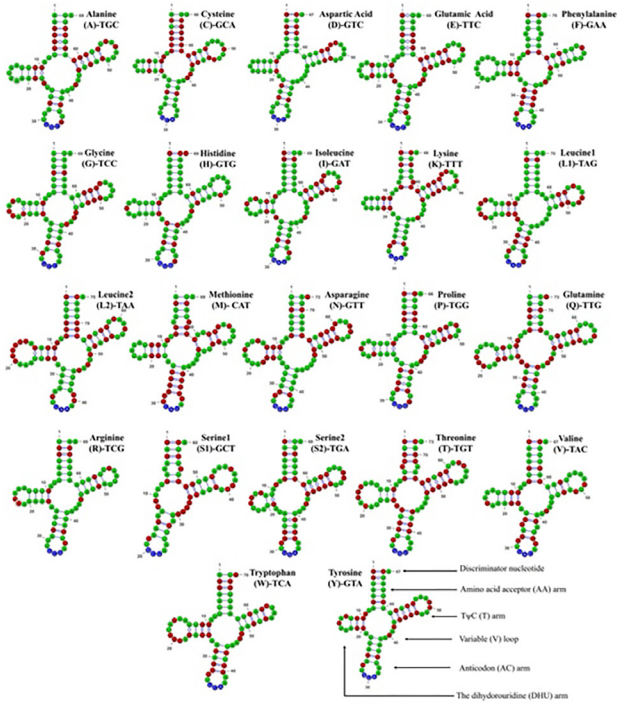

Figure 2. Predicted secondary structures of the 22 tRNAs identified in the mitochondrial genome of Turkish horses.

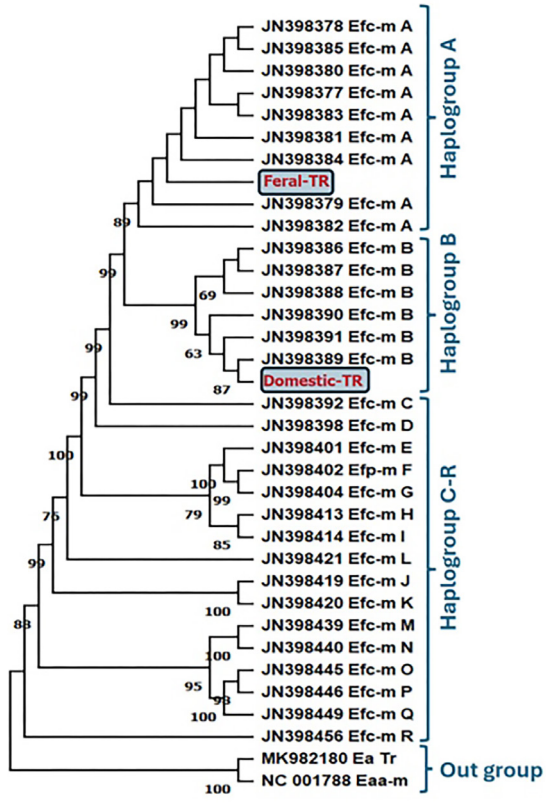

Figure 3. Phylogenetic tree constructed using the ML method, showing Turkish horses and reference samples from GenBank. ML = maximum likelihood.

Discussion

The two horse mitogenomes obtained in the present study exhibited structural features similar to previously reported horse mitogenomes (Achilli et al., 2012; Lippold et al., 2011; Luo et al., 2011; Sarkissian et al., 2015; Vilstrup et al., 2013), consisting of a circular molecule containing 37 gene regions (Figure 1, Table 2). According to the GenBank database, a total of 535 complete mitogenomes are currently available under the name *Equus caballus*, representing horse breeds from various regions worldwide, with lengths ranging from 16,403 to 16,681 bp (https://www.ncbi. nlm.nih.gov/nuccore (txid9796[Organism:noexp]): Access date: 02.11.2024). The reference horse mitogenome (*E. caballus*) (NC_001640/X79547) has a total length of 16,660 bp (Xiufeng & Árnason, 1994), which closely corresponds to that of the Turkish horse breeds (16,657 bp). The variation in sequence length observed among existing horse mitogenomes is primarily attributed to differences in the length of the control region sequence. Although both modern and ancient horse mitogenomes have been reported, the mitogenomes of Turkish horses were previously unavailable and are presented here for the first time.

The general structural characteristics of the Turkish horse mitogenomes were consistent with those of other vertebrates. The nucleotide composition displayed a distinct bias toward Adenine and Thymine (58% A + T), a common feature in vertebrate mitogenomes. Similarly, the presence of numerous intergenic gaps (45 bp) and overlaps (68 bp) reflects the compact organization typical for horse and other vertebrate mitogenomes (Guo et al., 2016; Ibis, 2019; Krause et al., 2008; Rohland et al., 2007; Wada et al., 2010). The occurence of incomplete stop codons ("T--" in *COX3* and *ND4*, and "TA-" in *ND3*) aligns with the reference horse mitogenome and other vertebrates (Ibis, 2019; Xiufeng & Árnason, 1994) where these codons function equivalently to complete stop codons (Ojala et al., 1981).

The codon usage pattern in Turkish horses, with "CUA," "AUC," and "AUA" being the most frequently used codons, was highly similar to that of the donkey mitogenome from Türkiye, suggesting a conserved codon usage pattern within the *Equus* genus (Ibis, 2019). The structural features of the tRNA genes in Turkish horses were also consistent with those typically observed in mammalian mitogenomes. The 22 identified tRNAs ranged from 60 to 75 bp in length, and all but one displayed the canonical cloverleaf secondary structure. The single exception, $tRNA^{Ser}$(AGY), lacked the DHU arm, a variation that is known to be functionally acceptable (Steinberg & Cedergren, 1994). Furthermore, the lengths of the ribosomal RNA genes (976 bp for s-rRNA and 1,580 bp for l-rRNA) and the D-loop region (1,192 bp), were nearly identical to those reported in the reference horse mitogenome (975 bp, 1,581 bp and 1,192 bp, respectively), indicating a high degree of structural conservation (Xiufeng & Árnason, 1994). The observed length differences among horse mitogenomes are mainly attributed to variations in the repeat regions within the D-loop, and it has been noted that variation in the number of repeat motifs within the D-loops, a regon known for its heteroplasmic nature (Xiufeng & Árnason, 1994).

In the ML phylogenetic tree reconstructed in this study, the Turkish horses mitogenomes clustered in accordance with the haplogroups defined by Achilli et al. (2012). The mitogenome of the Turkish feral horse grouped within Haplogroup A, whereas the domestic Turkish horse clustered within Haplogroup B. The findings indicate that the Turkish feral horse shares a common maternal lineage with other horses in Haplogroup A, which is widely distributed across global horse populations and may represent an ancient or broadly dispersed lineage. In contrast, the domestic Turkish horse's placement in Haplogroup B suggests a distinct maternal lineage, likely reflecting differences in breeding history or geographical origin. Consistent with previous research, a previous study reported that the Przewalski horse in Eurasia possesses only the F and J-K lineages, with the greatest haplogroup diversity observed on the Asian continent (Achilli et al., 2012). The broad distribution of Haplogroup A across North America, the Middle East, and Central Asia supports the hypothesis of a shared evolutionary history among geographically distinct horse populations. Similarly, the inclusion of the Turkish domestic horse in Haplogroup B indicates connections with Central and Southern European populations. The identification of Haplogroup B in both Italy and East Asia (Achilli et al., 2012; Cardinali et al., 2016) further highlights its historical dissemination and emphasizes the pivotal role of Anatolia in horse domestication history. The domestication process, which originated in the Eurasian steppes and subsequently spread across various regions (Lippold et al., 2011; Outram et al., 2009), underscores Türkiye's position as an integral part of this evolutionary and cultural pathway.

Conclusion

In conclusion, the complete mitochondrial genomes of Turkish horses, presented here for the first time, provide a valuable foundation for future genetic studies, including assessments of genetic diversity and conservation efforts within Türkiye. Further investigation of mitogenomic and genomic data from additional Turkish horse breeds, combined with comparative analyses across global datasets, will enhance understanding of horse evolutionary history and contribute to conservation strategies.

Ethics

Ethics Committee Approval: This study was approved by the Erciyes University Local Ethics Committee for Animal Experiments (approval number: 23/061, dated: 05.04.2023).

Data Sharing Statement: All data are available within the study.

Footnotes

Conflict of Interest: The author(s) have no conflicts of interest to declare.

Funding: This study was supported by The Scientific Research Projects (BAP) of Erciyes University (Project No.: FBAÜ-2023-12262).

References

Achilli, A., Olivieri, A., Soares, P., Lancioni, H., Kashani, B. H., Perego, U. A., & Torroni, A. (2012). Mitochondrial genomes from modern horses reveal the major haplogroups that underwent domestication. *Proceedings of the National Academy of Sciences, 109*(7), 2449–2454. https://doi.org/10.1073/pnas.1111637109

Ahlawat, S., Sharma, U., Niranjan, S. K., Chhabra, P., Arora, R., Sharma, R., Singh, K. V., Vijh, R. K., & Mehta, S. C. (2025). Unraveling the maternal heritage: Identifying the complex origins of indigenous Indian horse and pony breeds through mitochondrial genome analysis. *Mammalian Genome, 36*(1), 118–128. https://doi.org/10.1007/s00335-024-09963-0

Aksu, S., Aktoprakligil, D., Koban, E., & Aslan, O. (2010). Genetic characterization of native horse breeds within the scope of protection of gene resources and biodiversity. *Research Journal of Biological Sciences, 3*, 121–130. http://www.aensiweb.com/RJBS/

Bayram, D. (2005). The phenotypic characteristics of horses raised in Van region. *Van Veterinary Journal, 16*(1), 85–88. https://dergipark.org.tr/en/pub/vanvetj/issue/40274/487006

Brankovics, B., Dam, P., Rep, M., Hoog, G. S., Lee, J. A., Waalwijk, C., & Diepeningen, A. D. (2017). Mitochondrial genomes reveal recombination in the presumed asexual *Fusarium oxysporum* species complex. *BMC Genomics, 18*, 1–14. https://doi.org/10.1186/s12864-017-4066-7

Cardinali, I., Lancioni, H., Giontella, A., Capodiferro, M. R., Capomaccio, S., Buttazzoni, L., Biggio, G. P., Cherchi, R., Albertini, E., Olivieri, A., Cappelli, K., Achilli, A., & Silvestrelli, M. (2016). An overview of ten Italian horse breeds through mitochondrial DNA. *PLOS ONE, 11*(4), e0153004. https://doi.org/10.1371/journal.pone.0153004

Carpi, G., Kitchen, A., Kim, H. L., Ratan, A., Drautz-Moses, D. I., McGraw, J. J., & Schuster, S. C. (2016). Mitogenomes reveal diversity of the European Lyme borreliosis vector *Ixodes ricinus* in Italy. *Molecular Phylogenetics and Evolution, 101*, 194–202. https://doi.org/10.1016/j.ympev.2016.05.028

Castresana, J. (2000). Selection of conserved blocks from multiple alignments for their use in phylogenetic analysis. *Molecular Biology and Evolution, 17*(4), 540–552. https://doi.org/10.1093/oxfordjournals.molbev.a026334

Celik, S., Coskun, F., & Yilmaz, O. (2015). Investigation by different orthogonal methods of body sizes of Turkish spotted horses according to age group. *COMU Journal of Agriculture Faculty, 3*(1), 81–87. https://dergipark.org.tr/tr/pub/comuagri/issue/27156/285456

Darriba, D., Taboada, G. L., Doallo, R., & Posada, D. (2012). jModelTest 2: More models, new heuristics and high-performance computing. *Nature Methods, 9*(8), 772. https://doi.org/10.1038/nmeth.2109

Darty, K., Denise, A., & Ponty, Y. (2009). VARNA: Interactive drawing and editing of the RNA secondary structure. *Bioinformatics, 25*(15), 1974–1975. https://doi.org/10.1093/bioinformatics/btp250

Delsuc, F., Stanhope, M. J., & Douzery, E. J. P. (2003). Molecular systematics of armadillos (Xenarthra, Dasypodidae): Contribution of maximum likelihood and Bayesian analyses of mitochondrial and nuclear genes. *Molecular Phylogenetics and Evolution, 28*(2), 261–275. https://doi.org/10.1016/S1055-7903(03)00036-8

Donath, A., Jühling, F., Al-Arab, M., Bernhart, S. H., Reinhardt, F., Stadler, P. F., & Bernt, M. (2019). Improved annotation of protein-coding genes boundaries in metazoan mitochondrial genomes. *Nucleic Acids Research, 47*(20), 10543–10552. https://doi.org/10.1093/nar/gkz833

Du, W., Sun, Q., Hu, S., Yu, P., Kan, S., & Zhang, W. (2025). *Equus* mitochondrial pangenome reveals independent domestication imprints in donkeys and horses. *Scientific Reports, 15*(1), 6803. https://doi.org/10.1038/s41598-025-65526-6

Galtier, N., Nabholz, B., Glémin, S., & Hurst, G. D. D. (2009). Mitochondrial DNA as a marker of molecular diversity: A reappraisal. *Molecular Ecology, 18*(22), 4541–4550. https://doi.org/10.1111/j.1365-294X.2009.04380.x

Grant, J. R., & Stothard, P. (2008). The CGView server: A comparative genomics tool for circular genomes. *Nucleic Acids Research, 36*(suppl_2), 181–184. https://doi.org/10.1093/nar/gkn179

Guo, X., Pei, J., Chu, M., Wu, X., Bao, P., Ding, X., & Yan, P. (2016). The complete mitochondrial genome of Hequ horse. *Mitochondrial DNA Part A, 27*(6), 4657–4658. https://doi.org/10.3109/19401736.2015.1101548

Hacan, Ö., Koçak, S., Çelikeoğlu, K., Bozkurt, Z., Erdoğan, M., & Tekerli, M. (n.d.). The independent spirit of Turkey: Wild horse.

Hassanin, A., An, J., Ropiquet, A., Nguyen, T. T., & Couloux, A. (2013). Combining multiple autosomal introns for studying shallow phylogeny and taxonomy of Laurasiatherian mammals: Application to the tribe Bovini. *Molecular Phylogenetics and Evolution, 66*(3), 766–775. https://doi.org/10.1016/j.ympev.2012.11.003

Ibis, O. (2019). Türkiye Anadolu Eşeği (*Equus asinus*)'nin mitogenom karakterizasyonu ve filogenetik ilişkileri. *Türkiye Tarımsal Araştırmalar Dergisi, 6*(3), 257–267. https://doi.org/10.19159/tutad.460381

Iborra, F. J., Kimura, H., & Cook, P. R. (2004). The functional organization of mitochondrial genomes in human cells. *BMC Biology, 2*, 1–14. https://doi.org/10.1186/1741-7007-2-9

Jenuth, J. P., Peterson, A. C., Fu, K., & Shoubridge, E. A. (1996). Random genetic drift in the female germline explains the rapid segregation of mammalian mitochondrial DNA. *Nature Genetics, 14*(2), 146–151. https://doi.org/10.1038/ng1096-146

Jin, J. J., Yu, W. B., Yang, J. B., Song, Y., DePamphilis, C. W., Yi, T. S., & Li, D. Z. (2020). GetOrganelle: A fast and versatile toolkit for accurate de novo assembly of organelle genomes. *Genome Biology, 21*, 1–31. https://doi.org/10.1186/s13059-020-02154-5

Katoh, K., Misawa, K., Kuma, K. I., & Miyata, T. (2002). MAFFT: A novel method for rapid multiple sequence alignment based on fast Fourier transform. *Nucleic Acids Research, 30*(14), 3059–3066. https://doi.org/10.1093/nar/gkf436

Koban, E., Denizci, M., Aslan, O., Aktoprakligil, D., Aksu, S., Bower, M., & Arat, S. (2012). High microsatellite and mitochondrial diversity in Anatolian native horse breeds shows Anatolia as a genetic conduit between Europe and Asia. *Animal Genetics, 43*(4), 401–409. https://doi.org/10.1111/j.1365-2052.2011.02284.x

Koseman, A., Ozsensoy, Y., Erdogan, M., Yarali, C., Toprak, B., Zengin, K., & Seker, I. (2020). Investigation of genetic variations using microsatellite markers in colored horses in Turkey. *Russian Journal of Genetics, 56*, 592–602. https://doi.org/10.1134/S1022795420040073

Köseman, A., Ozsensoy, Y., Erdogan, M., Yaralı, C., Toprak, B., Zengin, K., & Şeker, İ. (2019). Investigation of genetic structures of coloured horses by mtDNA D-loop sequence analysis in Turkey. *Kafkas Üniversitesi Veteriner Fakültesi Dergisi, 25*(6), 769–778. https://doi.org/10.9775/kvfd.2019.22056

Krause, J., Unger, T., Noçon, A., Malaspinas, A. S., Kolokotronis, S. O., Stiller, M., & Hofreiter, M. (2008). Mitochondrial genomes reveal an explosive radiation of extinct and extant bears near the Miocene–Pliocene boundary. *BMC Evolutionary Biology, 8*, 1–12. https://doi.org/10.1186/1471-2148-8-224

Levine, M. A. (2005). Domestication and early history of the horse. In *The domestic horse: The origins, development and management of its behaviour*. Cambridge University Press.

Lippold, S., Matzke, N. J., Reissmann, M., & Hofreiter, M. (2011). Whole mitochondrial genome sequencing of domestic horses reveals incorporation of extensive wild horse diversity during domestication. *BMC Evolutionary Biology, 11*, 1–10. https://doi.org/10.1186/1471-2148-11-147

Lowe, T. M., & Chan, P. P. (2016). tRNAscan-SE online: Integrating search and context for analysis of transfer RNA genes. *Nucleic Acids Research, 44*(W1), 54–57. https://doi.org/10.1093/nar/gkw413

Luo, Y., Chen, Y., Liu, F., Jiang, C., & Gao, Y. (2011). Mitochondrial genome sequence of the Tibetan wild ass (*Equus kiang*). *Mitochondrial DNA, 22*(1–2), 6–8. https://doi.org/10.3109/10425171003618702

MacHugh, D. E., & Bradley, D. G. (2001). Livestock genetic origins: Goats buck the trend. *Proceedings of the National Academy of Sciences, 98*(10), 5382–5384. https://doi.org/10.1073/pnas.101126598

Naderi, S., Rezaei, H. R., Pompanon, F., Blum, M. G., Negrini, R., Naghash, H. R., & Taberlet, P. (2008). The goat domestication process inferred from large-scale mitochondrial DNA analysis of wild and domestic individuals. *Proceedings of the National Academy of Sciences, 105*(46), 17659–17664. https://doi.org/10.1073/pnas.0804782105

Ojala, D., Montoya, J., & Attardi, G. (1981). tRNA punctuation model of RNA processing in human mitochondria. *Nature, 290*(5806), 470–474. https://doi.org/10.1038/290470a0

Olivieri, A., Sidore, C., Achilli, A., Angius, A., Posth, C., Furtwängler, A., & Torroni, A. (2017). Mitogenome diversity in Sardinians: A genetic window onto an island's past. *Molecular Biology and Evolution, 34*(5), 1230–1239. https://doi.org/10.1093/molbev/msx086

Outram, A. K., Stear, N. A., Bendrey, R., Olsen, S., Kasparov, A., Zaibert, V., & Evershed, R. P. (2009). The earliest horse harnessing and milking. *Science, 323*(5919), 1332–1335. https://doi.org/10.1126/science.1168594

Ozbeyaz, C., & Akcapinar, H. (2010). *Course notes of horse breeding*. Ankara University Faculty of Veterinary Medicine.

Ramos, B., González-Acuña, D., Loyola, D. E., Johnson, W. E., Parker, P. G., Massaro, M., & Vianna, J. A. (2018). Landscape genomics: Natural selection drives the evolution of mitogenome in penguins. *BMC Genomics, 19*, 1–17. https://doi.org/10.1186/s12864-018-4840-7

Rezaei, H. R., Naderi, S., Chintauan-Marquier, I. C., Taberlet, P., Virk, A. T., Naghash, H. R., & Pompanon, F. (2010). Evolution and taxonomy of the wild species of the genus *Ovis* (Mammalia, Artiodactyla, Bovidae). *Molecular Phylogenetics and Evolution, 54*(2), 315–326. https://doi.org/10.1016/j.ympev.2009.09.008

Rohland, N., Malaspinas, A. S., Pollack, J. L., Slatkin, M., Matheus, P., & Hofreiter, M. (2007). Proboscidean mitogenomics: Chronology and mode of elephant evolution using mastodon as outgroup. *PLoS Biology, 5*(8), 207. https://doi.org/10.1371/journal.pbio.0050207

Saccone, C., Giorgi, C., Gissi, C., Pesole, G., & Reyes, A. (1999). Evolutionary genomics in Metazoa: The mitochondrial DNA as a model system. *Gene, 238*(1), 195–209. https://doi.org/10.1016/S0378-1119(99)00270-X

Sarkissian, C., Vilstrup, J. T., Schubert, M., Seguin-Orlando, A., Eme, D., Weinstock, J., & Orlando, L. (2015). Mitochondrial genomes reveal the extinct *Hippidion* as an outgroup to all living equids. *Biology Letters, 11*(3), 20141058. https://doi.org/10.1098/rsbl.2014.1058

Sheikh, A., Ahmed, M. M. M., Mutawakil, M. H. Z., Saini, K. S., Alsulaimany, F. A., Hanafy, A., & Sabir, J. S. M. (2019). SNP mapping and phylogenetic analysis of Saudi Arabian horse breeds based on mitochondrial genome sequencing. *Indian Journal of Experimental Biology, 58*, 225–230.

Sheikh, A. (2023). Mitochondrial DNA sequencing of Kehilan and Hamdani horses from Saudi Arabia. *Saudi Journal of Biological Sciences, 30*(9), 103741. http://nopr.niscpr.res.in/handle/123456789/51265

Steinberg, S., & Cedergren, R. (1994). Structural compensation in atypical mitochondrial tRNAs. *Nature Structural Biology, 1*(8), 507–510. https://doi.org/10.1038/nsb0894-507

Tamura, K., Stecher, G., & Kumar, S. (2021). MEGA11: Molecular evolutionary genetics analysis version 11. *Molecular Biology and Evolution, 38*(7), 3022–3027. https://doi.org/10.1093/molbev/msab120

Vilstrup, J. T., Seguin-Orlando, A., Stiller, M., Ginolhac, A., Raghavan, M., Nielsen, S. C., & Orlando, L. (2013). Mitochondrial phylogenomics of modern and ancient equids. *PLOS ONE, 8*(2), 55950. https://doi.org/10.1371/journal.pone.0055950

Wada, K., Okumura, K., Nishibori, M., Kikkawa, Y., & Yokohama, M. (2010). The complete mitochondrial genome of the domestic red deer (*Cervus elaphus*) of New Zealand and its phylogenic position within the family Cervidae. *Animal Science Journal, 81*(5), 551–557. https://doi.org/10.1111/j.1740-0929.2010.00762.x

Xiufeng, X., & Árnason, Ú. (1994). The complete mitochondrial DNA sequence of the horse, *Equus caballus*: Extensive heteroplasmy of the control region. *Gene, 148*(2), 357–362. https://doi.org/10.1016/0378-1119(94)90766-3

Xu, X., Gullberg, A., & Arnason, U. (1996). The complete mitochondrial DNA (mtDNA) of the donkey and mtDNA comparisons among four closely related mammalian species-pairs. *Journal of Molecular Evolution, 43*, 438–446. https://doi.org/10.1007/BF02337515

Yilmaz, O. (2013). Two new genetic sources specific to Ardahan–Igdir–Kars Basin: Colored horse and Dikkulak dog. *Turkey-Kars Governorship International Sarıkamış Symposium.* https://www.sariktur.org.tr/

Yong, H. S., Song, S. L., Lim, P. E., Chan, K. G., Chow, W. L., & Eamsobhana, P. (2015). Complete mitochondrial genome of *Bactrocera arecae* (Insecta: Tephritidae) by next-generation sequencing and molecular phylogeny of Dacini tribe. *Scientific Reports, 5*(1), 15155. https://doi.org/10.1038/srep15155

Zeder, M. A. (2008). Domestication and early agriculture in the Mediterranean Basin: Origins, diffusion, and impact. *Proceedings of the National Academy of Sciences, 105*(33), 11597–11604. https://doi.org/10.1073/pnas.0801317105

Trakya University Journal of Natural Sciences, 27(1), 14–29, 2026
DOI: 10.23902/trkjnat.2025715
www.tujns.org

Research Article

In silico characterization of *Plasmodium falciparum* FabI: Implications for the design of antimalarial drugs

Abdelaziz Brkhan[1], Hajar Almuree[1], Dima Joujeh[2]*

[1]*University of Aleppo, Faculty of Technical Engineering, Department of Biotechnology Engineering, Aleppo, Syria*
[2]*University of Aleppo, Faculty of Technical Engineering, Ph.D. in Biotechnology Engineering, Aleppo, Syria*

Cite this article as: Brkhan, A., Almuree, H., & Joujeh, D. (2025). In silico characterization of Plasmodium falciparum FabI: Implications for the design of antimalarial drugs. *Trakya University Journal of Natural Sciences, 27*(1), 14–29. https://doi.org/10.23902/trkjnat.2025715

Abstract

Background: The FabI enzyme, crucial for fatty acid synthesis, represents a promising target for antimalarial drug development, particularly in *Plasmodium falciparum*.

Aims: To comprehensively characterize the *P. falciparum* FabI enzyme by elucidating its evolutionary relationships, physicochemical properties, and detailed structural features using advanced *in silico* methodologies.

Methods: An extensive computational analysis was performed on 25 FabI protein sequences, encompassing those from *P. falciparum* as well as diverse protozoan and bacterial species.

Results: The predicted physicochemical properties indicated that *P. falciparum* FabI is comparatively larger, more hydrophilic, and exhibits a higher isoelectric point than its bacterial homologs. Sequence alignment and phylogenetic reconstruction revealed a clear evolutionary divergence of *P. falciparum* FabI from bacterial orthologs, supporting its origin through an ancient horizontal gene transfer event and its localization to the apicoplast. Further sequence analysis identified two conserved motifs mapped to a central NAD(P) binding Rossmann-fold domain, which is essential for the enzyme's catalytic function. The predicted three-dimensional (3D) structure of *P. falciparum* FabI exhibited a characteristic α/β-fold architecture forming a dimeric complex. A persistent challenge was noted in the N-terminal region, predicted to be a flexible, cleavable signal/transit peptide, accounting for its lower structural confidence. PDBsum analysis delineated its structural organization, consisting of 19 α-helices and 9 β-strands, with a notable absence of disulfide bridges. Additionally, proteolytic digestion produced multiple cleavage patterns. CASTp 3.0 analysis revealed a complex active site comprising several sub-pockets and key functional residues, along with buried cavities.

Özet

Dayanak: Yağ asidi sentezi için çok önemli olan FabI enzimi, özellikle *Plasmodium falciparum*'da sıtma ilacı geliştirme için umut verici bir hedef oluşturmaktadır.

Amaçlar: Çalışma, gelişmiş in silico metodolojileri kullanarak evrimsel ilişkilerini, fizikokimyasal özelliklerini ve ayrıntılı yapısal özelliklerini aydınlatarak *P. falciparum* FabI enzimini kapsamlı bir şekilde karakterize etmeyi amaçlamıştır.

Yöntemler: *Plasmodium falciparum*'dan ve çeşitli protozoa ve bakteri türlerinden alınan 25 FabI protein dizisi üzerinde kapsamlı bir hesaplamalı analiz gerçekleştirilmiştir.

Bulgular: Tahmin edilen fizikokimyasal özellikler, *P. falciparum* FabI'nin bakteriyel homologlarına kıyasla daha büyük, daha hidrofilik ve daha yüksek izoelektrik noktaya sahip olduğunu göstermiştir. Sekans hizalama ve filogenetik rekonstrüksiyon, *P. falciparum* FabI'nin bakteriyel ortologlarından açık bir evrimsel farklılık gösterdiğini ortaya koymuş ve bunun eski bir yatay gen transferi olayı yoluyla kökenini ve apikoplastta lokalizasyonunu desteklemiştir. Daha ileri sekans analizi, enzimin katalitik fonksiyonu için gerekli olan merkezi NAD(P) bağlayıcı Rossmann-fold alanına eşlenen iki korunmuş motif tanımladı. *P. falciparum* FabI'nin tahmin edilen üç boyutlu (3D) yapısı, dimerik bir kompleks oluşturan karakteristik bir α/β-fold mimarisi sergiledi. N-terminal bölgesinde, esnek, bölünebilir bir sinyal/geçiş peptidi olduğu tahmin edilen ve yapısal güvenilirliğinin düşük olmasına neden olan kalıcı bir zorluk tespit edildi. PDBsum analizi, disülfür köprülerinin belirgin bir şekilde yokluğuyla, 19 α-heliks ve 9 β-iplikçikten oluşan yapısal organizasyonunu ortaya koydu. Ek olarak, proteolitik sindirim çoklu bölünme modelleri üretti. CASTp 3.0 analizi, gömülü boşluklarla birlikte birkaç alt cep ve önemli fonksiyonel kalıntılardan oluşan karmaşık bir aktif bölge ortaya çıkardı.

Edited by: *Özkan Danış*

***Corresponding Author:** Dima Joujeh, **E-mail:** dimajoujeh@gmail.com*

***ORCID iDs of the authors:** AB. 0009-0007-4042-9062; HA. 0009-0005-3177-7693; DJ. 0000-0001-8240-9886*

Received: 13 August 2025, **Accepted:** 7 October 2025, **Epub:** 12 November, 2025, **Published:** 24 April 2026

Conclusion: These comprehensive structural and functional insights into the unique features of *P. falciparum* FabI provide a strong foundation for the rational design of novel antimalarial drugs.

Sonuç: *Plasmodium falciparum* FabI'nin benzersiz özelliklerine ilişkin bu kapsamlı yapısal ve fonksiyonel bilgiler, yeni sıtma ilaçlarının rasyonel tasarımı için güçlü bir temel sağlar.

Keywords: *Plasmodium falciparum*, FabI enzyme, phylogenetic analysis, conserved motifs, protein structure prediction

Introduction

Malaria, a febrile disease, is caused by *Plasmodium* parasites transmitted to humans through the bites of infected female *Anopheles* mosquitoes (A. Pandey et al., 2022). The growing resistance of malaria parasites to first-line therapies highlights the urgent need to develop new classes of antimalarial agents (Kane et al., 2022). Consequently, the systematic identification and detailed characterization of unique parasite biochemical pathways have become essential, as these pathways provide promising targets for both novel drug discovery and the optimization of existing or emerging therapeutic strategies (A. K. Pandey et al., 2019).

These intracellular parasites depend on lipids for their growth, proliferation, and developmental progression. They utilize a prokaryotic-like Type II fatty acid synthesis (FAS-II) system housed within the apicoplast, an organelle crucial for the parasite's blood-stage replication and overall pathogenicity (A. Pandey et al., 2022). Thus, the parasite's fatty acid biosynthesis (FAS-II) pathway has emerged as a compelling therapeutic target due to its essential role in parasite viability (Kane et al., 2022). The distinct organization of the FAS-II pathway, when compared to the mammalian FAS-I complex, highlights its unique potential as a selective drug target.

FabI, the principal enoyl-ACP reductase within the FAS II system, is among the most extensively studied enzyme of this pathway. It is widely conserved across multiple microorganisms, including *Staphylococcus aureus*, *Escherichia coli*, *Bacillus subtilis*, *Francisella tularensis*, *Burkholderia pseudomallei*, *Bacillus anthracis*, *Pseudomonas aeruginosa*, as well as the protozoan parasites *Toxoplasma gondii* (Hopf et al., 2022), and *Plasmodium falciparum* (Kane et al., 2022). Given its pivotal role across a broad spectrum of pathogens, an in-depth understanding of FabI's molecular and structural characteristics is of critical importance for guiding drug discovery efforts.

In recent years, *in silico* methodologies have become integral to modern drug discovery, offering powerful means to characterize molecular targets and facilitate rational inhibitor design. These computational approaches allow precise delineation of a protein's molecular properties, encompassing sequence architecture, physicochemical behavior, and evolutionary lineage, while identifying key functional elements such as conserved motifs, catalytic residues, and signal peptides. Such insights can be obtained prior to experimental validation or large-scale screening.

This study aimed to comprehensively characterize the *P. falciparum* FabI enzyme by elucidating its evolutionary relationships, physicochemical features, and intricate structural organization using advanced *in silico* techniques. The resulting findings establish a strong foundation for the rational design of selective FabI inhibitors, thereby contributing to the development of next-generation antimalarial therapeutics.

Materials and Methods

Sequence Retrieval and Alignment

Twenty-five enoyl-ACP reductase (FabI) sequences, representing both bacterial and eukaryotic (protozoan) origins, were retrieved from the UniProt (https://www.uniprot.org) (The UniProt Consortium, 2024). Sequence selection emphasized phylogenetic diversity and clinical relevance to human pathogenicity. Accession numbers for all sequences are listed in Supplementary Material (Table S1). Multiple sequence alignments were generated using the Clustal Omega algorithm (https://www.ebi.ac.uk/Tools/msa/clustalo/) (Madeira et al., 2024). The resulting alignments were visually examined and verified through manual inspection with the UniProt Alignment Viewer to ensure accurate alignment of conserved residues and the logical placement of gap regions.

Determination of Physicochemical Parameters

The physicochemical characteristics of FabI enzymes were computed from their amino acid sequences using the ExPASy ProtParam tool (http://web.expasy.org/protparam) (Gasteiger et al., 2005). The calculated parameters included molecular weight, isoelectric point (pI), extinction coefficient (EC), instability index (II), aliphatic index (AI), and grand average of hydropathicity (GRAVY).

Phylogenetic Tree Construction

A phylogenetic tree was constructed using the aligned amino acid sequences with the Simple Phylogeny tool available through EMBL-EBI (https://www.ebi.ac.uk/jdispatcher/phylogeny/simple_phylogeny) (Madeira et al., 2024). Evolutionary relationships among the taxa were inferred using the Neighbor-Joining algorithm, which operates on a pairwise distance matrix derived from the multiple sequence alignment.

Primary Structure Analysis

Primary structure analysis was conducted using the ExPASy ProtParam tool, specifically to determine the amino acid composition. Conserved protein motifs were identified with the MEME suite (http://meme.sdsc.edu/meme/meme.html) (Bailey & Elkan, 1994). Protein domains were examined using InterProScan (http://www.ebi.ac.uk/interpro/search/sequence/) (Blum et al., 2024).

Secondary Structure Analysis

The secondary structural content of the FabI sequences, including alpha helices, beta turns, extended strands, and random coils, was predicted using the SOPMA method available through the Network Protein Sequence Analysis (NPS@) server (https://npsa-prabi.ibcp.fr/cgibin/npsa_automat.pl?page=npsa_sopma.html) (Geourjon & Deléage, 1995).

Tertiary structure prediction for *P. falciparum* FabI was generated using ColabFold, an optimized AlphaFold2 implementation created for accelerated protein structure prediction. ColabFold was assessed through the COSMIC platform (https://cosmic-cryoem.org/tools/colabfold/) (Mirdita et al., 2021), and the resulting three-dimensional (3D) structural model was subsequently visualized using PyMOL.

The predicted 3D structure was further interpreted through the PDBsum tool (https://www.ebi.ac.uk/thornton-srv/databases/cgibin/pdbsum/GetPage.pl?pdbcode=index.html), which provided a secondary motif map and topology diagram. Predicted disulfide bridge patterns were evaluated using the CYS-REC tool (http://softberry.com/berry.phtml), allowing the identification of probable disulfide bonding between available Cysteine (Cys) residues.

Tertiary Structure Validation

The *P. falciparum* FabI model underwent extensive validation using multiple computational approaches. QMEAN (https://swissmodel.expasy.org/qmean) was employed to assess both global and local model quality (Benkert et al., 2010; Studer et al., 2014, 2019). Additional validation was performed through the SAVES server (https://servicesn.mbi.ucla.edu/SAVES) (Colovos & Yeates, 1993; Laskowski et al., 1996), which produced a Ramachandran plot using PROCHECK, and evaluated structural error rates using ERRAT. The Ramachandran plot served as the primary stereochemical quality indicator, while ERRAT confirmed crystallographic model accuracy. Predicted salt bridges were also analyzed using dedicated protein analysis tools.

Functional Analysis

Proteolytic cleavage sites, including those produced by chemical reagents, were predicted using PeptideCutter (http://web.expasy.org/peptide_cutter/) (Gasteiger et al., 2005). Signal peptide regions were prediction with SignalP 6.0 (https://services.healthtech.dtu.dk/services/SignalP-6.0/) (Teufel et al., 2022), which detects all five known signal peptide types (Sec/SPI, Sec/SPII, Tat/SPI, Tat/SPII, Sec/SPIII). The Computed Atlas of Surface Topography of proteins (CASTp 3.0) server (http://sts.bioe.uic.edu/) was used to identify active binding site pockets and to analyze the protein surface topography (Tian et al., 2018).

Results

Sequence Retrieval and Alignment

The protein sequences of FabI enzymes from a range of bacterial strains and protozoa were retrieved from UniProt, with FASTA format sequences selected and prioritized based on pathogens relevant to human health, as indicated in UniProt (Table S1).

Homology searching followed by multiple sequence alignment of the 25 FabI enzyme sequences revealed several regions of high conservation. The alignment displayed two particularly well conserved motifs, AKAALES (326–332), and RVNAISAGPIRT (348–359) (Figure 1). In addition to these conserved stretches, a set of 16 amino acid positions demonstrated 100% conservation across all sequences examined. These residues included Glycine (Gly) 128, Aspartic acid (Asp) 206, Histidine (His) 252, Serine (Ser) 282, Ser 285, Tyrosine (Tyr) 309, Tyr319, Methionine 323, Alanine (Ala) 338, Gly434, Leucine (Leu) 440,

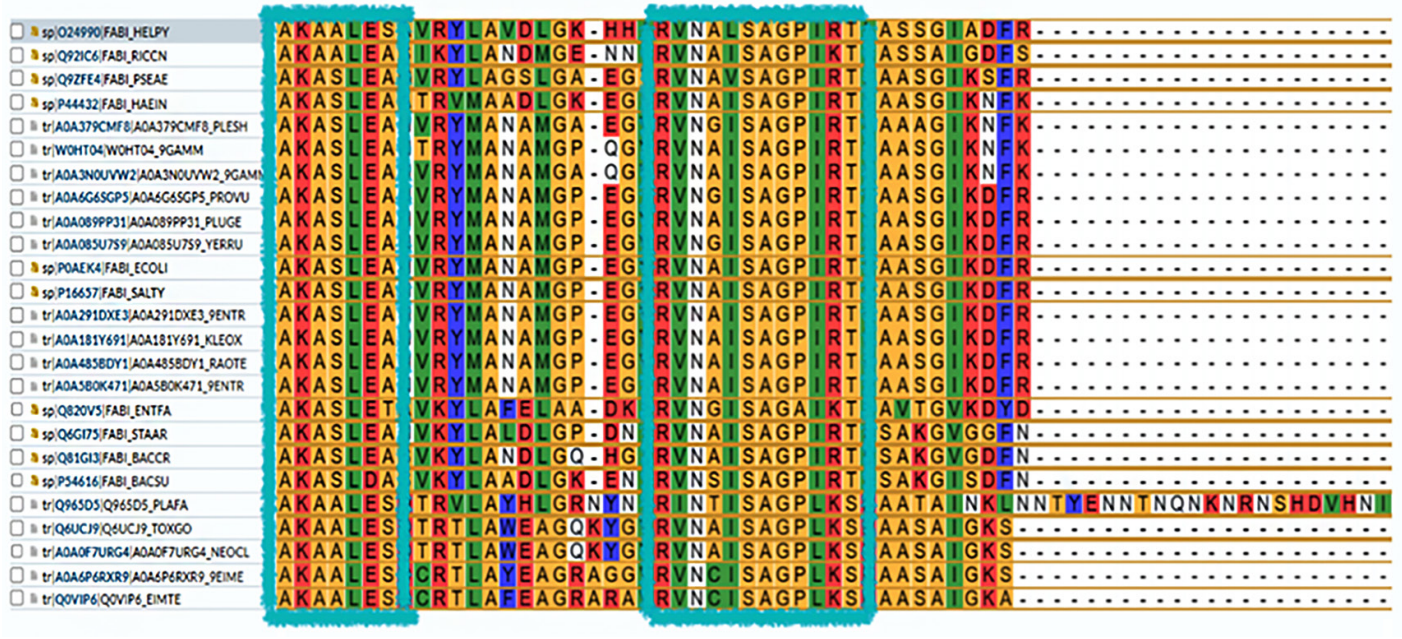

Figure 1. Close-up of multiple sequence alignment showing conserved motifs (cyan boxes).

Ser 442, Gly450, Valine 455, Asp456, and Gly458. Collectively, these fully conserved residues represented a braod spectrum of amino acid classes, including: nonpolar (Ala, Leu, Gly, Methionine, Valine), polar (Ser), aromatic (Tyr), acidic (Asp), and basic (His).

Phylogenetic Analysis of FabI Enzyme Sequences

The unrooted phylogenetic tree (Figure 2), constructed from FabI enzyme protein sequences, depicts the evolutionary relationships among the sampled bacterial and protozoan taxa. *Plasmodium* (evolutionary distance: 0.31445) is positioned within a distinct and well-supported clade of Apicomplexa parasites, clustering with *Neospora* (0.05476), *Toxoplasma* (0.06203), *Cyclospora* (0.10345), and *Eimeria* (0.11790). These taxa form a compact clade with short internal branch lengths, suggesting a recent common evolutionary origin among these protozoan parasites. The entire *Plasmodium*-containing clade remains clearly separated from all bacterial taxa represented in the tree, indicating substantial evolutionary divergence.

Physicochemical Properties of FabI Enzymes

Analysis of physicochemical properties demonstrated both shared features and distinct differences across FabI enzymes from protozoa and bacteria (Table 1). FabI enzymes from protozoan parasites were generally longer (393–432 amino acids), and possessed higher molecular weights (approximately 40–49 kDa), whereas bacterial FabI proteins were typically shorter (250–275 amino acids) with lower molecular weights (26–30 kDa).

Isoelectric point (pI) values also displayed a clear taxonomic distinction: protozoan FabI enzymes displayed higher pIs (6.01–9.11), with *P. falciparum* displaying the highest pI at 9.11, while most bacterial FabI enzymes had lower pI values (5.15–5.77). Notably, *Helicobacter pylori* (pI 7.1) and *Rickettsia conorii* (pI 7.71) were exceptions to this trend.

The AI indicated that a tendency toward greater aliphatic content among bacterial FabI proteins (85.92–105.72) compared to protozoan FabI (77.92–91.46), with *Enterococcus faecalis* demonstrating the highest value. GRAVY values similarly highlighted these differences: protozoan FabI enzymes displayed more hydrophilic properties (negative GRAVY values from 0.046 to −0.683), with *P. falciparum* being the most hydrophilic, whereas bacterial FabI enzymes were slightly hydrophobic (positive GRAVY values from 0.012 to 0.191). Instability indices for most FabI proteins were below 40, indicating overall structural stability, although *P. falciparum* showed a slightly higher instability value (45.92).

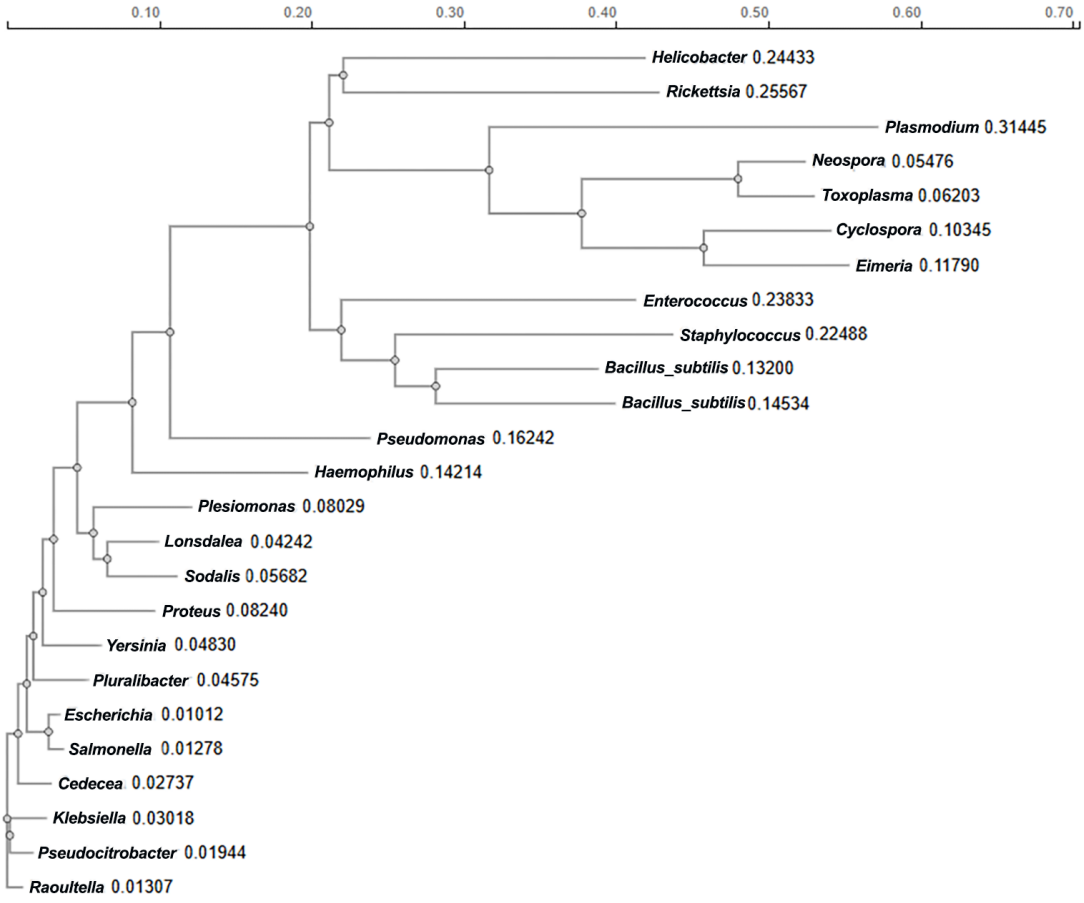

Figure 2. Unrooted phylogenetic tree of FabI enzyme sequences.

Protozoan FabI enzymes also contained larger numbers of both acidic (R- values from 35–47) and basic (R+ values from 35–57) residues compared to their bacterial FabI sequences, which typically contained fewer acidic (25–33) and basic (21–28) residues. In accordance with this trend, ECs were higher for protozoan enzymes (27390–48360) than for bacterial ones (13075–21680), aside from *H. pylori* and *R. conorii*, which again showed higher values than typical bacterial species.

Primary Sequence Analysis

The primary structure analysis, represented by the amino acid composition chart (Figure 3), highlights the relative abundance of amino acids within the FabI enzyme. Ala, is the most prevalent amino acid, comprising 16% of the total sequence, followed by Leu at 13.1%, Asparagine at 12.7%, Gly at 12.1%, and Ser at 10.6 (Figure 3). In contrast, several amino acids occur at very low frequencies. Tryptophan is the least abundant, accounting for only 1.2%, followed by Cys at 1.9% and His at 2.9%. The low proportion of Cys is particularly notable and suggests a minimal role in disulfide bond formation or catalytic stabilization within the overall protein structure.

A motif analysis of 25 FabI protein sequences (Figure 4) revealed that Motif 2 (FRKMLAHCEAVTPJRRTVTI-EDVGNSAAFLCSDLSAGISGEVLHVDGGFS) and Motif 3 (FLTGKRILVTGVASKLSIAYGIAQAMHREGAELAF TYQNEK) were present across all 25 sequences. By contrast, Motif 1 (YLGAERAIPNYNVMGLAKASLEANVRYMANAM GPEGVRVNAISAGPIRTL) was found exclusively in bacterial sequences, with complete absence in the five parasitic FabI sequences. Additionally, although motif architecture in bacterial sequences showed highly consistent spatial arrangement and spacing, parasitic sequences demonstrated variability in motif positioning.

Table 1. Physicochemical properties of FabI enzymes.

Organism	Length	Molecular weight	pI	AI	II	GRAVY	EC	R-	R+
Bacillus cereus	256	27740.46	5.45	97.54	34.38	-0.048	13075	33	26
B. subtilis	258	27873.74	5.67	97.21	37.09	0.017	14565	31	25
Cedecea neteri	263	28001.1	5.32	93.95	20.68	0.162	16180	31	24
C. cayetanensis	393	40696.96	6.01	84.07	35.55	-0.083	30495	39	35
E. tenella (Coccidian parasite)	410	42856.81	6.86	91.46	38.31	0.046	27390	38	38
E. faecalis	250	26766.7	5.29	105.72	13.22	0.124	19035	29	24
E. coli	262	27863.94	5.58	92.44	21.14	0.163	16180	29	24
Haemophilus influenzae	262	28119.1	5.35	92.18	23.65	0.07	17545	31	26
H. pylori	275	29981.45	7.1	100.04	27.5	0.012	28880	27	27
Klebsiella oxytoca	262	27909.01	5.59	93.97	27.39	0.151	21680	29	24
Lonsdalea populi	262	27862.81	5.15	94.31	23.56	0.184	14690	29	22
N. caninum	411	43022.49	7.11	81.34	35.78	-0.094	48360	39	39
P. falciparum	432	49755.30	9.11	77.92	45.92	-0.683	45395	47	57
Plesiomonas shigelloides (Aeromonas shigelloides)	263	27805.71	5.39	92.17	28.07	0.169	17670	28	22
P. gergoviae (Enterobacter gergoviae)	262	28014.15	5.77	94.35	21.11	0.145	20190	29	25
Proteus vulgaris	262	28234.34	5.48	89.85	22.04	0.023	19035	31	26
Pseudocitrobacter	262	28015.13	5.6	94.69	24.84	0.148	17670	29	24
P. aeruginosa	265	28005.82	5.64	85.92	24.03	0.028	20065	30	26
Raoultella terrigena (Klebsiella terrigena)	262	27928.05	5.6	94.103	25.08	0.174	16180	29	24
R. conorii	260	28211.34	7.71	91.23	24.55	-0.059	31525	25	26
S. typhimurium	262	27760.82	5.57	92.44	20.58	0.191	16180	28	23
S. praecaptivus	262	27916.86	5.37	92.48	26.1	0.175	17670	27	21
S. aureus	256	27991.87	5.64	99.8	33.91	-0.143	13410	33	28
T. gondii	417	43658.17	8.54	85.25	34.87	-0.086	41370	37	39
Yersinia ruckeri	262	27889.98	5.59	92.48	24.77	0.159	16180	28	23

InterPro analysis of Motif 1, Motif 2, and Motif 3 further confirmed that all three motifs map to a single conserved functional domain, corresponding to the NAD(P) binding Rossmann-fold domain.

Secondary Structure Composition of FabI Enzymes

Analysis of predicted secondary structure composition for FabI enzymes across bacterial and protozoan taxa revealed conserved structural features along with notable taxonomic differences (Table 2). Alpha helices represented the predominant secondary structural element in all FabI enzymes, consistently accounting for more than 42% of the sequences, with *P. falciparum* displaying the highest value at 49.77%.

In contrast, protozoan FabI enzymes exhibited lower proportions of extended strands (9.92%–14.39%) and beta turns (5.12%–6.94%) compared with bacterial sequences, which typically contained extended strands ranging from 15.65% to 19.38%, and beta turns between 7.31% and 9.16%. Correspondingly, FabI proteins from *Cyclospora cayetanensis*, *Eimeria tenella*, *Neospora caninum*, and *T. gondii* contained notably higher proportions of random coils (35.49%–38.42%) than most bacterial FabI enzymes (25%–31%), with *P. falciparum* serving as an exception among protozoa at 30.56%.

Significantly, the prediction for disulfide bridges was "none" across all FabI sequences analyzed, indicating a consistent absence of disulphide-bond stabilization within the predicted structures.

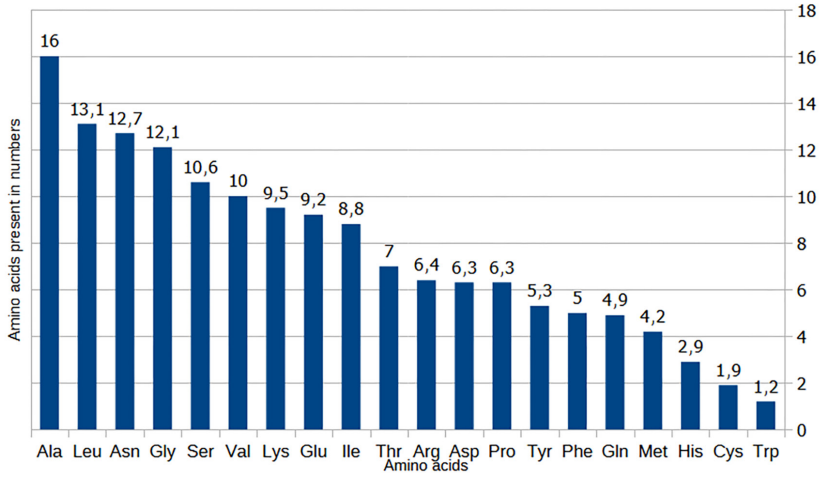

Figure 3. Amino acid composition of FabI enzymes.

Table 2. Predicted secondary structure composition of FabI enzymes from various organisms.

Organism	Entry	Alpha helix	Extended strand	Beta turn	Random coil	Disulfide bridges prediction
B. cereus	Q81GI3	45.70%	18.36%	7.42%	28.52%	None
B. subtilis	P54616	43.02%	19.38%	8.91%	28.68%	None
C. neteri	A0A291DXE3	44.11%	18.25%	8.37%	29.28%	None
C. cayetanensis	A0A6P6RXR9	45.55%	9.92%	6.11%	38.42%	None
E. tenella (Coccidian parasite)	Q0VIP6	46.83%	12.20%	5.12%	35.85%	None
E. faecalis	Q820V5	46.40%	18.80%	8.00%	26.80%	None
E. coli	P0AEK4	45.80%	17.94%	8.02%	28.24%	None
H. influenzae	P44432	43.89%	17.56%	8.02%	30.53%	None
H. pylori (Campylobacter pylori)	O24990	45.09%	16.73%	8.00%	30.18%	None
K. oxytoca	A0A181Y691	43.13%	18.70%	9.16%	29.01%	None
L. populi	A0A3N0UVW2	45.04%	15.65%	8.40%	30.92%	None
N. caninum	A0A0F7URG4	45.26%	12.17%	5.84%	36.74%	None
P. falciparum	Q965D5	49.77%	12.73%	6.94%	30.56%	None
P. shigelloides (Aeromonas shigelloides)	A0A379CMF8	44.87%	16.35%	8.37%	30.42%	None

Table 2. Continued.

Organism	Entry	Alpha helix	Extended strand	Beta turn	Random coil	Disulfide bridges prediction
Pluralibacter gergoviae (Enterobacter gergoviae)	A0A089PP31	45.80%	17.18%	8.40%	28.63%	None
P. vulgaris	A0A6G6SGP5	47.71%	16.79%	8.40%	27.10%	None
Pseudocitrobacter	A0A5B0K471	47.71%	17.18%	8.40%	26.72%	None
P. aeruginosa	Q9ZFE4	44.53%	16.98%	8.30%	30.19%	None
R. terrigena (Klebsiella terrigena)	A0A485BDY1	46.56%	18.32%	8.40%	26.72%	None
R. conorii	Q92IC6	42.31%	19.23%	7.31%	31.15%	None
Salmonella typhimurium	P16657	44.66%	18.32%	8.02%	29.01%	None
Sodalis praecaptivus	W0HT04	45.04%	16.79%	7.63%	30.53%	None
S. aureus	Q6GI75	42.19%	18.36%	8.98%	30.47%	None
T. gondii	Q6UCJ9	43.88%	14.39%	6.24%	35.49%	None
Y. ruckeri	A0A085U7S9	48.47%	17.18%	8.78%	25.57%	None

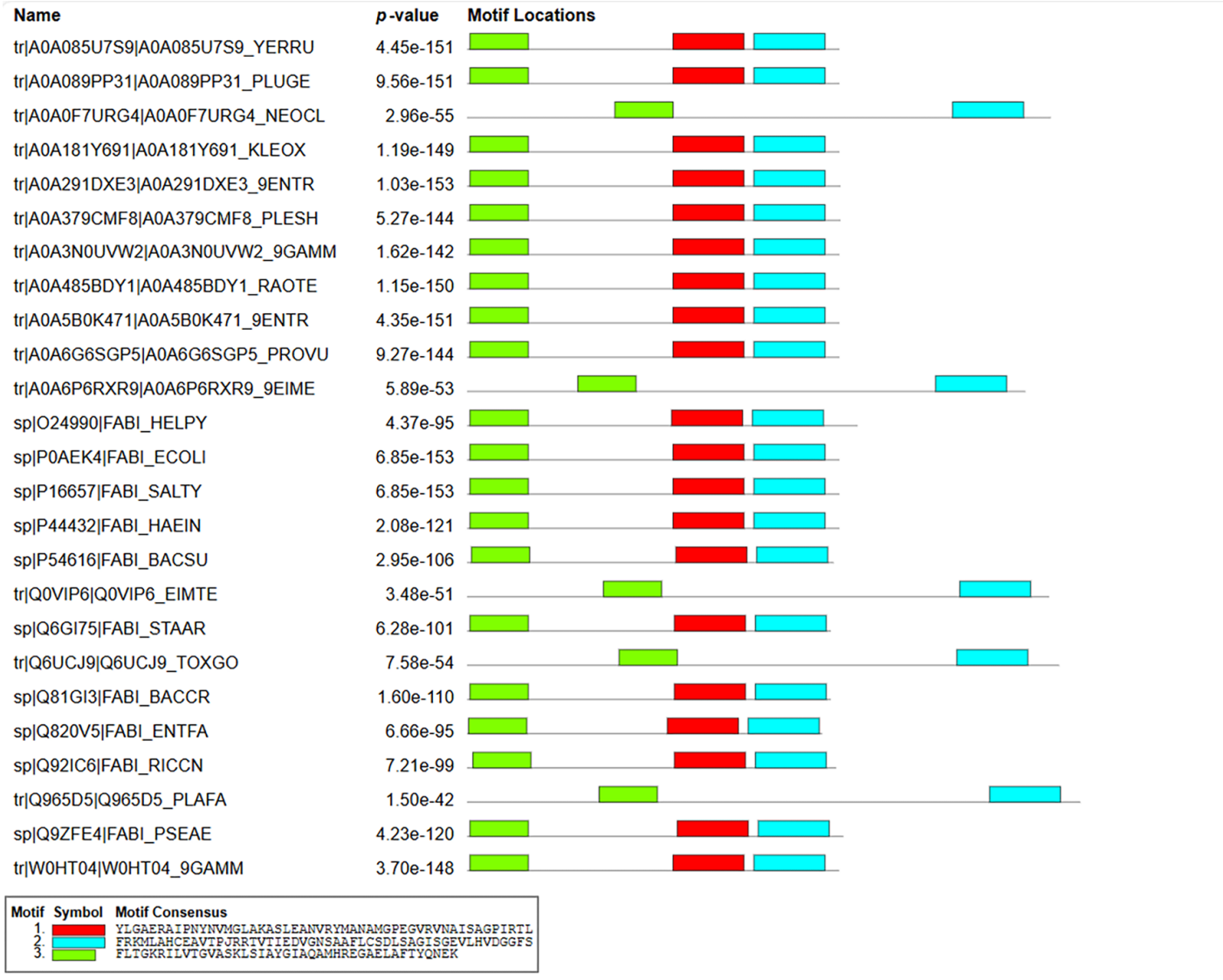

Figure 4. Conserved motifs identified in FabI enzyme sequences.

Further structural interpretation via PDBsum, generated using the predicted *P. falciparum* FabI structure as a reference model (Figure 5), revealed a mixed alpha/beta fold typical of metabolic enzymes.

The FabI structure is predominantly helical, comprising 19 alpha helices (H1–H19) (Figure 6), distributed throughout the polypeptide chain, along with 9 beta-strands forming multiple beta sheets that contribute to the protein's core stability. These regular secondary structure elements are interconnected via loops and turns, forming the characteristic topological arrangement depicted in the PDBsum analysis.

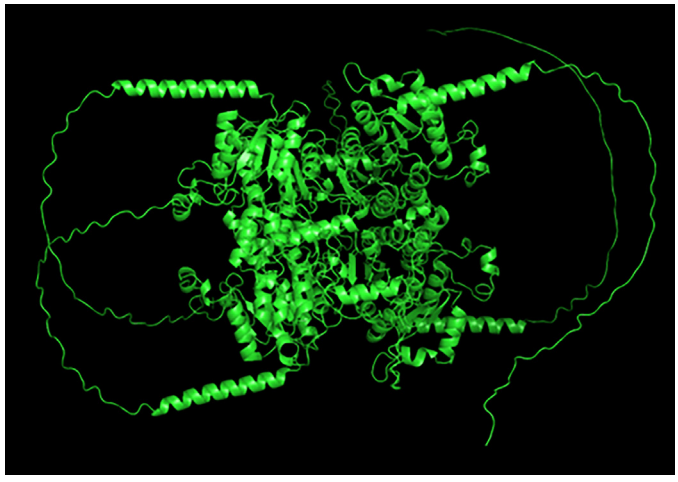

Figure 5. Predicted 3D structure of *P. falciparum* FabI enzyme.

Tertiary Structure Analysis

The stereochemical quality of the predicted FabI enzyme structure was assessed using a Ramachandran plot generated by PROCHECK (Figure 7). The results demonstrated that the majority of amino acid residues occupy energetically favorable conformational regions. Specifically, 71.5% (1144 residues) were located in the most favored regions, while 21.8% (349 residues) fell within additionally allowed regions. A further 6.4% (103 residues) were present in generously allowed regions. Only 4 residues (0.2%) appeared in disallowed regions. Given that 1600 non-Gly and non-Proline (Pro) residues were evaluated (with Gly and Pro excluded due to their atypical conformational flexibility), this extremely low percentage of disallowed residues indicates high stereochemical quality and provides strong confidence in the predicted FabI model.

ERRAT analysis was subsequently performed to evaluate overall and local model quality (Figure 8). The predicted structure achieved an Overall Quality Factor of 78.71%. The ERRAT output highlights several regions with elevated error values, indicated by prominent red peaks. These occur primarily within the residue ranges 20–40 and 120–130, where error values approach the 95% rejection limit.

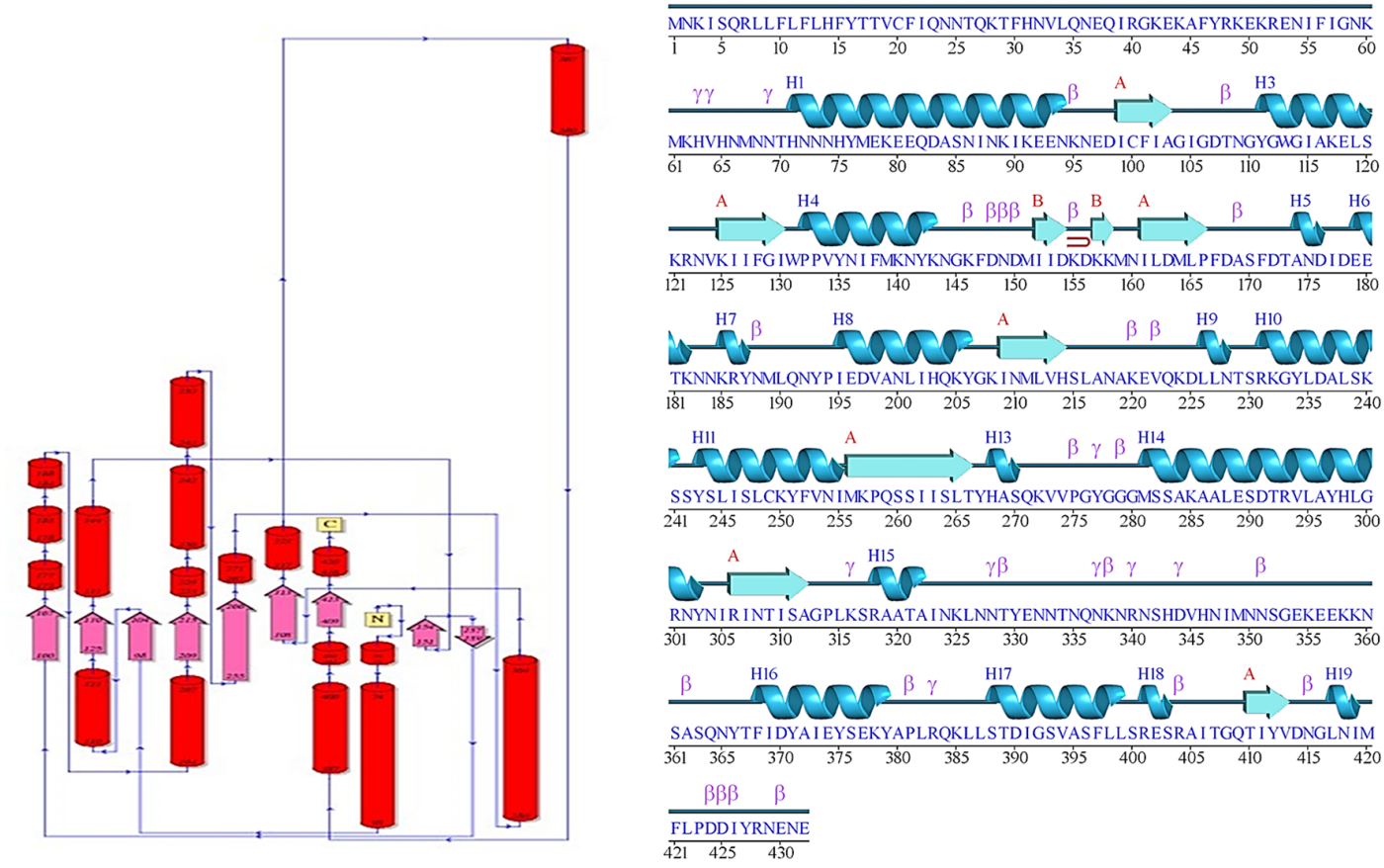

Figure 6. PDBsum analysis showing the predicted structural features of the FabI enzyme.

Local model reliability was further assessed through the Local Quality Estimate plot (Figure 9), which provides confidence values on a per-residue basis. For most of the structure (approximately residue 75 onward), the predicted confidence remains consistently above 0.7, indicating high accuracy in these regions.

In contrast, the N-terminal segment (residues 0–75) displays substantially lower confidence, with scores frequently dropping below 0.5 and, in several positions, approaching 0.1. Additionally but comparatively minor dips in confidence occur near residue 330 and toward the C-terminus region beyond residue 380.

Functional Analysis

Signal Peptide Prediction

The N-terminal sequence of the FabI enzyme was examined using SignalP 6.0 to determine the presence and likely location of a signal peptide (Figure 10). The prediction profile displays a prominent n-region (Sec/SPI n, solid red line) at the extreme N-terminus, corresponding to a positively charged stretch. This is followed by a strong hydrophobic h-region (Sec/SPI h, orange line), which extends from approximately residue 3 to residue 15, and peaks near residue 10.

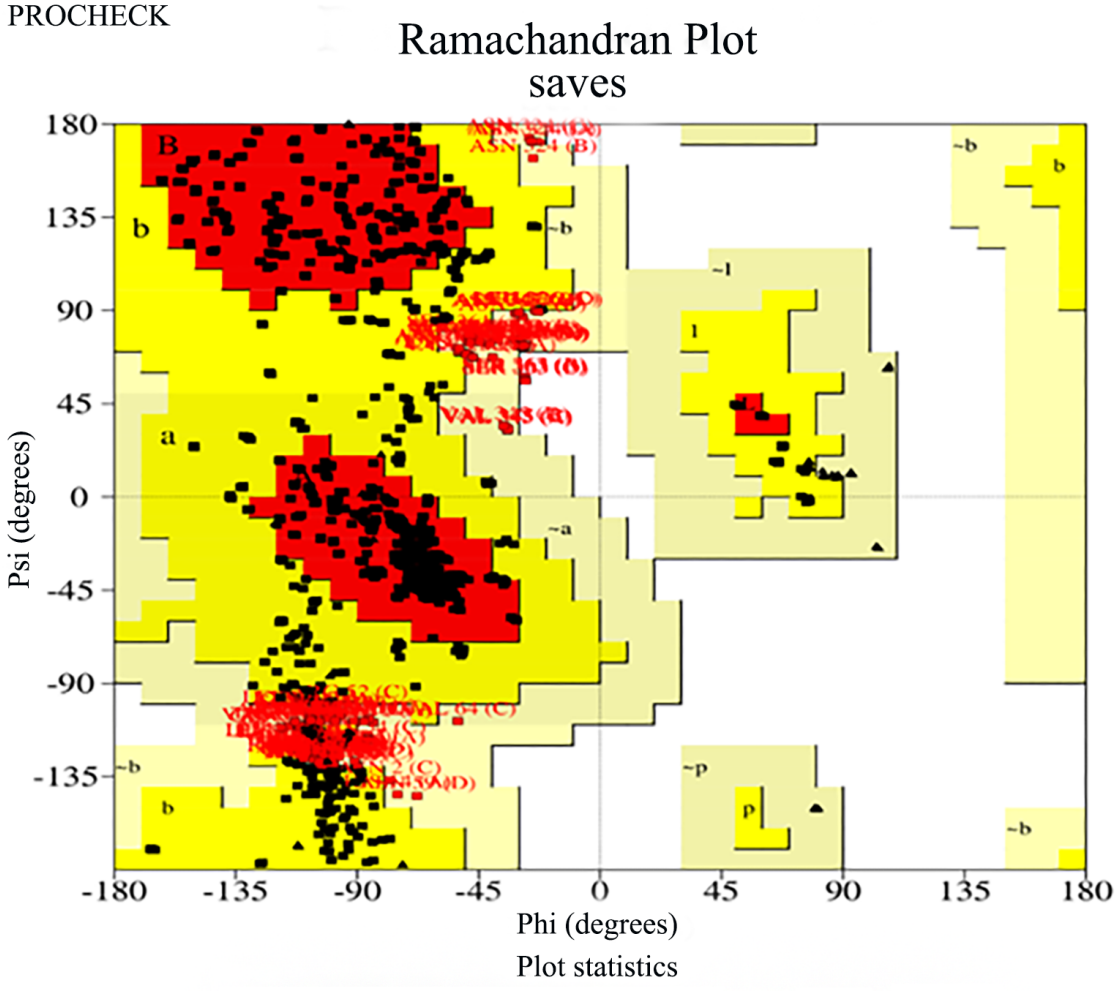

Plot statistics

Residues in most favoured regions [A,B,L]	1144	71.5%
Rexidues in adkitional allowod regions [a,b,l,p]	349	21.8%
Residues in gencrously allowed regions [-a,-b,-1,-p]	103	6.8%
Residues in disallowed regions	4	0.2%
	----	-------
Number of non-glycine and non-proline residues	1600	100.0%
Number of end-residucs (exel, Gly and Pro)	8	
Number of glycine residues (shown as triangles)	84	
Number of proline residues	36	

Total number of residues	1728	

Bascl on an analysis of 118 structures of resolution of at least 2.0 Angstroms and R-factor no greater than 20%, a good quality model would be expected to have over 90% in the most favoured regions.

Figure 7. Ramachandran plot for the predicted *P. falciparum* FabI structure, generated by PROCHECK.

Subsequently, the c-region (Sec/SPI c, yellow line) reaches its maximum probability around residue 24, indicating the most likely cleavage site. After residue 25, the probability for "OTHER" (non-signal peptide regions, dashed red line) increases sharply, marking the transition into the mature protein. Collectively, these predicted profiles indicate a canonical Sec/SPI signal peptide at the N-terminal region, with the cleavage site estimated between residues 22 and 25.

In Silico Proteolytic Digestion

An *in silico* proteolytic digestion analysis was carried out to predict potential cleavage sites and fragment numbers across the FabI enzyme using multiple proteases and chemical reagents (Table 3). The number of predicted cleavage events varied widely, ranging from a single cut to as many as 194, depending on protease specificity.

Proteinase K showed the highest cleavage frequency, with 194 predicted sites, followed by Thermolysin (120 cleavage sites), Pepsin at pH > 2 (98 cleavage sites), and Chymotrypsin (low-specificity) (94 cleavage sites), all of which would generate numerous small peptide fragments.

In contrast, enzymes with narrow specificity, such as Caspase1 and Pro endopeptidase, produced only a single predicted cleavage event. Similarly, BNPS-Skatole and Iodosobenzoic acid each generated two cuts, while Hydroxylamine and NTCB produced three cuts. Enzymes with moderate specificity, such as Trypsin (54 cleavages) and high specificity-Chymotrypsin (40 cleavages), yielded intermediate fragmentation patterns.

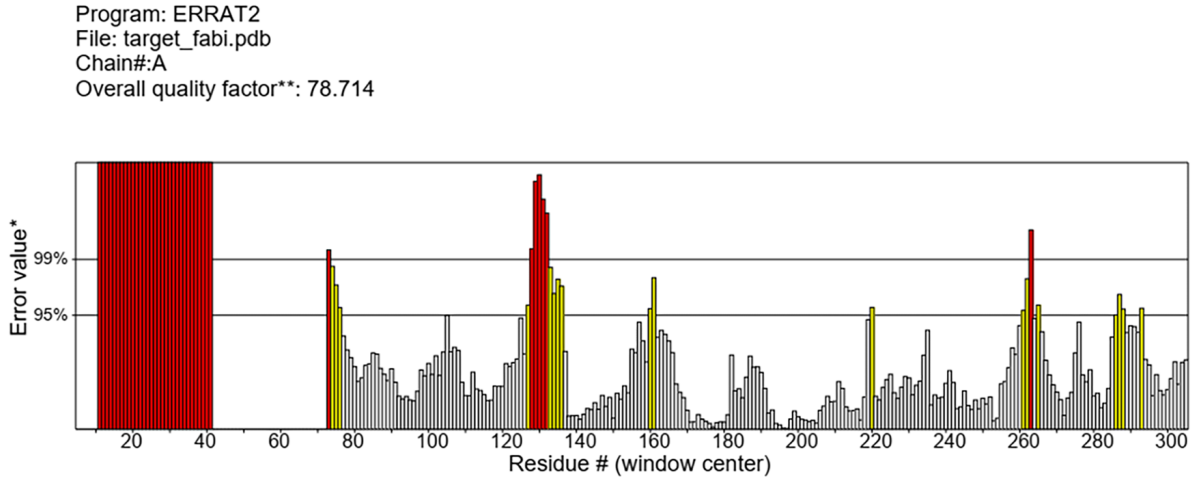

Figure 8. ERRAT plot for the predicted *P. falciparum* FabI enzyme structure.

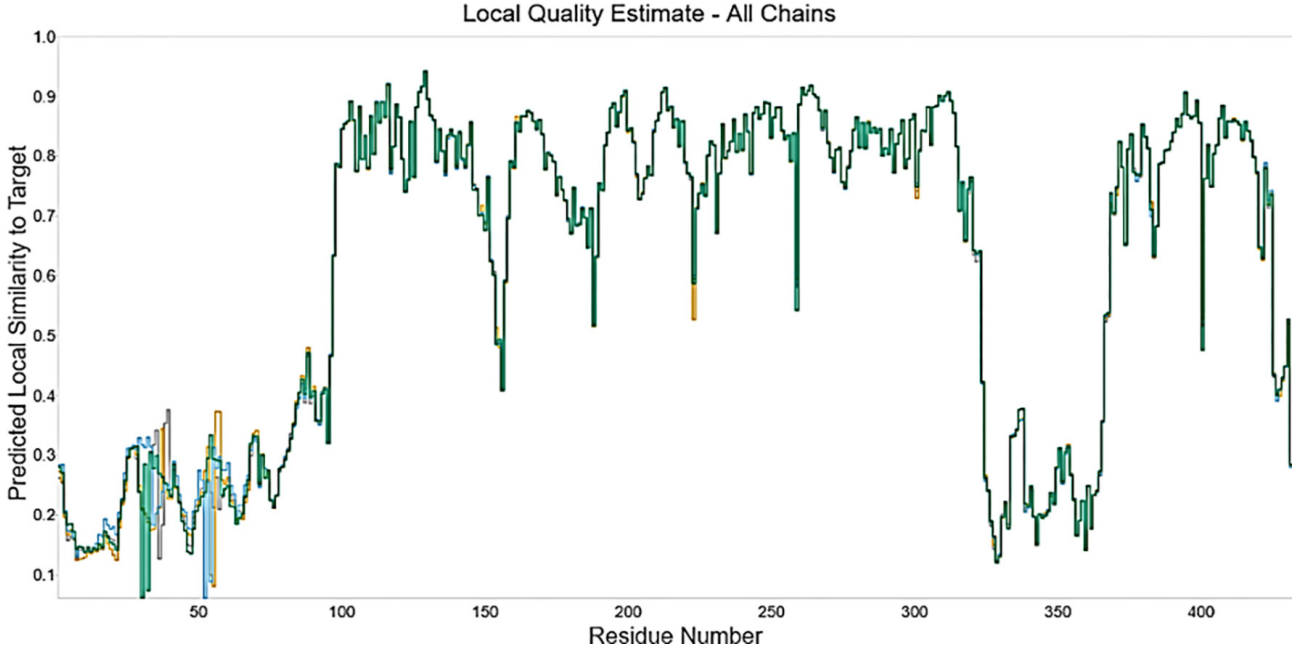

Figure 9. Local quality estimate of the predicted *P. falciparum* FabI structure, showing per-residue confidence scores.

Characterization of Active Site and Other Pockets via CASTp 3.0

The CASTp 3.0 server was used to perform a detailed topological analysis of the *P. falciparum* FabI protein, with particular emphasis on the characterization of active site pockets. The most prominent active site was represented by four discrete pocket instances, exhibiting solvent-accessible surface areas of 8.368 Å², 8.360 Å², 8.375 Å², and 8.147 Å², with corresponding volumes of 43.996 Å³, 43.763 Å³, 43.429 Å³, and 43.133 Å³, respectively. Functionally important residues identified within these pockets included Tyr267, His268, Ser311, Ala312, Gly313, and Pro314, Ala372, Tyr375, and Asp414.

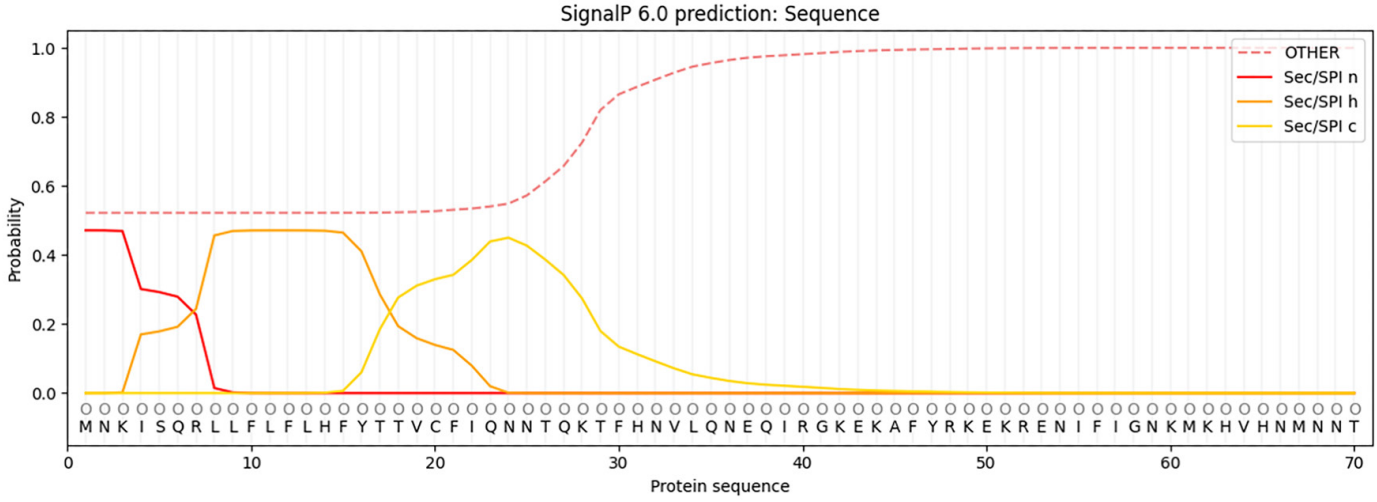

Figure 10. SignalP 6.0 prediction of the *P. falciparum* FabI N-terminal sequence, illustrating probabilities for n-region (Sec/SPI n), h-region (Sec/SPI h), c-region (Sec/SPI c), and non-signal peptide (OTHER).

Table 3. Predicted proteolytic cleavage sites for *P. falciparum* FabI enzyme.

Name of enzyme	Number of cleavages	Positions of cleavage sites
Arg-C proteinase	16	7 40 48 52 122 186 231 293 301 306 318 340 383 401 404 428
Asp-N endopeptidase	22	82 97 106 147 149 153 155 162 167 171 175 177 196 224 235 290 343 369 389 413 423 424
Asp-N endopeptidase + N-terminal Glu	47	36 42 49 52 77 79 80 82 91 92 96 97 106 117 147 149 153 155 162 167 171 175 177 178 179 195 196 220 224 235 288 290 330 343 353 355 356 369 373 376 389 401 413 423 424 429 431
BNPS-Skatole	2	113 131
Caspase1	1	390
Chymotrypsin-high specificity (C-term to [FYW], not before P)	40	10 12 15 16 21 30 46 47 56 76 101 111 113 128 135 138 142 147 167 171 187 206 234 243 251 252 267 277 297 303 330 366 368 371 375 379 397 412 421 427
Chymotrypsin-low specificity (C-term to [FYWML], not before P)	94	1 8 9 10 11 12 13 14 15 16 21 30 31 34 46 47 56 61 63 65 67 71 75 76 77 101 111 113 119 128 135 138 139 142 147 151 159 162 164 167 171 187 189 190 201 203 206 211 212 214 216 226 227 234 235 238 243 245 248 251 252 256 265 267 268 277 281 288 295 297 298 299 303 315 326 330 346 349 366 368 371 375 379 382 386 387 397 398 399 412 417 420 421 427
Clostripain	16	7 40 48 52 122 186 231 293 301 306 318 340 383 401 404 428
CNBr	14	1 61 67 77 139 151 159 164 189 211 256 281 349 420
Formic acid	22	83 98 107 148 150 154 156 163 168 172 176 178 197 225 236 291 344 370 390 414 424 425
Glutamyl endopeptidase	25	37 43 50 53 78 80 81 92 93 97 118 179 180 196 221 289 331 354 356 357 374 377 402 430 432

Table 3. Continued.

Name of enzyme	Number of cleavages	Positions of cleavage sites
Hydroxylamine	3	109 144 415
Iodosobenzoic acid	2	113 131
LysC	41	3 28 42 44 49 51 60 62 79 89 91 95 117 121 125 140 143 146 155 157 158 182 185 205 208 220 224 232 240 250 257 272 285 316 325 338 355 358 359 378 385
LysN	41	2 27 41 43 48 50 59 61 78 88 90 94 116 120 124 139 142 145 154 156 157 181 184 204 207 219 223 231 239 249 256 271 284 315 324 337 354 357 358 377 384
NTCB (2-nitro-5-thiocyanobenzoic acid)	3	19 99 248
Pepsin (pH > 2)	98	8 10 11 12 13 14 15 20 21 29 34 45 47 55 56 75 76 100 101 110 111 112 113 118 128 135 137 138 141 146 147 161 162 165 166 170 171 189 190 193 200 201 206 211 212 215 225 227 235 237 238 243 244 245 247 248 250 251 264 265 266 267 277 288 294 296 297 298 299 302 314 325 326 329 330 365 366 367 368 370 371 374 375 378 381 386 396 397 398 399 411 412 416 417 420 422 426 427
Pepsin (pH1.3)	66	8 10 11 12 13 14 15 20 21 29 34 45 55 56 100 101 118 128 137 138 146 147 161 162 165 166 170 171 189 190 200 201 211 212 215 225 227 235 237 238 244 245 247 248 251 264 265 288 294 298 299 314 325 326 367 368 381 386 396 397 398 399 416 417 420 422
Pro endopeptidase [*]	1	258
Proteinase K	194	4 8 9 10 11 12 13 15 16 17 18 19 21 22 26 29 30 33 34 37 39 43 45 46 47 50 53 55 56 57 64 70 76 78 80 81 84 87 90 92 93 97 99 101 102 103 105 108 111 113 115 116 118 119 124 126 127 128 130 131 134 135 137 138 142 147 152 153 161 162 165 167 169 171 173 174 177 179 180 181 187 190 193 195 196 198 199 201 202 206 209 212 213 216 217 219 221 222 226 227 229 234 235 237 238 243 245 246 248 251 252 253 255 262 263 265 266 267 269 273 274 277 284 286 287 288 289 292 294 295 296 297 299 303 305 307 309 310 312 315 319 320 321 322 323 326 329 330 331 334 345 348 354 356 357 362 366 367 368 369 371 372 373 374 375 377 379 380 382 386 387 389 391 394 395 397 398 399 402 405 406 407 410 411 412 413 417 419 421 422 426 427 430 432
Staphylococcal peptidase I	21	37 43 50 53 78 80 92 97 118 179 196 221 289 331 354 356 374 377 402 430 432
Thermolysin	120	3 7 8 9 10 11 12 14 18 20 21 29 32 33 38 44 45 54 55 56 60 63 66 76 86 89 100 101 102 104 114 115 123 125 126 127 129 133 136 137 138 146 151 152 158 160 161 166 170 173 188 189 194 198 200 201 208 210 211 212 215 216 218 226 234 237 244 245 247 251 252 254 255 261 262 264 268 272 280 283 285 286 287 293 294 295 298 304 306 309 311 314 318 319 321 322 325 347 348 361 367 368 371 372 381 385 386 393 394 396 397 398 404 405 410 412 416 418 419 420
Trypsin	54	3 7 28 40 42 44 48 49 51 52 60 62 79 89 91 95 117 121 122 125 140 143 146 157 158 182 185 186 205 208 220 224 231 232 240 272 285 293 301 306 316 318 325 338 340 355 358 359 378 383 385 401 404 428
Total	943	

In addition to these active site pockets, CASTp analysis revealed another large and centrally located pocket with a substantially greater surface area (951.472 Å²) and volume (851.864 Å³). Key residues lining this central cavity included His268, Ser270, and Glutamine 271 (Gln271), together with Threonine 292 (Thr292), Arginine 293 (Arg293), Tyr412, and Isoleucine 419 (Ile419). The 3D representation of these identified pockets is shown in (Figure 11), where the four active site-associated pockets are highlighted in pink and the centrally located pocket is depicted in black.

Discussion

Two highly conserved regions, AKAALES and RVNAISAGPIRT, were identified within FabI enzyme sequences, underscoring their likely functional importance. Although conservation is broadly maintained, several amino acid positions exhibit specific substitutions. Some substitutions retain similar physicochemical properties (conservative), while others introduce marked changes (non-conservative).

In the AKAALES region, Ala329 occasionally undergoes a non-conservative substitution to Ser, thereby introducing a polar hydroxyl group in place of the nonpolar methyl group typically resides there. Conversely, Glutamic Acid 331 shows a highly conservative change to Asp since both are acidic, negatively charged amino acids, which ensures that the electrostatic role of the site is preserved. At the position 332, a notable degree of variation is observed, directly influencing the local polarity. The substitution from Ser to Ala is non-conservative because it shifts the residue's characteristic from polar to nonpolar. Furthermore, in one instance, Thr (T) is present at this site. When considering this change, a substitution from Ser to Thr is conservative, as both are polar amino acids possessing similar hydroxyl groups; however, if Ala were replaced by Thr, it would constitute a non-conservative change.

Within the longer RVNAISAGPIRT region, variations at position 349 (Valine to Ile), and at position 352 (Ile to Valine or Leu) are conservative, since all involved amino acids are nonpolar, branched-chain hydrophobics and collectively maintain the local hydrophobic environment. Similarly, the alternations at positions 357 (Leu/Ile), 358 (Lysine/Arg), 359 (Ser/Thr), are also conservative. However, at position 351 (typically Ala) in RVNAISAGPIRT there are diverse non-conservative substitutions to Gly, Ser, Thr, or Cys. These changes can either alter local flexibility (Gly) or significantly modify the polarity (Ser, Thr, Cys). The Cys substitution is particularly notable because its reactive thiol group could introduce new chemical functionalities. Lastly, the change from Pro to Ala at position 356 is non-conservative, as this substitution, observed in only one instance, fundamentally alters the local structural rigidity. Altogether, these patterns highlight a strategic balance, in which conservative substitutions maintain core function through preservation of essential physicochemical properties, while non-conservative changes may reflect specific evolutionary adaptations that influence enzyme characteristics and could impact activity, substrate specificity, or stability in different host environments.

The phylogenetic analysis of FabI enzyme sequences yields crucial insights into their evolutionary origins and relationships across diverse taxa. A key finding is the clear and substantial evolutionary distance observed between the *Plasmodium*-containing Apicomplexa clade and all bacterial lineages represented in the tree. This distinct separation, in which *Plasmodium*'s FabI clusters tightly with other apicomplexan orthologs yet remains phylogenetically distant from all bacterial FabI sequences, is highly significant because FabI is fundamentally a prokaryotic (bacterial) FAS enzyme. The presence of such a typically bacterial enzyme

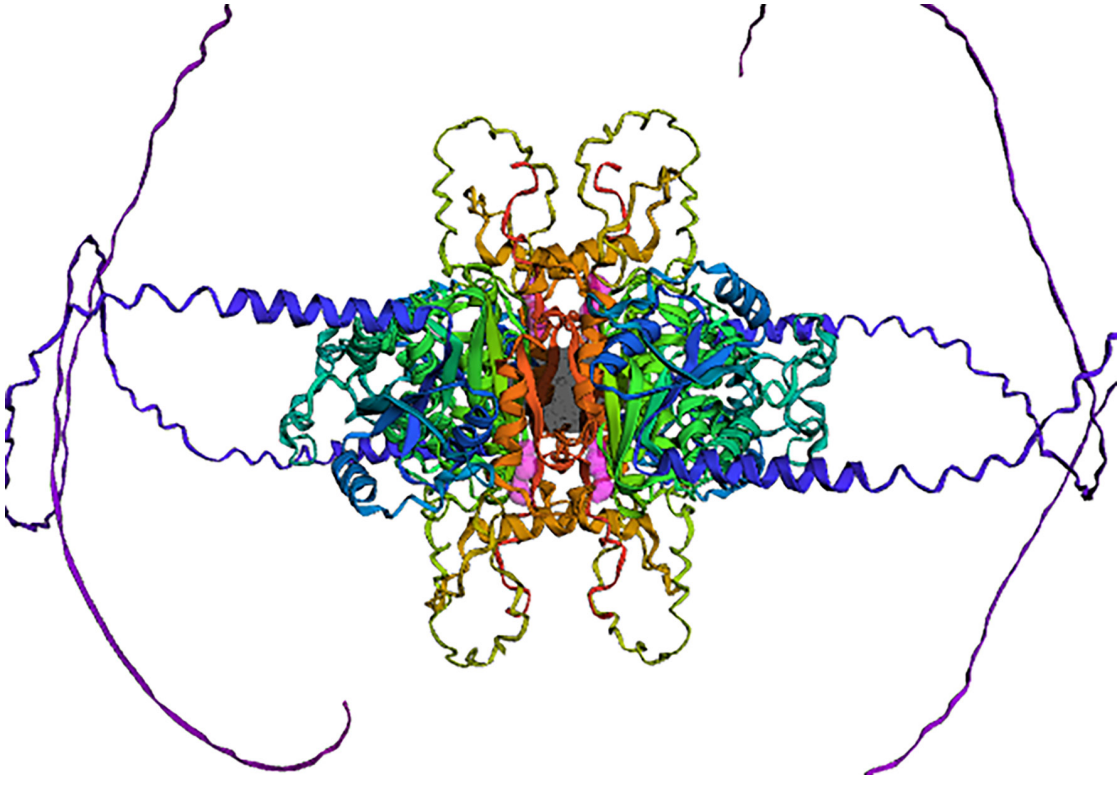

Figure 11. 3D representation of *P. falciparum* FabI enzyme, highlighting predicted CASTp 3.0 pockets. The four active site-related pockets are shown in pink, and another significant central pocket is depicted in black.

within a eukaryotic parasite like *Plasmodium*, as evidenced by its unique branching pattern in the tree, strongly supports its acquisition through an ancient horizontal gene transfer (HGT) event. This transferred gene likely originated from a bacterial ancestor that became endosymbiotic and ultimately gave rise to the apicoplast-a non-photosynthetic plastid within Apicomplexa that houses the bacterial-derived FAS-II pathway. This profound evolutionary divergence of apicomplexan FabI from extant bacterial enzymes together with its distinctness from human FAS pathways, positions it as a highly promising target for anti-parasitic drug development.

The observed distinct physicochemical profiles between protozoan and bacterial FabI enzymes offer valuable insights into their functional adaptations and evolutionary trajectories. The larger size and higher molecular weight of FabI from protozoan parasites, together with their generally higher isoelectric points (pI) and greater hydrophilicity (negative GRAVY values), stand in sharp contrast to the smaller, more hydrophobic, and typically lower pI bacterial FabI. This comparison suggests that protozoan FabI enzymes, such as those in *Plasmodium* with its notably high pI and hydrophilicity, may be specifically adapted for different intracellular environments or protein interaction partners than their bacterial counterparts. For instance, increased hydrophilicity could indicate greater surface exposure or more extensive interactions with the aqueous lumen of the apicoplast, where these enzymes function.

Furthermore, the higher count of charged residues (acidic and basic) in protozoan FabI contributes to their distinct pI values and to potentially more complex electrostatic interactions. While most bacterial FabI display consistent characteristics, the exceptions, such as the higher pI observed in *H. pylori* and *R. conorii*, might reflect adaptations to unique intracellular or extracellular niches and corroborate the distinct branching patterns observed in the phylogenetic analysis.

A motif analysis was performed on 25 FabI protein sequences. Notably, despite the overall conservation of Motif 2 and Motif 3, several parasitic FabI sequences showed shifts in the relative positions of these motifs compared to their bacterial counterparts. Such positional shifts may reflect structural adaptations or domain rearrangements specific to the parasite's cellular environment or evolutionary history. The absence of Motif 1 in protozoan FabI sequences, despite its broad and consistent presence in bacteria, further suggests a significant evolutionary divergence. This indicates that protozoan FabI either performs its function using a different molecular mechanism that does not require Motif 2, or that this region was lost or became highly divergent following the initial HGT event from a bacterial ancestor.

The precise mapping of all three identified conserved motifs to a specific domain within *P. falciparum* FabI provides critical insights into its functional architecture, and this domain's identification as a NAD(P) binding Rossmann-fold domain is highly significant.

The Rossmann fold is a well-established supersecondary structural motif that is essential for binding nucleotides, particularly NAD(P)H, which serves as a vital cofactor for a vast array of oxidoreductases. Given that FabI (enoyl-ACP reductase) is an oxidoreductase that absolutely requires NAD(P)H for its catalytic activity, locating these three conserved motifs precisely within this NAD(P) binding Rossmann-fold domain directly confirms the structural basis for cofactor recognition and enzymatic function. Their presence within this specialized domain also strongly suggests direct involvement in substrate binding, catalysis, or cofactor interaction.

The predicted secondary structure profiles additionally highlight lineage-specific adaptations of FabI enzymes. The predominance of alpha-helical content across all analyzed FabI sequences points to a shared compact globular architecture that is essential for enzymatic function. However, compared to their bacterial counterparts, protozoan FabI enzymes generally contain lower proportions of extended strands and beta turns while exhibiting higher random coil content, indicating a potentially greater inherent flexibility. Notably, *P. falciparum* is distinct among protozoa, with a random coil percentage more closely aligned with bacterial FabI, suggesting a particular structural adaptation possibly tied to unique functional requirements or its intracellular environment. Most significantly, the universal absence of predicted disulfide bridges across all FabI enzymes strongly indicates that these proteins operate in reducing cellular environments, such as the bacterial cytoplasm or the apicoplast lumen, where stabilizing bonds are not typically formed.

The ERRAT analysis provided a important assessment of the predicted FabI enzyme structure. Although the overall quality factor suggests a plausible structural model, the most prominent areas of concern are highly localized within the N-terminal region, particularly around residues 20–40. This clustering of high error values (red spikes) is strongly suggestive of a cleavable N-terminal signal or transit peptide. Because *P. falciparum* FabI is known to be targeted to the apicoplast, such targeting sequences are inherently flexible or unstructured in the mature protein and are normally cleaved off following import into the organelle. As a result, computational modeling tools frequently struggle to accurately predict the conformation of these dynamic or absent regions, leading to their erroneous classification by quality assessment programs like ERRAT. For this reason, the localized discrepancy does not invalidate the accuracy of the predicted 3D structure of the mature, functional FabI enzyme.

The Local Quality Estimate plot provides a crucial residue-level assessment of the predicted FabI enzyme structure and offers insights into the reliability of different regions. Across the majority of the protein, the confidence scores remain generally high (typically above 0.7 from residue ~75 onwards), which is encouraging and suggest that the previously described core structural elements and overall fold are well-predicted and represent a reliable model for the mature, functional enzyme.

In contrast, the N-terminal segment (residues 0 to ~75) displays a prominent and consistent region of significantly low confidence, and this pattern constitues a key observationthat warrants specific discussion. The same region has been highlighted in the ERRAT

plot through high error values, and the agreement between between both analyses strongly supports the interpretation that this segment reprsents an intrinsically disordered or highly flexible N-terminal signal/transit peptide.

This conclusion is further supported by SignalP 6.0, which predicts a cleavable signal peptide with a likley cleavage site near residues 22–25, consistent withprevious indicators that the N-terminus remains unstructured before processing.

The *in silico* proteolytic digestion analysis also provides a useful guidance for future biochemical characterization of *P. falciparum* FabI. The wide range in predicted cleavage events, from a single cut to almost 200, reflects the diverse specificities of the proteases and chemical reagents tested.

Broad specificity enzymes such as Proteinase K, Thermolysin, Pepsin, and low-specificity Chymotrypsin are effective for extensive digestion, which may be useful for amino acid composition analysis or generating small peptides for mass spectrometry identification.

Conversely, proteases like Caspase1 and Pro-endopeptidase, which each yield only one cleavage site, are highly selective and therefore valuable for isolating large, well-defined fragments for structural studies or targeted protein engineering. Limited cleavage by chemical reagents such as BNPS-Skatole and Hydroxylamine similarly confirms their utility for generating a few large peptides by acting on less common amino acid residues. Together, this cleavage map forma an important foundation for experimental design, including peptide fingerprinting, structural domain isolation, and verifying recombinant protein integrity.

The CASTp 3.0 analysis further contributes by characterizing the surface features and internal topography of the FabI enzyme.

The prominent active site appears as four relatively small pocket instances (each with areas of 8 Å² and volumes of 43 Å³), suggesting a more complex architecture than a single cavity. These multiple sub-pockets may accommodate different substrate regions or catalytic intermediates involved in multi-step FAS. The central cavity could also function as an allosteric binding site, a channel for substrate/product passage, or a location involved in conformational shifts. Altogether, these detailed topographical insights are invaluable for understanding catalytic mechanism, predicting ligand binding, and guiding inhibitor design.

Conclusion

This comprehensive computational structural and functional study has meticulously characterized the *P. falciparum* FabI enzyme, which serves as a critical antimalarial target. The work provides a robust foundation for researchers to gain a detailed understanding of its protein structure, thereby facilitating the rational design of novel compounds with desirable characteristics for exploiting them as potential drug targets against malaria. However, further experimental (*in vitro* and *in vivo*) studies are essential to validate these computational predictions.

Ethics

Ethics Committee Approval: Not required.

Data Sharing Statement: All data are available within the study and in the Supplementary Material.

Footnotes

Authorship Contributions: Conceptualization: D.J.; Design/ methodology: D.J.; Execution/investigation: A.B., H.A., and D.J.; Resources/materials: A.B., H.A., and D.J.; Data acquisition: A.B. and H.A.; Data analysis/interpretation: D.J.; Writing – original draft: A.B., H.A., and D.J.; Writing – review & editing/critical revision: D.J.

Conflict of Interest: The authors have no conflicts of interest to declare.

Funding: The authors declare that this study has received no financial support.

Supplementary Material. https://d2v96fxpocvxx.cloudfront.net/34c1fd7d-947b-4954-9ae2-39560c57d146/content-images/2ee739d7-4c4b-448c-aa9a-8a68b7a2a269.pdf

References

Bailey, T. L., & Elkan, C. (1994). Fitting a mixture model by expectation maximization to discover motifs in biopolymers. *Proceedings of the International Conference on Intelligent Systems for Molecular Biology, 2*, 28–36. https://pubmed.ncbi.nlm.nih.gov/7584402/

Benkert, P., Biasini, M., & Schwede, T. (2010). Toward the estimation of the absolute quality of individual protein structure models. *Bioinformatics, 27*(3), 343–350. https://doi.org/10.1093/bioinformatics/btq662

Blum, M., Andreeva, A., Florentino, L. C., Chuguransky, S. R., Grego, T., Hobbs, E., Pinto, B. L., Orr, A., Paysan-Lafosse, T., Ponamareva, I., Salazar, G. A., Bordin, N., Bork, P., Bridge, A., Colwell, L., Gough, J., Haft, D. H., Letunic, I., Llinares-López, F., ... Bateman, A. (2024). InterPro: The protein sequence classification resource in 2025. *Nucleic Acids Research, 53*(D1), D444–D456. https://doi.org/10.1093/nar/gkae1082

Colovos, C., & Yeates, T. O. (1993). Verification of protein structures: Patterns of nonbonded atomic interactions. *Protein Science, 2*(9), 1511–1519. https://doi.org/10.1002/pro.5560020916

Gasteiger, E., Hoogland, C., Gattiker, A., Wilkins, M. R., Appel, R. D., & Bairoch, A. (2005). Protein identification and analysis tools on the ExPASy server. In *Humana Press eBooks* (pp. 571–607). https://doi.org/10.1385/1-59259-584-7:531

Geourjon, C., & Deléage, G. (1995). SOPMA: Significant improvements in protein secondary structure prediction by consensus prediction from multiple alignments. *Bioinformatics, 11*(6), 681–684. https://doi.org/10.1093/bioinformatics/11.6.681

Hopf, F. S. M., Roth, C. D., De Souza, E. V., Oliveira, S. A., & Zamboni, D. S. (2022). Bacterial enoyl-reductases: The ever-growing list of Fabs, their mechanisms, and inhibition. *Frontiers in Microbiology, 13,* 891610. https://doi.org/10.3389/fmicb.2022.891610

Kane, N. F., Kyama, M. C., Nganga, J. K., Hassanali, A., Diallo, M., & Kimani, F. T. (2022). Expression of the Fab enzymes (FabI and FabZ) from *Plasmodium falciparum* after exposure to *Artemisia afra* plant extracts and drugs screening. *Journal of Parasitic Diseases, 47*(1), 46–58. https://doi.org/10.1007/s12639-022-01537-8

Laskowski, R. A., Rullmann, J. A. C., MacArthur, M. W., Kaptein, R., & Thornton, J. M. (1996). AQUA and PROCHECK-NMR: Programs for checking the quality of protein structures solved by NMR. *Journal of Biomolecular NMR, 8*(4), 477–486. https://doi.org/10.1007/bf00228148

Madeira, F., Madhusoodanan, N., Lee, J., Squires, G., Lopez, R., & Künsting, M. (2024). The EMBL-EBI Job Dispatcher sequence analysis tools framework in 2024. *Nucleic Acids Research, 52*(W1), W521–W525. https://doi.org/10.1093/nar/gkae241

Mirdita, M., Schütze, K., Moriwaki, Y., Heo, L., Ovchinnikov, S., & Steinegger, M. (2021). ColabFold: Making protein folding accessible to all. *bioRxiv*. https://doi.org/10.1101/2021.08.15.456425

Pandey, A., Shyamal, S. S., Shrivastava, R., Ekka, S., & Mali, S. N. (2022). Inhibition of *Plasmodium falciparum* fatty acid biosynthesis (FAS-II pathway) by natural flavonoids: A computer-aided drug designing approach. *Chemistry Africa, 5*(5), 1469–1491. https://doi.org/10.1007/s42250-022-00449-7

Pandey, A. K., Siddiqui, M. H., & Dutta, R. (2019). Drug-likeness prediction of designed analogues of isoniazid standard targeting FabI enzyme regulation from *P. falciparum*. *Bioinformation, 15*(5), 364–368. https://doi.org/10.6026/97320630015364

Studer, G., Biasini, M., & Schwede, T. (2014). Assessing the local structural quality of transmembrane protein models using statistical potentials (QMEANBrane). *Bioinformatics, 30*(17), i505–i511. https://doi.org/10.1093/bioinformatics/btu457

Studer, G., Rempfer, C., Waterhouse, A. M., Gumienny, R., Haas, J., & Schwede, T. (2019). QMEANDisCo—Distance constraints applied on model quality estimation. *Bioinformatics, 36*(6), 1765–1771. https://doi.org/10.1093/bioinformatics/btz828

Teufel, F., Armenteros, J. J. A., Johansen, A. R., Gíslason, M. H., Pihl, S. I., Tsirigos, K. D., Winther, O., Brunak, S., von Heijne, G., & Nielsen, H. (2022). SignalP 6.0 predicts all five types of signal peptides using protein language models. *Nature Biotechnology, 40*(7), 1023–1025. https://doi.org/10.1038/s41587-021-01156-3

The UniProt Consortium. (2024). UniProt: The universal protein knowledgebase in 2025. *Nucleic Acids Research, 53*(D1), D609–D617. https://doi.org/10.1093/nar/gkae1010

Tian, W., Chen, C., Lei, X., Zhao, J., & Liang, J. (2018). CASTp 3.0: Computed atlas of surface topography of proteins. *Nucleic Acids Research, 46*(W1), W363–W367. https://doi.org/10.1093/nar/gky473

Trakya University Journal of Natural Sciences, 27(1), 30–36, 2026
DOI: 10.23902/trkjnat.2025914
www.tujns.org

Research Article

Royal jelly maintains telomere length and antioxidant parameters in the pancreas of streptozotocin-induced rats

Selcen Çakır*

Çanakkale Onsekiz Mart University, Vocational School of Health Services, Çanakkale, Türkiye

Cite this article as: Çakır, S. (2025). Royal jelly maintains telomere length and antioxidant parameters in the pancreas of streptozotocin-induced rats. *Trakya University Journal of Natural Sciences, 27*(1), 30–36. https://doi.org/10.23902/trkjnat.2025914

Abstract

Background: Streptozotocin (STZ) is an agent with selective toxicity targeting pancreatic β-cells and is commonly used to establish models of pancreatic damage. Royal jelly (RJ) is a natural product rich in biologically active compounds and has been shown in various studies to exert antioxidative and cytoprotective effects.

Aims: This study aimed to evaluate the potential protective effects of RJ against STZ-induced pancreatic damage and to investigate these effects in terms of oxidative stress (OS) and telomere biology.

Methods: Twenty-four female Wistar albino rats were randomly divided into four groups: control, RJ (350 mg/kg), STZ, and STZ + RJ (350 mg/kg). Telomere length in pancreatic tissue and serum levels of 8-hydroxy-2'-deoxyguanosine (8-OHdG), paraoxonase-1 (PON1), and telomerase were analyzed using commercial enzyme-linked immunosorbent assay kits.

Results: STZ administration significantly increased oxidative DNA damage (8-OHdG) and decreased PON1 levels, indicating elevated OS. RJ treatment effectively reversed these changes, bringing 8-OHdG and PON1 levels closer to those of the control group. Moreover, RJ administration significantly increased the reduced pancreatic telomere length and serum telomerase levels in the STZ group.

Conclusion: These findings suggest that RJ may mitigate STZ-induced oxidative stress and telomere shortening. Further studies are needed to elucidate the therapeutic mechanisms of RJ in OS-related pancreatic disorders.

Özet

Dayanak: Streptozotosin (STZ), özellikle pankreasın β-hücrelerini hedef alan seçici toksisiteye sahip bir ajandır ve pankreatik hasar modellerinin oluşturulmasında sıklıkla kullanılmaktadır. Arı sütü (RJ) ise biyolojik olarak aktif bileşiklerce zengin doğal bir ürün olup oksidatif stres (OS) karşıtı ve hücre koruyucu etkileri çeşitli çalışmalarda gösterilmiştir.

Amaçlar: Bu çalışma, RJ'nin STZ ile indüklenen pankreas hasarına karşı potansiyel koruyucu etkilerini değerlendirmeyi ve bu etkileri oksidatif stres ile telomer biyolojisi açısından incelemeyi amaçlamıştır.

Yöntemler: Yirmi dört dişi Wistar albino sıçan rastgele dört gruba ayrılmıştır: Kontrol, RJ (350 mg/kg), STZ ve STZ + RJ (350 mg/kg). Pankreas doku örneklerinden telomer uzunluğu; kan serumundan da 8-hidroksi-2'-deoksiguanozin (8- OHdG), paraoksonaz-1 (PON1) ve telomeraz düzeyleri enzim bağlantılı immünosorbent analizi kitleri kullanılarak analiz edilmiştir.

Bulgular: STZ uygulaması, oksidatif DNA hasarını (8-OHdG) anlamlı derecede artırmış ve PON1 düzeylerini azaltarak artmış OS'yi ortaya koymuştur. RJ tedavisi bu değişiklikleri etkili bir şekilde tersine çevirerek 8-OHdG ve PON1 düzeylerini kontrol grubu değerlerine yaklaştırmıştır. Ayrıca, RJ uygulamasının STZ grubunda azalan pankreas telomer uzunluğunu ve serum telomeraz düzeyini anlamlı biçimde artırdığı belirlenmiştir.

Sonuç: Bu bulgular, RJ'nin STZ kaynaklı oksidatif stresi ve telomer kısalmasını azaltabileceğini göstermektedir. OS ile ilişkili pankreatik bozukluklarda RJ'nin terapötik mekanizmasını en iyi şekilde ortaya koymak için ileri çalışmalara ihtiyaç vardır.

Keywords: 8-OHdG, pancreas, PON1, royal jelly, streptozotocin, telomere length, telomerase

Edited by: *Belgin Süsleyici*

***Corresponding Author:** Selcen Çakır, **E-mail:** selcencakir@comu.edu.tr*

***ORCID iDs of the author(s):** SÇ. 0000-0002-6474-9032*

Received: 11 October 2025, **Accepted:** 20 November 2025, **Epub:** 16 December 2025, **Published:** 24 April 2026

Introduction

Royal jelly (RJ) is a nutrient-rich compound secreted by the hypopharyngeal glands of worker honey bees. It is a complex mixture of lipids, glucose, proteins, vitamins, and minerals. The longevity and fertility of queen bees have been attributed to their exclusive feeding on RJ (Özkök et al., 2021). RJ is widely utilized commercially in the medical and cosmetic fields. Animal studies have demonstrated that RJ possesses multiple bioactivities, including antioxidant (Ghanbari et al., 2016), anti-inflammatory (Fujiwara et al., 1990), antihypertensive (Tokunaga et al., 2004), and immunomodulatory (Vucevic et al., 2007) effects. One of its most remarkable properties is its ability to stimulate cell proliferation and influence antidiabetes therapeutic processes (Ghanbari et al., 2015).

Streptozotocin (STZ), is a monofunctional nitrosourea derivative isolated from *Streptomyces achromogenes*, which exhibits broad-spectrum antibiotic activity and antineoplastic properties. STZ is widely employed in experimental models to induce selective pancreatic β-cell damage due to its potent DNA-alkylating properties, resulting in random DNA synthesis, strand breaks, adducts, alkali-labile sites, micronuclei formation, sister chromatid exchanges, chromosomal aberrations, and cell death. These impacts render STZ a powerful mutagen in bacterial and mammalian cells (Tural Çifçi & Tuzcu, 2025; Paviolo et al., 2015). The selective uptake of STZ by pancreatic β-cells is mediated via the GLUT2 glucose transporter, leading to DNA alkylation and the subsequent activation of poly(ADP-ribose) polymerase, NAD^+ depletion, reduced ATP levels, and the inhibition of insulin production. Moreover, STZ generates reactive oxygen species, contributing further to DNA damage and cytotoxicity (Tural Çifçi & Tuzcu, 2025; Saha et al., 2025). STZ is administered to obtain experimental models, as either a single high dose or multiple low doses, to reliably induce diabetes, providing a reproducible platform for assessing pancreatic tissue responses to pharmacological agents independent of systemic glucose levels (Lenzen, 2008; Like & Rossini, 1976).

Telomeres are specialized nucleoprotein complexes located at the ends of linear chromosomes, playing a crucial role in preserving genomic stability and cell replicative capacity (Blackburn, 1991). Telomere shortening, which occurs naturally with each cell division, may be further accelerated by external factors such as oxidative stress (OS) and DNA damage, leading to cell senescence or apoptosis (Epel et al., 2004). In this context, telomere length is not only a biomarker of cell aging but also a critical determinant of cell proliferative potential (Blackburn, 2001). Since pancreatic β-cell regeneration is limited and sensitive to OS, monitoring telomere integrity provides valuable insights into tissue homeostasis under pathological conditions (Zhang et al., 2019). Furthermore, OS-induced telomere attrition has been implicated in the dysfunction of several tissues, including pancreatic islets, making telomere dynamics a relevant parameter for metabolic and degenerative diseases (Epel et al., 2004; Zhang et al., 2019).

This study primarily aimed to evaluate the potential of RJ, a natural bioactive compound, to mitigate STZ-induced β-cell damage. Specifically, considering the antioxidant, antiapoptotic, and cytoprotective properties of RJ, this study investigated its impacts on STZ-induced DNA damage, OS, and telomere dysfunction. Overall, it elucidates the alleviative potential of RJ against STZ-induced pancreatic injury and the contribution of natural bioactive agents in maintaining pancreatic homeostasis under metabolic and genotoxic stress.

Materials and Methods

This study was carried out with the approval of Çanakkale Onsekiz Mart University Animal Experiments Local Ethics Committee (approval number: 2021/01-01, dated: 12.02.2021).

Experimental Plan

The RJ used is commercially available and is produced by the BeeO R&D Laboratory, İstanbul Technical University, İstanbul, Türkiye. The RJ dose administered was determined based on the effective doses reported for similar animal models (Çakır, 2023). For the experiments, 24 Wistar albino female rats weighing 200–250 g were divided into four groups, with six rats in each group. They were named as control, RJ (350 mg/kg RJ), STZ, and STZ + RJ (350 mg/kg RJ) groups (Figure 1). The environmental conditions were maintained at 21 °C ± 2 °C and 50% ± 5% humidity, under a 12/12 h light/dark cycle. The STZ group animals were intraperitoneally (i.p.) administered with 50 mg/kg STZ in citrate buffer. RJ was administered by the gavage method. At the end of the 4-week experiment, the rats were kept on a fast for 10 h and anesthetized with 70 mg/kg ketamine and 7 mg/kg xylazine (i.p.). Blood was collected from their hearts after puncture and transferred to tubes without an anticoagulant for serum. After the tubes were spun in an NF 1200 centrifuge (Nüve, TX, USA) at 1,400 g and 4 °C for 10 min, the serum was separated and stored in labeled tubes at -80 °C.

Serum Analysis

In the study, commercially available enzyme-linked immunosorbent assay (ELISA) kits were used to measure telomerase level (E-EL-R0947; Elabscience, TX, USA), 8′-hydroxy-2′-deoxyguanosine (8-OHdG, MBS701076; MyBiosource, CA, USA) levels, and PON1 (MBS453155; MyBiosource) contents. An ELx800 ELISA device (BioTek Instruments, Inc., VT, USA) and an ELx50 washer (BioTek) were used.

Tissue Homogenization

A clinic/cell SV mini tissue extraction kit (108-101; GeneAll Biotechnology Co., Ltd., Seoul, Korea), 0.2 mm stainless steel beads, and a Digital Disruptor Cell Disruptor (#3591456; Bio-Rad Laboratories, CA, USA) were employed to homogenize the pancreatic tissues.

Telomere Lengths

In this study, the average telomere length of the pancreatic tissue cells was determined using the Telomere Length Quantification qPCR Test Kit (R8918; ScienCell Research Laboratories, CA, USA) and the Absolute Rat Telomere Length Kit (R8918;

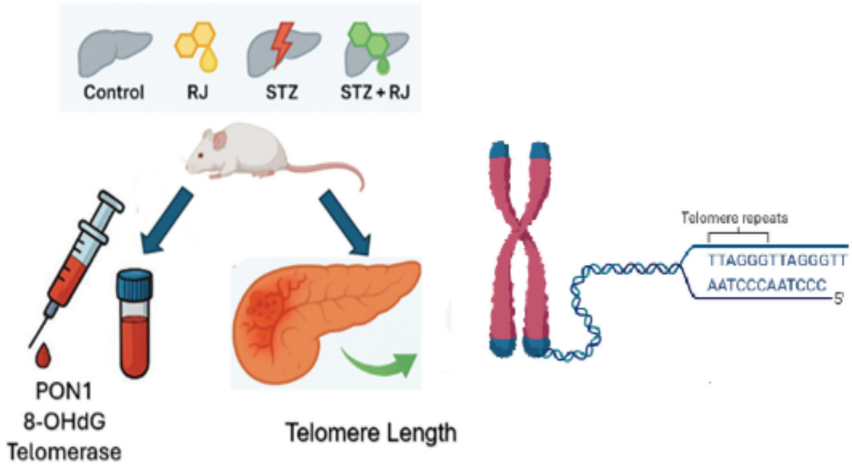

Figure 1. Experimental plan.
8-OHdG = 8-hydroxy-2'-deoxyguanosine; PON1 = paraoxonase-1; STZ = streptozotocin; RJ = royal jelly.

ScienCell Research Laboratories). A single-copy reference (SCR) primer, which amplifies a 100-bp region of chromosome 17, was employed for data normalization. Genomic DNA with a known telomere length served as a reference for calculating the telomere lengths of the study samples.

ΔCq (TEL) = Cq (TEL, target sample)- Cq (TEL, reference sample)

ΔCq (SCR) = Cq (SCR, target sample)- Cq (SCR, reference sample)

$\Delta\Delta Cq = \Delta Cq$ (TEL)- ΔCq (SCR) = Telomere length of reference sample $\times 2^{-\Delta\Delta Cq}$

The average telomere length in the target genomic DNA was 5.05 ± 0.18 Mb. Rat diploid cells have 84 telomeres; the average length of each telomere is = 5.05 ± 0.18 Mb/84 = 60.1 ± 2.1 kb per diploid cell or chromosome end (Çakır, 2023; O'Callaghan & Fenech, 2011).

Statistical Analysis

All data are expressed as mean ± standard deviation (SD). Normality and homogeneity of variances were assessed using the Shapiro–Wilk and Levene tests, respectively. Variables with homogenous variances were analyzed using one-way analysis of variance (ANOVA), followed by Tukey's post-hoc test, while variables with unequal variances were analyzed using Welch ANOVA, followed by Games–Howell post-hoc comparisons. Statistical significance was set at $p < 0.05$, and post-hoc differences are indicated in the tables as $^{*}p < 0.05$, $^{**}p < 0.01$, and $^{***}p < 0.001$. All analyses were performed using GraphPad Prism 9 (GraphPad Software, CA, USA).

Results

The serum 8-OHdG levels varied markedly among the groups (Table 1). They declined and elevated significantly in the RJ and STZ groups, respectively, compared to the control ($p < 0.001$). Co-treatment with RJ and STZ significantly reduced 8-OHdG levels compared to STZ alone ($p < 0.001$), although the contents of both groups remained slightly higher than that of the control group ($p < 0.05$).

Table 1. Serum 8-OHdG levels (ng/mL).

Group	Mean ± SD	Post-hoc
Control	1.445 ± 0.011	*
RJ	1.253 ± 0.034	**
STZ	1.718 ± 0.021	***
STZ + RJ	1.465 ± 0.046	*

8-OHdG: Group means ± SD. Normality was confirmed ($p > 0.05$), but homogeneity of variances was not confirmed according to Levene's test. Therefore, group differences were analyzed using Welch ANOVA, followed by Games–Howell post-hoc test for pairwise comparisons, and significance levels are indicated in the table as $^{*}p < 0.05$, $^{**}p < 0.01$, and $^{***}p < 0.001$. 8-OHdG = 8-hydroxy-2'-deoxyguanosine; RJ = royal jelly; SD = standard deviation; STZ = streptozotocin.

PON1 activity differed remarkably between the groups (Table 2). It significantly increased and decreased in the RJ and STZ groups, respectively, compared to the control group ($p < 0.001$). STZ and RJ cotreatment increased PON1 activity compared to STZ alone, restoring it closer to the control group levels ($p < 0.05$).

The pancreatic tissue telomere lengths varied significantly among the groups (Table 3). The telomere length decreased markedly in the STZ group but increased significantly in the STZ + RJ group compared to the STZ group ($p < 0.01$), although it was not fully restored to the same length as the control group.

The serum telomerase levels also differed among the groups (Table 4). They declined markedly in the STZ group, but did not differ significantly in the RJ and STZ + RJ groups, compared to the control group ($p > 0.05$). these findings indicate that RJ administration partially mitigated such STZ-induced decrease.

Table 2. Serum PON1 activity (U/mL).

Group	Mean ± SD	Post-hoc
Control	218.7 ± 4.4	*
RJ	229.7 ± 7.4	**
STZ	187.0 ± 2.6	***
STZ + RJ	212.0 ± 5.0	*

PON1: Values are presented as mean ± SD. Normality and homogeneity of variances were confirmed, and group differences were analyzed using one-way ANOVA, followed by Tukey's post-hoc test. Significance levels are indicated as *$p < 0.05$, **$p < 0.01$, and ***$p < 0.001$.
PON1 = paraoxonase-1; RJ = royal jelly; SD = standard deviation; STZ = streptozotocin.

Table 3. Pancreatic telomerase length (kb).

Group	Mean ± SD	Post-hoc
RJ	96.64 ± 3.10	*
Control	100.94 ± 1.84	*
STZ	7.31 ± 0.29	***
STZ + RJ	44.82 ± 0.32	**

Telomere length: Values are presented as mean ± SD. Normality and homogeneity of variances were confirmed, and group differences were analyzed using one-way ANOVA, followed by Tukey's post-hoc test. Significance levels are indicated as *$p < 0.05$, **$p<0.01$, and ***$p < 0.001$. RJ = royal jelly; SD = standard deviation; STZ = streptozotocin.

Table 4. Serum telomerase levels (ng/mL).

Group	Mean ± SD	Post-hoc
Control	0.398 ± 0.036	*
RJ	0.348 ± 0.037	*
STZ	0.281 ± 0.064	**
STZ + RJ	0.348 ± 0.046	*

Telomerase levels: Values are presented as mean ± SD. Normality and homogeneity of variances were confirmed, and group differences were analyzed using one-way ANOVA, followed by Tukey's post-hoc test. Significance levels are indicated as *$p < 0.05$, **$p < 0.01$. RJ = royal jelly; SD = standard deviation; STZ = streptozotocin.

Discussion

STZ is widely employed to construct experimental diabetes models due to its selective cytotoxicity toward pancreatic β-cells within the islets of Langerhans. Structurally similar to glucose, STZ enters β-cells via the GLUT2 transporter and induces cell damage through mechanisms including DNA alkylation, nitric oxide production, and free radical generation. This process not only suppresses insulin biosynthesis but also promotes profound OS and inflammation in pancreatic tissues (Fu et al., 2010; Lenzen, 2008). In the present study, a single intraperitoneal dose of 50 mg/kg STZ was administered to initiate tissue-level pancreatic injury. This dosage has been identified as optimal, since lower doses (30–40 mg/kg) failed to elicit a consistent diabetic response, and higher doses (≥70 mg/kg) were associated with severe systemic toxicity and increased mortality (Ar'Rajab & Ahrén, 1993).

Beyond its use in diabetes modeling, STZ induces persistent genomic instability. Studies in rat-derived ADIPO-P2 cells demonstrated that STZ exposure triggers long-term telomeric dysfunction, characterized by a loss in telomere FISH signals and duplications, independent of telomerase level or telomere length (Paviolo et al., 2015). Similarly, *in vivo* studies reveal that STZ damages the DNA of the proximal tubular epithelial cells and activates p53-based signaling pathways, leading to site-specific cytotoxicity, which, in certain contexts, could be mitigated pharmacologically (Nakai et al., 2023). In neuronal models, differentiated SH-SY5Y cells displayed altered sensitivity to STZ-induced cytotoxicity and insulin resistance, highlighting the role of cell maturity in the STZ response (Bagaméry et al., 2021). Additionally, STZ induces retinal progenitor cell damage in neonatal rats independent of hyperglycemia, suggesting direct cytotoxic effects in developing tissues (Lin et al., 2024).

The health-benefiting influence of RJ stems from its rich composition of bioactives. RJ contains flavonoids and phenolics known for their potent antioxidant activity, enabling it to counteract OS implicated in the pathogenesis of various diseases (Kocot et al., 2018). Furthermore, major RJ proteins (MRJPs) and peptides derived from RJ demonstrate metal-chelating as well as antioxidant capabilities involving mechanisms such as hydrogen peroxide, superoxide, and hydroxyl radical scavenging. The proteolysis of RJ proteins produces peptides that exhibit a robust antioxidant potential (Guo et al., 2021).

Given the increasing interest in natural bioactive compounds, this study aimed to evaluate the potential protective effects of RJ against STZ-induced pancreatic injury, with particular attention to telomere length as a molecular indicator of cell viability. In addition, oxidative state alterations were assessed using specific biomarkers, 8-OHdG for DNA oxidative damage and PON1 for enzymatic antioxidant status, to elucidate the redox-modulatory role of RJ within the pancreatic microenvironment (Aviram & Rosenblat, 2004; Kasai, 1997; Mackness et al., 2004; Valavanidis et al., 2009).

In addition to telomere length, serum telomerase level was also evaluated to gain insights into the status of telomere maintenance mechanisms following STZ-induced pancreatic damage and to assess the modulatory effects of RJ on this process. Although serum telomerase levels may not fully reflect tissue-level enzyme activity, they can provide complementary information regarding systemic telomere dynamics (Kim & Wu, 1997).

The toxic effects of STZ are not limited to the selective damage of pancreatic β-cells but also to an increased systemic OS burden (Lenzen, 2008; Szkudelski, 2001). However, RJ administration increased PON1 activity and significantly reduced 8-OHdG concentrations. These results suggest that RJ exerts protective effects not only by alleviating oxidative DNA damage but also by reducing lipid peroxidation.

These results of previous studies support these findings. For instance, Çakır (2023) demonstrated that RJ markedly enhanced PON1 activity and suppressed 8-OHdG concentrations during liver toxicity induced in rats. Similarly, Çakır (2022) reported that different doses of RJ exerted beneficial effects on OS, as indicated by biomarker levels and telomerase level in rats exposed to cadmium. Prior investigations have emphasized the effectiveness of RJ in alleviating diabetes-associated biochemical disturbances and OS from various perspectives. Moreover, RJ promotes healing by stimulating cell division and tissue regeneration (El-Seedi et al., 2024; Oršolić & Jazvinšćak Jembrek, 2024). PON1 exerts beneficial effects in various diseases, including diabetes, by modulating the signaling pathways associated with inflammation and OS (Marsillach et al., 2009). The decrease in PON1 activity following cisplatin administration was extensively preserved in rats treated with RJ (Yildirim et al., 2012). Similarly, in the present study, STZ administration suppressed the PON1 activity, which were restored to near-control values following RJ treatment.

8-OHdG is a well-established biomarker used to detect base modifications induced by mutagenic damage to DNA and RNA (Alper et al., 2005; Wong et al., 2006). Experimental diabetes models have also demonstrated elevated OS marker and 8-OHdG levels, highlighting the oxidative nature of diabetic damage and the role of 8-OHdG as a molecular indicator of this process (Alper et al., 2005; Mis et al., 2018). In this study, plasma 8-OHdG concentrations were consistently and remarkably enhanced in STZ-treated rats compared to controls. The notable reduction in 8-OHdG levels following RJ administration is attributed to the potent antioxidant properties of RJ.

The findings of the present study are consistent with those reported in the literature, indicating that telomere integrity and telomerase level are closely associated with tissue damage, OS, and inflammation. Processes such as genome instability, heterochromatin loss, and telomere attrition accelerate cell senescence and aging, particularly under conditions of tissue injury and inflammatory stress (Wu et al., 2024). Comprehensive meta-analyses investigating the relationship between telomere dynamics and OS have provided substantial evidence that, although complex, OS accelerates *in vivo* telomere attrition, especially in studies employing structural telomere measurements such as TRF (Armstrong & Boonekamp, 2023). Similarly, Tilekli et al. (2024) reported that OS and proinflammatory responses directly affect telomere length, and that diets low in saturated fats or high in unsaturated fats, along with regular physical activity, help maintain telomere integrity.

Conversely, several studies have demonstrated that telomerase can be activated to a limited but critical level during regenerative processes. Notably, TERT expression-based interventions using adeno-associated viral vectors improved tissue function, reduced the levels of molecular aging markers, and remarkably extended lifespan even in adult and aged models (Bernardes de Jesus et al., 2012). These findings suggest that telomerase level may play a decisive role in tissue regeneration and post-injury recovery processes.

In this study, telomerase levels reached statistical significance following RJ administration. Telomere attrition accelerates under conditions of increased metabolic activity and inflammatory burden, and this effect may vary between species, methods, and tissues (Simoroz et al., 2025). Therefore, the marked reduction in telomerase levels observed in the STZ group and the increase seen in the RJ group reflect a pattern consistent with the literature.

The telomere length in the RJ group increased significantly, but did not fully reach the control levels, which can be attributed to persistent telomeric damage induced by STZ. As a potent DNA-methylating agent, STZ causes persistent structural alterations at the telomeric regions, which manifest as telomere dysfunction, instability, and associated chromosomal aberrations at the cytogenetic level (Paviolo et al., 2015). Under such persistent damage, even if regenerative mechanisms are activated, complete restoration of telomere integrity may not be achievable. Thus, the substantial improvement in telomere structure induced by RJ, yet not achieving control levels, can be considered a consequence of STZ-induced long-lasting telomeric injury.

Although telomeres naturally shorten with each cell division, certain factors, particularly tissue injury, can accelerate this process (Çakır, 2023; Epel et al., 2004). Telomerase activity can be readily monitored in continuously dividing cells such as cancer cells; however, its detection in somatic tissues is considerably more challenging (Blackburn, 1991). Telomerase activity can be observed during tissue regeneration processes (Cherif et al., 2003; Çakır, 2022, 2023; Shay & Bacchetti, 1997). In a study monitoring the regenerative status of rat pancreatic tissues, telomerase was found to be actively regulated (Oh et al., 2002).

A study investigating the applicability of telomere length as a biomarker of cell aging and tissue damage reported a remarkable shortening of the telomere in type 2 diabetes (Tarry-Adkins et al., 2021). Jiang et al. (2018) demonstrated that MRJPs exert anti-aging effects in human fibroblast cell lines and also enhance the number of cells with longer telomeres under *in vivo* conditions. Additionally, MRJPs elevate DNA and protein synthesis by modulating four age-related genes: *MTOR*, *SOD1*, *CTNNB1*, and *TP53* (Jiang et al., 2018). A cell viability assay highlighted the stimulatory effects of RJ on stem cell growth (Özkök et al., 2021). Similarly, Çakır (2023) reported that RJ improved telomere length, antioxidant parameters, and serum biochemical markers in rats with CCl_4-induced liver injury. RJ promotes cell survival, proliferation, and antioxidant responses while protecting telomeres during cell crises (Jenkhetkan et al., 2017). Furthermore, RJ protects human cells from genotoxicity, potentially through its antiapoptotic, antioxidative, and antiaging properties (Jenkhetkan et al., 2018). In this study, STZ administration markedly reduced telomere length in pancreatic cells, whereas RJ supplementation at the dose applied remarkably improved telomere integrity.

Conclusion

The findings of the present study indicate that RJ protects against STZ-induced pancreatic damage primarily by attenuating OS and supporting telomere integrity. STZ significantly increased oxidative DNA damage (8-OHdG levels) and reduced PON1 activity, confirming elevated OS levels. RJ effectively reversed these changes, restoring 8-OHdG and PON1 levels similar to those of the control group. Additionally, RJ partially improved telomerase level and telomere length, but not to levels occurring in the control group. This partial reversal of STZ-induced telomere shortening can be attributed to persistent DNA methylation and telomere dysfunction caused by STZ, which have been shown to result in lasting telomere instability. Further detailed investigations are warranted to better elucidate the bioactive components and therapeutic potential of RJ.

Ethics

Ethics Committee Approval: This study was carried out with the approval of Çanakkale Onsekiz Mart University Animal Experiments Local Ethics Committee (approval number: 2021/01-01, dated: 12.02.2021).

Data Sharing Statement: All data are available within the study.

Footnotes

Conflict of Interest: The author(s) have no conflicts of interest to declare.

Funding: The author(s) declare that this study has received no financial support.

References

Alper, G., Irer, S., Duman, E., Caglayan, O., & Yilmaz, C. (2005). Effect of L-deprenyl and gliclazide on oxidant stress/antioxidant status and DNA damage in a diabetic rat model. *Endocrine Research, 31*(3), 199–212. https://doi.org/10.1080/07435800500371805

Ar'Rajab, A., & Ahrén, B. (1993). Long-term diabetogenic effect of streptozotocin in rats. *Pancreas, 8*(1), 50–57. https://doi.org/10.1097/00006676-199301000-00011

Armstrong, E., & Boonekamp, J. (2023). Does oxidative stress shorten telomeres in vivo? A meta-analysis. *Ageing Research Reviews, 85*, 101854. https://doi.org/10.1016/j.arr.2023.101854

Aviram, M., & Rosenblat, M. (2004). Paraoxonases and cardiovascular diseases: Pharmacological and nutritional influences. *Current Drug Targets, 5*(3), 339–348. https://doi.org/10.2174/1389450043347732

Bagaméry, F., Varga, K., Kecsmár, K., Vincze, I., Szökő, É., & Tábi, T. (2021). Effects of differentiation on cytotoxicity and insulin sensitivity in streptozotocin-treated SH-SY5Y cells. *Neurochemical Research, 46*(6), 1350–1358. https://doi.org/10.1007/s11064-021-03390-1

Bernardes de Jesus, B., Vera, E., Schneeberger, K., Tejera, A. M., Ayuso, E., Bosch, F., & Blasco, M. A. (2012). Telomerase gene therapy in adult and old mice delays aging and increases longevity without increasing cancer. *EMBO Molecular Medicine, 4*(8), 691–704. https://doi.org/10.1002/emmm.201200245

Blackburn, E. H. (1991). Structure and function of telomeres. *Nature, 350*(6319), 569–573. https://doi.org/10.1038/350569a0

Blackburn, E. H. (2001). Telomere states and cell fates. *Nature, 408*(6808), 53–56. https://doi.org/10.1038/35040600

Cherif, H., Tarry, J. L., Ozanne, S. E., & Hales, C. N. (2003). Ageing and telomeres: A study into organ- and gender-specific telomere shortening. *Nucleic Acids Research, 31*(5), 1576–1583. https://doi.org/10.1093/nar/gkg208

Çakır, S. (2022). Effects of different doses of royal jelly on oxidative stress and telomerase enzyme in rats with cadmium toxicity. *Cukurova Medical Journal, 47*(4), 1516–1522. https://doi.org/10.17826/cumj.1139113

Çakır, S. (2023). The effect of royal jelly on telomere length and some biochemical parameters in Wistar albino rats with liver damage caused by carbon tetrachloride. *Journal of Medicinal Food, 26*(8), 580–585. https://doi.org/10.1089/jmf.2023.0042

El-Seedi, H. R., Salama, S., Abd El-Wahed, A. A., Guo, Z., Di Minno, A., Daglia, M., Li, C., Chen, L., Durazzo, A., Lucarini, M., Ahmed, H. S., Xiao, J., Cho, W. C., Bishayee, A., & Nabavi, S. M. (2024). Exploring the therapeutic potential of royal jelly in metabolic disorders and gastrointestinal diseases. *Nutrients, 16*(3), 292. https://doi.org/10.3390/nu16030392

Epel, E. S., Blackburn, E. H., Lin, J., Dhabhar, F. S., Adler, N. E., Morrow, J. D., & Cawthon, R. M. (2004). Accelerated telomere shortening in response to life stress. *Proceedings of the National Academy of Sciences, 101*(49), 17312–17315. https://doi.org/10.1073/pnas.0407162101

Fu, Y. Y., Kang, K. J., Ahn, J. M., Kim, H. R., Na, K. Y., Chae, D. W., Kim, S., & Chin, H. J. (2010). Hyperbilirubinemia reduces the streptozotocin-induced pancreatic damage through attenuating the oxidative stress in the Gunn rat. *Tohoku Journal of Experimental Medicine, 222*(4), 265–273. https://doi.org/10.1620/tjem.222.265

Fujiwara, S., Imai, J., Fujiwara, M., Yaeshima, T., Kawashima, T., & Kobayashi, K. (1990). A potent antibacterial protein in royal jelly: Purification and determination of the primary structure of royalisin. *Journal of Biological Chemistry, 265*(19), 11333–11337. https://doi.org/10.1016/s0021-9258(19)38596-5

Ghanbari, E., Nejati, V., & Khazaei, M. (2016). Improvement in serum biochemical alterations and oxidative stress of liver and pancreas following use of royal jelly in streptozotocin-induced diabetic rats. *Cell Journal, 18*(3), 362–370. https://doi.org/10.22074/cellj.2016.4564

Ghanbari, E., Nejati, V., Najafi, G., Khazaei, M., & Babaei, M. (2015). Study on the effect of royal jelly on reproductive parameters in streptozotocin-induced diabetic rats. *International Journal of Fertility & Sterility, 9*(1), 113–120.

Guo, J., Wang, Z., Chen, Y., Cao, J., Tian, W., Ma, B., & Dong, Y. (2021). Active components and biological functions of royal jelly. *Journal of Functional Foods, 82*, 104514. https://doi.org/10.1016/j.jff.2021.104514

Jenkhetkan, W., Thitiorul, S., Jansom, C., & Ratanavalachai, T. (2017). Molecular and cytogenetic effects of Thai royal jelly: Modulation through c-MYC, h-TERT, NRF2, HO-1, BCL2, BAX, and cyclins in human lymphocytes in vitro. *Mutagenesis, 32*(5), 525–531. https://doi.org/10.1093/mutage/gex020

Jenkhetkan, W., Thitiorul, S., Jansom, C., & Ratanavalachai, T. (2018). Genoprotective effects of Thai royal jelly against doxorubicin in human lymphocytes in vitro. *Natural Product Communications, 13*(1), 79–84. https://doi.org/10.1177/1934578X1801300124

Jiang, C., Liu, X., Li, C., Qian, H., Chen, D., Lai, C., & Shen, L. (2018). Anti-senescence effect and molecular mechanism of the major royal jelly proteins on human embryonic lung fibroblast (HFL-I) cell line. *Journal of Zhejiang University Science B, 19*(12), 960–972. https://doi.org/10.1631/jzus.B1800257

Kasai, H. (1997). Analysis of a form of oxidative DNA damage, 8-hydroxy-2'-deoxyguanosine, as a marker of cellular oxidative stress during carcinogenesis. *Mutation Research/Reviews in Mutation Research, 387*(3), 147–163. https://doi.org/10.1016/s1383-5742(97)00035-5

Kim, N. W., & Wu, F. (1997). Advances in quantification and characterization of telomerase activity by the telomeric repeat amplification protocol (TRAP).

Nucleic Acids Research, 25(13), 2595–2597. https://doi.org/10.1093/nar/25.13.2595

Kocot, J., Kiełczykowska, M., Luchowska-Kocot, D., Kurzepa, J., & Musik, I. (2018). Antioxidant potential of propolis, bee pollen, and royal jelly: Possible medical application. *Oxidative Medicine and Cellular Longevity, 2018*, 7074209. https://doi.org/10.1155/2018/7074209

Lenzen, S. (2008). The mechanisms of alloxan- and streptozotocin-induced diabetes. *Diabetologia, 51*(2), 216–226. https://doi.org/10.1007/s00125-007-0886-7

Like, A. A., & Rossini, A. A. (1976). Streptozotocin-induced pancreatic insulitis: New model of diabetes mellitus. *Science, 193*(4251), 415–417. https://doi.org/10.1126/science.180605

Lin, Y., Du, W., Fu, X., Huang, L., Hong, Y., Tan, H., Xiao, L., Ren, X., Wang, Y., & Chen, D. (2024). Hyperglycemia-independent neonatal streptozotocin-induced retinopathy (NSIR) in rats. *Frontiers in Pharmacology*, 15, 1395887. https://doi.org/10.3389/fphar.2024.1395887

Mackness, M., Durrington, P., & Mackness, B. (2004). Paraoxonase 1 activity, concentration, and genotype in cardiovascular disease. *Current Opinion in Lipidology, 15*(4), 399–404. https://doi.org/10.1097/01.mol.0000137862.21179.7d

Marsillach, J., Camps, J., Ferré, N., Beltran, R., Rull, A., Mackness, B., Mackness, M., & Joven, J. (2009). Paraoxonase-1 is related to inflammation, fibrosis, and PPAR delta in experimental liver disease. *BMC Gastroenterology, 9*, 3. https://doi.org/10.1186/1471-230X-9-3

Mis, L., Comba, B., Uslu, S., & Yeltekin, A. (2018). Effect of wheatgrass on DNA damage, oxidative stress index, and histological findings in diabetic rats. *International Journal of Morphology, 36*(4), 1235–1240.

Nakai, K., Umehara, M., Minamida, A., Yamauchi-Sawada, H., Sunahara, Y., Matoba, Y., Okuno-Ozeki, N., Nakamura, I., Nakata, T., Yagi-Tomita, A., Uehara-Watanabe, N., Ida, T., Yamashita, N., Kamezaki, M., Kirita, Y., Konishi, E., Yasuda, H., Matoba, S., Tamagaki, K., & Kusaba, T. (2023). Streptozotocin induces proximal tubular injury via p53 signaling activation. *Scientific Reports, 13*, 8705. https://doi.org/10.1038/s41598-023-35850-w

O'Callaghan, N. J., & Fenech, M. (2011). A quantitative PCR method for measuring absolute telomere length. *Biological Procedures Online, 13*(1), 3. https://doi.org/10.1186/1480-9222-13-3

Oh, B. K., Seong, J. K., Lee, J. E., Chae, K. J., Roh, K. J., Park, C., & Park, Y. N. (2002). Induction of telomerase activity during an early burst of proliferation in pancreatic regeneration. *Cancer Letters, 186*(1), 93–98. https://doi.org/10.1016/S0304-3835(02)00320-8

Oršolić, N., & Jazvinšćak Jembrek, M. (2024). Royal jelly: Biological action and health benefits. *International Journal of Molecular Sciences, 25*(11), 6023. https://doi.org/10.3390/ijms25116023

Özkök, A., Akbay, E., Tanuğur Samancı, A. E., Mayda, N., & Onur, M. A. (2021). Evaluation of bioactive compounds and proliferation properties of different royal jelly samples. *Progress in Nutrition*, 23(1), 1–8. https://doi.org/10.23751/pn.v23i1.9360

Paviolo, N. S., Santinaque, F. F., Castrogiovanni, D. C., Folle, G. A., & Bolzán, A. D. (2015). The methylating agent streptozotocin induces persistent telomere dysfunction in mammalian cells. *Mutation Research/Genetic Toxicology and Environmental Mutagenesis, 794*, 17–24. https://doi.org/10.1016/j.mrgentox.2015.06.006

Saha, A., Chakrovorty, A., Bhattacharjee, B., Nandi, S., & Samadder, A. (2025). Curcumin reduces streptozotocin-induced genotoxicity in vivo by activating p53 protein and preventing oxidative stress and chromosomal aberrations. *Combinatorial Chemistry & High Throughput Screening, 28*(8), 1290–1300. https://doi.org/10.2174/1386207328666250408150913

Shay, J. W., & Bacchetti, S. (1997). A survey of telomerase activity in human cancer. *European Journal of Cancer A, 33*(5), 787–791. https://doi.org/10.1016/S0959-8049(97)00062-2

Simoroz, E. V., Vasilevska, J., Arakelyan, N. A., Manakhov, A. D., & Rogaev, E. I. (2025). Unusual animal models for studying the role of telomeres in aging and longevity. *Vavilov Journal of Genetics and Breeding, 29*(4), 496.

Szkudelski, T. (2001). The mechanism of alloxan and streptozotocin action in β-cells of the rat pancreas. *Physiological Research, 50*(6), 537–546. https://www.biomed.cas.cz/physiolres/2001/issue6/szkudelski.htm

Tarry-Adkins, J. L., Aiken, C. E., Dearden, L., Fernandez-Twinn, D. S., & Ozanne, S. (2021). Exploring telomere dynamics in aging male rat tissues: Can tissue-specific differences contribute to age-associated pathologies? *Gerontology*, 67(2), 233–242. https://doi.org/10.1159/000511608

Tilekli, M. M., Yılmaz, A. K., Yasul, Y., Çon, N., Mercan, S., & Tek, N. (2024). Effects of diet and exercise on leukocyte telomere length, oxidative stress, and inflammation markers in rats. *Experimental and Molecular Pathology, 140*, 104947. https://doi.org/10.1016/j.yexmp.2024.104947

Tokunaga, K., Yoshida, C., Suzuki, K. M., Maruyama, H., Futamura, Y., Araki, Y., & Mishima, S. (2004). Antihypertensive effect of peptides from royal jelly in spontaneously hypertensive rats. *Biological & Pharmaceutical Bulletin, 27*(2), 189–192. https://doi.org/10.1248/bpb.27.189

Tural Çifçi, A., & Tuzcu, M. (2025). Diabetes induction models in rats. In F. Kazak Akçakavak & G. Akçakavak (Eds.), *Current evaluations in veterinary physiopathology: Modern analysis, findings, and research* (pp. 25–43). Livre de Lyon.

Valavanidis, A., Vlachogianni, T., & Fiotakis, C. (2009). 8-hydroxy-2'-deoxyguanosine (8-OHdG): A critical biomarker of oxidative stress and carcinogenesis. *Journal of Environmental Science and Health, Part C, 27*(2), 120–139. https://doi.org/10.1080/10590500902885684

Vucevic, D., Melliou, E., Vasilijic, S., Gasic, S., Ivanovski, P., Chinou, I., & Colic, M. (2007). Fatty acids isolated from royal jelly modulate dendritic cell-mediated immune response in vitro. *International Immunopharmacology*, 7(9), 1211–1220. https://doi.org/10.1016/j.intimp.2007.05.009

Wong, Y. T., Ruan, R., & Tay, F. E. H. (2006). Relationship between levels of oxidative DNA damage, lipid peroxidation and mitochondrial membrane potential in young and old F344 rats. *Free Radical Research, 40*(4), 393–402. https://doi.org/10.1080/10715760600556074

Wu, Z., Qu, J., & Liu, G. H. (2024). Roles of chromatin and genome instability in cellular aging and their links to age-related diseases. *Nature Reviews Molecular Cell Biology, 25*(12), 979–1000. https://doi.org/10.1038/s41580-024-00579-3

Yildirim, S., Karadeniz, A., Karakoç, A., Yildirim, A., Kalkan, Y., & Şimşek, N. (2012). Effects of royal jelly on liver paraoxonase activity in rats treated with cisplatin. *Turkish Journal of Medical Sciences, 42*(3), 367–375. https://doi.org/10.3906/sag-1102-1373

Zhang, A. M. Y., Magrill, J., de Winter, T. J. J., Hu, X., Skovsø, S., Schaeffer, D. F., Kopp, J. L. & Johnson, J. D. (2019). Endogenous hyperinsulinemia contributes to pancreatic cancer development. *Cell Metabolism, 30*(3), 403–404. https://doi.org/10.1016/j.cmet.2019.07.009

Trakya University Journal of Natural Sciences, 27(1), 37–46, 2026
DOI: 10.23902/trkjnat.02579
www.tujns.org

Research Article

Probiotic and metabolite profiling of poongar rice fermentation matrix: A zebrafish-based intervention study for gut dysbiosis

Preyenga Ramesh, Arockiya Anita Margret*, Harishma Sekar

Bishop Heber College (Autonomous), Affiliated to Bharathidasan University, Department of Biotechnology, Tiruchirappalli, India

Cite this article as: Ramesh, P., Margret, A. A., & Sekar, H. (2025). Probiotic and metabolite profiling of poongar rice fermentation matrix: A zebrafish-based intervention study for gut dysbiosis. *Trakya University Journal of Natural Sciences, 27*(1), 37–46. https://doi.org/10.23902/trkjnat.02579

Abstract

Background: Traditional rice-based fermented foods, prevalent across Asia particularly India, constitute an unexplored reservoir of probiotic microorganisms with high commercial potential for functional foods and synbiotics.

Aims: This study investigates the probiotic properties and therapeutic efficacy of a fermented matrix derived from *Oryza sativa* (Poongar rice) against antibiotic-induced gut dysbiosis.

Methods: Fermented Poongar rice water underwent microbial isolation, biochemical characterization, and 16S rRNA sequencing, which confirmed the presence of *Lactococcus lactis* with 96.7% homology. The isolated strain was assessed for its tolerance to acidic pH, bile salts, and salinity. Gas chromatography–mass spectrometry analysis was employed to characterize its bioactive metabolite profile, including short-chain fatty acids (SCFAs). Nutritional composition analysis and exopolysaccharides (EPS) quantification were also performed. Zebrafish (*Danio rerio*) were utilized to evaluate acute toxicity (LC_{50} = ~2,138 ppm) and to examine gut recovery following erythromycin-induced dysbiosis.

Results: The isolated strain exhibited high survivability under simulated gastrointestinal conditions and demonstrated the production of SCFAs and EPS, both of which contribute to gut health. Zebrafish administered the probiotic matrix after antibiotic exposure displayed restored swimming behavior and significant improvement in intestinal histoarchitecture, characterized by reduced goblet cell hyperplasia and diminished villi damage.

Özet

Dayanak: Özellikle Hindistan olmak üzere Asya›da yaygın olan geleneksel pirinç bazlı fermente gıdalar, fonksiyonel gıdalar ve sinbiyotikler için yüksek ticari potansiyele sahip, keşfedilmemiş bir probiyotik mikroorganizma rezervuarı oluşturmaktadır.

Amaçlar: Bu çalışma, *Oryza sativa* (Poongar pirinci) kaynaklı fermente matrisin antibiyotik kaynaklı bağırsak disbiyozuna karşı probiyotik özelliklerini ve terapötik etkinliğini araştırmaktadır.

Yöntemler: Fermente Poongar pirinç suyu, mikrobiyal izolasyon, biyokimyasal karakterizasyon ve 16S rRNA dizileme işlemlerinden geçirilmiş ve %96,7 homoloji ile *Lactococcus lactis* varlığı doğrulanmıştır. İzole edilen suş, asidik pH, safra tuzları ve tuzluluğa karşı toleransı açısından değerlendirilmiştir. Gaz kromatografisi-kütle spektrometrisi analizi, kısa zincirli yağ asitleri (SCFAs) dahil olmak üzere biyoaktif metabolit profilini karakterize etmek için kullanılmıştır. Besin bileşimi analizi ve ekzopolisakkarit (EPS) miktarının belirlenmesi de gerçekleştirildi. Zebra balığı (*Danio rerio*) akut toksisiteyi (LC_{50} = ~2.138 ppm) değerlendirmek ve eritromisin kaynaklı disbiyozis sonrası bağırsakların iyileşmesini incelemek için kullanıldı.

Bulgular: İzole edilen suş, simüle edilmiş gastrointestinal koşullar altında yüksek hayatta kalma oranı sergilemiş ve bağırsak sağlığına katkıda bulunan SCFAs ve EPS üretimi göstermiştir. Antibiyotik maruziyetinden sonra probiyotik matris uygulanan zebra balıkları, yüzme davranışlarının düzeldiğini ve bağırsak histoarkitektüründe, goblet hücre hiperplazisinin azalması ve villus hasarının azalması ile karakterize edilen önemli bir iyileşme göstermiştir.

Edited by: *Reşat Ünal*

***Corresponding Author:** Arockiya Anita Margret, **E-mail:** anitamargret.bi@bhc.edu.in*

***ORCID iDs of the author(s):** PR. 0000-0003-2325-1884, AAM. 0000-0002-0417-2462, HS. 0009-0003-7740-1355*

Received: 11 September 2025, **Accepted:** 27 November 2025, **Epub:** 22 December 2025, **Published:** 24 April 2026

Conclusion: Fermented Poongar rice contains a functionally robust strain of *L. lactis* capable of restoring gut integrity *in vivo*. The findings supports its potential development as a culturally rooted, cost-effective probiotic candidate for gut health applications.

Sonuç: Fermente Poongar pirinci, *in vivo* bağırsak bütünlüğünü geri kazanabilen, işlevsel olarak güçlü bir *L. lactis* suşu içerir. Bulgular, bağırsak sağlığı uygulamaları için kültürel kökenli, uygun maliyetli bir probiyotik adayı olarak potansiyel gelişimini desteklemektedir.

Keywords: Short-chain fatty acids, intestinal microbiota modulation, host–microbe interaction, functional fermented foods, aquatic toxicology model, gut-brain axis signaling

Introduction

The human gastrointestinal tract harbors trillions of microorganisms that collectively form a dynamic and highly complex ecosystem referred to as the gut microbiota. This microbial community plays a crucial role in digestion, immune modulation, nutrient metabolism, and the maintenance of intestinal barrier integrity (Hills et al., 2019). Disruptions in this delicate balance, known as gut dysbiosis, have been associated with a wide range of health disorders, including metabolic dysfunctions, gastrointestinal inflammation, and neuropsychiatric diseases (Ogunrinola et al., 2020). Probiotics, defined as live microorganisms that confer health benefits when administered in adequate amounts have gained considerable attention as therapeutic agents capable of restoring microbial homeostasis (Nagpal et al., 2012). Commonly employed probiotic genera, including *Lactobacillus*, *Bifidobacterium*, and *Lactococcus*, have demonstrated significant efficacy in improving gut health, reducing pathogen load, and modulating immune responses (Kechagia et al., 2013). However, the effectiveness of probiotics is highly strain-specific and largely dependent on their capacity to withstand gastrointestinal stressors such as acidic pH, bile salts, and digestive enzymes (Binda et al., 2020). Traditional fermented foods represent a natural and rich reservoir of beneficial microorganisms. In this context, indigenous rice varieties such as Poongar rice present promising potential for probiotic development. Poongar rice is a red-husked, unpolished grain cultivated in Tamil Nadu's Cauvery Delta and is known for its high content of micronutrients, antioxidants, and dietary fiber. Historically utilized in Ayurvedic medicine, it is reputed for its benefits in supporting reproductive health, regulating blood glucose levels, and improving skin and digestive health (Radha et al., 2022; Rathna Priya et al., 2019). Despite these traditional claims, scientific validation of the microbiota-enhancing properties of Poongar rice remains limited, with few studies like fermented rice water screening (*Leuconostoc lactis*, *Weissella cibaria*; >80% gastric survival) and general synbiotic effects of fermented rice beverages (*Pediococcus pentosaceus* isolation) providing preliminary evidence but lacking Poongar-specific microbiota modulation data (Chavan et al., 2022). The present study investigates the probiotic potential of a fermented Poongar rice matrix through the isolation and characterization of native microbial strains. The study further evaluates the ability of these strains to endure simulated gastrointestinal conditions and identifies key functional metabolites, including short-chain fatty acids (SCFAs) and exopolysaccharides (EPS). To validate the *in vivo* efficacy and safety of the fermented matrix, a Zebrafish (*Danio rerio*) gut dysbiosis model is employed, leveraging its genetic homology with humans and its transparent gut morphology, which facilitates microbiome assessment (Lu et al., 2021).

This research integrates traditional food knowledge with contemporary microbial science to advance the development of culturally rooted probiotic interventions aimed at restoring gut microbial balance.

Materials and Methods

Sample Collection and Fermentation of Poongar Rice

Traditional Poongar rice grains were procured from Rengachipatti, Thalinji village in Tamil Nadu. The rice (100 g) was thoroughly washed and boiled for one hour. The resulting cooking water was allowed to cool to room temperature, transferred into sterile glass containers, and loosely sealed to permit limited air exchange. Fermentation was carried out at ambient temperature (approximately 28 $\pm$ 2 °C) for three days under semi-aerobic conditions. To minimize microbial contamination, all vessels and utensils were sterilized prior to use, and the entire setup was maintained under clean environmental conditions. The fermented rice water thus obtained was used as the base medium for probiotic screening, following the method of Fuloria et al. (2022).

Isolation and Morphological Analysis of Probiotic Strain

To isolate potential probiotic candidates, the fermented rice water was subjected to serial dilution and spread onto de Man, Rogosa, and Sharpe (MRS) agar plates. The plates were incubated at 30 °C for 24 hours. Morphologically distinct colonies were selected and subcultured repeatedly to obtain pure isolates. Microscopic examination, including Gram staining and the hanging drop technique, were performed to determine cellular morphology and motility.

Biochemical Profiling

The purified isolate was subjected to comprehensive biochemical characterization using standard assays. These included the IMViC tests and enzymatic activity assays. The tests evaluated indole production, methyl red, Voges-Proskauer reaction, citrate utilization, catalase and oxidase activities, triple sugar iron utilization, and starch hydrolysis.

Molecular Confirmation Using 16S rRNA Gene Sequencing

Genomic DNA was extracted using the HiPurA® purification kit. The 16S rRNA gene was amplified by polymerase chain reaction using universal primers 27f and 1492r. The amplified products

were confirmed by agarose gel electrophoresis. The obtained sequences were analyzed using the BLAST tool, and phylogenetic relationships were inferred using MEGA11 software to support taxonomic identification.

Evaluation of Probiotic Survivability Under Stress Conditions

The robustness of the isolate was assessed by evaluating its tolerance to acidic pH, bile salts, and elevated sodium chloride concentrations. Acid tolerance was tested at pH 3.0. Salt tolerance was examined using nutrient broth supplemented with varying NaCl concentrations, while bile salt resistance was evaluated using agar infused containing bile salts.

Gas Chromatography–Mass Spectrometry (GC–MS)-Based Metabolite Profiling

An aqueous extract of the fermented Poongar rice matrix was prepared and analyzed using GC–MS to identify the major metabolic compounds produced during fermentation.

Quantification of EPS Production

EPS was quantified using the Anthrone reagent method. Polysaccharide concentration was determined by comparing absorbance values against a glucose standard calibration curve, enabling estimation of EPS content in the fermented matrix.

Nutritional Composition Analysis

The fermented substrate was analyzed for its macronutrient composition. Total carbohydrate content was estimated using the Anthrone assay. Lipids were quantified using the Bligh and Dyer extraction method, and protein concentration was determined by the Bradford assay.

Zebrafish Toxicity Assay and Maintenance Protocol

Ethical approval for zebrafish maintenance and handling was obtained from the Saveetha Dental College & Hospital Institutional Human Ethical Committee (SDC-IHEC) (reference number: 24/BIOCHEM/049, dated: 28.05.2024). Adult *Danio rerio* were randomly allocated into six groups comprising one control and five treatment groups, with 10 fish per group and a total of 60 individuals. The fish were maintained in aquaria under controlled laboratory conditions at 28.5 °C with a 14-hour light and 10-hour dark photoperiod. Freeze-dried probiotic matrix was administered at concentrations of 0, 400, 800, 1600, 3200, and 6,400 ppm. These concentrations were selected to cover the complete dose–response spectrum, enabling the assessment of both sub-lethal and lethal effects for accurate LC_{50} determination. Each concentration was tested in triplicate to perform acute toxicity evaluation, and the median LC_{50} was calculated using probit regression analysis.

Induction of Gut Dysbiosis and Probiotic Remediation Strategy

Gut Dysbiosis was experimentally induced by exposing zebrafish to erythromycin at a concentration of 0.6 mg/mL for a duration of 96 hours. Following antibiotic exposure, a subset of fish received the probiotic formulation. Behavioral parameters were monitored after treatment to assess recovery and physiological normalization.

Histological Examination of Intestinal Tissue

After treatment, zebrafish intestinal tissues were excised and fixed in 4% formalin. Standard paraffin embedding procedures were followed, and tissue sections were prepared. The sections were stained with hematoxylin and eosin (H&E) and examined microscopically for histopathological changes related to mucosal and structural integrity.

Statistical Analysis

All experimental assays were performed in triplicate. The fish were exposed to the fermented Poongar matrix for 96 hours under static conditions. Mortality was confirmed when no visible movement, including opercular motion, was observed and when stimulation of the caudal peduncle elicited no response. Mortalities and visible abnormalities in appearance and behavior were recorded. The concentrations required to cause 50% mortality (LC_{50}) was determined (Singleman & Holtzman, 2014). Acute toxicity over 96 h was calculated as LC_{50} and subjected to probit analyses using Finney's method (Finney, 1971). Results with $p < 0.05$ were considered statistically significant. The LC_{50} value was obtained both arithmetically using regression equations and graphically by plotting logarithmic concentration values against probit mortality. Differences among treatment groups were analyzed using regression analysis and one-way analysis of variance (ANOVA) with a 95% confidence interval. Toxicological data were further modeled using residual and probability output metrics to assess goodness of fit and predictive accuracy. All statistical analyses were performed using Microsoft (MS) Excel 2007 with the Analysis Toolpak enabled for data validation and advanced statistical computation (Praskova et al., 2011).

Results

Fermentation of Poongar rice led to the emergence of distinct microbial colonies after 72 hours. Following serial dilution and plating on MRS agar, the colonies exhibited a cocci morphology upon microscopic observation and were identified as Gram-positive. Hanging drop analysis further confirmed that the isolates were non-motile. These morphological characteristics are typical of lactic acid bacteria, which are commonly associated with probiotic properties.

The isolated strain was subsequently subjected to a series of biochemical assays for further characterization. The strain tested positive for methyl red and triple sugar fermentation, while it was negative for indole production, Voges-Proskauer reaction, citrate utilization, catalase activity, oxidase activity, and motility. Additionally, the presence of a clear zone in the starch hydrolysis assay confirmed the organism's ability to produce extracellular amylase. These biochemical features are consistent with the established metabolic profile of *Lactococcus* spp., which are known for efficient carbohydrate fermentation and growth under acidic conditions.

Genomic DNA extracted from the isolate was of high quality, as confirmed by agarose gel electrophoresis (Figure 1). Amplification of the 16S rRNA gene using universal primers produced a distinct and specific band. Sequence analysis using BLAST revealed a 96.7% identity with *Lactococcus lactis*.

Phylogenetic tree analysis further validated the molecular identification by clustering the isolate within the *Lactococcus* genus, a taxonomic group widely recognized for its probiotic applications in food systems (Figure 2).

Acid tolerance studies demonstrated the robust survival of the isolate at pH 3.0, thereby simulating gastric conditions. Likewise, the strain tolerated NaCl concentrations of up to 8%, confirming its ability to persist in high salt environments such as the human gastrointestinal tract or preserved food matrices. Bile salt tolerance was further confirmed by visible colony growth on bile agar plates after 24 hours of incubation. Collectively these traits highlight the isolate's potential to survive in gastrointestinal conditions - an essential requirement for probiotics intended for oral administration (Figure 3).

GC–MS Analysis of SCFAs

The aqueous extract of the fermented Poongar rice matrix was analyzed using GC–MS, which revealed the presence of various SCFAs and other bioactive compounds (Figure 4 and Table 1). Among the detected metabolites, beta-D-glucopyranoside tetraacetate and 2-ketobutyric acid were identified as the predominant components. These compounds are known to be associated with enhanced intestinal barrier function and anti-inflammatory activity. Their detection in the fermented matrix contributes to the functional significance of the rice-based probiotic formulation.

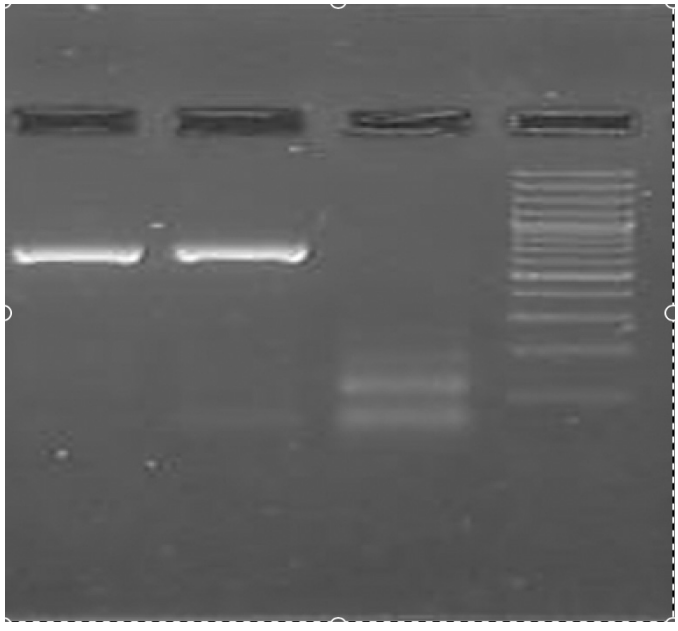

Figure 1. Agarose gel electrophoresis showing the genomic DNA of the isolated strain.

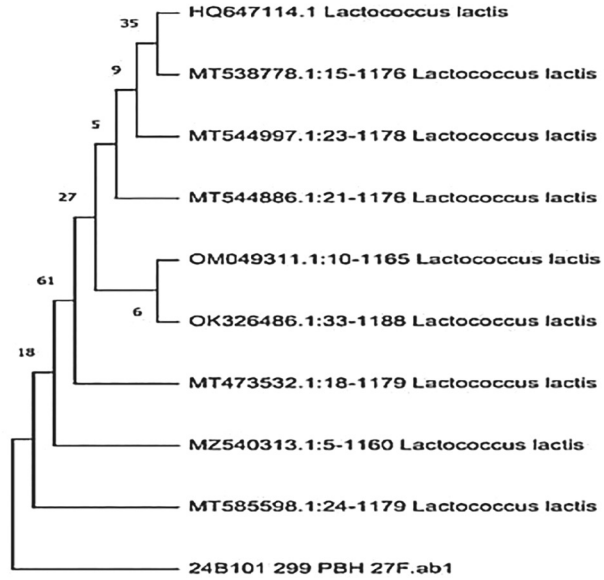

Figure 2. Phylogenetic tree showing the highest percentage of sequence similarity, constructed using MEGA11 software.

The Anthrone assay revealed that the EPS content of the fermented matrix was 0.506 g per 100 g of rice powder. EPS s are known to enhance microbial adhesion, modulate immune responses, and contribute to the prebiotic potential of probiotic formulations (Table 2). The relatively high EPS concentration further confirms the isolate's ability to support gut health through both effective colonization and metabolic activity. Biochemical profiling also indicated that the fermented rice matrix is nutritionally rich, with the lipid content estimated at 40% using the Bligh and Dyer method. The carbohydrate and protein contents were calculated as 0.089 g and 0.055 g per 100 g of rice powder, respectively. These macronutrients may serve as essential energy sources that support the viability and metabolic performance of probiotic strains during gastrointestinal transit and subsequent colonization in the gut.

To evaluate safety, zebrafish were exposed to a concentration range of 400–3,600 ppm of the lyophilized rice-probiotic matrix. This range was selected to encompass sub-therapeutic to elevated doses, thereby capturing a comprehensive toxicity profile. This chosen concentrations included levels both below and above the anticipated LC_{50}, allowing for robust determination of toxicity thresholds and ensuring the detection of adverse effects at higher doses. Statistical analyses using ANOVA and regression revealed a significant treatment effect on zebrafish toxicity ($f = 12.58$, $p < 0.039$), with the regression model indicating that toxicity increased by approximately 4.62 units per unit increase in concentration ($p < 0.04$). The LC_{50} value of 2,138 ppm, derived using MS Excel 2007 Probit analysis, reflects moderate toxicity. The LC_{50} value determined using non-linear regression analysis in GraphPad Prism was 1,828 ppm, while the 95% confidence interval ranged from 1,294 to 2,487 ppm, which closely aligns with the value

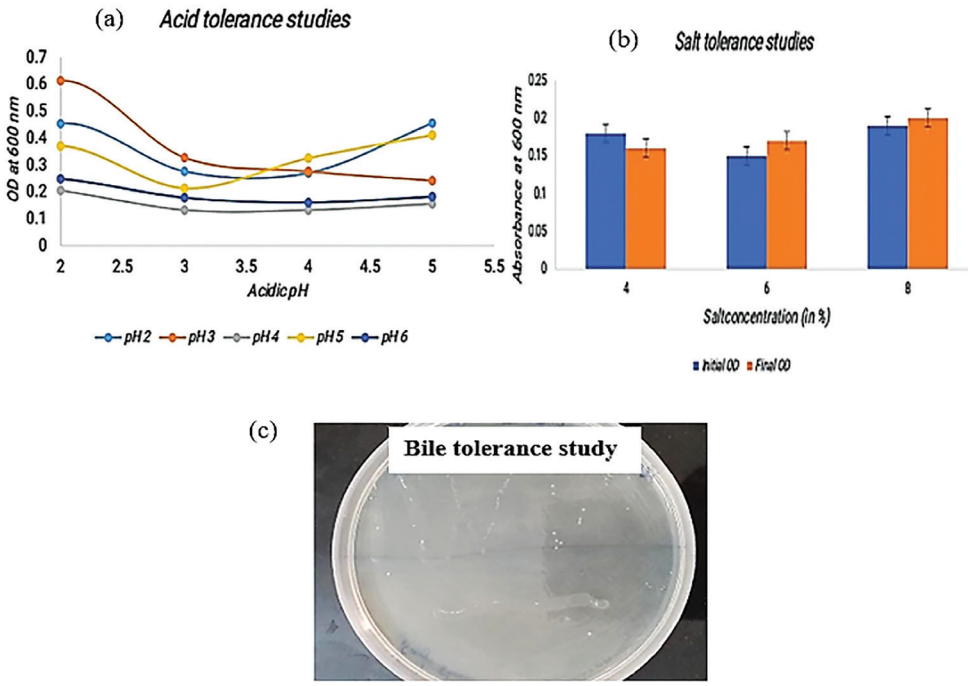

Figure 3. Probiotic endurance studies showing (a) bacterial growth under different pH conditions ranging from acidic to basic; (b) bacterial growth under varying salt concentrations; (c) growth of the probiotic strain on bile salt agar medium.

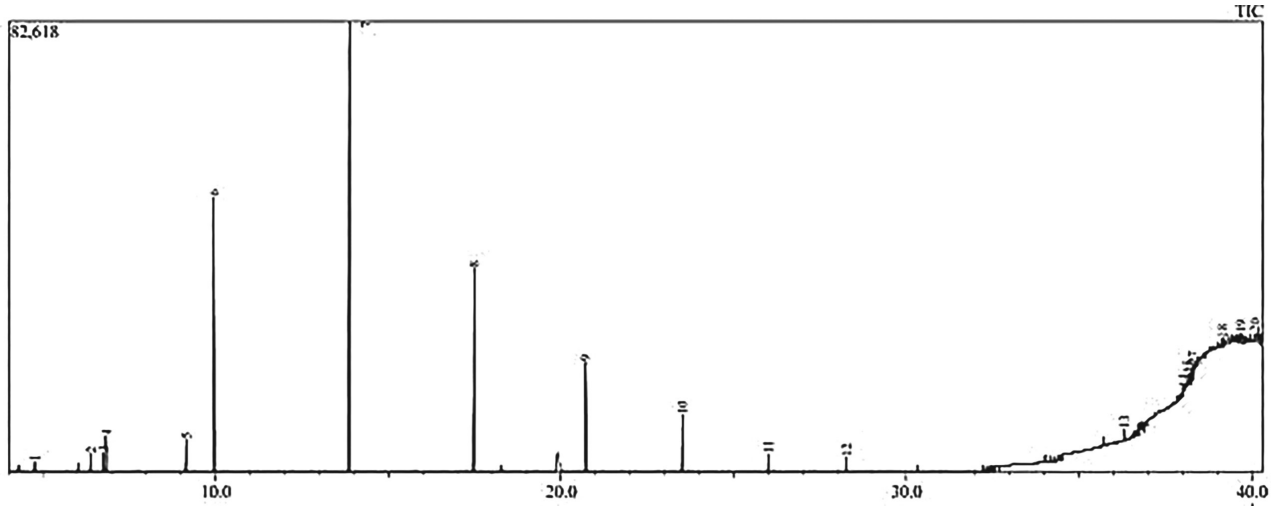

Figure 4. GC–MS spectrum of fermented Poongar rice.

obtained from the MS Excel regression-based data validation. Probit modeling further confirmed that concentrations below this threshold did not induce significant mortality or adverse effects, thereby supporting the safety of the formulations at therapeutically relevant doses. Zebrafish exposed to sub-lethal concentrations maintained normal shoaling, swimming, and exploratory behaviors, without no observable stress-related responses. Imaging and visual assessments also revealed no developmental abnormalities, organ damage, or morphological alterations below the LC_{50} level (Figures 5 and 6; Tables 3–5).

Antibiotic-induced gut dysbiosis was established by treating zebrafish with erythromycin (0.6 mg/mL) for a period of 96 hours. The treated fish exhibited reduced motility, loss of appetite, and increased mortality. In contrast, fish that received the probiotic matrix following antibiotic exposure demonstrated marked recovery in swimming behavior and body weight. These observations suggest that the formulation supported effective gut recolonization and promoted systemic physiological recovery.

Table 1. GC–MS-identified compounds of fermented Poongar rice.

Number	Name	Retention	Peak area %
1	**2-Keto-butyric-acid****	4.767	0.80
2	(2.Alpha.,3.alpha.,4a.beta.,5.beta.,8a.alpha.)-(+-)-3,4,4a,5,6,7,8,8a-octahydra- 4a,7,7-trimethyl-5-[[(1,1- dimethyl)dimethy	6.391	1.53
3	2-(2-oxo-2-phenyl-ethyl)-1,3-dioxolane	6.745	1.29
4	Dodecane,1,1-difluro-	6.823	2.72
5	Dodecane,1,1-difluro-	9.142	1.99
6	Cyclopentasiloxane, decamethyl-	9.949	20.79
7	Cyclohexasiloxane, dodecamethyl-	13.869	35.54
8	Cyclohexasiloxane, tetradecamethyl-	17.48	15.23
9	**Benzoic acid,2,4-bis(trimethylsiloxy0-,trimethyl ester****	20.714	8.45
10	Phosphonous dibromide,[2,2,2-(trifluoromethyl)-1-[(trimethylsilyl)oxy]ethyl]-	23.511	3.59
11	1,3-diphenyl-1-((trimethylsily)oxy)-1(z) heptane	25.998	1.12
12	Tri-o-trimethylsilyl,n-pentafluoropropionyl derivative of terbutaline	28.267	0.72
13	**Beta.-d-glucopyranoside,ethyl,tetra acetate****	36.316	0.92
14	n-(t-butyl)-2-benzoylbenzamide	38.021	0.33
15	n-(t-butyl)-2-benzoylbenzamide	38.155	0.67
16	n-(t-butyl)-2-benzoylbenzamide	38.193	0.73
17	2-fluro-5-trifluromethylbenzoic acid,pentyl ester	38.286	0.65
18	Trans-6-(hydroxmethyl)-5- (trimethylsilyl) bicycol[4.4.0]-ene	39.145	1.06
19	Ethanone,1-[4([1,1- dimethylethoxy)methyl]phenyl]-	39.687	0.88
20	Cesium trimethylfluro)aluminate	40.292	0.95

**The SCFAs and benzoic acid derivatives essential for gut health.

Table 2. Nutritional and EPS profile of the fermented rice matrix.

Component	Content (g/100 g of rice powder)	Method used
EPS	0.506	Anthrone assay
Lipid	40	Bligh and dyer
Carbohydrate	0.089	Anthrone assay
Protein	0.055	Bradford assay

Histological examination of zebrafish intestinal tissue provided further confirmation of the therapeutic efficacy of the Poongar rice matrix (Figure 7). Fish exposed to erythromycin showed pronounced mucosal erosion, villus destruction, and goblet cell hyperplasia—classic indicators of intestinal tissue damage. Conversely, probiotic-treated fish exhibited restoration of villus architecture, reduced inflammatory infiltration, and normalization of mucosal integrity. These histological improvements reinforce the role of the formulation in modulating gut health and restoring epithelial function.

Discussion

Lactococcus lactis was isolated from fermented Poongar rice, underscoring the potential of traditional rice-based diets to function as reservoirs of beneficial microorganisms (Radha et al., 2022). The demonstrated tolerance to acidic pH (as low as 3.0), bile salts, and elevated salt concentrations reflects the physiological resilience required for survival and functionality within the gastrointestinal tract. Recent studies have further emphasized the probiotic potential of *L. lactis* strains, documenting their capacity to endure gastrointestinal stresses while exhibiting antibacterial activity (Paul et al., 2025). The *L. lactis* strain isolated from fermented Poongar rice exhibits notable probiotic potential through the activation of immune signaling pathways such as the mitogen-activated protein kinase cascade, involving phosphorylation of c-Jun N-terminal kinase and extracellular signal-regulated kinase. These molecular events regulate cytokine production and immune responses, thereby supporting gut homeostasis. Additionally, the strain produces antimicrobial substances that inhibit pathogenic bacteria and promote a balanced gut microbiota. The secretion of bioactive molecules such as α-mannosidase further influences immune signaling and contributes to the protection of gut epithelial cells.

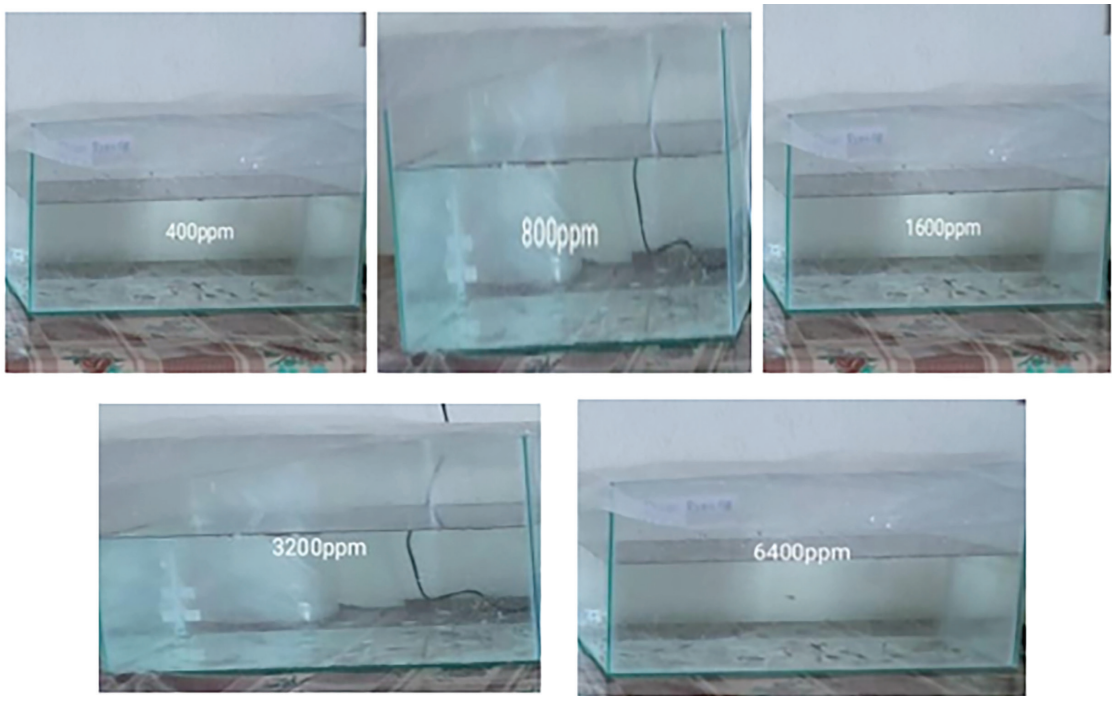

Figure 5. Experimental grouping of zebrafish treatment sets.

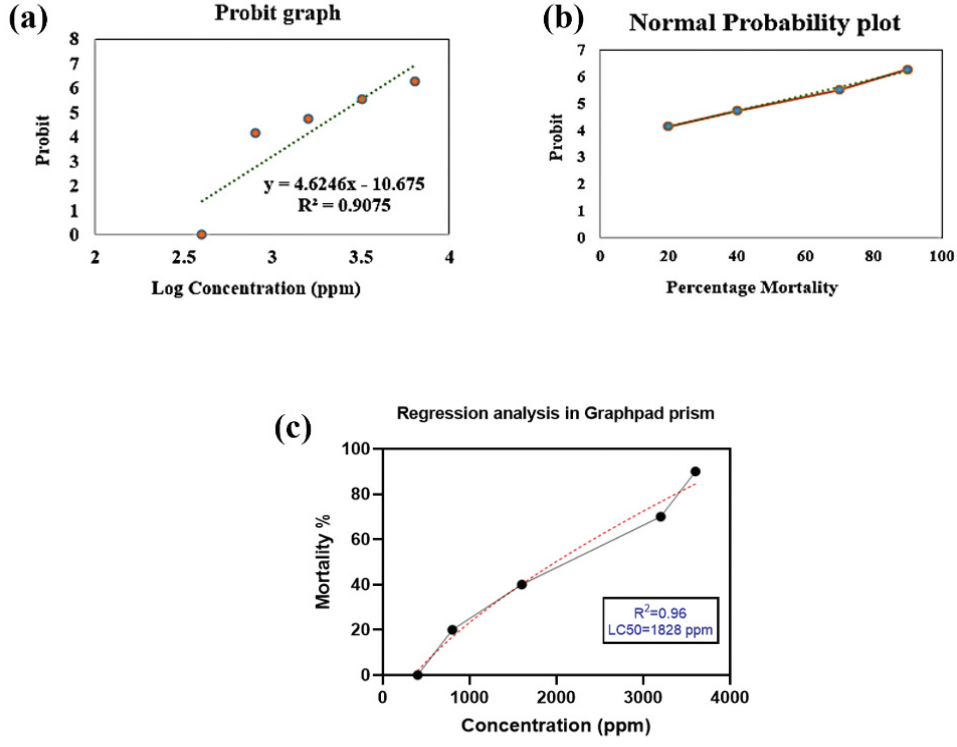

Figure 6. Probit plot generated using MS Excel 2007-Analysis Toolpak (a); normal probability plot of regression analysis (MS Excel 2007) (b); regression analysis performed using GraphPad Prism (c).

Table 3. Probit analysis of zebrafish mortality using Finney's method.

Conc. (ppm)	$\log_{10}$(Conc.)	Zebrafish (n = 10)	Number of death after 96 h exposure	Percentage mortality	Probit value
400	2.602	10	0	0	0
800	2.903	10	2	20	4.16
1,600	3.204	10	4	40	4.75
3,200	3.505	10	7	70	5.52
6,400	3.806	10	9	90	6.28

Conc. = concentration.

Table 4. ANOVA and regression analysis performed using MS Excel 2007.

Source	df	SS	MS	f	Significance *f*			
Regression	1	19.37664	19.37664	12.58376	0.038163			
Residual	3	4.61944	1.539813					
Total	4	23.99608	t stat					
Term	**Coefficients**	**SE**	**-2.53347**	***p*-value**	**Lower 95%**	**Upper 95%**	**Lower 95.0%**	**Upper 95.0%**
Intercept	-10.6752	4.213661	3.547359	0.085165	-24.0849	2.734579	-24.0849	2.734579
X variable 1	4.624585	1.30367		0.038163	0.475726	8.773443	0.475726	8.773443

Df = degrees of freedom; SS = sum of squares; SE = standard error; MS = mean square.

Table 5. Non-linear regression analysis performed using GraphPad Prism.

[Inhibitor] vs. normalized response–variable slope	
Best-fit values	
IC_{50}	**1.828**
HillSlope	2.140
$\log_{IC50}$	3.262
95% confidence interval (profile likelihood)	
IC_{50}	1.294–2.487
HillSlope	1.159–4.251
$\log_{IC50}$	3.112–3.396
Goodness of fit	
Degrees of Freedom	3
R squared	0.9663
Sum of Squares	179.3
p-value	<0.05

GC–MS analysis of the fermented Poongar rice matrix identified key SCFAs and related bioactive metabolites, including 2-ketobutyric acid, benzoic acid derivatives, and beta-D-glucopyranoside ethyl tetra acetate at notable concentrations. These compounds are closely associated with the probiotic activity of *L. lactis*. SCFAs such as 2-ketobutyric acid play essential roles in reinforcing gut barrier integrity by stimulating tight junction protein expression and enhancing mucus production, thereby preventing pathogenic invasion. Benzoic acid and its derivatives are shown to support gut health by modulating microbiota composition, exerting mild antimicrobial effects, and influencing immune cell responses (Bui et al., 2025). Beta-D-glucopyranoside compounds provide prebiotic-like support by promoting the growth and colonization of beneficial microbes. Collectively, these molecular signatures identified through GC–MS correlate directly with *L. lactis*-mediated immune regulation, stimulation of T-regulatory cells, modulation of cytokine production, and maintenance of gut homeostasis. The presence of these metabolites also implies potential influences on neurotransmitter synthesis, indicating a possible gut-brain axis effect and aligning biochemical output with the observed physiological benefits of probiotic fermentation (Falcinelli et al., 2015).

The EPS content measured in this study (0.506 g per 100 g of fermented matrix) aligns with previous reports demonstrating that *Lactococcus*-derived EPS contributes significantly to colonic health and mucosal immunity. EPS synthesized by lactic acid bacteria has been shown to exert immunomodulatory effects, enhance adherence to the intestinal mucosa, and resist enzymatic degradation, thereby improving digestive persistence (Salazar et al., 2016). Moreover, EPS can function as prebiotic substrate, selectively promoting the growth and metabolic activity of beneficial gut microbiota and therefore improving overall intestinal health (Monteagudo-Mera et al., 2019).

The *in vivo* zebrafish model proved to be an effective platform for evaluating both probiotic safety and therapeutic efficacy. Zebrafish (*Danio rerio*) have emerged as an powerful model for investigating gut microbiota in relation to human diseases such

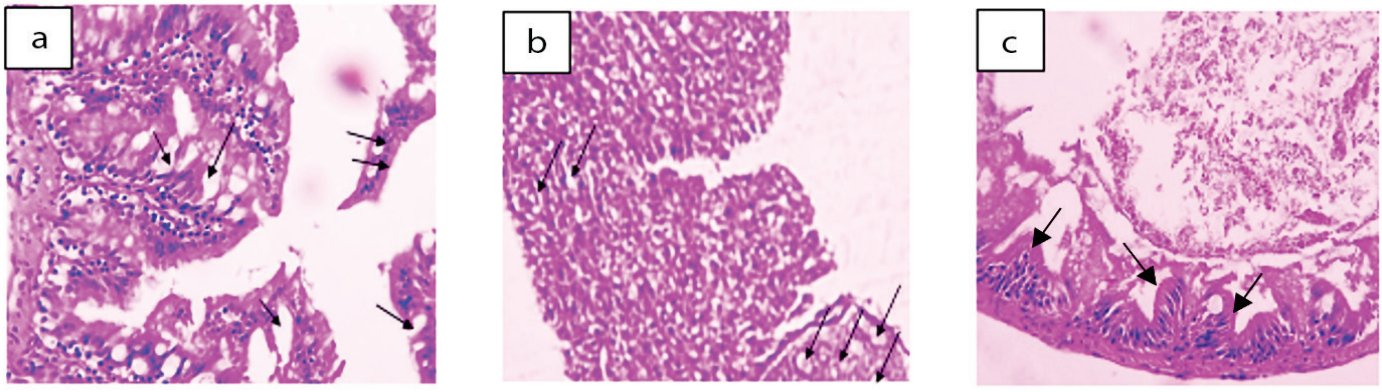

Figure 7. Histological analysis of zebrafish intestinal tissue under different treatment conditions using H&E staining. Normal control with no antibiotic exposure, showing intact villi structure with goblet cells indicated by arrows (a); negative control treated with antibiotic only, showing goblet cell proliferation and disrupted villi morphology (arrows) (b); positive control treated with both antibiotics and fermented rice matrix, showing blood cell accumulation at the villus margins, suggesting the initiation of tissue repair (arrows) (c).

as hypertension and cardiovascular disorders (Brugman, 2016). In the present study, zebrafish exposed to erythromycin exhibited marked behavioral disturbances and histological gastrointestinal damage. However, administration of the fermented Poongar matrix facilitated restoration of intestinal villi architecture, reduction of goblet cell hyperplasia, and normalization of behavior, closely mirroring patterns reported in earlier probiotic rescue studies (Falcinelli et al., 2015).

The safety of the formulation is supported by its low toxicity, with an LC_{50} value as high as 2,138 ppm. Comparable outcomes from oral toxicity studies of conventional lactic acid bacteria validate their Generally Recognized As Safe status and suitability for functional food applications (Sanders et al., 2010). The rice-probiotic formulation maintained gut integrity and did not induce immune stress markers, consistent with literature demonstrating that cereal-based prebiotics and probiotics generally support vertebrate health and physiological tolerance. Statistical analyses comprehensively tested the research hypothesis and revealed significant differences among treatment groups through regression and probit modeling, indicating strong dose-dependent toxicity and robust model fitting (Chakraborty et al., 2022; Preskova et al., 2011). These findings are consistent with prior zebrafish toxicity studies in which probit analysis is recognized for reliable LC_{50} determination and regression analysis confirms exposure-response relationships (Khan et al., 2025). The application of MS Excel 2007 with the Analysis Toolpak enabled systematic data validation and reproducible statistical workflows, aligning with best practices in experimental aquatic toxicology (Ahmed et al., 2015).

Collectively, the findings demonstrate that fermented Poongar rice represents a feasible probiotic formulation, offering a low-cost, culturally relevant alternative to commercial probiotic products. Future integration of advanced omics approaches, including metabolomics and transcriptomics, could substantially enhance mechanistic understanding while facilitating scale-up for clinical translation and nutritional interventions.

Conclusion

The present study highlights the strong probiotic potential of a fermented matrix derived from Poongar rice, an indigenous variety native to the Cauvery Delta region. *L. lactis* was successfully isolated and identified from the fermented rice matrix, and its remarkable tolerance to acidic pH, bile salts, and high salt tolerance supports its suitability as a robust probiotic candidate. In addition to its nutritional value, the matrix was found to produce substantial quantities of bioactive scompounds, including SCFAs and EPSs. Importantly, *in vivo* validation using a zebrafish model confirmed that the formulation is both non-toxic and effective in restoring gut integrity following antibiotic-induced dysbiosis. The histological recovery of the gastrointestinal lining, along with the normalization of behavioral patterns, clearly demonstrates its therapeutic efficacy. Collectively, these findings establish the fermented Poongar rice matrix as a culturally relevant, safe, and functional platform for gut health interventions. Future studies should focus on optimizing the delivery format, conducting comprehensive omics-level investigations, and extending validation to mammalian models and human clinical trials in order to fully realize its potential in the development of customized probiotic or functional food-based therapeutics.

Acknowledgment

The authors sincerely acknowledge Bishop Heber College, Tiruchirappalli, for permitting the completion of this work and for providing substantial support through the Minor Faculty Research Grant (F. No. MRP/1014/2023). The infrastructural facilities were funded by the Department of Science and Technology, India, under grant number DST/FST/College-2024/161315892/IT3.D10/PT.01.02/P/T/2023.

Ethics

Ethics Committee Approval: Ethical approval for zebrafish maintenance and handling was obtained from the Saveetha Dental College & Hospital Institutional Human Ethical Committee (SDC-IHEC) (reference number: 24/BIOCHEM/049, dated: 28.05.2024).

Data Sharing Statement: All data are available within the study.

Footnotes

Authorship Contributions: Conceptualization: P.R., A.M.A., and H.S.; Design/methodology: P.R.; Execution/ investigation: P.R. and H.S.; Resources/materials: P.R., A.M.A., and H.S.; Data acquisition: P.R.; Data analysis/interpretation: P.R. and H.S.; Writing – original draft: P.R. and H.S.; Writing – review & editing/critical revision: A.M.A.

Conflict of Interest: The author(s) have no conflicts of interest to declare.

Funding: The study was supported and funded by Tamil Nadu State Government of Science and Technology with grant number: TNSCST-13301/RFRS/MS/VM/2024-25.

AI Use Declaration: The authors declare that artificial intelligence (AI) tools were used in the preparation of this manuscript solely for language editing, grammar refinement, and improvement of readability. During the preparation of this work, the author(s) used ChatGPT, Grammarly, and Paperpal for text editing and language correction. After using these tools, the author(s) carefully reviewed and edited the content as required and take(s) full responsibility for the accuracy and integrity of the final publication.

References

Ahmed, S. I., Ahmmed, M. K., Ghosh, S. K., Islam, M. M., & Shahjahan, M. (2015). Histo-architectural changes of intestinal morphology in zebrafish (*Danio rerio*) exposed to Sumithion. *Research in Agriculture, Livestock and Fisheries, 2*(3), 499–506. https://doi.org/10.3329/ralf.v2i3.26174

Binda, S., Hill, C., Johansen, E., Obis, D., Pot, B., Sanders, M. E., & Ouwehand, A. C. (2020). Criteria to qualify microorganisms as "probiotic" in foods and dietary supplements. *Frontiers in Microbiology, 11*, 1662. https://doi.org/10.3389/fmicb.2020.01662

Brugman, S. (2016). The zebrafish as a model to study intestinal inflammation. *Developmental & Comparative Immunology, 64*, 82–92. https://doi.org/10.1016/j.dci.2016.02.020

Bui, T. N. Y., Paul, A., Guleria, S., O'Sullivan, J. M., & Toldi, G. (2025). Short-chain fatty acids—a key link between the gut microbiome and T-lymphocytes in neonates? *Pediatric Research.* In press. https://doi.org/10.1038/s41390-025-04075-0

Chakraborty, T., Roy, S., Mandal, D., & Begum, J. (2022). Assessment of developmental toxicity in zebrafish model. In *Biosafety Assessment of Probiotic Potential* (pp. 339–346). Springer US. https://doi.org/10.1007/978-1-0716-2509-5_34

Chavan, S., Mehta, J., Talukdar, M. P., Sekar, M., Gan, S. H., Subramaniyan, V., & Fuloria, N. K. (2022). Synbiotic effects of fermented rice on human health and wellness: A natural beverage that boosts immunity. *Frontiers in Microbiology, 13,* 950913. https://doi.org/10.3389/fmicb.2022.950913

Falcinelli, S., Rodiles, A., Unniappan, S., Picchietti, S., Gioacchini, G., Merrifield, D. L., & Carnevali, O. (2015). Probiotic treatment reduces appetite and glucose level in the zebrafish model. *Scientific Reports, 5*, 12193. https://doi.org/10.1038/srep12193

Finney, J. (1971). *Probit analysis* (3rd ed.). Cambridge University Press. https://doi.org/10.1002/jps.2600600940

Fuloria, S., Mehta, J., Talukdar, M. P., Sekar, M., Gan, S. H., Subramaniyan, V., Rani, N. N. I. M., Begum, M. Y., Chidambaram, K., Nordin, R., Maziz, M. N. H., Sathasivam, K. V., Lum, P. T., & Fuloria, N. K. (2022). Synbiotic effects of fermented rice on human health and wellness: A natural beverage that boosts immunity. *Frontiers in Microbiology, 13*, 950913. https://doi.org/10.3389/fmicb.2022.950913

Hills, R. D., Pontefract, B. A., Mishcon, H. R., Black, C. A., Sutton, S. C., & Theberge, C. R. (2019). Gut microbiome: Profound implications for diet and disease. *Nutrients, 11*(7), 1613. https://doi.org/10.3390/nu11071613

Kechagia, M., Basoulis, D., Konstantopoulou, S., Dimitriadi, D., Gyftopoulou, K., Skarmoutsou, N., & Fakiri, E. M. (2013). Health benefits of probiotics: A review. *ISRN Nutrition, 2013*, 481651. https://doi.org/10.5402/2013/481651

Khan, I. A., Yu, T., Yang, M., Liu, J., & Chen, Z. (2025). A systematic review of toxicity, biodistribution, and biosafety in upconversion nanomaterials: Critical insights into toxicity mitigation strategies and future directions for safe applications. *BME Frontiers, 6*, 0120. https://doi.org/10.34133/bmef.0120

Lu, J., Lu, L., Yu, Y., & Cluett, C. (2021). Zebrafish as a model for microbiome research. *Frontiers in Microbiology, 12*, 650210. https://doi.org/10.3389/fmicb.2021.650210

Monteagudo-Mera, A., Rastall, R. A., Gibson, G. R., Charalampopoulos, D., & Chatterjee, R. (2019). *In vitro* evaluation of the intestinal fate of *Lactobacillus plantarum* CECT 7527, 7528 and 7529 strains and their impact on the gut microbiota. *Journal of Functional Foods, 55*, 224–235. https://doi.org/10.1016/j.jff.2019.02.021

Nagpal, R., Kumar, A., Kumar, M., Behare, P. V., Jain, S., & Yadav, H. (2012). Probiotics, their health benefits and applications for developing healthier foods: A review. *FEMS Microbiology Letters, 334*(1), 1–15. https://doi.org/10.1111/j.1574-6968.2012.02593.x

Ogunrinola, G. A., Oyewale, J. O., Oshamika, O. O., & Olasehinde, G. I. (2020). The human microbiome and its implications in health and disease. *Saudi Journal of Biological Sciences, 27*(7), 1814–1820. https://doi.org/10.1016/j.sjbs.2020.01.007

Paul, A., Bui, T. N. Y., Guleria, S., & O'Sullivan, J. M. (2025). Probiotic potential and bioactive properties of *Lactococcus lactis* isolated from fermented dairy products. *Food Bioscience, 50*, 100073. https://doi.org/10.1016/j.fbio.2025.100073

Praskova, E., Voslarova, E., Siroka, Z., Plhalova, L., Macova, S., Marsalek, P., & Svobodova, Z. (2011). Assessment of diclofenac LC_{50} reference values in juvenile and embryonic stages of the Zebrafish (*Danio rerio*). *Polish Journal of Veterinary Sciences, 14*(4). https://doi.org/10.2478/v10181-011-0081-0

Radha, P., Selvanayaki, S., Tilak, M., & Gurusamy, A. (2022). Medicinal properties of traditional rice varieties. *Just Agriculture, 3*(3), 1–3. https://doi.org/10.31018/jans.v16i3.5784

Rathna Priya, T. S., Eliazer Nelson, A. R. L., Ravichandran, K., & Antony, U. (2019). Nutritional and functional properties of coloured rice varieties of South India: A review. *Journal of Ethnic Foods, 6*(1), 1–11.

Salazar, N., Gueimonde, M., de los Reyes-Gavilán, C. G., & Ruas-Madiedo, P. (2016). Exopolysaccharides produced by lactic acid bacteria and bifidobacteria as fermentable substrates by the intestinal microbiota. *Critical Reviews in Food Science and Nutrition, 56*(9), 1440–1453. https://doi.org/10.1080/10408398.2013.772358

Sanders, M. E., Akkermans, L. M., Haller, D., Hammerman, C., Heimbach, J., Hörmannsperger, G., & Huys, G. (2010). Safety assessment of probiotics for human use. *Gut Microbes, 1*(3), 164–185. https://doi.org/10.4161/gmic.1.3.12127

Singleman, C., & Holtzman, N. G. (2014). Growth and maturation in the Zebrafish, *Danio rerio*: A staging tool for teaching and research. *Zebrafish, 11*, 396–406. https://doi.org/10.1089/zeb.2014.0976

Trakya University Journal of Natural Sciences, 27(1), 47–56, 2026
DOI: 10.23902/trkjnat.202573
www.tujns.org

Research Article

Chemical inhibition of the heat shock response downregulates *ERCC1* gene expression and shifts carboplatin-induced necrosis to apoptosis in TNBC cells

Beyza Reisoğlu[1], Mehmet Alper Arslan[2]*

[1]*Institute of Graduate Studies, Ondokuz Mayıs University, Department of Molecular Medicine, Samsun, Türkiye*
[2]*Ondokuz Mayıs University, Faculty of Medicine, Department of Medical Biology, Samsun, Türkiye*

Cite this article as: Reisoğlu, B., & Arslan, M. A. (2026). Chemical inhibition of the heat shock response downregulates *ERCC1* gene expression and shifts carboplatin-induced necrosis to apoptosis in TNBC cells. *Trakya University Journal of Natural Sciences, 27*(1), 47–56. https://doi.org/10.23902/trkjnat.202573

Abstract

Background: Triple-negative breast cancer (TNBC) is an aggressive cancer type associated with poor prognosis and limited therapeutic options. Due to the absence of targetable receptors, conventional chemotherapy remains the primary treatment approach. *ERCC1* is a critical component of the nucleotide excision repair system, responsible for repairing DNA damaged by platinum-based agents like carboplatin. Heat shock response (HSR) is a fundamental, stress-induced defense mechanism that supports cancer cell survival.

Aims: This study aims to investigate the effects of HSR inhibition by KNK437 on *ERCC1* gene expression and carboplatin sensitivity in the TNBC cell line MDA-MB-231.

Methods: The IC_{50} values of carboplatin and KNK437 were determined using WST-8 cytotoxicity assay. *ERCC1* gene expression levels were quantified by real-time quantitative polymerase chain reaction. Apoptotic and necrotic cell death induced by carboplatin and KNK437 was assessed by flow cytometry using FITC-Annexin V assay.

Results: The IC_{50} values of carboplatin and KNK437 were 247.5 μM and 89.74 μM, respectively. Carboplatin or KNK437 monotherapy significantly decreased *ERCC1* expression by 42.8% and 49.5%, respectively, while their combined application caused a 54.9% reduction. Furthermore, co-treatment markedly increased total cell death by 34.1% compared to carboplatin alone. Interestingly, necrosis induced by carboplatin shifted toward apoptosis upon co-treatment with KNK437, as confirmed by light microscopy and flow cytometry.

Özet

Dayanak: Üçlü negatif meme kanseri (TNBC), kötü prognoz ve sınırlı tedavi seçenekleri ile ilişkili agresif bir kanser türüdür. Hedeflenebilir reseptörlerin bulunmaması nedeniyle, geleneksel kemoterapi birincil tedavi yaklaşımı olmaya devam etmektedir. *ERCC1*, karboplatin gibi platin bazlı ajanlar tarafından hasar gören DNA'yı onarmaktan sorumlu olan nükleotid eksizyon onarım sisteminin kritik bir bileşenidir. Isı şoku yanıtı (HSR), kanser hücrelerinin hayatta kalmasını destekleyen, stres ile indüklenen temel bir savunma mekanizmasıdır.

Amaçlar: Bu çalışma, KNK437 aracılı HSR inhibisyonunun TNBC hücre hattı MDA-MB-231'de *ERCC1* gen ekspresyonu ve karboplatin duyarlılığı üzerindeki etkilerini araştırmayı amaçlamaktadır.

Yöntemler: Karboplatin ve KNK437'nin IC_{50} değerleri WST-8 sitotoksisite testiyle belirlenmiştir. *ERCC1* gen ekspresyon düzeyleri gerçek zamanlı kantitatif polimeraz zincir reaksiyonu ile ölçülmüştür. Karboplatin ve KNK437 tarafından indüklenen apoptotik ve nekrotik hücre ölümü, FITC-Annexin V testi kullanılarak akış sitometrisi ile saptanmıştır.

Bulgular: Karboplatin ve KNK437'nin IC_{50} değerleri sırasıyla 247,5 μM ve 89,74 μM olarak hesaplanmıştır. Karboplatin veya KNK437 monoterapisi *ERCC1* ekspresyonunu sırasıyla %42,8 ve %49,5 oranında azaltırken, bunların kombine uygulaması %54,9 oranında bir azalmaya neden olmuştur. Ayrıca, kombine uygulama karboplatinin tek başına kullanımına kıyasla toplam hücre ölümünü %34,1 oranında belirgin şekilde artırmıştır. İlginç olarak, karboplatin tarafından indüklenen nekroz, KNK437 ile kombine uygulamada apoptoza

Edited by: *Ayşegül Çerkezkayabekir*
***Corresponding Author:** Mehmet Alper Arslan, **E-mail:** alper.arslan@omu.edu.tr*
***ORCID iDs of the author(s):** BR. 0000-0003-1149-9022; MAA. 0000-0002-3113-7195*

Received: 18 August 2025, **Accepted:** 9 December 2025, **Epub:** 13 January 2026, **Published:** 24 April 2026

Conclusion: HSR inhibition by KNK437 enhances carboplatin sensitivity in TNBC cells and downregulates *ERCC1* gene expression. Given the aggressive nature of TNBC and its limited treatment options, our results suggest that KNK437 may offer therapeutic advantages when combined with carboplatin, particularly in contexts where carboplatin-induced necrosis contributes to inflammation-related complications.

Sonuç: Bulgularımız, KNK437 aracılı HSR inhibisyonunun TNBC hücrelerinde karboplatin duyarlılığını artırdığını ve *ERCC1* gen ekspresyonunu aşağı regüle ettiğini göstermektedir. TNBC'nin agresif doğası ve sınırlı tedavi seçenekleri göz önüne alındığında, sonuçlarımız KNK437'nin karboplatin ile kombine edildiğinde, özellikle karboplatin kaynaklı nekrozun inflamasyonla ilişkili komplikasyonlara katkıda bulunduğu durumlarda, terapötik avantajlar sunabileceğini göstermektedir.

Keywords: KNK437, carboplatin, *ERCC1*, heat shock response, triple-negative breast cancer

Introduction

Triple-negative breast cancer (TNBC) is a distinct breast cancer subtype characterized by the lack of estrogen receptor, progesterone receptor, and human epidermal growth factor receptor 2 (HER2) proteins (Bou Zerdan et al., 2022). TNBC represents a heterogeneous group of clinically challenging tumors, distinguished by early recurrence, poor overall survival, and development of resistance to chemotherapy. Compared to other subtypes, the therapeutic options for TNBC are limited as it does not respond well to hormone-based therapies or HER2-targeting drugs. Additionally, only a small fraction of TNBC patients respond effectively to novel targeted treatment methods and immunotherapeutic approaches. Therefore, platinum-based chemotherapy, either individually or in combination with these novel agents, continues to serve as the mainstay of TNBC treatment (Lee, 2023). However, there is an urgent need to identify new prognostic and predictive biomarkers for TNBC that can help improve treatment outcomes and guide more effective and individualized therapeutic strategies.

Platinum-based agents are compounds that exert cell apoptosis or necrosis by inducing the formation of adducts and crosslinks within the DNA helix, ultimately disrupting replication and transcription (Brabec & Kasparkova, 2005; de Sousa, 2014). A meta-analysis incorporating 12 clinical studies covering 4,580 patients reported that platinum-based chemotherapy significantly improves pathological complete response rates and prognosis in TNBC patients, with greater efficacy compared to non-platinum regimens (Lin et al., 2022). Carboplatin is a second-generation platinum-based chemotherapeutic agent that exhibits a more favorable toxicity profile compared to its predecessor, cisplatin, with notably suppressed nephrotoxicity, neurotoxicity, and gastrointestinal side effects. Several meta-analyses have demonstrated that the inclusion of carboplatin in neoadjuvant/adjuvant chemotherapy markedly improved disease-free and overall survival in TNBC (Bian et al., 2021; Pathak et al., 2022).

The nucleotide excision repair (NER) pathway is a critical DNA repair mechanism that removes a wide range of helix-distorting lesions, such as intrastrand crosslinks and bulky adducts induced by ultraviolet (UV) radiation, chemical mutagens, and certain chemotherapeutic agents. Excision repair cross-complementation group 1 (*ERCC1*) is a key component protein of the NER pathway; it forms a heterodimeric complex with Xeroderma Pigmentosum group F (XPF), an endonuclease, which catalyzes an excision step close to the site of DNA damage, crucial for the restoration of genomic integrity (Marteijn et al., 2014). Therefore, *ERCC1* expression levels may be useful in predicting the responses of TNBC patients to platinum-based chemotherapy, with high or low *ERCC1* levels associated with a poor or favorable response, respectively (Hashmi et al., 2025; Ma & El Kashef, 2017; Sidoni et al., 2008).

Heat shock response (HSR) is a highly conserved cell defense mechanism induced by various forms of stress, functioning to maintain protein homeostasis (proteostasis) under unfavorable conditions. Heat shock factor1 (HSF1) is the principal transcriptional regulator of the HSR and the expression of heat shock proteins (HSPs)/chaperones. Beyond its classical role in proteostasis, HSF1 promotes oncogenic transformation by coordinating a broad transcriptional network that encompasses pathways involved in protein synthesis, cell proliferation, survival, adhesion, and energy metabolism (Dai et al., 2007; Mendillo et al., 2012; Yun et al., 2019). KNK437 is a synthetic benzylidene lactam that inhibits the HSR by suppressing HSF1 transcriptional activity, and thus the expression of various HSPs, thereby exerting antitumor effects against various cancer types (Powers & Workman, 2007; Yun et al., 2019).

A recent study investigating the stability dynamics of the *ERCC1*–XPF complex proposed that the complex maintains its stability and cellular levels with the help of DCAF7, the proper folding of which is mediated by the molecular chaperone TRiC (Kawara et al., 2019). Based on this finding as well as evidence from previous research, we hypothesized that KNK437 may alter *ERCC1* expression in TNBC cells, thereby modulating the cytotoxicity induced by carboplatin. Therefore, the present study aims to elucidate the impacts of the HSR inhibitor KNK437 on *ERCC1* gene expression and carboplatin sensitivity in TNBC cells.

Materials and Methods

Human TNBC Cancer Cell Culture

The human TNBC cell line MDA-MB-231, obtained from the American Type Culture Collection (VA, USA), was used as a study model. The cells were cultured in GlutaMAX™ Dulbecco's

Modified Eagle Medium (Thermo Fisher Scientific, MA, USA) supplemented with 10% fetal bovine serum, 100 U/mL penicillin, and 100 µg/mL streptomycin. Cells were cultured at 37 °C in a Heracell 240i™ incubator and humidified atmosphere containing 5% CO_2 (Thermo Fisher Scientific) and subcultured every 2–3 days upon reaching a confluency of approximately 85%–90%. For passaging, the cells were detached using 0.05% trypsin–EDTA at 37 °C. Viable cells were counted with a hemocytometer after Trypan blue staining and reseeded at appropriate densities into new plates. All cell culture reagents used were purchased from Gibco (Thermo Fisher Scientific).

Cytotoxicity Analysis and IC_{50} Determination

To determine the IC_{50} values of carboplatin (C2538; Sigma-Aldrich Chemicals, MO, USA) and KNK437 (HY-100110; MedChemExpress, NJ, USA), cells were seeded into 96-well plates at a density of 1×10^4 cells/well, 24 h before drug treatments. A wide range of concentrations, each at 2-fold serial dilution, was employed to accurately determine the IC_{50}. The cells were treated with carboplatin or KNK437 at final concentrations of 2000, 1000, 500, 250, 125, 62.5, 31.25, 15.62, 7.81 µM; and 500, 250, 125, 62.5, 31.25, 15.62, 7.81 µM, respectively, for 48 h. Then, cell viability was assessed using the WST-8 assay (Abcam, Cambridge, UK), according to the manufacturer's instructions. In brief, 10 µL of the WST-8 reagent was added to each well, and the plates were incubated at 37 °C for 2 h. The OD_{460} was then measured using a Syn4 spectrophotometer (Biotek Instruments, Inc., VT, USA), in duplicate. The mean absorbance values were corrected by subtracting the absorbance of blank wells containing only culture medium. Dose-response curves were generated by setting the viability of untreated control cells to 100%, and IC_{50} values were calculated using the software GraphPad Prism version 10.0 (https://www.graphpad.com/).

Total RNA Isolation

Cells were seeded into 6-well plates at a density of 2.5×10^5 cells/well. The next day, they were treated with various concentrations of dimethyl sulfoxide (DMSO) (vehicle control for KNK437), carboplatin, KNK437, or carboplatin + KNK437 for 48 h. Following treatments, the culture medium was removed, and the cells were gently washed with 1X PBS. Then, TRIzol reagent (Invitrogen, Thermo Fisher Scientific) was added, the lysates were collected into a microcentrifuge tube by scraping, and incubated at room temperature for 10 min to allow complete homogenization. Chloroform was added to the lysates at a ratio of 1:5 (v/v), followed by vigorous shaking and incubation at room temperature for 5 min. For phase separation, solutions were cold-centrifuged using a 3K30 refrigerated benchtop centrifuge (Sigma Aldrich) at 11,500×g for 15 min. The clear upper aqueous phase containing the total RNA was carefully transferred to a fresh tube. An equal volume of 70% RNase-free ethanol was added slowly and gently mixed by pipetting. The mixture was then loaded onto a silica-based spin column provided with the FavorPrep™ RNA isolation kit (Favorgen Biotech Corp., Ping Tung, Taiwan), and then the manufacturer's instructions were followed. Total RNA was finally eluted in 50 µL of RNase-free water and stored at -80 °C until further use. RNA concentration was measured, and purity was assessed with a Jenway Genova Nano spectrophotometer (Bibby Scientific**,** Staffordshire, UK).

cDNA Synthesis and Quantitative Real-Time Polymerase Chain Reaction (qPCR)

For cDNA synthesis, 500 ng of the total RNA from each sample was reverse transcribed in a 20 µL reaction volume containing random hexamer primers, oligo(dT), and MMLV reverse transcriptase, provided with the iScript™ cDNA synthesis kit (Bio-Rad Laboratories, CA, USA), following the manufacturer's protocol. The thermal cycle profile used was as follows: 5 min at 25 °C (primer annealing), 30 min at 46 °C (cDNA synthesis), and 1 min at 95 °C (enzyme inactivation); GeneAmp 9700 PCR System (Applied Biosystems, Thermo Fisher Scientific). Freshly prepared cDNA was processed immediately for qPCR. The qPCR reaction mix with a total volume of 20 µL contained 1 µL of cDNA and 250 nM each of the forward and reverse primers specific to *ERCC1* and the reference *GAPDH*. An SsoAdvanced™ Universal SYBR® Green Supermix kit (Bio-Rad) was used, and the protocol provided was applied. The primer sequences were designed in-house using the PrimerBLAST tool (https://www.ncbi.nlm.nih.gov/tools/primer-blast/), set up with the universal primer design criteria. The 5'–3' sequences of the forward (F) and reverse (R) primers were F, *GAPDH*: CCATCTTCCAGGAGCGAGATC; R, *GAPDH*: GGCAGAGATGATGACCCTTTTG; and F, *ERCC1*: TTTGGCGACGTAATTCCCGA; R, *ERCC1*: CCTGCTGGGGATCTTTCACA. The thermal cycle profile employed was 30 sec at 98 °C (initial denaturation), followed by 40 cycles each of 10 sec at 98 °C (denaturation) and 30 sec at 60 °C (annealing/extension), and a CFX Connect™ Real-Time PCR Detection System (Bio-Rad) was employed. Melting curves were analyzed at the end of each run to confirm amplicon specificity. All reactions were performed in duplicate. Relative fold changes in *ERCC1* expression levels between the different drug treatment groups were calculated based on mean C_t values and utilizing the $2^{-\Delta\Delta Ct}$ method, and analyzed with REST 2009 software (QIAGEN, Venlo, Netherlands).

Agarose Gel Electrophoresis

To verify the specificity and expected sizes of the qPCR amplicons (146 and 175 bp for *GAPDH* and *ERCC1*, respectively), agarose gel electrophoresis was performed. Briefly, 2% agarose (HS-8000, Prona, Biomax) gel was prepared in 1X TAE buffer and added with a SafeView™ Classic Nucleic Acid Gel stain (Applied Biological Materials, BC, Canada). After the qPCR run was completed, 10 µL of the amplicons from two randomly selected wells per target gene (*GAPDH* and *ERCC1*) was mixed with 2 µL of 6X DNA loading dye (TriTrack, Thermo Fisher Scientific), and loaded into the gel wells along with a DNA ladder (GeneRuler 50 bp, Thermo Fisher Scientific). Electrophoresis was carried out at 100 V for 45 min using a Sub-Cell GT Horizontal Electrophoresis System (Bio-Rad), and the gel was subsequently imaged under UV transillumination on a ChemiDoc Go Imaging System (Bio-Rad).

Apoptosis/Necrosis Analysis by Annexin V Assay

To examine the effects of KNK437 on carboplatin-induced cytotoxicity in MDA-MB-231 cells, apoptosis and necrosis were assessed using an FITC-Annexin V apoptosis detection kit (BD Biosciences, NJ, USA), following the manufacturer's instructions. Cells were seeded into 6-well plates at a density of 2.5×10^5 cells/well. The next day, cells were treated with various concentrations of DMSO (vehicle control for KNK437), carboplatin, or KNK437, or combinations of carboplatin and KNK437 for 48 h. Next, the culture medium of each well containing the floating, dead cells was taken into a fresh tube; later, the media were pooled along with the corresponding adherent cells collected by trypsinization. The cells were gently washed with cold 1X PBS, and approximately 1×10^5 cells were resuspended in 100 µL of 1X Annexin V binding buffer. For staining, 2.5 µL of FITC-Annexin V and 2.5 µL of 7-AAD were added to each sample, gently mixed, and incubated at room temperature for 20 min in the dark. Finally, 400 µL of 1X Annexin V binding buffer was added to each tube, and cells were immediately analyzed using a BD FACS Calibur™ flow cytometer (BD Biosciences). Fluorescence signals in the FL1 (530/30) channel for FITC-Annexin V and the FL3 (670 LP) channel for 7-AAD were detected. A total of 20,000 gated events were acquired per sample, and quadrant lines were set employing the appropriate single- and double-stained controls. Data were analyzed using the BD CellQuest Pro™ software (BD Biosciences), and the proportions of necrotic (7-AAD$^+$ only), late apoptotic/necrotic (7-AAD$^+$ and FITC-Annexin V$^+$), and total dead (the sum of these two populations) cells were determined (in %) based on quadrant statistics.

Statistical Analysis

Statistical analyses and IC_{50} value calculations were performed using GraphPad Prism software version 10.0 (GraphPad Inc., CA, USA). Data are presented as the mean ± standard deviation (SD). Statistical evaluation of the relative fold changes in gene expression was conducted using the REST 2009 software (Qiagen). Student's t-test was applied for pairwise comparisons in the Annexin cell death assay. The *p*-values were considered statistically significant at $*p < 0.05$, $**p < 0.01$, and $***p < 0.001$.

Results

Determination of IC_{50} Values for Carboplatin and KNK437 in MDA-MB-231 Cells

To determine the IC_{50} values of carboplatin and KNK437, MDA-MB-231 cells were seeded in 96-well plates and treated with 2-fold serially increasing concentrations of carboplatin (7.81 µM to 2 mM) or KNK437 (7.81 µM to 500 µM) for 48 h. Cell viability was measured by the WST-8 assay, and dose-response curves were generated utilizing GraphPad Prism. The IC_{50} values obtained were 247.5 µM for carboplatin (Figure 1A) and 89.74 µM for KNK437 (Figure 1B), comparable to those of previous reports (Barrio et al., 2013; Wang et al., 2010).

Effects of Carboplatin and KNK437 on *ERCC1* Gene Expression as Single or Combined Treatments

To investigate the effects of carboplatin and KNK437, administered either alone or in combination, on *ERCC1* expression in MDA-MB-231 cells, a series of real-time qPCR experiments was conducted. Before proceeding with the main investigations, the lengths of the qPCR amplicons were verified by agarose gel electrophoresis. As shown in Figure 2A, amplicon bands corresponding to the expected sizes of the target genes—146 bp for *GAPDH* and 175 bp for *ERCC1*—were detected. The sharpness and positions of the bands, without any non-specific products, confirmed both the accuracy and specificity of the primer pairs designed for the target genes.

To assess the effect of carboplatin on *ERCC1* gene expression, the IC_{50} of the compound was used as the median dose, based on which the treatment concentrations were determined in a series of 2-fold dilutions. Accordingly, cells were treated with increasing concentrations of carboplatin (dissolved in water) ranging from 62.5 µM to 1 mM for 48 h. qPCR analysis revealed that *ERCC1* expression decreased significantly by 30%–40% across the concentrations tested compared to the untreated control (Figure 2B). Notably, carboplatin did not exhibit any dose-dependent suppression, as expression was reduced to similar levels, regardless of concentration.

To evaluate the effects of KNK437 on *ERCC1* expression, the cells were treated with increasing concentrations of KNK437 (dissolved in DMSO) ranging from 31.25 µM to 500 µM for 48 h. This concentration range was estimated based on the relative fold difference between the IC_{50} values of carboplatin and KNK437. To determine whether DMSO influenced *ERCC1* expression, the cells were also treated with only 2.5% (v/v) DMSO, the same concentration to which the cells were exposed when treated with the highest dose of KNK437 at 500 µM. As shown in Figure 2C, qPCR analysis revealed that *ERCC1* expression was remarkably reduced by 40%—60% across all concentrations tested, compared to the untreated control. However, treatment with DMSO alone also suppressed *ERCC1* expression by 60%, a level that was similar to that observed with 500 µM KNK437, indicating that the downregulation observed at 500 µM may not be due to KNK437, but rather DMSO (Figure 2C). Therefore, we decided to perform an additional set of qPCR experiments using DMSO alone to determine a DMSO concentration that did not interfere significantly with *ERCC1* expression.

The cells were exposed for 48 h to DMSO alone at 0.078%, 0.156%, 0.312%, and 0.625% (v/v), corresponding to the DMSO contents of the 15.62 µM, 31.25 µM, 62.5 µM, and 125 µM KNK437 treatments, respectively. Compared to the untreated control, *ERCC1* expression levels did not show any statistically significant alterations at any concentration tested ($p > 0.05$) (Figure 2D). However, as a slight decline was observed at 0.625% DMSO, a onefold lower concentration–0.312%–was selected for the subsequent combination treatment experiments. A comparative

analysis of Figures 2C and 2D clearly indicated that 62.5 μM KNK437 reduced *ERCC1* expression by approximately 50%, an effect which was also independent of any interference by DMSO.

Considering the proportional difference between the IC_{50} values of the two agents, 125 μM carboplatin was used in combination with 62.5 μM KNK437. To assess the synergistic effect of carboplatin and KNK437 on *ERCC1* expression, the cells were treated with only 125 μM carboplatin, only 62.5 μM KNK437, or a combination of the two for 48 h. Compared to the untreated control, carboplatin or KNK437 alone suppressed gene expression by 42.8% and 49.5%, respectively, whereas their combined application induced a 54.9% reduction (Figure 2E). Such results with single-agent treatments were consistent with our findings obtained previously at the two respective doses (Figure 2B for 125 μM carboplatin and Figure 2C for 62.5 μM KNK437). When the reduction ratios with single and combined treatments were compared, it was observed that KNK437 exerted a more robust influence than carboplatin in suppressing *ERCC1* gene expression (Figure 2E, carboplatin alone vs. combination: 21%, KNK437 alone vs. combination: 10%).

Effects of Carboplatin and KNK437 on Cell Death in MDA-MB-231 Cells as Single or Combined Treatments

To investigate the cytotoxic effects of carboplatin and KNK437, administered either alone or in combination, on MDA-MB-231 cells, a series of flow cytometry-based Annexin V assays was conducted. Based on previous experience from our studies investigating the impacts of carboplatin on the same cell line, a 1 mM dose was selected, as it consistently induced total cell death at ~40%. It was regarded as the baseline appropriate for the drug combination experiments, considering the potential of the second drug to either enhance or suppress this cytotoxicity ratio. Based on the proportional differences between the IC_{50} values of the two agents, doses of 250 and 500 μM KNK437 were selected.

Cells were treated with 2.5% DMSO alone (v/v; corresponding to the DMSO content at 500 μM KNK437), 1 mM carboplatin, 250 μM or 500 μM KNK437, and varying combinations of both drugs, for 48 h. The cells were subsequently visualized under an inverted phase-contrast light microscope (Figure 3A). Compared to the untreated cells (control), DMSO-only-treated cells exhibited a phenotypic shift toward an elongated, spindle-like morphology. Similar morphological changes were observed in the cells treated with 250 and 500 μM KNK437, suggesting that these effects were largely induced by DMSO. In contrast, the cells treated with only 1 mM carboplatin displayed morphological features, such as membrane disruption, cell disintegration, and swelling, which are characteristic of necrosis (white arrows, Figure 3A). Remarkably, a combination of carboplatin and KNK437 dramatically shifted the morphology, to a one characterized by rounded cells with intact membranes and evident shrinkage, indicative of apoptosis (black arrows, Figure 3A). The cell morphologies observed were consistent with the criteria well-established in the literature for distinguishing apoptosis and necrosis (Balvan et al., 2015).

Following the morphological analyses, to evaluate the cytotoxic impacts of carboplatin and KNK437, FITC-Annexin V assays were performed, followed by flow cytometry. MDA-MB-231 cells were treated for 48 h with carboplatin and KNK437, either alone or in combination, at the concentrations mentioned before, and the proportions of necrotic (7-AAD$^+$ only), late apoptotic/necrotic (7-AAD$^+$ and FITC-Annexin V$^+$), and total number of dead cells were quantified (%) by applying quadrant statistics (Figures 3B and 3C). Thus, our results indicate that KNK437 alone did not induce any remarkable cytotoxicity. At a lower dose of 250 μM, the total cell death rate remained comparable to that of the untreated and DMSO controls (~10%), while the 500 μM dose induced only a modest enhancement of 21%. In contrast, 1 mM carboplatin alone resulted in a total cell death of 42% (Figure 3C), with a majority of the dead cells located within the necrotic (lower right) quadrant (Figure 3B), consistent with their morphology, typical of necrotic cells, previously observed under light microscopy (Figure 3A). Remarkably, co-treatment with 250 μM KNK437 did not induce any substantial change compared to carboplatin alone (both 42%–44%, Figure 3C). However, a distinct shift from necrosis to late apoptosis was observed, reflected by a redistribution of the cell population from the lower right to the upper right quadrants (Figure 3B). Such an effect was more pronounced with a combination of carboplatin with 500 μM KNK437, at which the total cell death enhanced to 56.3%, representing a significant increase of 34.1% compared to carboplatin alone (Figure 3C). Such a trend was

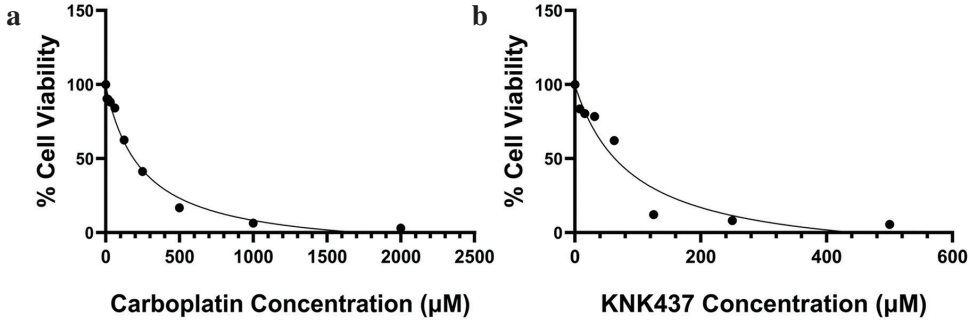

Figure 1. Dose-response curves and determination of IC_{50} values for carboplatin and KNK437 in MDA-MB-231 cells. Cells were seeded at a density of 10,000 cells/well in 96-well plates and treated for 48 h with 2-fold increasing concentrations of (a) carboplatin (7.81 μM–2 mM), or (b) KNK437 (7.81–500 μM). Cell viability was assessed using the WST-8 assay. Absorbance values for all drug concentrations were measured in duplicate. The dose-response curves were generated by considering the viability of the untreated control cells as 100%, and IC_{50} values were calculated using GraphPad Prism software.

again largely due to the shift from necrosis (carboplatin alone) to apoptosis (combination with KNK437) (Figure 3B), consistent with their respective morphologies previously observed using light microscopy (Figure 3A). Collectively, our light microscopy and flow cytometry findings demonstrate that necrosis induced by carboplatin is replaced by apoptosis upon co-treatment with KNK437.

Discussion

Platinum-based chemotherapy, either as a monotherapy or combined with other cancer therapeutics, remains the cornerstone of current TNBC treatments. However, a critical need to discover reliable prognostic and predictive biomarkers and thereby enhance clinical outcomes, guide personalized treatment approaches, and elucidate the mechanisms underlying therapeutic resistance and recurrence still arises (Lee, 2023). The present study investigated the effects of single and combined applications of carboplatin and the HSR inhibitor KNK437 on apoptosis or necrosis-induction and *ERCC1* gene expression in the TNBC cell line MDA-MB-231.

The NER pathway is a mechanism critical to the repair of DNA damage caused by platinum-based chemotherapeutic agents. Upregulation of the genes involved in the NER enables cancer cells to effectively repair such damage, ultimately contributing to the development of resistance (de Sousa, 2014).

Elevated *ERCC1* mRNA and protein levels in cisplatin-resistant human ovarian cancer cells have been reported (Li et al., 2000). Similarly, *ERCC1* mRNAs were markedly higher in tumor biopsies of cisplatin-resistant gastric cancer patients (Metzger et al., 1998). In contrast, *XPA*, *XPF*, and *ERCC1* expression was low in cisplatin-sensitive testicular cancer cell lines, indicating their limited capacity to mitigate cisplatin-induced DNA damage (Welsh et al., 2004). Similarly, in our study, since MDA-MB-231 cells are not resistant to carboplatin, their primal response to carboplatin-induced DNA damage was to suppress *ERCC1* expression (Figure 2B), and commit to cell death rather than to DNA repair and survive (Figure 3C). Moreover, a combination of carboplatin and KNK437 further decreased *ERCC1* expression (Figure 2E), thereby enhancing the sensitivity of MDA-MB-231 cells to carboplatin and ultimately increasing cell death levels compared to that induced by carboplatin alone (Figure 3C). This finding of ours where HSF1 was chemically inhibited by KNK437, is consistent with a previous report in which the shRNA-mediated knockdown of *HSF1* also rendered MDA-MB-231 cells more sensitive to carboplatin (Desai et al., 2013).

DMSO is a polar, amphipathic, aprotic organic molecule that is ideal for dissolving poorly soluble polar and non-polar compounds, due to which it is widely used in toxicology and pharmacology studies, and also for the cryopreservation of cells. Although conventionally DMSO is considered non-toxic at concentrations ≤ 10% (v/v),

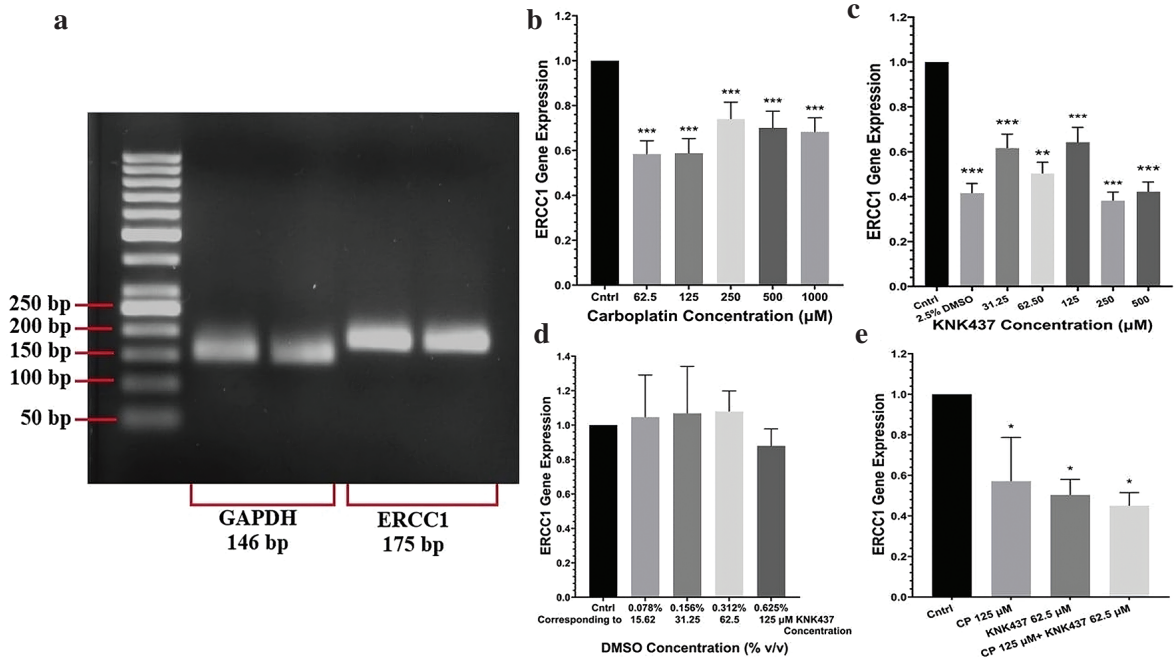

Figure 2. Carboplatin and KNK437 decreases *ERCC1* gene expression individually, with further suppression when used in combination. (a) Verification of the specificity of amplified qPCR products for *GAPDH* and *ERCC1* by agarose gel electrophoresis. Following qPCR, 10 µL of each amplicon was loaded onto a 2% agarose gel, electrophoresed, and visualized under UV light. Expected amplicon sizes were 146 bp for *GAPDH* and 175 bp for *ERCC1*. (b–d) The relative *ERCC1* expression levels in MDA-MB-231 cells treated for 48 h with increasing concentrations of carboplatin (b), KNK437 (c), or DMSO (d). (e) The relative *ERCC1* gene expression levels in cells treated for 48 h with carboplatin, KNK437, or their combination. For all experiments, 500 ng of total RNA isolated from each sample was converted to cDNA, and real-time qPCR was performed using 1 µL of the cDNA with gene-specific primers and SYBR Green master mix. Fold changes in gene expression and their statistical significance were analyzed using the REST 2009 software, and pairwise comparisons were made relative to the untreated control (*$p < 0.05$, **$p < 0.01$, ***$p < 0.001$).

exposure of 3D cardiac and hepatic microtissues to DMSO at levels as low as 0.1% (v/v) markedly altered the functioning of cellular processes, including significant changes in transcription and translation as well as the epigenetic landscape, as revealed by comprehensive transcriptomic, proteomic, and DNA methylation profiling (Verheijen et al., 2019). To further elucidate the cytotoxic effects of DMSO at the concentration ranges (0.1%–1.5% [v/v]) typically used in cell-based studies, epithelial colon cancer cells were treated with DMSO; and it has been reported that DMSO alters both DNA and protein topologies, in addition to significantly suppressing the expression of certain proteins at concentrations ≥ 0.5% (v/v) (Tuncer et al., 2018). Similarly, we observed that DMSO, used as a solvent for KNK437, reduced *ERCC1* expression at concentrations ≥ 0.625% (v/v) (Figures 2C and 2D). Therefore, additional qPCR assays using increasing concentrations of only DMSO were conducted to determine a concentration that did not impact *ERCC1* transcription. Consequently, we identified 0.312% (v/v) as the maximum level that did not induce any detectable background suppression of *ERCC1* expression, and thus, 62.5 µM was the highest KNK437 concentration that could be used free of any interference by DMSO (Figure 2D). The subsequent qPCR experiments involving combined drug treatments employed this level as the reference (Figure 2E).

The Annexin V cell death assays conducted later demonstrated that even 2.5% (v/v) DMSO, corresponding to 500 µM KNK437, did not remarkably enhance cell death compared to the untreated control (Figure 3C), but induced distinct changes in cell morphology, including elongation and the production of spindle-like extensions (Figure 3A). In line with the findings of the two studies mentioned earlier, our results highlight the need for considerable caution when using DMSO as a solvent, as its toxic effects can manifest at the level of gene expression without being reflected by cell death rate. Although DMSO is widely regarded as a "universal solvent" with a diverse range of biological applications, its potential adverse effects should not be overlooked, and the working concentration should be minimized to the extent possible.

The effects of DMSO on TNBC cell morphology observed in our study are consistent with several previous reports. For instance, polyclonal human ovarian cancer cells exposed to 1% DMSO for several days displayed a similar spindle-like morphology and a monolayer growth pattern characterized by contact inhibition (Grunt et al., 1991), as was also reported in several human lymphoblastoid and HeLa cell lines exposed to 2% DMSO suggesting that such a morphological response was independent of tissue origin (Aranda-Anzaldo et al., 2024). Our observations agreed with these studies, as exposure to 2.5% (v/v) DMSO caused the MDA-MB-231 cells to adopt a spindle-like morphology (Figure 3A). Similar morphological changes were also detected in cells treated with 250 and 500 µM KNK437 (Figure 3A), which were most likely due to the background effect of DMSO.

KNK437 inhibits the HSR by blocking the transcriptional activity of HSF1 (Powers & Workman, 2007). Our observation that

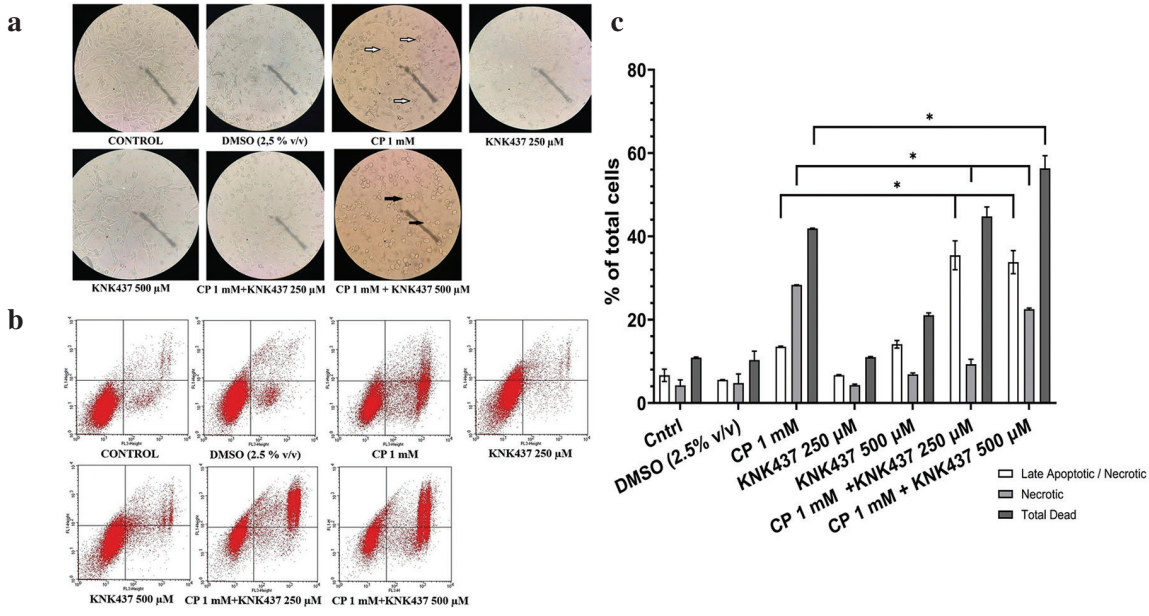

Figure 3. KNK437 co-treatment enhances the cytotoxic effects of carboplatin and shifts carboplatin-induced necrosis toward apoptosis. (a) Representative light microscopy images showing cell morphologies following 48 h of treatment with the indicated concentrations of DMSO, carboplatin, KNK437, or their combinations (100X magnification). White and black arrows indicate the necrotic and apoptotic cells, respectively. (b) Representative flow cytometry plots displaying the cell population distribution assessed by the FITC-Annexin V/7-AAD cell death assay. Following 48 h of treatment with the indicated agents at the concentrations specified, cells were collected by trypsinization, stained, and analyzed by flow cytometry using FL1 (y-axis) and FL3 (x-axis) channels to detect the FITC-Annexin V and 7-AAD-associated fluorescence signals, respectively. (c) Quantification of the proportions of cells in the upper right (late apoptotic/necrotic) and lower right (necrotic) quadrants from (b), and their sum (total dead). Data represent the mean ± SD of two independent experiments (*$p < 0.05$, Student's t-test, pairwise comparisons relative to 1 mM carboplatin alone).

ERCC1 gene expression decreased significantly even at low doses of KNK437 (31.25 μM, Figure 2C) suggested that *ERCC1* might indeed be a genuine transcriptional target of HSF1. To explore this possibility, we comprehensively reviewed the literature and examined the supplementary data of high-throughput genome-wide transcriptomic and chromatin immunoprecipitation microarray studies conducted on HSF1. In two such reports, *ERCC1* was listed among the genes that are transcriptionally upregulated by HSF1 (Kovács et al., 2019; Page et al., 2006). These microarray-based findings provide a possible explanation for the reduction in *ERCC1* expression induced by KNK437, and further support the notion that *ERCC1* might be a bona fide HSF1 target gene. Future studies employing chromatin immunoprecipitation to assess HSF1 binding at the *ERCC1* promoter, combined with functional luciferase reporter assays, are warranted to provide direct evidence of such transcriptional regulation.

Carboplatin acts by binding to DNA and inducing the formation of adducts and crosslinks, which disrupt replication and transcription, thereby activating signaling pathways that ultimately lead to apoptosis or necrosis (Brabec & Kasparkova, 2005; de Sousa, 2014). In our study, morphological aberrations such as membrane disruption, disintegration, and swelling observed in cells treated with 1 mM carboplatin were indicative of necrosis (white arrows, Figure 3A). This finding was also supported by our flow cytometry-based apoptosis/necrosis analysis, which revealed necrosis as the predominant mode of death in MDA-MB-231 cells exposed to only carboplatin (Figure 3B). In conjunction, these results indicate that carboplatin primarily induces necrosis rather than apoptosis in MDA-MB-231 cells. Such an association between carboplatin and necrosis is also supported by the literature, as evidenced by reports of a scleroderma patient with lung cancer who developed digital necrosis following chemotherapy (Clowse & Wigley, 2003) and of a lymphocytic leukemia patient who died due to acute liver necrosis following carboplatin therapy (Hruban et al., 1991).

When cells were treated with a combination of carboplatin and KNK437, marked changes in cell morphology were observed compared to those treated with only carboplatin, such as rounded, shrunken cells with a largely preserved membrane integrity, which are characteristic features of apoptosis (black arrows, Figure 3A). These results were supported by our further flow cytometry-based apoptosis/necrosis analysis, where a redistribution of the cell population from the lower right to the upper right quadrants indicated apoptosis as the predominant mode of cell death in response to combined carboplatin and KNK437 exposure (Figure 3B). Notably, the cell morphologies observed were fully consistent with the well-established characteristics for apoptosis and necrosis reported in the literature (Balvan et al., 2015). In summary, these results indicate that in MDA-MB-231 cells, necrosis induced by carboplatin alone is replaced by apoptosis when combined with KNK437. The pro-apoptotic influence of KNK437 is corroborated by a previous study where the inhibition of HSR by KNK437 significantly enhanced the apoptosis induced by the proteasome inhibitor bortezomib in multiple myeloma cells and mouse embryonic fibroblasts, as evidenced by increased Annexin V staining and DNA fragmentation (Voorhees et al., 2007). Altogether, our study demonstrates that KNK437 co-treatment promotes apoptosis at low (250 μM) and high (500 μM) doses, and enhances carboplatin-induced cytotoxicity by 34.1% at the higher dose (Figure 3C). These findings underline the promising potential of KNK437 to improve the efficacy of carboplatin chemotherapy against TNBC.

Study Limitations

There were several limitations to our study. First, the drug concentrations used to assess *ERCC1* gene expression could not be directly employed in the Annexin V cell death assays, as these doses were too low to produce any differential cytotoxic response in this assay. However, as the higher KNK437 doses (250 and 500 μM) applied could have interfered with *ERCC1* gene expression due to their high DMSO content, the effects observed in cell death might result from other biological actions of KNK437. Second, only a single TNBC cell line was used throughout the study, which may limit the generalizability of our findings to other TNBC models. Third, *ERCC1* expression was assessed only at the mRNA level; therefore, potential post-transcriptional regulations or functional effects at the protein level could not be evaluated. Future studies involving additional TNBC cell lines and functional analyses of *ERCC1* protein would help provide a more comprehensive understanding of the underlying mechanisms.

Conclusion

In conclusion, our findings reveal that the chemical inhibition of the HSR by KNK437 downregulated *ERCC1* expression and increased carboplatin sensitivity in TNBC cells. Interestingly, necrosis triggered by carboplatin was replaced by apoptosis when it was administered in combination with KNK437. Excessive inflammation evoked by chemotherapy-induced necrosis at the tumor microenvironment is well known to contribute to adverse clinical outcomes such as therapy resistance, tumor progression, angiogenesis, and metastasis (Akkız et al., 2025; Vyas et al., 2014). In such cases, as suggested by the present study, redirecting tumor cells from necrosis to apoptosis and thereby evading inflammation through KNK437 co-administration may offer significant therapeutic advantages for the treatment of TNBC—an aspect that requires further investigation by more comprehensive studies in the future.

Acknowledgements

This study is based on the master's thesis of Beyza Reisoğlu, conducted under the supervision of Assist. Prof. Dr. M. Alper Arslan as the thesis advisor. We would like to thank OMU-KÖKMER Center for their assistance with flow cytometry used in Annexin V cell death assay.

Ethics

Ethics Committee Approval: Not applicable.

Data Sharing Statement: All data are available within the study.

Footnotes

Authorship Contributions:

Conceptualization: M.A.A.; Design/methodology: M.A.A.; Execution/investigation: B.R. and M.A.A.; Resources/materials: M.A.A.; Data acquisition: B.R. and M.A.A.; Data analysis/interpretation: B.R. and M.A.A.; Writing – original draft: B.R. and M.A.A.; Writing – review & editing/critical revision: M.A.A.

Conflict of Interest: The author(s) have no conflicts of interest to declare.

Funding: This study was supported by Ondokuz Mayıs University Scientific Research Projects Coordination Unit under project number BAP04-A-2024-4886.

References

Akkız, H., Şimşek, H., Balcı, D., Ülger, Y., Onan, E., Akçaer, N., & Delik, A. (2025). Inflammation and cancer: Molecular mechanisms and clinical consequences. *Frontiers in Oncology, 15*, 1564572. https://doi.org/10.3389/fonc.2025.1564572

Aranda-Anzaldo, A., Dent, M. A. R., Segura-Anaya, E., & Martinez-Gomez, A. (2024). Protein folding, cellular stress and cancer. *Progress in Biophysics and Molecular Biology, 191*, 40–57. https://doi.org/10.1016/j.pbiomolbio.2024.07.001

Balvan, J., Krizova, A., Gumulec, J., Raudenska, M., Sladek, Z., Sedlackova, M., Babula, P., Sztalmachova, M., Kizek, R., Chmelik, R., & Masarik, M. (2015). Multimodal holographic microscopy: Distinction between apoptosis and oncosis. *PLOS ONE, 10*(3), e0121674. https://doi.org/10.1371/journal.pone.0121674

Barrio, S., Gallardo, M., Arenas, A., Ayala, R., Rapado, I., Rueda, D., Jimenez-Ubieto, A., Albizua, E., Burgaleta, C., Gilsanz, F., & Martinez-Lopez, J. (2013). Inhibition of related JAK/STAT pathways with molecular targeted drugs shows strong synergy with ruxolitinib in chronic myeloproliferative neoplasm. *British Journal of Haematology, 161*(5), 667–676. https://doi.org/10.1111/bjh.12308

Bian, L., Yu, P., Wen, J., Li, N., Huang, W., Xie, X., & Ye, F. (2021). Survival benefit of platinum-based regimen in early stage triple negative breast cancer: A meta-analysis of randomized controlled trials. *NPJ Breast Cancer, 7*(1), 157. https://doi.org/10.1038/s41523-021-00367-w

Bou Zerdan, M., Ghorayeb, T., Saliba, F., Allam, S., Bou Zerdan, M., Yaghi, M., Bilani, N., Jaafar, R., & Nahleh, Z. (2022). Triple negative breast cancer: Updates on classification and treatment in 2021. *Cancers, 14*(5), 1253. https://doi.org/10.3390/cancers14051253

Brabec, V., & Kasparkova, J. (2005). Modifications of DNA by platinum complexes: Relation to resistance of tumors to platinum antitumor drugs. *Drug Resistance Updates, 8*(3), 131–146. https://doi.org/10.1016/j.drup.2005.04.006

Clowse, M. E., & Wigley, F. M. (2003). Digital necrosis related to carboplatin and gemcitabine therapy in systemic sclerosis. *The Journal of Rheumatology, 30*(6), 1341–1343. https://www.ncbi.nlm.nih.gov/pubmed/12784412

Dai, C., Whitesell, L., Rogers, A. B., & Lindquist, S. (2007). Heat shock factor 1 is a powerful multifaceted modifier of carcinogenesis. *Cell, 130*(6), 1005–1018. https://doi.org/10.1016/j.cell.2007.07.020

Desai, S., Liu, Z., Yao, J., Patel, N., Chen, J., Wu, Y., Ahn, E. E., Fodstad, O., & Tan, M. (2013). Heat shock factor 1 (HSF1) controls chemoresistance and autophagy through transcriptional regulation of autophagy-related protein 7 (ATG7). *Journal of Biological Chemistry, 288*(13), 9165–9176. https://doi.org/10.1074/jbc.M112.422071

Grunt, T. W., Somay, C., Pavelka, M., Ellinger, A., Dittrich, E., & Dittrich, C. (1991). The effects of dimethyl sulfoxide and retinoic acid on the cell growth and the phenotype of ovarian cancer cells. *Journal of Cell Science, 100*(3), 657–666. https://doi.org/10.1242/jcs.100.3.657

Hashmi, A. A., Ajaz, Y., Sajjad, M., Zia, F., Irfan, M., Abu Bakar, S. M., Khan, E. Y., & Faridi, N. (2025). Predictive value of excision repair cross complementation group 1 (*ERCC1*) by immunohistochemistry for determining neoadjuvant chemotherapy response in triple-negative breast cancers. *The Breast Journal, 2025*, 8410670. https://doi.org/10.1155/tbj/8410670

Hruban, R. H., Sternberg, S. S., Meyers, P., Fleisher, M., Menendez-Botet, C., & Boitnott, J. K. (1991). Fatal thrombocytopenia and liver failure associated with carboplatin therapy. *Cancer Investigation, 9*(3), 263–268. https://doi.org/10.3109/07357909109021323

Kawara, H., Akahori, R., Wakasugi, M., Sancar, A., & Matsunaga, T. (2019). DCAF7 is required for maintaining the cellular levels of *ERCC1*-XPF and nucleotide excision repair. *Biochemical and Biophysical Research Communications, 519*(1), 204–210. https://doi.org/10.1016/j.bbrc.2019.08.147

Kovács, D., Sigmond, T., Hotzi, B., Bohar, B., Fazekas, D., Deak, V., Vellai, T., & Barna, J. (2019). HSF1Base: A comprehensive database of HSF1 (heat shock factor 1) target genes. *International Journal of Molecular Sciences, 20*(22), 5815. https://doi.org/10.3390/ijms20225815

Lee, J. (2023). Current treatment landscape for early triple-negative breast cancer (TNBC). *Journal of Clinical Medicine, 12*(4), 1524. https://doi.org/10.3390/jcm12041524

Li, Q., Yu, J. J., Mu, C., Yunmbam, M. K., Slavsky, D., Cross, C. L., Bostick-Bruton, F., & Reed, E. (2000). Association between the level of ERCC-1 expression and the repair of cisplatin-induced DNA damage in human ovarian cancer cells. *Anticancer Research, 20*, 645–652.

Lin, C., Cui, J., Peng, Z., Qian, K., Wu, R., Cheng, Y., & Yin, W. (2022). Efficacy of platinum-based and non-platinum-based drugs on triple-negative breast cancer: Meta-analysis. *European Journal of Medical Research, 27*(1), 201. https://doi.org/10.1186/s40001-022-00839-0

Ma, E. L. B., & El Kashef, W. F. (2017). *ERCC1* expression in metastatic triple negative breast cancer patients treated with platinum-based chemotherapy. *Asian Pacific Journal of Cancer Prevention, 18*(2), 507–513. https://doi.org/10.22034/APJCP.2017.18.2.507

Marteijn, J. A., Lans, H., Vermeulen, W., & Hoeijmakers, J. H. (2014). Understanding nucleotide excision repair and its roles in cancer and ageing. *Nature Reviews Molecular Cell Biology, 15*(7), 465–481. https://doi.org/10.1038/nrm3822

Mendillo, M. L., Santagata, S., Koeva, M., Bell, G. W., Hu, R., Tamimi, R. M., Fraenkel, E., Ince, T. A., Whitesell, L., & Lindquist, S. (2012). HSF1 drives a transcriptional program distinct from heat shock to support highly malignant human cancers. *Cell, 150*(3), 549–562. https://doi.org/10.1016/j.cell.2012.06.031

Metzger, R., Leichman, C. G., Danenberg, K. D., Danenberg, P. V., Lenz, H. J., Hayashi, K., Groshen, S., Salonga, D., Cohen, H., Laine, L., Crookes, P., Silberman, H., Baranda, J., Konda, B., & Leichman, L. (1998). *ERCC1* mRNA levels complement thymidylate synthase mRNA levels in predicting response and survival for gastric cancer patients receiving combination cisplatin and fluorouracil chemotherapy. *Journal of Clinical Oncology, 16*(1), 309–316. https://doi.org/10.1200/JCO.1998.16.1.309

Page, T. J., Sikder, D., Yang, L., Pluta, L., Wolfinger, R. D., Kodadek, T., & Thomas, R. S. (2006). Genome-wide analysis of human HSF1 signaling reveals a transcriptional program linked to cellular adaptation and survival. *Molecular BioSystems, 2*(12), 627–639. https://doi.org/10.1039/b606129j

Pathak, N., Sharma, A., Elavarasi, A., Sankar, J., Deo, S. V. S., Sharma, D. N., Mathur, S., Kumar, S., Prasad, C. P., Kumar, A., & Batra, A. (2022). Moment of truth—Adding carboplatin to neoadjuvant/adjuvant chemotherapy in triple negative breast cancer improves overall survival: An individual participant data and trial-level meta-analysis. *The Breast, 64*, 7–18. https://doi.org/10.1016/j.breast.2022.04.006

Powers, M. V., & Workman, P. (2007). Inhibitors of the heat shock response: Biology and pharmacology. *FEBS Letters, 581*(19), 3758–3769. https://doi.org/10.1016/j.febslet.2007.05.040

Sidoni, A., Cartaginese, F., Colozza, M., Gori, S., & Crino, L. (2008). *ERCC1* expression in triple negative breast carcinoma: The paradox revisited. *Breast Cancer Research and Treatment, 111*(3), 569–570. https://doi.org/10.1007/s10549-007-9804-4

de Sousa, G. F., Wlodarczyk, S. R., & Monteiro, G. (2014). Carboplatin: Molecular mechanisms of action associated with chemoresistance. *Brazilian Journal of Pharmaceutical Sciences, 50*(4), 693–701. https://doi.org/10.1590/S1984-82502014000400004

Tuncer, S., Gurbanov, R., Sheraj, I., Solel, E., Esenturk, O., & Banerjee, S. (2018). Low dose dimethyl sulfoxide driven gross molecular changes have the potential to interfere with various cellular processes. *Scientific Reports, 8*(1), 14828. https://doi.org/10.1038/s41598-018-33234-z

Verheijen, M., Lienhard, M., Schrooders, Y., Clayton, O., Nudischer, R., Boerno, S., Timmermann, B., Selevsek, N., Schlapbach, R., Gmuender, H., Gotta, S., Geraedts, J., Herwig, R., Kleinjans, J., & Caiment, F. (2019). DMSO induces drastic changes in human cellular processes and epigenetic landscape in vitro. *Scientific Reports, 9*(1), 4641. https://doi.org/10.1038/s41598-019-40660-0

Voorhees, P. M., Chen, Q., Kuhn, D. J., Small, G. W., Hunsucker, S. A., Strader, J. S., Corringham, R. E., Zaki, M. H., Nemeth, J. A., & Orlowski, R. Z. (2007). Inhibition of interleukin-6 signaling with CNTO 328 enhances the activity of bortezomib in preclinical models of multiple myeloma. *Clinical Cancer Research, 13*(21), 6469–6478. https://doi.org/10.1158/1078-0432.CCR-07-1293

Vyas, D., Laput, G., & Vyas, A. K. (2014). Chemotherapy-enhanced inflammation may lead to the failure of therapy and metastasis. *OncoTargets and Therapy, 7*, 1015–1023. https://doi.org/10.2147/OTT.S60114

Wang, S., Zhang, H., Cheng, L., Evans, C., & Pan, C. X. (2010). Analysis of the cytotoxic activity of carboplatin and gemcitabine combination. *Anticancer Research, 30*(11), 4573–4578. https://www.ncbi.nlm.nih.gov/pubmed/21115908

Welsh, C., Day, R., McGurk, C., Masters, J. R., Wood, R. D., & Koberle, B. (2004). Reduced levels of XPA, *ERCC1* and XPF DNA repair proteins in testis tumor cell lines. *International Journal of Cancer, 110*(3), 352–361. https://doi.org/10.1002/ijc.20134

Yun, C. W., Kim, H. J., Lim, J. H., & Lee, S. H. (2019). Heat shock proteins: Agents of cancer development and therapeutic targets in anti-cancer therapy. *Cells, 9*(1), 60. https://doi.org/10.3390/cells9010060

Trakya University Journal of Natural Sciences, 27(1), 57–66, 2026
DOI: 10.23902/trkjnat.202562
www.tujns.org

Research Article

Amylase production by *Streptomyces* species and its application in orange juice clarification

Elizabeth Aghogho Odjoji[1], Samuel Adedayo Fasiku[2]*, Olaoluwa Kehinde Alao[3], Kehinde Olamide Salawu[4], Michael Tunde Dada[5], Olubusola Ayoola Odeniyi[1], Sherifah Monilola Wakil[1]

[1]*University of Ibadan, Microbial Physiology and Biochemistry Research Unit, Department of Microbiology, Ibadan, Nigeria*
[2]*Ajayi Crowther University, Department of Microbiology and Biotechnology, Oyo, Nigeria*
[3]*Precious Cornerstone University, Department of Natural Sciences, Ibadan, Nigeria*
[4]*Crescent University, Department of Biological Sciences, Abeokuta, Nigeria*
[5]*First Technical University, Department of Microbiology and Biotechnology, Ibadan, Nigeria*

Cite this article as: Odjoji, E. A., Fasiku, S. A., Alao, O. K., Salawu, K. O., Dada, M. T., Odeniyi, O. A., & Wakil, S. M. (2026). Amylase production by *Streptomyces* species and its application in orange juice clarification. *Trakya University Journal of Natural Sciences, 27*(1), 57–66. https://doi.org/10.23902/trkjnat.202562

Abstract

Background: Amylases are enzymes that break down starch and help clarify fruit juices.

Aims: This study focused on screening amylolytic *Streptomyces* spp. isolated from soil samples for their potential for amylase production and fruit juice clarification.

Methods: Select organisms produced amylase, which was assayed by measuring the reducing sugar content of the fermentation medium. The effects of pH, carbon and nitrogen source, as well as agitation and incubation periods, were evaluated to optimize amylase synthesis.

Results: A total of 22 species were isolated, with five—FE4, ELI1, FL2, MS2, and MS5—demonstrating high amylase production ability, which occurred at a pH ranging from slightly acidic to slightly alkaline. Cassava peels supported optimal amylase production in *Streptomyces* spp. A4 (0.834), ELI1 (0.910), and FE4 (0.814 U/mL). The maximum yield of 0.930 U/mL was observed with ELI1 when urea was used as the nitrogen source, at an agitation speed of 100–150 rpm, and peaking on the fourth day of fermentation. It was identified as *S. griseoflavus* ELI_1 using 16S rRNA gene sequencing and submitted to the GenBank with accession number OQ930232. The amylase produced by it was partially purified, markedly increasing its specific activity from 1.50 to 4.56 U/mL. Its ability to clarify orange juice was tested; the turbidity reduced significantly by 16.8% after amylase treatment (p <0.05).

Özet

Dayanak: Amilazlar, nişastayı parçalayan ve meyve sularının arıtılmasına yardımcı olan enzimlerdir.

Amaçlar: Bu çalışma, toprak örneklerinden izole edilen amilolitik *Streptomyces* türlerinin amilaz üretimi ve meyve suyu berraklaştırma potansiyelinin taranmasına odaklanmıştır. Seçilen organizmalar, hücrelerin indirgen şeker içeriği ölçülerek test edilen amilaz üretmiştir.

Yöntemler: Amilaz sentezini optimize etmek için pH, karbon ve azot kaynağı ile çalkalama ve inkübasyon sürelerinin etkileri değerlendirilmiştir.

Bulgular: Toplam 22 tür izole edildi ve bunlardan beş tanesi (FE4, ELI1, FL2, MS2 ve MS5) hafif asidik ila hafif alkali pH aralığında yüksek amilaz üretim kabiliyeti gösterdi. Manyok kabukları, *Streptomyces* spp. A4 (0,834), ELI1 (0,910) ve FE4 (0,814 U/mL) türlerinde optimal amilaz üretimini destekledi. Üre azot kaynağı olarak kullanıldığında, 100-150 rpm çalkalama hızında ve fermantasyonun dördüncü gününde zirveye ulaştığında, ELI1 ile 0,930 U/mL'lik maksimum verim gözlemlenmiştir. 16S rRNA gen dizilemesi kullanılarak *S. griseoflavus* ELI_1 olarak tanımlanmış ve GenBank'a OQ930232 erişim numarasıyla kaydedilmiştir. Bu suş tarafından üretilen amilaz kısmen saflaştırılmış ve spesifik aktivitesi 1,50'den 4,56 U/mL'ye önemli ölçüde artmıştır. Portakal suyunu berraklaştırma kabiliyeti test edilmiş ve amilaz tedavisi

Edited by: *Mustafa Yamaç*

***Corresponding Author:** Samuel Adedayo Fasiku, **E-mail:** samfash4@yahoo.com*

***ORCID iDs of the author(s):** EAO. 0009-0005-4324-240X; SAF. 0000-0001-7541-8530; OKA. 0000-0003-1647-879X; KOS. 0009-0005-8042-9222; MTD. 0000-0002-0235-8917; OAO. 0000-0002-0826-791X; SMW. 0000-0002-7439-1644*

Received: 8 July 2025, **Accepted:** 9 December 2025, **Epub:** 13 January 2026, **Published:** 24 April 2026

Conclusion: Amylolytic *Streptomyces* spp. were isolated from soil samples, and their amylase yield was optimized. The Amylase of *S. griseoflavus* ELI_1 could optimally clarify orange juice.

sonrasında bulanıklık %16 oranında önemli ölçüde azalmıştır (p <0,05).

Sonuç: Böylece, toprak örneğinden izole edilen amilolitik tür *S. griseoflavus* ELI_1, portakal suyunu en iyi şekilde berraklaştırabildi.

Keywords: *Streptomyces* species, amylolytic bacteria, fruit juice clarification, partial purification, urea

Introduction

Enzymes are essential biocatalysts and find diverse industrial applications (Fasiku et al., 2023). Their enhanced synthesis by easily cultivable and genetically manipulated microorganisms enabled higher yields and bulk production for application to commercial purposes, making them more preferable catalysts over plant- and animal-sourced counterparts (Adrio & Demain, 2014; Liu et al., 2013; Mokrani & Nabti, 2024; Patel et al., 2023), in addition to being more stable and cheaper to produce on a large scale. Different microorganisms produce isozymes with varying properties. Microbial enzymes are non-toxic and biodegradable and can substitute conventional toxic chemical catalysts (Illanes et al., 2012; Khan, 2025; Saravanan et al., 2021). Enzyme-catalyzed processes are more environmentally friendly, economical, and time and energy-efficient than those mediated by traditional methods (Saravanan et al., 2021; Thulasisingh et al., 2024).

Amylolytic enzymes catalyze the hydrolytic cleavage of α-1,4-glycosidic bonds in starch molecules to produce low molecular weight sugars, like maltose, dextrin, and glucose, which have many applications, including for detergent production, brewing, baking, and the paper and textile industries (Fasiku et al., 2020; Gómez-Villegas et al., 2021; Li et al., 2012). The ability of microbes to produce amylases has been widely documented (Fasiku et al., 2020; Oyenado & Omoruyi, 2024; Vojnovic et al., 2024), including that of *Streptomyces* spp. (Al-Dhabi et al., 2020; El-Sayed et al., 2024; Rathore & Singh, 2021). Optimizing key physiological parameters and culture conditions, such as inoculum size, pH, agitation, and temperature, is crucial for maximizing amylase productivity (Arifeen et al., 2024; Oussadi & Kitouni, 2015).

The benefits provided by fruit juices have led to a continuous increase in their consumption among health-conscious individuals (Kahraman et al., 2017). However, undesirable turbidity, haze formation, and sedimentation in fruit juice-based food products can deter their purchase. One of the many factors influencing the turbidity of fruit juices is the starch content. Although an initial centrifugation step can eliminate starch to a significant extent, typically, ~5% remains. Enzymes play a crucial technological role in clarifying juices, with amylase being a key enzyme involved in starch breakdown, which enhances filterability, post-extraction yield, and clarity of the juice (Bamigboye et al., 2022; Casas et al., 2025; Oliveira et al., 2018).

Amylases derived from *Streptomyces* spp. are highly valued for their properties of extracellular secretion, broad substrate specificity, and stability and activity across a broad temperature and pH range, which are critical for industrial applicability (Barman & Dkhar, 2024). Additionally, alkaliphilicity and resistance to metal ions and detergents, which facilitate elevated amylase production and yield under cost-effective fermentation conditions, are desirable properties (Ali et al., 2023; Suthar et al., 2024). The yield can be enhanced significantly under optimal production parameters such as carbon and nitrogen sources, incubation period, aeration, etc. (Fahmy, 2022). The ability of amylase to effectively hydrolyze starch and related polysaccharides responsible for turbidity and viscosity of fruit juices makes them desirable biocatalysts (Bamigboye et al., 2022).

Given the rising demand for industrial-use enzymes with greater efficiency, there remains a need to explore novel *Streptomyces* species for amylase production. This study aimed to clarify fruit juice using amylase produced by *Streptomyces* species isolated from soil.

Materials and Methods

Soil from five locations in Ibadan, Nigeria, was sampled. They include the botanical garden (7.4558° N, 3.8965° E), dump site (7.3776° N, 3.8738° E), mechanical site (7.4408° N, 3.9080° E), palm oil production facility (7.3740° N, 3.8398° E), and the Department of Microbiology, University of Ibadan (7.3776° N, 3.9471° E). The samples were collected from depths of 2–10 cm from the soil surface with a spatula, placed in sterile zip-lock bags, and immediately transported to the laboratory. The samples were then mixed to obtain a composite, passed through a sieve, and air-dried overnight at room temperature.

Isolation of *Streptomyces* spp.

Streptomyces species were isolated from soil samples on inorganic salt starch agar using the pour plate method. The samples were first serially diluted. The culture medium employed was International *Streptomyces* Project (ISP) Medium No. 4. It was composed of 10g/L starch, 1g/L K_2HPO_4, 1g/L $MgSO_4$, 1g/L NaCl, 2g/L $(NH_2)_4SO_4$, 2g/L $CaCO_3$, 0.001g/L $FeSO_4$, 0.001g/L $MnCl_2$, 0.001g/L $ZnSO_4$, and 20g/L agar-agar. The components were mixed in required amounts, the pH was adjusted to 7.2, and the prepared medium was steam-sterilized. It was then supplemented with 50 µg/mL nystatin and 30 µg/mL rifampicin, cooled down, and poured into plates containing 1 mL aliquots of each serial dilution. The agar was allowed to solidify, and the plates were incubated at 28 °C for 5 days (Kharel et al., 2010).

Identification of *Streptomyces* Isolates

Subculturing involved repeated streaking to obtain pure isolates, which were then characterized by Gram staining, spore formation ability, biochemical tests (oxidase, citrate, catalase, and starch hydrolysis), and macroscopic examinations of colony color and pigment formation.

Screening for Amylolytic Activity

Streptomyces spp. were screened for amylase production based on starch hydrolysis. The microorganisms were inoculated into ISP4 medium and incubated at 28 °C for 72 h. The plates were then flooded with Gram's iodine solution. Dark blue coloration is observed when iodine reacts with starch. Amylolytic organisms formed a clear hydrolysis zone, unlike non-amylolytic ones (Abd-Elhalem et al., 2015).

Inoculum Preparation

First, 50 mL of ISP4 broth was dispensed into a 250 mL Erlenmeyer flask, sterilized, and allowed to cool. The broth was inoculated with a loopful of the microbial culture and incubated at 37 °C in a rotary shaker for 24 h.

Amylase Assay

For this, 1 mL of each inoculum was aseptically transferred into individual 250 mL Erlenmeyer flasks containing 50 mL of ISP-4 broth (fermentation medium; pH 7.0), and the microbes were grown aerobically at 28 °C for 96 h with agitation at 120 rpm. Subsequently, the medium and its contents were centrifuged at 5,000 rpm for 20 min. The supernatant was collected and used as crude amylase. Amylase activity was quantitatively assessed, employing the 3,5-dinitrosalicylic (DNS) method (Gusakov et al., 2011) with slight modifications. A 0.2 mL aliquot of the crude amylase was added to 0.5 mL of 0.1 M sodium phosphate (pH 7.0) containing 1% starch solution. The reaction mix was then incubated at 35 °C for 30 min, and then, the reaction was terminated by adding 1.0 mL of the DNS reagent. The reaction mix was placed in a boiling water bath for 10 min. The OD_{540} was measured with a UV-Vis spectrophotometer (Gusakov et al., 2011). Amylase production was ascertained by extrapolating the absorbance values to a standard graph, and the best amylase producers were selected for further studies.

Effect of Culture Parameters on Amylase Production

The effects of diverse cultivation conditions on amylase productivity were assessed using 50 mL media (Krishna et al., 2015). Buffers of various pH values—5.0, 6.0, 7.0, 8.0, and 9.0—were used to prepare ISP4 media and assess the influence of pH on amylase production. The impacts of different carbon (C) (soluble starch, mannitol, cassava peels, wheat bran, and sucrose at 10 g/L) and nitrogen (N) (urea, potassium nitrate, yeast extract, peptone, and ammonium sulfate at 10 g/L) sources on amylase production were examined. Each medium was inoculated with selected *Streptomyces* spp. and incubated at 28 °C for 96 h at 120 rpm in a rotary shaker. The effect of agitation on bacterial growth and amylase yield was estimated by culturing select *Streptomyces* spp. in ISP4 media at 28 °C on a rotary shaker set to different rpm: 100, 150, and 200 rpm for 96 h. To study the impacts of incubation time, the isolates were inoculated into ISP4 media and cultured on a rotary shaker for 2, 4, 6, and 8 days. Amylase productivity under each fermentation condition was determined via amylase assay.

Partial Purification and Specific Activity Determination

The stock inoculum of the highest amylase-producing isolate was added to the best production medium and cultured under optimal conditions. The enzyme produced was recovered after incubation: 100 mL of the cell-free crude extract was brought to 40% saturation with ammonium sulfate for 30 min and constantly stirred until the salt was completely dissolved. The solution was incubated at 4 °C for 24 h and then centrifuged at 5,000 rpm for 20 min. The precipitated pellet was resuspended in 0.1 M sodium phosphate buffer (pH 7.0), poured into a dialysis tube, and sealed. The tube was filled with four times the volume of the suspension contained and dialyzed for 18 h. The partially purified amylase was quantified by applying Lowry's method (Lowry et al., 1951), and the OD_{660} was measured against a blank solution on a UV-Vis spectrophotometer. The specific activity of the enzyme was determined using the formula-

$$\text{Specific activity} = \text{Enzyme activity (U/mL)/Protein concentration (mg/mL)}$$

Fruit Juice Clarification Ability

Sweet orange (*Citrus sinensis*) fruits were purchased from Ajibode, Ibadan, and washed thoroughly under running water. Their juice was extracted aseptically, and 10 mL aliquots were dispensed into sterile test tubes, sealed with sterile non-absorbent cotton wool, and pasteurized by heating at 85 °C for 3 min (Kareem & Adebowale, 2007). Then, 1 mL of amylase was aseptically dispensed into each test tube, while the one added with distilled water served as a blank. The contents were aliquoted at onset (0 h) and then at 30 min. They analyzed for clarity by spectrophotometrically measuring the transmittance (%) at 660 nm.

Percentage clarity was calculated as follows:

$$\% \text{ Clarity} = \frac{\text{Tt} - \text{Tc}}{\text{Tc}} \times 100\%$$

T_t = Transmittance of the test solution.

T_c = Transmittance of the control solution.

Molecular Species-Level Identification of the Isolate

DNA was extracted per the procedure described by Haque et al. (2022). The 16S rRNA gene was PCR-amplified using a GeneAmp 9700 PCR System Thermal cycler (Applied Biosystems Inc., USA). The reaction mixture contained 1 µL of 10 mM dNTPs mix, 3 µL of 25 mM $MgCl_2$, 10 µL of 5x GoTaq colorless reaction mix (Promega, WI, USA), 1 µL of each primer (10 pmol), 0.3 U of Taq DNA polymerase (Promega), 8 µL of DNA template, and 42 µL of sterile distilled water. The primers used were 1525R: 5'- AAGGAGGTGATCCAGCC-3' and 27F: 5'- AGAGTTTGATCMTGGCTC AG-3'. The amplicons were

sequenced on a 31310xl Genetic Analyzer (Applied Biosystems, MA, USA), utilizing a BigDye Terminator V3.1 Cycle Sequencing Kit (Applied Biosystems). All gene data were analyzed using MEGA 11 (Kumar et al., 2018; Tamura & Nei, 1993).

Statistical Analysis

All experiments in this work were carried out in duplicate. The mean and standard error of the mean of amylase activities were graphically represented. One-way analysis of variance (ANOVA) followed by Tukey's post-hoc test was used to determine the statistical significance of the differences in mean values at $p < 0.05$.

Results

Isolation, Quantitative Screening for Amylase, and Presumptive Identification of *Streptomyces* spp.

In total, 45 pure isolates were obtained from the soil samples. Preliminary identification indicated only 22 isolates as presumptive amylolytic *Streptomyces* spp. The enzyme yields of these isolates were quantified, based on which, five *Streptomyces* spp. with maximum amylase production were selected. These included: MS2, A1, FE4, A4, and ELI1, demonstrating activities of 0.654, 0.767, 0.787, 0.806, and 0.878 U/mL, respectively. All of them were citrate-positive, but catalase- and oxidase-negative. They could ferment glucose, fructose, and sucrose, as well as hydrolyze starch (Table 1).

Effects of Culture- and Nutrition-Associated Parameters on the Levels of Amylase Produced by the Five Isolates

The ANOVA test was conducted, and the means of amylases were plotted. The effect of pH on the five *Streptomyces* spp. to produce amylase is presented in Figure 1. A pH of 6.0 supported amylase production in ELI1 at 0.89 U/mL, which varied significantly ($p < 0.05$) from the yields of the other species. At a pH of 7.0, amylase production by FE4, MS2, A1, and A4 was 0.80, 0.658, 0.808, and 0.816 U/mL, respectively.

Adding cassava peels to the culture medium as a carbon source supported amylase production in A4, ELI1, and FE4 at 0.834, 0.91, and 0.814 U/mL. The amylase yield of ELI1 differed significantly ($p < 0.05$) when compared with the other four. However, starch as a carbon source supported amylase production to the maximum extent by A1 at 0.84 U/mL and MS2 at 0.750 U/mL (Figure 2). As N sources, peptone supported maximum amylase production by FE4 (0.818 U/mL); urea by ELI1 (0.930 U/mL) and A4 (0.884 U/mL); and KNO_3 by A1 (0.864 U/mL) and MS2 (0.802 U/mL). The highest yield detected was by ELI1, which did not vary significantly ($p > 0.05$) from that of A4 with urea (Figure 3).

The effects of different agitation speeds—100, 150, and 200 rpm—on amylase production are presented in Figure 4. At an agitation speed of 100 rpm, amylase production by A1, A4, and MS2 was 0.864, 0.880, and 0.840 U/mL; at 150 rpm, it was 0.980 and 0.920 U/mL by ELI1 and FE4, respectively.

Table 1. Cultivation and biochemical characteristics of five selected *Streptomyces* spp. isolated from soil samples.

Isolate code	Colony color	Soluble pigment	Cell morphology	Gram stain	Spore formation	Citrate	Oxidase	Catalase	Starch hydrolysis	Glucose	Fructose	Sucrose	Mannitol	Lactose	Galactose
Streptomyces sp. A1	Cream	ND	Cocci	+	+	+	-	-	+	+	+	+	+	+	+
Streptomyces sp. A4	Cream	ND	Cocci	+	+	+	-	-	+	+	+	+	+	+	+
Streptomyces sp. FE4	Gray	Gray	ND	+	+	+	-	-	+	+	+	+	+	+	+
Streptomyces sp. ELI1	Gray	Gray	ND	+	+	+	-	-	+	+	+	+	+	+	+
Streptomyces sp. MS2	White	White	Cocci	+	+	+	-	-	+	+	+	+	+	+	+

+ = positive; – = negative; ND = not determined.

The yield of ELI1 differed significantly ($p < 0.05$) from those of the other four species at all three agitation speeds. During the 8-day incubation period, amylase production started on day 2 and gradually rose till day 4 before declining (Figure 5). Maximum and minimum yields recorded on days 4 and 8 were 0.890 and 0.680 U/mL for A4, 0.866 and 0.640 U/mL for A1, and 0.910 and 0.780 U/mL for MS2, respectively. The highest yield recorded was with ELI1 at all fermentation periods and varied significantly ($p < 0.05$) when compared with the other four *Streptomyces* species.

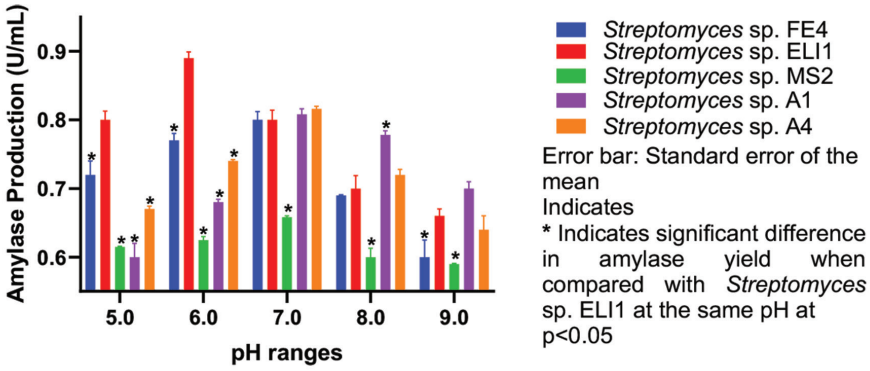

Figure 1. Effect of pH on amylase production by the five selected *Streptomyces* species.

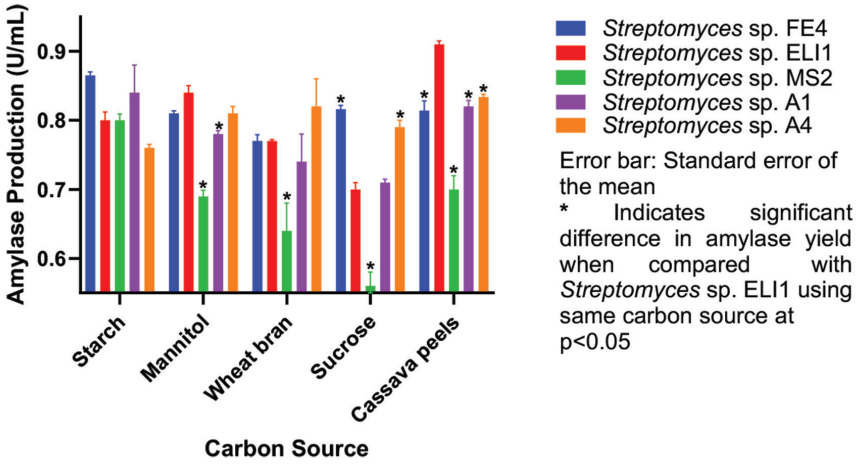

Figure 2. Effect of carbon source on amylase production by the five selected *Streptomyces* species.

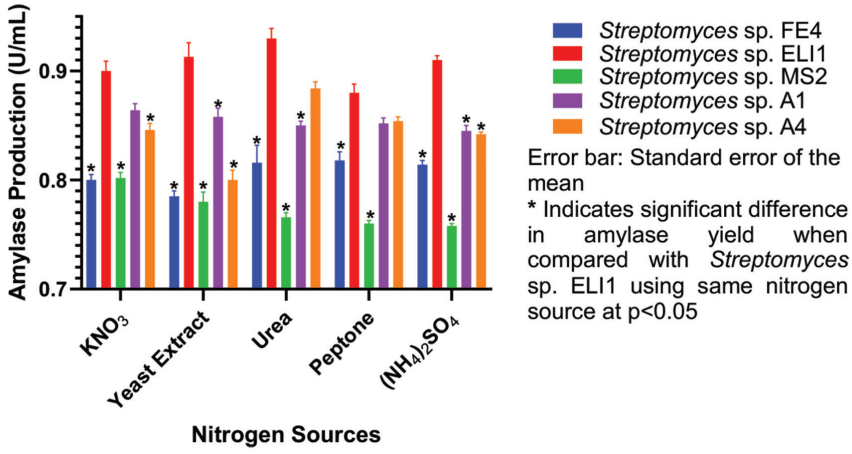

Figure 3. Effect of nitrogen source on amylase production by the five selected *Streptomyces* species.

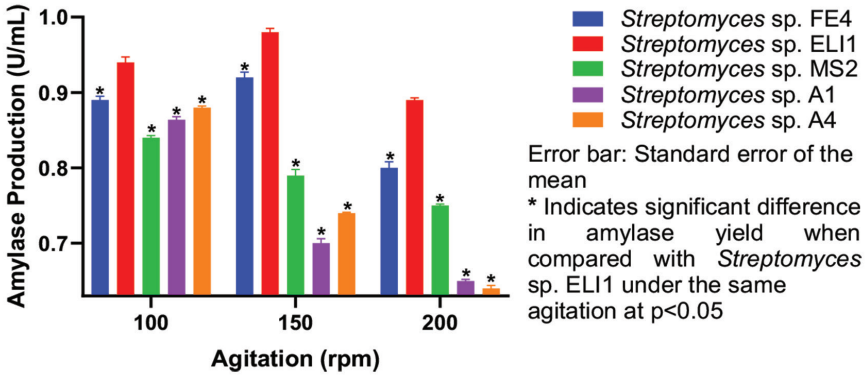

Figure 4. Effect of agitation on amylase production by the five selected *Streptomyces* species.

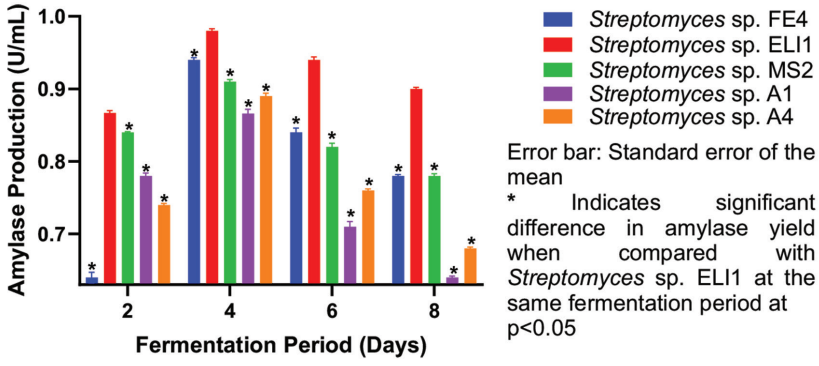

Figure 5. Effect of fermentation day on amylase production by the five selected *Streptomyces* species.

Partial Purification of Amylase

Streptomyces sp. ELI1 was selected due to its consistently high amylase production, and the enzyme synthesized by it was partially purified. Table 2 summarizes the purification steps. Ammonium sulfate precipitation increased the specific activity from 1.500 to 2.930 U/mL, and further to 4.560 U/mL by dialysis. However, the protein content of the crude declined from 0.653 mg/mL to 0.434 mg/mL after ammonium sulfate precipitation and further to 0.317 mg/mL post-dialysis.

Clarification of Orange Juice Using Amylase

The fruit juice clarifying potential was determined based on the increased transmittance of juice, which was 16.8% within 30 min of incubation with the amylase produced by ELI1. The value differed significantly from the initial one ($p < 0.05$); the amylolytic activity was 3.234 U/mL. This result confirmed the breakdown of starch, one of the factors responsible for turbidity.

Molecular Identification of the ELI1 Isolate

The best amylase producer among the five selected *Streptomyces* sp., ELI1, was identified at the molecular level as *S. griseoflavus* ELI_1. The sequence of the gene encoding amylase was submitted to the National Center for Biotechnology Information GenBank (Accession number: OQ930232). It was closely related to that of *S. griseoflavus* LMG 19344 with accession number: NR042291 (Figure 6).

Discussion

Different amylolytic species of *Streptomyces* were isolated from the soil samples collected in Ibadan, Nigeria. They were identified based on biochemical and morphological characteristics. Their amylolytic ability was determined based on the size of the zones of hydrolysis observed around the colonies growing on starch agar. The isolation of amylase-producing *Streptomyces* spp. from soil samples has been reported (Ali et al., 2023; Saadoun et al., 2023; Shu et al., 2025), confirming that soil is a repository of amylase-producing microbes.

The production and stability of enzymes are sensitive to pH (Kizhakedathil & Subathra, 2021). Among the different pH levels studied, *S. griseoflavus* ELI_1 produced the highest quantity of amylase at pH 6. This result is similar to that reported by Saad et al. (2021), using *Bacillus licheniformis* WF67. However, Olakusehin and Oyedeji (2021) reported that the maximum yield with *Aspergillus flavus* S2-OY was at pH 5.

Table 2. Step-wise purification of amylase produced by *Streptomyces* sp. ELI1.

	Activity	Volume	Protein (mg/mL)	Total protein	Total activity	Specific activity (U/mL)	Recovery (%)	Purification fold
Crude	0.980[c]	100	0.653[a]	65.3[a]	98.00[a]	1.500[c]	100.00[a]	1.00[c]
Ammonium sulfate precipitation (40%)	1.272[b]	50	0.434[b]	21.7[b]	63.60[b]	2.930[b]	64.89[b]	1.95[b]
Dialysis	1.447[a]	10	0.317[c]	3.17[c]	14.47[c]	4.560[a]	14.76[c]	3.04[a]

Mean values with various alphabetical superscripts along the column indicate statistically significant differences at $p < 0.05$.

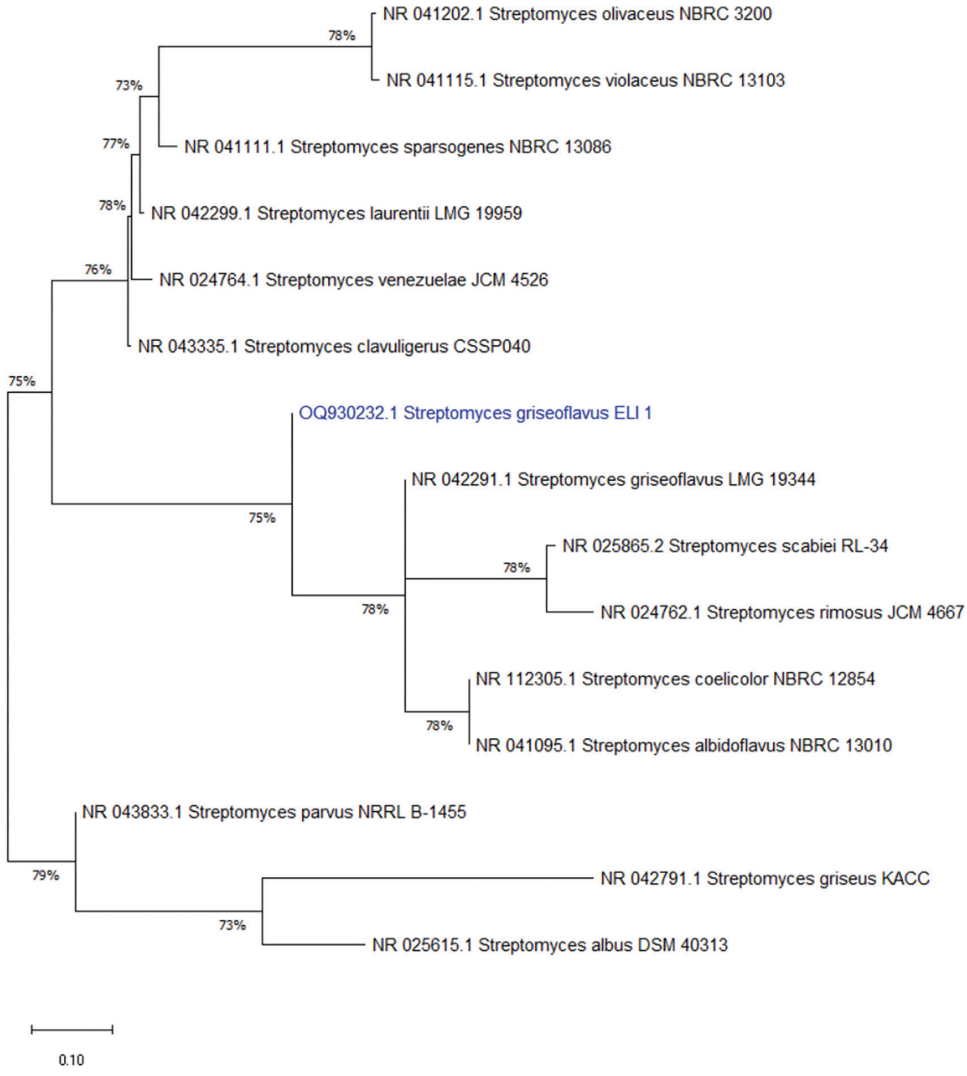

Figure 6. Phylogenetic tree indicating *S. griseoflavus* ELI_1 and other closely related microorganisms.

The type of C source is critical for media formulation, as it determines the growth rate of microorganisms and affects the production of metabolites such as amylase, etc. (Kizhakedathil & Subathra, 2021). In this study, the type of C source used in the fermentation medium markedly affected amylase production. The highest amylase production was recorded when agro-waste (cassava peels) was employed. Similarly, Iram et al. (2020) reported that the best yield of amylase was observed when grape fruit peels, as an agro-waste, were used. Adebare et al. (2021) utilized cassava peels for the production of amylase by *Aspergillus niger*. Varying types of agro-wastes have been used for amylase production (Abd-Elhalem et al., 2015; Iram et al., 2020; Olakusehin & Oyedeji, 2021; Sahu et al., 2024), as they are rich in carbon, with a few also containing a small proportion of N. The use of agrowastes as a C source can help reduce amylase production costs.

Nitrogen affects the synthesis of amino acids and thus, microbial growth. N can serve as a secondary energy source and influences enzyme production (Kizhakedathil & Subathra, 2021). The absence of many types of amino acids and other N sources in the production medium has been linked to remarkable effects on amylase biosynthesis (Singh et al., 2016). Peptone supported amylase production by *Streptomyces* FE4. Kavitha and Vijayalakshmi (2010) reported enhanced amylase production by *Streptomyces tendea* TK-VL-33 when peptone was utilized. Fahmy (2022) also reported better yield with peptone compared to yeast extract, ammonium sulfate, potassium nitrate, and urea.

Another critical parameter affecting microbial enzyme production is agitation, which influences O_2 distribution. Oxidative reactions utilize O_2 as a terminal electron acceptor to provide energy for various cellular activities. Agitation speed also affects morphology and subsequent biosynthetic activity (Ibrahim et al., 2015). In this study, a speed of 100 rpm optimized amylase production by A1, A4, MS2, and FE4, while 150 rpm was the best for ELI1. However, a further increase in speed reduced amylase yield, most likely due to the adverse effects, such as mechanical and oxidative stress, that were induced in cells (Prabakaran & Pugalvendhan, 2009). The maximum amylase production was by ELI1 at 150 rpm, aligning with the findings of Ahmed et al. (2015) and Niyomukiza et al. (2023) in *Penicillium notatum* and *Bacillus subtilis* W3SFR5, respectively.

Metabolite production, growth rate, and culture characteristics of microbes are influenced by the incubation period (Chowdary et al., 2018; Fasiku & Wakil, 2022). Earlier reports indicated better amylase production by *Streptomyces* spp. on day 4 (Singh et al., 2020), which is consistent with the results of this study. Further prolongation suppressed amylase production, which could be due to cells predominantly being in the decline phase of growth, leading to nutrient depletion and the accumulation of toxins in the culture medium, ultimately reducing growth and consequently enzyme production (Baysal et al., 2003).

Suspended colloidal or insoluble compounds such as starch, pectin, hemicellulose, cellulose, proteins, and other cell-wall fragments released during fruit processing cause fruit juices to become turbid (Sharma et al., 2017; Wang et al., 2022). Turbidity may be desirable in naturally cloudy juices or undesirable in juices intended to be clear, i.e., depending on the product (Sharma et al., 2017). In this work, the turbidity of fruit juice decreased after treatment with the amylase produced by *S. griseoflavus* ELI_1. Fruit juice clarity is one of the properties that determines consumer interest (Bamigboye et al., 2022), which led to a search for cost-effective and efficient clarification processes. In this work, the clarity of orange juice was enhanced by the amylase produced by ELI1. Starch is one of the compounds that contribute to fruit juice turbidity and post-concentration haze formation, as it can induce gel formation and membrane fouling, thereby decreasing the filtration rate (Hossain et al., 2024). Amylase helps reduce turbidity by breaking down the starch, clearing haziness, turbidity, and cloudiness, thereby improving the quality and shelf life of the juice (Hossain et al., 2024). Clarification of grape (Sondhi et al., 2021), orange (Bamigboye et al., 2022; Sondhi et al., 2021), apple (Hossain et al., 2024, Roheen et al., 2024), pear (Liviu et al., 2022), and banana (Shwe & Win, 2019) juice has been reported.

Study Limitations

This study was limited to soil samples collected from a single geographic region, which may not represent the full diversity of amylolytic *Streptomyces* spp. present in other environments. The enzyme was only partially purified, and characterization was restricted to basic assays without detailed kinetic or structural analysis. The juice of only one fruit type, orange, was used for testing clarification ability, which limits generalization to other fruit juices with different physicochemical properties. The degree of clarification was assessed via turbidity reduction, without any accompanying comprehensive sensory or nutrient retention analyses. Moreover, this study did not evaluate enzyme reusability or stability under conditions relevant to industrial processing. Future research should focus on large-scale optimization, purification, kinetic analysis, and broader application to enhance industrial relevance.

Conclusion

A total of 22 amylase-producing *Streptomyces* spp. were isolated from soil samples. Acidity or alkalinity, C and N source, agitation, and fermentation period affected amylase production. *S. griseoflavus* ELI_1 was the best amylase producer under optimized conditions; purification of the enzyme produced increased its activity. The turbidity of orange juice was reduced by 16.8% upon treating with the amylase produced by ELI_1, as it effectively hydrolyzed starch, thereby enhancing juice clarity. Thus, this enzyme has potential for juice clarification and can be used on an industrial scale.

Ethics

Ethics Committee Approval: Since the article does not contain any studies with human or animal subject, its approval to the ethics committee was not required.

Data Sharing Statement: All data are available within the study.

Footnotes

Authorship Contributions: Conceptualization: O.A.O. and S.M.W.; Design/methodology: O.A.O. and S.M.W.; Execution/investigation: E.A.O., O.A.O., and S.M.W.; Resources/materials: E.A.O. and S.M.W.; Data acquisition: E.A.O.; Data analysis/interpretation: E.A.O., S.A.F., O.K.A., K.O.S., M.T.D., O.A.O., and S.M.W.; Writing – original draft: E.A.O., S.A.F., O.K.A., K.O.S., M.T.D., and O.A.O.; Writing – review & editing/critical revision: S.A.F., O.A.O, and S.M.W.

Conflict of Interest: The author(s) have no conflicts of interest to declare.

Funding: The author(s) declare that this study has received no financial support.

References

Abd-Elhalem, B. T., El-Sawy, M., Gamal, R. F., & Abou-Taleb, K. A. (2015). Production of amylases from *Bacillus amyloliquefaciens* under submerged fermentation using some agro-industrial by-products. *Annals of Agricultural Sciences, 60*(2), 193–202. https://doi.org/10.1016/j.aoas.2015.06.001

Adebare, B. S., Johnson, A. A., Olanrewaju, T. M., Titilope, A. O., Femi, B. P., Bankole, S. A., Joseph, I. O., & Joshua, A. A. (2021). Production and optimization of alpha amylase from *Aspergillus niger* using TME 419 cassava peel as substrate. *African Journal of Biological Sciences, 3*(4), 50–59. https://doi.org/10.33472/AFJBS.3.4.2021.50-59

Adrio, J. L., & Demain, A. L. (2014). Microbial enzymes: Tools for biotechnological processes. *Biomolecules, 4*(1), 117–139. https://doi.org/10.3390/biom4010117

Ahmed, K., Munawar, S., & Khan, M. A. (2015). Cultural conditions for maximum alpha-amylase production by *Penicillium notatum* IBGE 03 using shaken flask technique of submerged fermentation. *Pure Applied Biology, 4*(3), 306–312. http://dx.doi.org/10.19045/bspab.2015.43005

Al-Dhabi, N. A., Esmail, G. A., Ghilan, A. M., Arasu, M. V., Duraipandiyan, V., & Ponmurugan, K. (2020). Isolation and purification of starch hydrolysing amylase from *Streptomyces* sp. Al-Dhabi-46 obtained from the Jazan region of Saudi Arabi with industrial applications. *Journal of King Saud University – Science, 32*, 1226–1232. https://doi.org/10.1016/j.jksus.2019.11.018

Ali, I., Sultan, S., Mahmood, R. T., Tariq, M., Shamim, Z., Mushtaq, A., & Asiri, M. (2023). Production and characterisation of α-amylase from indigenously isolated *Streptomyces* sp. *Bioresources, 18*(1), 6–18. https://doi.org/10.15376/biores.18.1.6-18

Arifeen, S., Jamil, J., Sarwar, A., Ullah, N., Nelofer, R., Aziz, T., Alharbi, M., Alasmari, A. F., Alshammari, A., & Albekairi, T. H. (2024). Biosynthesis and optimization of amylase from *Bacillus* sp. isolated from soil samples using agro-industrial waste as substrate. *Applied Ecology and Environmental Research, 22*(4), 2927–2940. http://dx.doi.org/10.15666/aeer/2204_29272940

Bamigboye, C. O., Okonji, R. E., Oluremi, I. O., & James, V. (2022). Stain removing, juice-clarifying, and starch liquefying potentials of amylase from *Pleurotus tuberregium* in submerged fermentation system. *Journal of Genetic Engineering and Biotechnology, 20*, Article 23. https://doi.org/10.1186/s43141-022-00298-4

Barman, D., & Dkhar, M. S. (2024). Purification and characterization of moderately thermostable raw-starch digesting α-amylase from endophytic *Streptomyces mobaraensis* DB13 associated with *Costus speciosus*. *The Journal of General and Applied Microbiology, 69*(6), 293–300. https://doi.org/10.2323/jgam.2023.08.001

Baysal, Z., Uyar, F., & Aytekin, C. (2003). Solid state fermentation for production of α-amylase by a thermotolerant *Bacillus subtilis* from hot spring water. *Process Biochemistry, 38*, 1665–1668. https://doi.org/10.1016/S0032-9592(02)00150-4

Casas, S. D., Orozco, J. L., Cardenas, A. J., Perez, H. L. R., & Brizuelas, L. G. (2025). Influence of the use of alpha amylase for the splitting of starches on color, ash and reducing sugars. *Afinidad. Journal of Chemical Engineering Theoretical and Applied Chemistry, 82*, 359–366. https://doi.org/10.55815/431129

Chowdary, A. R., Prakash, P. O., & Kishor, W. A. (2018). Optimization of amylase production by *Bacillus cereus* using solid state fermentation. *Journal of Biotechnology Resource, 4*, 56–65.

El-Sayed, M. H., Gomaa, A. E., Atta, O. M., & Hassane, A. M. (2024). Characteristics and kinetics of thermophilic actinomycetes' amylase production on agro-wastes and its application for ethanol fermentation. *World Journal of Microbiology and Biotechnology, 40*, Article 255. https://doi.org/10.1007/s11274-024-04009-8

Fahmy, N. M. (2022). Characterization of amylase-producing *Streptomyces* sp. NAA-28 isolated from mangrove sediment, Red Sea, Egypt. *Egyptian Journal of Aquatic Biology and Fisheries, 26*(4), 1053–1065.

Fasiku, S. A., Bello, M. A., & Odeniyi, O. A. (2023). Production of xylanase by *Aspergillus niger* GIO and *Bacillus megaterium* through solid-state fermentation. *Access Microbiology, 5*, 000506.v5. https://doi.org/10.1099/acmi.0.000506.v5

Fasiku, S. A., & Wakil, S. M. (2022). Screening of factors responsible for conversion of maize straw into bioethanol. *Journal of Microbiology, Biotechnology and Food Sciences, 12*(2), e5901. https://doi.org/10.55251/jmbfs.5901

Fasiku, S. A., Ogunsola, O. F., Fakunle, A., & Olanbiwoninu, A. A. (2020). Isolation of bacteria with potential of producing extracellular enzymes (amylase, cellulase and protease) from soil samples. *Journal of Advances in Microbiology, 20*(3), 21–26. https://doi.org/10.9734/jamb/2020/v20i330224

Gómez-Villegas, P., Viagra, J., Rumero, L., Gotor, C., Raposo, S., Gonçalves, B., & Léon, R. (2021). Biochemical characterization of the amylase activity from the new haloarchaeal strain *Haloarcula* sp. HS isolated in the Odiel Marshlands. *Biology, 10*(4), 337. https://doi.org/10.3390/biology10040337

Gusakov, A. V., Kondratyeva, E. G., & Sinitsyn, A. P. (2011). Comparison of two methods for assaying reducing sugars in the determination of carbohydrase activities. *International Journal of Analytical Chemistry, 2011*, 283658. https://doi.org/10.1155/2011/283658

Haque, A., Marwaha, S., Deb, S. K., Nigam, S., Arora, A., Hooda, K. S., Soujanya, P. L., Aggarwal, S. K., Lall, B., Kumar, M., Islam, S., Panwar, M., Kumar, P., & Agrawal, R. C. (2022). Deep learning based approach for the identification of diseases in maize crop. *Scientific Reports, 12*(1), 1–14. https://doi.org/10.1038/s41598-022-10140-z

Hossain, K. M., Khan, U., Rahman, S. M. M., & Khan, M. S. (2024). Potential antimicrobial and fruit juice clarification activity of amylase enzyme from *Bacillus* strains. *Biotechnology Reports, 44*, e00861. https://doi.org/10.1016/j.btre.2024.e00861

Ibrahim, D., Weloosamy, H., & Lim, S. (2015). Effect of agitation speed on the morphology of *Aspergillus niger* HFD5A-1 hyphae and its pectinase production in submerged fermentation. *World Journal of Biological Chemistry, 6*(3), 265. https://doi.org/10.4331/wjbc.v6.i3.265

Illanes, A., Cauerhff, A., Wilson, L., & Castro, G. R. (2012). Recent trends in biocatalysis engineering. *Bioresource Technology, 115*, 48–57. https://doi.org/10.1016/j.biortech.2011.12.050

Iram, N., Shakir, H. A., Irfan, M., Khan, M., Ali, S., Answer, A., Saeed, S., & Qazi, J. I. (2020). Statistical optimization of amylase production using grape fruit peels in submerged fermentation. *Acta Scientiarum Technology, 43*, e50538. https://doi.org/10.4025/actascitechnol.v43i1.50538

Kahraman, O., Lee, H., Zhang, W., & Feng, H. (2017). Manothermosonication (MTS) treatment of apple–carrot juice blend for inactivation of *Escherichia coli* O157:H7. *Ultrasonic Sonochemistry, 38*, 820–828. https://doi.org/10.1016/j.ultsonch.2016.11.024

Kareem, S. O., & Adebowale, A. A. (2007). Clarification of orange juice by crude fugal pectinase from citrus peel. *Nigeria Food Journal, 24*, 130–137. https://doi.org/10.4314/nifoj.v25i1.33661

Kavitha, A., & Vijayalkshmi, M. (2010). Production of amylases by *Streptomyces tendea* TK-VL-333. *International Journal of Current Resources, 10*, 110–114.

Khan, F. K. (2025). Recent advances in microbial enzymes applications for sustainable textile processing and waste management. *Sci, 7*, Article 46. https://doi.org/10.3390/sci7020046

Kharel, M., Shepherd, M. D., Nybo, S. E., Smith, M. L., & Bosserman, M. A. (2010). Isolation of *Streptomyces* species from soil. *Current Protocols in Microbiology, 19*(1), 4–5. https://doi.org/10.1002/9780471729259.mc10e04s19

Kizhakedathil, M. P. J., & Subathra, D. C. (2021). Acid stable α-amylase from *Pseudomonas balearica* VITPS19 – Production, purification and characterization. *Biotechnology Reports, 30*, e00603.

Krishna, N., Muvva, V., Munaganti, R. K., & Bindu, H. (2015). Studies on optimization of amylase production by *Streptomyces cheonanensis* VUK-A

isolated from mangroove habitats. *Journal of Advances in Biology and Biotechnology, 3*(4), 165–172. https://doi.org/10.9734/JABB/2015/18025

Kumar, S., Stecher, G., Li, M., Knyaz, C., & Tamura, K. (2018). MEGA X: Molecular evolutionary genetics analysis across computing platforms. *Molecular Biology and Evolution, 35*, 1547–1549. https://doi.org/10.1093/molbev/msy096

Li, S., Yang, X., Yang, S., Zhu, M., & Wang, X. (2012). Technology prospecting on enzymes: Application, marketing and engineering. *Computational and Structural Biotechnology Journal, 2*(3), 10–12. https://doi.org/10.5936/csbj.201209017

Liu, L., Yang, H., & Shin, H. D. (2013). How to achieve high-level expression of microbial enzymes: Strategies and perspectives. *Bioengineering, 4*(4), 212–223. https://doi.org/10.4161/bioe.24761

Liviu, G., Olivian, C., & Cristian, H. (2022). Fruit juices clarification with α-amylases. *Annals of the University of Craiova, Biology, Horticulture, Food Products Processing Technology, Environmental Engineering, 27*(63), 173–176.

Lowry, O. H., Rosebrough, N. J., Farr, A. L., & Randall, R. J. (1951). Protein measurement with the Folin phenol reagent. *Journal of Biological Chemistry, 193*, 265–275.

Mokrani, S., & Nabti, E. H. (2024). Recent status in production, biotechnological applications, commercial aspects, and future prospects of microbial enzymes: A comprehensive review. *International Journal of Agricultural Science and Food Technology, 10*(1), 006–020. https://dx.doi.org/10.17352/2455-815X.000202

Niyomukiza, S., Owino, W., Mathara, J. M., & Maina, N. (2023). Isolation, purification and biochemical characterization of alkaline amylase from *Bacillus subtilis* strain W3SFR5 isolated from kitchen wastes. *Applied Food Biotechnology, 20*(1), 9–19. http://dx.doi.org/10.22037/afb.v10i1.39495

Olakusehin, V. O., & Oyedeji, O. (2021). Production of α-amylase from *Aspergillus flavus* S2-OY using solid substrate fermentation of potato (*Solanum tuberosum* L.) peel. *International Journal of Biological and Chemical Sciences, 15*(5), 1950–1967. https://dx.doi.org/10.4314/ijbcs.v15i5.21

Oliveira, R. L., Dias, J. L., da Silva, O. S., & Porto, T. S. (2018). Immobilization of pectinase from *Aspergillus aculeatus* in alginate beads and clarification of apple and umbu juices in a packed bed reactor. *Food Bioproduction Process, 109*, 9–18. https://doi.org/10.1016/j.fbp.2018.02.005

Oussadi, M. I., & Kitouni, M. (2015). Statistical optimization of cultural conditions of an halophilic alpha-amylase production by halophilic *Streptomyces* sp. grown on orange waste powder. *Biocatalysis and Agricultural Biotechnology, 4*(4), 685–693. http://dx.doi.org/10.1016/j.bcab.2015.08.011

Oyenado, O. A., & Omoruyi, I. M. (2024). Review of amylase production by microorganisms and their industrial application. *Ife Journal of Science, 26*(2), 537–553. https://dx.doi.org/10.4314/ijs.v26i2.23

Patel, A. K., Dong, C. D., Chen, C. W., Pandey, A., & Singhania, R. R. (2023). Production, purification, and application of microbial enzymes. In *Biotechnology of microbial enzymes* (pp. 25–57). https://doi.org/10.1016/B978-0-443-19059-9.00019-0

Prabakaran, G., & Pugalvendhan, R. (2009). Production and immobilization of alpha-amylase by using *Bacillus subtilis*. *Recents Research in Science and Technology, 1*(4), 189–194. https://doi.org/10.3923/pjbs.2007.2039.2047

Rathore, D. S., & Singh, S. P. (2021). Kinetics of growths and co-production of amylase and protease in novel marine actinomycete, *Streptomyces lopnurensis* KaM5. *Folia Microbiologia, 66*, 303–316. https://doi.org/10.1007/s12223-020-00843-z

Roheen, T., Ramzan, R., Nadeem, M., Atif, F. A., Munir, M., & Qureshi, T. M. (2024). Synthesis and characterization of CMC/PAM-amy hydrogel and its efficacy in apple juice clarification. *Processes, 12*, 2264. https://doi.org/10.3390/pr12102264

Saad, W. F., Othman, A. M., Abdel-Fatah, M., & Ahmad, M. S. (2021). Response surface methodology as an approach for optimization of α-amylase production by the new isolated thermotolerant *Bacillus licheniformis* WF67 strain in submerged fermentation. *Biocatalysis and Agricultural Biotechnology, 32*, 101944. https://doi.org/10.1016/j.bcab.2021.101944

Saadoun, I., Alawawdeh, M., Jaradat, Z., Ababneh, Q., Al-joubori, B. M., & Elsheikh, E. A. E. (2023). Characterization of diesel-degrading, hydrolytic enzymes-producing *Streptomyces* spp. isolated from fuel-oil polluted soils. *Arab Journal of Basic and Applied Sciences, 30*(1), 248–255. https://doi.org/10.1080/25765299.2023.2196110

Sahu, P. K., Singh, R., Shrivastava, M., Darjee, S., Mageshwaran, V., Phurailtpan, L., & Rohatgi, B. (2024). Microbial production of α-amylase from agro-waste: An approach towards biorefinery and bio-economy. *Energy Nexus, 14*, 100293. https://doi.org/10.1016/j.nexus.2024.100293

Saravanan, A., Kumar, P. S., Dai-Viet, N. V., Jeevanantham, S., Karishma, S., & Yaashikaa, R. (2021). A review on catalytic-enzyme degradation of toxic environmental pollutants: Microbial enzymes. *Journal of Hazardous Materials, 419*, 126451. https://doi.org/10.1016/j.jhazmat.2021.126451

Sharma, H. P., Patel, H., & Sugandha. (2017). Enzymatic added extraction and clarification of fruit juices – A review. *Critical Reviews in Food Science and Nutrition, 57*(6), 1215–1227. http://dx.doi.org/10.1080/10408398.2014.977434

Shu, W., Ruckert-Reed, C., Gromyko, O., Tistechok, S., Kalinowski, J., Luzhetskyy, A., & Wittmann, C. (2025). Description of *Streptomyces explomaris* sp. nov., isolated from the coastal soil rhizosphere of *Juniperus excelsa* and reclassification of *Streptomyces libani* as a later heterotypic synonym of *Streptomyces nigrescens*. *International Journal of Systematic and Evolutionary Microbiology, 75*, 006711. https://doi.org/10.1099/ijsem.0.006711

Shwe, K. K. W., & Win, S. S. (2019). Effect of amylolytic enzyme treatment on banana juice preparation, yield and clarification: A preliminary approach. *International Journal of Science and Engineering Applications, 8*(2), 75–78.

Singh, R., Kumar, M., Mittal, A., & Mehta, P. K. (2016). Microbial enzymes: Industrial progress in 21st century. *3 Biotechnology, 6*, 174. https://doi.org/10.1007/s13205-016-0485-8

Singh, T. A., Jajoo, A., & Bhasin, S. (2020). Production and application of glucose isomerase from *Streptomyces enissocaesilis* and amylase from *Streptomyces* sp. for the synthesis of high fructose corn syrup. *SN Applied Sciences, 2*(12), 1968. https://doi.org/10.1007/s42452-020-03757-0

Sondhi, S., Kaur, P. S., Sura, H., Juglani, M., & Sharma, D. (2021). Amylase based clarification of apple, orange and grape juice. *International Journal of Contemporary Technology and Research, 3*(3), 187–190. https://doi.org/10.46860/cgcijctr.2021.06.31.187

Suthar, S., Joshi, D., Patel, H., Patel, D., & Kikani, B. A. (2024). Optimization and purification of a novel calcium-independent thermostable, α-amylase produced by *Bacillus licheniformis* UDS-5. *World Journal of Microbiology and Biotechnology, 40*(12), Article 385. https://doi.org/10.1007/s11274-024-04188-4

Tamura, K., & Nei, M. (1993). Estimation of the number of nucleotide substitutions in the control region of mitochondrial DNA in humans and chimpanzees. *Molecular Biology and Evolution, 10*, 512–526. https://doi.org/10.1093/oxfordjournals.molbev.a040023

Thulasisingh, A., Ananthakrishnan, K., Raja, A., & Kannaiyan, S. (2024). Bioprospecting of novel and industrially appropriate enzymes: A review. *Water, Air and Soil Pollution, 235*, 12. https://doi.org/10.1007/s11270-023-06831-6

Vojnovic, S., Aleksic, I., Ilic-Tomic, T., Stevanovic, M., & Nikodinovic-Runic, J. (2024). *Bacillus* and *Streptomyces* spp. as hosts for production of industrially relevant enzymes. *Applied Microbiology and Biotechnology, 108*, Article 185. https://doi.org/10.1007/s00253-023-12900-x

Wang, H., Yuan, J., Chen, L., Ban, Z., Zheng, Y., Jiang, Y., Jiang, Y., & Li, X. (2022). Effects of fruit storage temperature and time on cloud stability of not from concentrated apple juice. *Foods, 11*, 2568. https://doi.org/10.3390/foods11172568

Trakya University Journal of Natural Sciences, 27(1), 67–75, 2026
DOI: 10.23902/trkjnat.2025104
www.tujns.org

Research Article

Process optimization for third-generation bioethanol production from *Chlorella vulgaris* as a feedstock by *Candida boidinii*

Aybüke Kut Yılmaz, Melike Kartal, Gönül Dönmez, Sevgi Ertuğrul Karatay*

Ankara University, Faculty of Science, Department of Biology, Ankara, Türkiye

Cite this article as: Kut Yılmaz, A., Kartal, M., Dönmez, G., & Ertuğrul Karatay, S. (2026). Process optimization for third-generation bioethanol production from *Chlorella vulgaris* as a feedstock by *Candida boidinii*. *Trakya University Journal of Natural Sciences, 27*(1), 67–75. https://doi.org/10.23902/trkjnat.20257104

Abstract

Background: Microalgae offer significant advantages for third-generation bioethanol production due to their rapid growth rates, high photosynthetic efficiency, and ability to accumulate substantial amounts of carbohydrates. Unlike agricultural food crops, microalgae can be cultivated on non-arable land using saline or wastewater resources, thereby avoiding competition with food crops. Moreover, their low lignin contained cell wall structure enables milder pretreatment requirements and more efficient enzymatic hydrolysis, which ultimately leads to improved sugar production and higher ethanol yields. In addition, microalgae-based bioethanol production contributes to carbon dioxide mitigation through CO_2 fixation, enhancing the overall environmental sustainability of the process. For the mentioned reasons *Chlorella vulgaris* biomass was used as a feedstock for third-generation bioethanol production in the present study.

Aims: The aim of this study is to develop a sustainable and integrated process for third generation bioethanol production by utilizing domestic food waste. Specifically, the research focuses on: investigating the effects of ZnO nanoparticles on the fermentation process; evaluating the performance of *C. boidinii* yeast in the presence of nanoparticle catalysts; optimizing cultivation conditions to achieve efficient microalgal growth and enhanced bioethanol production by *C. boidinii*; and examining the influence of key parameters, such as pretreatment methods (1% H_2SO_4 and 1% NaOH), biomass loading (50, 100, 200 g/L), and media composition, on the ethanol yield.

Methods: In this study, *C. vulgaris* was used as a feedstock for bioethanol several key parameters were optimized, including microalgal cultivation conditions (photoautotrophic, photoheterotrophic with glucose, and photoheterotrophic with carrot pomace), pretreatment

Özet

Dayanak: Mikroalgler; hızlı büyüme oranları, yüksek fotosentetik verimlilikleri ve önemli miktarda karbonhidrat biriktirme yetenekleri nedeniyle üçüncü nesil biyoetanol üretimi için önemli avantajlar sunmaktadır. Tarımsal gıda ürünlerinin aksine, mikroalgler tarıma elverişli olmayan arazilerde, tuzlu su veya atık su kaynakları kullanılarak yetiştirilebilir; bu sayede gıda ürünleriyle rekabetten kaçınılır. Ayrıca, düşük lignin içeriğine sahip hücre duvarı yapıları, daha ılımlı ön işlem koşullarına ve daha verimli bir enzimatik hidrolize olanak tanır, bu da sonuç olarak şeker üretiminin artmasına ve daha yüksek etanol verimine yol açar. Ek olarak, mikroalg tabanlı biyoetanol üretimi, CO_2 fiksasyonu yoluyla karbondioksit azaltımına katkıda bulunarak sürecin genel çevresel sürdürülebilirliğini artırır. Bahsedilen bu nedenlerden dolayı, mevcut çalışmada üçüncü nesil biyoetanol üretimi için hammadde olarak *Chlorella vulgaris* biyokütlesi kullanılmıştır.

Amaçlar: Bu çalışmanın amacı, evsel gıda atıklarından yararlanarak üçüncü nesil biyoetanol üretimi için sürdürülebilir ve entegre bir süreç geliştirmektir. Araştırma spesifik olarak şu konulara odaklanmaktadır: ZnO (Çinko Oksit) nanopartiküllerinin fermantasyon süreci üzerindeki etkilerinin araştırılması; nanopartikül katalizörlerin varlığında *C. boidinii* mayasının performansının değerlendirilmesi; *C. boidinii* ile verimli mikroalgal büyüme ve artırılmış biyoetanol üretimi sağlamak için kültivasyon koşullarının optimize edilmesi, ön işlem yöntemleri (%1 H_2SO_4 ve %1 NaOH), biyokütle yüklemesi (50, 100, 200 g/L) ve besiyeri bileşimi gibi temel parametrelerin etanol verimi üzerindeki etkisinin incelenmesi.

Yöntemler: Bu çalışmada, *C. vulgaris* biyoetanol için hammadde olarak kullanılmış ve mikroalg yetiştirme koşulları (fotootrofik, glikozlu fotoheterotrofik ve havuç posası ile fotoheterotrofik), ön

Edited by: *Tuğba Ongun Sevindik*

***Corresponding Author:** Sevgi Ertuğrul Karatay, **E-mail:** sertugrul@ankara.edu.tr*

***ORCID iDs of the author(s):** AKY. 0000-0001-5682-6942; MK. 0009-0007-5962-5477; GD. 0000-0001-7972-5570; SEK. 0000-0001-9544-0276*

Received: 30 October 2025, **Accepted:** 22 December 2025, **Epub:** 21 January 2026, **Published:** 24 April 2026

type (1% H_2SO_4 and 1% NaOH), biomass loading (50, 100, and 200 g/L), and nutrient supplementation (Medium 1 and Medium 2).

Results: *Candida boidinii* exhibited the highest bioethanol production and productivity at 3.29 ± 0.14 g/L and 0.26 ± 0.01g/L.h, respectively. When Medium 1 was applied, bioethanol concentration and productivity further increased to 4.54 ± 0.18 g/L and 0.38 ± 0.01 g/L.h, respectively.

Conclusion: These findings demonstrate that fermentable sugars derived from *C. vulgaris* can be effectively converted into third-generation bioethanol by *C. boidinii*.

işlem türü (1% H_2SO_4 ve 1% NaOH), biyokütle yüklemesi (50, 100 ve 200 g/L) ve besin takviyesi (Ortam 1 ve Ortam 2) gibi önemli parametreler optimize edilmiştir.

Bulgular: *Candida boidinii*, sırasıyla 3,29 ± 0,14 g/L ve 0,26 ± 0,01 g/L.h ile en yüksek biyoetanol üretimi ve verimliliğini sergilemiştir. Orta 1 uygulandığında, biyoetanol konsantrasyonu ve verimliliği sırasıyla 4,54 ± 0,18 g/L ve 0,38 ± 0,01 g/L.h'ye yükseldi.

Sonuç: Bu bulgular, *C. vulgaris*'ten elde edilen fermente edilebilir şekerlerin *C. boidinii* tarafından üçüncü nesil biyoetanola etkili bir şekilde dönüştürülebileceğini göstermektedir.

Keywords: Microalgae, fermentation, supplement, bioethanol, carrot pomace

Introduction

In recent decades, the energy crisis and global warming have emerged as some of the most critical global concerns. These challenges are closely associated with population growth and the excessive consumption of fossil fuels. Consequently, the exploration of renewable energy sources has become a key factor in achieving sustainability (Medipally et al., 2015). Solar, wind, biomass, and geothermal energy are commonly referred to as alternative renewable sources, and they possess significant potential to reduce both environmental pollutants and greenhouse gas emissions (Panwar et al., 2011).

Biomass-based energy sources offer several advantages, including renewability, wide availability, and cost-effectiveness. Among these, bioethanol is the most extensively studied biofuel and can be produced from various raw materials such as corn, rice, lignocellulosic biomass, photosynthetic organisms, and genetically modified microorganisms (Dutta et al., 2014; Srilatha et al., 2019).

Edible raw materials used in the food industry, including sugar beet, rice, corn, and cassava, are classified as first-generation bioethanol sources. In contrast, non-edible lignocellulosic feedstocks are utilized for second-generation bioethanol production (Kiran et al.,2014; Lavanya et al., 2020). Photosynthetic organisms, particularly microalgae, serve as feedstocks for third-generation bioethanol production. Microalgae utilize sunlight and CO_2 as carbon sources for growth, which offers a distinct advantage by potentially lowering production costs (Sarkar & Shimizu, 2015). They are easy to cultivate and possess high lipid, protein, and carbon contents. Moreover, the low lignin content of microalgae allows for the release of fermentable sugars without requiring harsh pretreatment conditions (Jambo et al., 2016). In addition to their lipid content, microalgae contain significant amounts of carbohydrates, such as glucose and xylose. Several genera, including *Chlorella*, *Dunaliella*, *Chlamydomonas*, *Scenedesmus*, and *Spirulina*, have been reported to accumulate carbohydrates comprising up to approximately 50% of their dry biomass, making them strong candidates for bioethanol production (John et al., 2011).

Numerous studies on bioethanol production have demonstrated that *Chlorella vulgaris* contains carbohydrates accounting for 37%–55% of its dry biomass. These carbohydrates include glucose, xylose, galactose, arabinose, mannose, fucose, and rhamnose (Agwa et al., 2017; Caetano et al., 2022).

Phototrophic, heterotrophic, photoheterotrophic, and mixotrophic conditions represent the primary cultivation strategies for microalgae, each supporting growth under different carbon and energy sources (Tandon & Jin, 2017). In phototrophic systems, microalgae rely exclusively on light and CO_2 for metabolic activity. In contrast, heterotrophic cultivation enables growth through the utilization of organic carbon sources, in the absence of light. Photoheterotrophic cultivation combines illumination with organic substrates to support cellular growth (Abreu et al., 2012). Although photoheterotrophic cultivation has received comparatively limited attention in bioethanol-focused studies, existing reports suggest its potential to enhance biomass accumulation and increase lipid content (Selvakumar & Umadevi, 2014).

Agricultural and industrial food wastes are rich in fermentable sugars and growth-promoting factors such as proteins and minerals (Roy et al., 2023). Carrot pomace represents an important raw material, as it contains fermentable sugars including xylose, glucose, and galactose along with mineral salts (Mg, Ca, K, P, Na), carotenoids, and vitamins (Barzee et al., 2019). For these reasons, carrot pomace was employed as an organic carbon source to support microbial growth and fermentable sugar accumulation during the photoheterotrophic cultivation of *C. vulgaris*.

Candida boidinii is a methylotrophic yeast characterized by considerable intraspecies variability and significant biotechnological relevance. It can be isolated from diverse natural habitats as well as environments influenced by human activities. The organism is capable of growth across a broad temperature range (15 °C–37 °C) and is widely distributed across various geographic regions (Camiolo et al., 2017; da Silva Almeida et al., 2024). Importantly, its metabolic capacity extends beyond hexose sugars, as it can also efficiently utilize pentose sugars. This metabolic versatility positions *C. boidinii* as a promising alternative ethanologenic yeast to *Saccharomyces cerevisiae* (Fehér et al., 2021).

Additives such as nitrogen sources and mineral salts play a crucial role in supporting microbial growth and ethanol tolerance.

For example, mineral salts act as cofactors in various metabolic reactions during fermentation (Rees & Stewart, 1997). Conversely, nitrogen sources, including amino acids, improve cell viability and increase ethanol tolerance (Yamaoka et al., 2014).

In the first phase of this study, the effects of different cultivation conditions were investigated to achieve more efficient microalgal growth and enhanced bioethanol production by *C. boidinii*. Subsequently, the influence of key parameters, including pretreatment methods (1% H_2SO_4 and 1% NaOH), biomass loading (50, 100, 200 g/L), and media composition, on bioethanol production by *C. boidinii* was examined. This study represents the first report on microalgal-based bioethanol production using *C. boidinii*.

Materials and Methods

Microalgae and Cultivation Conditions

Chlorella vulgaris was obtained from the culture collection of Ankara University, Department of Biology, Biotechnology Research Laboratory Culture Collection. To initiate cultivation, 10 mL of pre-cultured microalgae was inoculated into 250 mL flasks containing 100 mL of BG-11 medium. The composition of BG-11 medium was as follows (per liter): 1.5 g $NaNO_3$, 75 mg $MgSO_4.7H_2O$, 40 mg K_2HPO_4, 36 mg $CaCl_2.2H_2O$, 6 mg ferric ammonium citrate, 6 mg citric acid H_2O, 1 mg $Na_2EDTA.2H_2O$, 2.86 mg H_3BO_3, 20 mg Na_2CO_3, 1.81 mg $MnCl_2.4H_2O$, 0.39 mg $Na_2MoO_4.2H_2O$, 0.22 mg $ZnSO_4.7H_2O$, 0.0494 mg $Co(NO_3)_2.6H_2O$, and 0.079 mg $CuSO_4.5H_2O$ (Park et al., 2014; Rippka, 1988). The working volume was maintained at 100 mL in 250 mL Erlenmeyer flasks. The cultures were incubated at 30 °C under cool-white fluorescent light with an intensity of 12.5 W m^{-2} (2400 lx). During photoautotrophic cultivation, no external sugar source was added to the BG-11 medium. Under photoheterotrophic conditions, microalgal cultures were grown in BG-11 supplemented with either 0.5 g/L glucose or 0.5 g/L carrot pomace (CP)-derived sugars under continous illumination. To assess the effect of CP, cultures supplemented with 0.5 g/L CP-derived sugars were incubated for 12 days under photoheterotrophic conditions at 30 °C and 2400 lx.

Microalgal biomass was harvested after 12 days by centrifugation at 5,000 rpm for 10 min using a Hettich Rotofix 32A centrifuge. The harvested cells were dried overnight at 70 °C. The resulting dried microalgal biomass was then used in fermentation assays (Acebu et al., 2022; Agwa et al., 2017; Wistara et al., 2016).

Pretreatment of CP

CP was supplied by BELSO/Türkiye and dried overnight in an oven at 80 °C. Dried CP (100 g/L) was pretreated with 1% H_2SO_4 at 121 °C for 15 min. Following pretreatment, the liquid fraction was separated by filteration using Whatman No. 1 filter paper.

Fermentation Conditions

Candida boidinii was obtained from the culture collection of Ankara University, Department of Biology, Biotåechnology Research Laboratory Culture Collection. For pre-incubation, *C. boidinii* was cultivated for 24 hours in PGY medium, containing 10 g/L peptone, 20 g/L glucose, and 3 g/L yeast extract. Prior to fermentation, the microalgal biomass was subjected to a pretreatment process. Initially, the biomass was homogenized using an IKA T18 Ultra-Turrax at 13,000 rpm for 1 min. The homogenized biomass was then treated with 1% H_2SO_4 and sterilized by autoclaving at 121 °C for 15 min using an ALP/CL-40 M autoclave (ALP/CL-40 M, Germany). The inoculation ratio was adjusted to 10% (v/v). All fermentation experiments were conducted in 100 mL Erlenmeyer flasks with a working volume of 40 mL. Fermentations were carried out at 30 °C and 100 rpm in a shaking incubator (Gerhardt/Thermoshake THO 500/1/Germany). The fermentation pH was mainatined at 5. Initial sugar and ethanol concentrations were measured after 6, 12, and 24 hours of fermentation.

Effect of Pretreatment on Bioethanol Production

Two different pretreatment methods were applied to *C. vulgaris* biomass. The microalgal biomass was treated with either 1% H_2SO_4 or 1% NaOH and autoclaved at 121 °C for 15 min using an autoclave (ALP/CL-40 M/Germany). After pretreatment, the samples were centrifuged at 5,000 rpm for 10 min. The solid pellet was discarded, and the resulting liquid fractions were used for subsequent fermentation experiments.

Effects of Initial Biomass Loading on Bioethanol Production

To determine the effect of initial biomass loading on bioethanol production, three different microalgal biomass concentrations (50, 100, 200 g/L) were examined. *C. vulgaris* biomass was pretreated with 1% H_2SO_4 at 121 °C for 15 min in an autoclave. This pretreated microalgal biomass was subsequently used as the carbon source for fermentation.

Effect of Different Supplements on Bioethanol Production

To assess the effect of nutient supplementation on bioethanol production, two different fermentation media containing *C. vulgaris* biomass were evaluated. Medium 1 consisted of 5 g/L peptone, 3 g/L yeast extract, 0.5 g/L $MgSO_4.7H_2O$, 1 g/L KH_2PO_4, 0.1 g/L $CaCl_2$, and 0.05 $ZnSO_4$ prior to fermentation (Demiray et al., 2020). Medium 2 contained 1 g/L yeast extract, 0.4 g/L KH_2PO_4, and 0.2 g/L NH_4Cl as mineral and nitrogen sources (Yu et al., 2020).

Analytical Methods

Ethanol concentration was determined by gas chromatography using a Shimadzu GC-2010 system. For sample preparation, 1.5 mL of fermentation broth was centrifuged at 10,000 rpm and 4 °C for 10 min using a Hettich centrifuge. The resulting supernatant was filtered through a 0.22 µm membrane filter and subjected to gas chromatography analysis. Ethanol was quantified using a flame ionization detector equipped with an RTX-Wax capillary column (60 m length, 0.25 mm internal diameter). A sample volume of 1 µL was injected into the injection port. The injection and detector temperatures were maintained at 140 °C and 160 °C, respectively. The initial column temperature was set at 50 °C and increased to 150 °C over 19 min. The column flow rate was 1.86 mL/min, with

a total carrier gas flow of 190.4 mL/min; nitrogen was used as the carrier gas (Wistara et al., 2016).

Total reducing sugar concentrations were determined using the DNS method (Miller, 1959). Reducing sugars reacted with the DNS reagent to produce an orange-brown colored compound. Sodium potassium tartrate was used to stabilize the color and prevent precipitation. Absorbance was measured spectrophotometrically at 540 nm, with a color intensity directly proportional to the reducing sugar concentration. Yeast growth was monitored spectrophotometrically at 600 nm.

Theoretical ethanol yield was calculated using Equation (1) (Kim & Lee, 2007).

$$\text{Theoretical ethanol yield (\%)} = \frac{\text{ethanol (g/L)}}{\text{(initial sugar (g/L)} \times 0.511)} \text{ x100} \quad (1)$$

Volumetric ethanol productivity (Q_p) was calculated using Equation (2) (Roca & Olsson, 2003).

$$\text{Volumetric ethanol productivity (g/Lh)} = \frac{\text{ethanol (g/L)}}{h_{max}} \quad (2)$$

Ethanol yield based on substrate consumption ($Y_{P/S}$) was calculated using Equation (3) (Yücel & Aksu, 2015).

$$\text{Ethanol yields (g/g)} = \frac{\text{(maximum ethanol (g/L)}}{\text{consumed sugar (g/L)}} \quad (3)$$

Statistical Analysis

Initially, the dataset was evaluated for compliance with the assumptions of normality and homogeneity of variances using the Shapiro–Wilk and Levene's test, respectively. As the data met the requirements for parametric analysis, statistical comparisons were performed using one-way analysis of variance. When significant differences were detected ($p < 0.05$), Tukey's honestly significant difference test was applied for post hoc pairwise comparisons. Results are reported as mean ± standard deviation. Groups within the same column sharing the same superscript letter was not significantly different among treatments. All statistical analyses were conducted using R software (version 4.5.2).

Results

Effect of Different Cultivation Strategies on Microalgal Growth

Cultivation strategy has a direct influence on microbial growth (Aziz et al., 2020). For this reason, *C. vulgaris* was cultivated under both photoautotrophic and photoheterotrophic conditions. Photoheterotrophic cultivation was further evaluated using two different carbon sources: glucose and CP. CP is an inexpensive and abundant by-product of the food industry and contains a considerable amount of reducing sugars (Yoon et al., 2005; Yu et al., 2013). Therefore, CP was selected as an alternative carbon source for the photoheterotrophic growth of *C. vulgaris*. A synthetic medium containing only glucose was used as a control.

The growth of *C. vulgaris* under different cultivation strategies is presented in Figure 1. According to the results, all cultivation conditions supported microalgal growth. The highest growth was observed under photoheterotrophic conditions with CP as the carbon source. Under this condition, the biomass concentration of *C. vulgaris* reached 0.46 g/L after 12 days. In comparison, growth reached 0.33 g/L under photoheterotrophic conditions with glucose, while the lowest biomass concentration of 0.21 g/L was observed under photoautotrophic cultivation. Interestingly, the initial microbial growth values under photoautotrophic cultivation, glucose containing photoheterotrophic, and CP-containing photoheterotrophic cultivations were 0.02, 0.03 and 0.07 g/L, respectively. The results indicate that photoheterotrophic cultivation with CP, resulted in significantly higher initial growth compared to other strategies. A plausible explanation for this observation is the differences inn pre-adaptation media, as cultivation under distinct conditions for 12 days may have led to variations in growth rates. In all experimental groups, microbial growth accelerated after 8 days and approached its maximum level by day 12. No significant increase in biomass was observed beyond this time point. Consequently, *C. vulgaris* growth experiments were terminated after 12 days.

Effect of Pretreatment on Reducing Sugar and Bioethanol Production

Pretreatment is a critical step for the release of fermentable sugars from microalgal biomass. The reducing sugar concentrations and bioethanol production obtained from *C. vulgaris* biomass subjected to different pretreatment methods (1% H_2SO_4 and 1% NaOH) are presented in Figure 2. According to the results, acid pretreatment yielded higher reducing sugar concentrations than alkali pretreatment. The highest initial reducing sugar

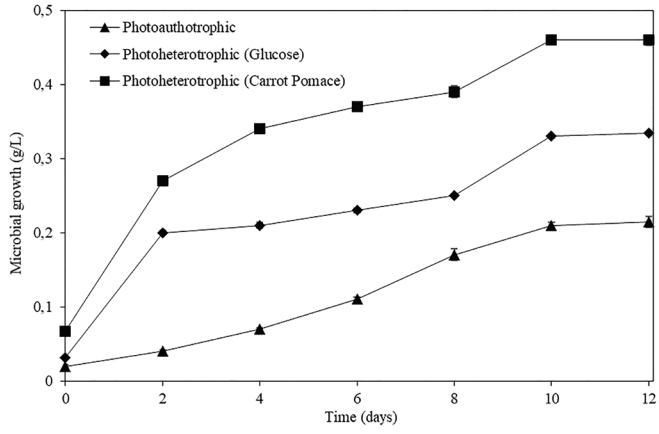

Figure 1. Effects of different carbon sources and cultivation conditions on microalgal growth (BG-11 medium; 0.5 g/L glucose; 0.5 g/L carrot pomace sugar; 2400 lx; 30 °C; pH:7; incubation time, 12 days).

concentration was achieved with 1% H_2SO_4 (9.98 g/L), whereas the lowest concentration was observed following 1% NaOH pretreatment (6.86 g/L).

In parallel with reducing sugar concentrations, the highest bioethanol production was obtained from biomass pretreated with 1% H_2SO_4, reaching 3.29 g/L at 12 h of fermentation. In contrast, bioethanol production decreased to 2.93 g/L when 1% NaOH pretreatment was applied. The kinetic parameters calculated for the different pretreatment methods are shown in Table 1. The highest theoretical bioethanol yield (72.95%) was observed for biomass pretreated with 1% NaOH, which can be attributed to the lower initial reducing sugar concentration compared to acid-pretreated biomass. Conversely, the lowest theoretical yield (65.10%) was obtained following 1% H_2SO_4 pretreatment. However, biomass pretreated with 1% H_2SO_4 exhibited higher volumetric ethanol productivity (Q_p) and ethanol yield (Y_p/s) than biomass treated with 1% NaOH. The maximum Q_p and Y_p/s values for 1% H_2SO_4 were 0.26 g/L·h and 0.49 g/g, respectively, whereas these values decreased to 0.24 g/L·h and 0.45 g/g, respectively, for 1% NaOH pretreatment.

Effects of Initial Biomass Loading on Sugar Concentrations and Ethanol Production

Initial biomass loading is a critical parameter influencing fermentation performance. In this study, the effects of three different initial biomass loadings (50, 100, and 200 g/L) on bioethanol production by *C. boidinii* were evaluated. Prior to fermentation, *C. vulgaris* biomass was pretreated with 1% H_2SO_4 at 121 °C for 15 min.

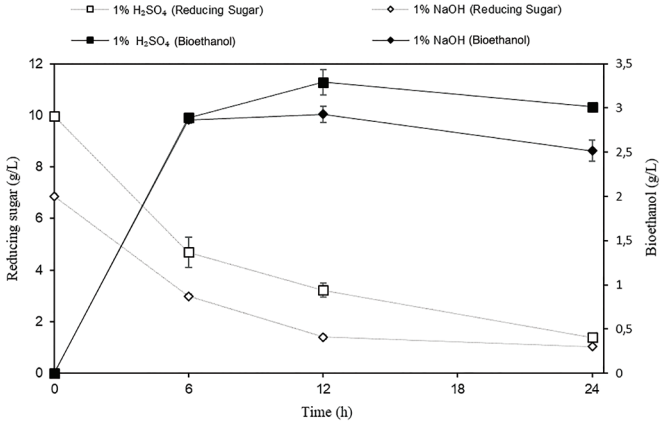

Figure 2. Effects of different pretreatment methods from *C. vulgaris* biomass (initial biomass loading: 50 g/L, pretreatments: 1% H_2SO_4 and 1% NaOH, 121 °C, 15 min, pH: 5, T: 30 °C).

The reducing sugar concentrations obtained from increasing *C. vulgaris* biomass loadings are presented in Table 2. The results indicate that higher biomass loadings led to increased reducing sugar concentrations. The maximum reducing sugar concentration was observed at a biomass loading of 200 g/L biomass (16.23 g/L), whereas the lowest concentration was detected at 50 g/L (9.98 g/L). An intermediate reducing sugar concentration of 13.03 g/L was obtained ata biomass loading of 100 g/L.

In parallel with reducing sugar concentrations, the highest bioethanol concentration was achieved at a biomass loading of 200 g/L biomass (3.89 g/L), while the lowest concentration was obtained at 50 g/L (3.29 g/L) after 12 hours of fermentation (Figure 3). At an initial biomass loading of 100 g/L, *C. boidinii* produced 3.32 g/L bioethanol. The results demonstrate that both reducing sugar and ethanol concentrations increased proportionally with increasing biomass loading. Moreover, high biomass loading (200 g/L) did not inhibit microbial growth or bioethanol production, as the reducing sugar concentrations remained below the tolerance limit of *C. boidinii* (Velazquez-Lucio et al., 2018).

Kinetic parameters associated with the different biomass loadings are summarized in Table 2. Although bioethanol concentrations increased with increasing biomass loading, the maximum theoretical bioethanol yield decreased from 65.10% to 47.39% as the biomass loading increased from 50 g/L to 200 g/L. From the highest biomass loading (200 g/L), the maximum volumetric ethanol productivity (Q_p) and bioethanol yield (Y_p/s) were 0.32 g/L·h and 0.35 g/g, respectively.

Effects of Different Supplements on Sugar Consumption and Bioethanol Production

Mineral salts and nitrogen sources are key factors influencing microbial growth and bioethanol production. In this study, two different fermentation media were evaluated for their effect on *C. boidinii* fermentation. Medium 1 contained 5 g/L peptone, 3 g/L yeast extract, 0.5 g/L $MgSO_4 \cdot 7H_2O$, 1 g/L KH_2PO_4, 0.1 g/L $CaCl_2 \cdot 2H_2O$, and 0.05 g/L $ZnSO_4 \cdot 7H_2O$ as nitrogen and mineral sources. Medium 2 contained 1 g/L yeast extract, 0.4 g/L KH_2PO_4, and 0.2 g/L NH_4Cl as organic and inorganic nitrogen and mineral sources.

Both media positively influenced the fermentation performance of *C. boidinii*. However, Medium 1 resulted in 1.06 fold higher bioethanol concentrations compared to Medium 2. The maximum bioethanol concentration achieved in this study was 4.54 g/L in Medium 1, whereas a concentration of 4.29 g/L was obtained in Medium 2 (Figure 4).

Table 1. Kinetic parameters of *C. boidinii* fermentation under different pretreatment conditions (initial *C. vulgaris* biomass: 50 g/L; pretreatments: 1% H_2SO_4 and 1% NaOH, 121 °C for 15 min; pH 5; incubation temperature: 30 °C).

Pretreatment	Maximum bioethanol (g/L)$_{12h}$	Theoretical yield (%)$_{12h}$	Q_P (g/L.h)$_{12h}$	$Y_{P/S}$ (g/g)$_{12h}$
1% H_2SO_4	$3.29^a \pm 0.14$	$65.10^a \pm 2.80$	$0.26^a \pm 0.01$	$0.49^a \pm 0.01$
1% NaOH	$2.93^b \pm 0.09$	$72.95^b \pm 2.29$	$0.24^b \pm 0.01$	$0.45^b \pm 0.02$

*Different superscript letters within the same column indicates statistically significant difference ($p < 0.05$).

Theoretical ethanol yields were higher for both supplemted media compared to the unsupplemented 200 g/L biomass condition (47.39%), reaching 54.74% and 51.73% for Medium 1 and Medium 2, respectively (Table 3). A similar trend was observed for reducing sugar consumption. In the unsupplemented 200 g/L biomass, the reducing sugar concentration was 5.04 g/L after 12 hours of fermentation, whereas concentrations decreased to 4.26 g/L and 4.24 g/L in the presence of Medium 1 and Medium 2, respectively.

Discussion

Experiments were conducted under different cultivation conditions, including photoautotrophic cultivation, photoheterotrophic cultivation with 0.5 g/L glucose, and photoheterotrophic cultivation with 0.5 g/L CP. The growth performance of *C. vulgaris* varied significantly among these conditions, with the highest biomass accumulation observed under photoheterotrophic cultivation supplemented with CP-derived sugars.

Previous studies have reported that the presence of organic carbon sources in growth media can increase microalgae growth (Abreu et al., 2012; Park et al., 2014). In the present study, microalgal growth under photoheterotrophic conditions was approximately 2.2-fold higher than that under photoautotrophic conditions after 12 days of incubation. Similarly, Grama et al. (2016) reported that *Dactylococcus* sp. cultivated under photoheterotrophic conditions exhibited 43% higher growth under photoautotrophic conditions. Although both CP- and glucose-supplemented photoheterotrophic media contained the same initial reducing sugar concentrations (0.5 g/L), higher microbial growth was observed in the CP-containing medium. This difference may be attributed to additional growth-promoting components present in CP, such as minerals and vitamins, which may stimulate *C. vulgaris* growth. Based on these findings, CP was selected as a cost-effective raw material for further studies.

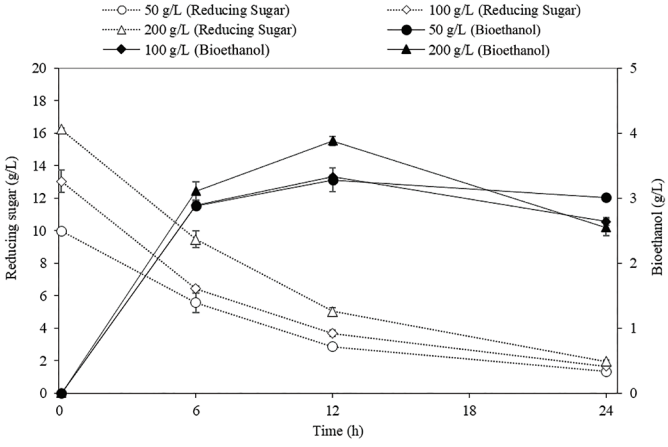

Figure 3. Effects of different *C. vulgaris* biomass loadings on bioethanol production and reducing sugar consumption by *C. boidinii* (pretreatment: 1% H_2SO_4 at 121 °C for 15 min).

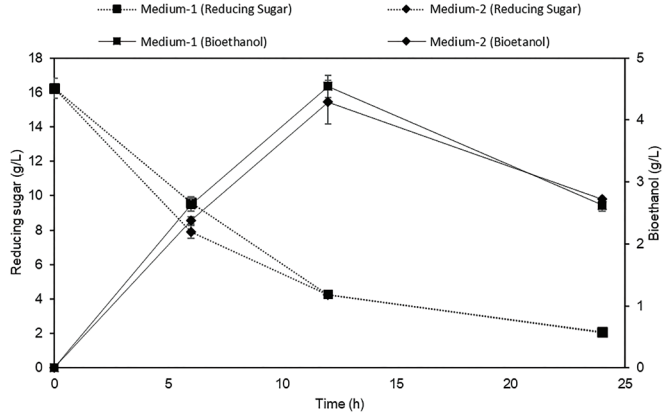

Figure 4. Bioethanol production and reducing sugar consumption by C. boidinii in the presence of different supplement media using 200 g/L initial C. vulgaris biomass (pretreatment: 1% H_2SO_4, 121 °C, 15 min, pH: 5, Medium 1: 5 g/L peptone, 3 g/L yeast extract, 0.5 g/L $MgSO_4.7H_2O$, 1 g/L KH_2PO_4, 0.1 g/L $CaCl_2.2H_2O$, and 0.05 g/L $ZnSO_4$. $7H_2O$, Medium 2; 1 g/L yeast extract, 0.4 g/L KH_2PO_4, and 0.2 g/L NH_4Cl, T: 30 °C).

Table 2. Bioethanol production by *C. boidinii* at three different initial *C. vulgaris* biomass loadings (pretreatment: 1% H_2SO_4 at 121 °C for 15 min).

Biomass loading	Reducing sugar $(g/L)_h$	Maximum bioethanol $(g/L)_{12h}$	Theoretical yield $(\%)_{12h}$	Q_P $(g/L.h)_{12h}$	$Y_{P/S}$ $(g/g)_{12h}$
50 g/L	$9.98^a \pm 0.12$	$3.29^a \pm 0.14$	$65.10^a \pm 2.80$	$0.26^a \pm 0.01$	$0.49^a \pm 0.01$
100 g/L	$13.03^b \pm 0.70$	$3.32^a \pm 0.01$	$50.31^b \pm 0.42$	$0.28^b \pm 0.002$	$0.35^b \pm 0.005$
200 g/L	$16.23^c \pm 0.10$	$3.89^b \pm 0.05$	$47.39^b \pm 0.34$	$0.32^b \pm 0.002$	$0.35^b \pm 0.01$

*Different superscript letters within the same column indicates statistically significant differences.

Table 3. Effect of different media compositions on bioethanol production by *C. boidinii* (initial biomass loading: 200 g/L *C. vulgaris*, pretreatment: 1% H_2SO_4, 121 °C, 15 min, pH: 5, Medium 1: 5 g/L peptone, 3 g/L yeast extract, 0.5 g/L $MgSO_4.7H_2O$, 1 g/L KH_2PO_4, $CaCl_2.2H_2O$, and 0.05 g/L $ZnSO_4.7H_2O$. Medium 2: 1 g/L yeast extract, 0.4 g/L KH_2PO_4 and 0.2 g/L NH_4Cl, T: 30 °C).

	Reducing sugar (g/L)	Maximum bioethanol $(g/L)_{12h}$	Theoretical yield $(\%)_{12h}$	Q_P $(g/L.h)_{12h}$	$Y_{P/S}$ $(g/g)_{12h}$
Medium 1	$16.23^a \pm 0.10$	$4.54^a \pm 0.18$	$54.74^a \pm 2.13$	$0.38^a \pm 0.01$	$0.38^a \pm 0.01$
Medium 2	$16.23^a \pm 0.10$	$4.29^a \pm 0.35$	$51.73^a \pm 4.26$	$0.36^a \pm 0.02$	$0.36^a \pm 0.03$

*Different superscript letters within the same column indicate statistically significant differences.

Different pretreatment methods (1% H_2SO_4 and 1% NaOH) were evaluated for their effectiveness in releasing fermentable sugars from *C. vulgaris* biomass cultivated on CP. The results indicated that pretreatment method significantly influenced fermentable sugar release and subsequent bioethanol production. Acid pretreatment more effectively disrupted the microalgal cell wall more by hydrolyzing hemicellulose and cellulose and degrading starch into smaller molecules. In contrast, alkali pretreatment primarily reduced polymer size without comparable sugar release (Kusmiyati et al., 2022; Purewal et al., 2023). The superior performance of acid pretreatment observed in this study is consistent with previous reports. Ngamsirisomsakul et al. (2019) reported a reducing sugar concentration of 6.50 g/L from acid-pretreated *C. vulgaris* biomass, while El-Souod et al. (2021) achieved 24.77 g per 100 g of dried biomass. In the present study, acid pretreatment (1% H_2SO_4) resulted in higher reducing sugar concentrations and bioethanol productivity than 1% NaOH, despite yielding a slightly lower theoretical ethanol yield. These findings suggest that acid pretreatment is more effective for maximizing sugar release and ethanol production. Therefore, *C. vulgaris* biomass pretreated with 1% H_2SO_4 at 121 °C for 15 minutes was selected for further experiments.

The results also demonstrate that increasing the initial biomass loading enhanced both sugar release and bioethanol production. Higher biomass loadings provided a greater amount of fermentable substrate, leading to elevated ethanol titers. Although the theoretical ethanol yield decreased at higher biomass loadings, the highest overall bioethanol concentration was achieved at 200 g/L biomass. This suggests that the sugar concentrations generated remained within the tolerance limits of *C. boidinii*, allowing efficient fermentation (Osawa et al., 2009; Velazquez-Lucio et al., 2018). Previous studies have confirmed the suitability of *C. vulgaris* as a feedstock for bioethanol production. Ngamsirisomsakul et al. (2019) reported that *S. cerevisiae* TISTR 5339 produced 5.62 g/L bioethanol from acid-pretreated *C. vulgaris* biomass containing 18 g/L sugar. Similarly, de Farias Silva and Bertucco (2017) achieved 4.97 g/L bioethanol from 100 g/L *C. vulgaris* biomass. Collectively, these findings indicate that an initial biomass loading of 200 g/L provides the highest ethanol concentration without inhibiting microbial activity, making it optimal for subsequent experiments.

Nitrogen sources and mineral salts were found to positively influence fermentation performance and accelerate sugar consumption. Although both fermentation media contained identical initial sugar concentrations, Medium 1 resulted in slightly higher bioethanol production. This enhancement can be attributed to additional supplements such as peptone, magnesium, calcium, and zinc. Minerals, especially magnesium, function as essential cofactors in key metabolic pathways such as glycolysis (Somda et al., 2011; Stehlik-Tomas et al., 2004). Similar beneficial effects of minerals and nitrogen supplementation on microbial growth and fermentation efficacy have been reported in previous studies (de Souza et al., 2016; Rees & Stewart, 1997). These findings confirm that appropriate supplementation with nitrogen and mineral salts improves ethanol production and accelerates fermentable sugar utilzation during *C. boidinii* fermentation.

Conclusion

In the present study, the effects of different cultivation conditions on *C. vulgaris* growth were optimized, and the influences of pretreatment method, initial biomass loading, and medium composition on bioethanol production by *C. boidinii* were investigated. Photoheterotrophic cultivation uisng CP promoted superior microalgal growth, while acid pretreatment resulted in higher fermentable sugar concentrations compared to alkali pretreatment. Increaing the highest ethanol titer achieved at 200 g/L biomass. Moreover, optimization of the fermentation medium increased bioethanol production by *C. boidinii* to 4.54 g/L. Under these conditions, the bioethanol yield and volumetric productivity reached 0.38 g/g and 0.38 g/L.h, respectively, after 12 h of fermentation. The current work demonstrates that photoheterotrophic cultivation with CP supports microalgal growth. Moreover, *C. vulgaris* is a suitable feedstock for third-generation bioethanol production, and *C. boidinii* was shown to effectively convert microalgal-derived fermentable sugars for ethanol fermentation.

Ethics

Ethics Committee Approval: Not required.

Data Sharing Statement: All data are available within the study.

Footnotes

Authorship Contributions: Conceptualization: S.E.K.; Design methodology: S.E.K.; Execution/investigation: S.E.K.; Resources/materials: S.E.K. and G.D.; Resources/materials: G.D.; Data acquisition: A.K.Y. and M.K.; Data analysis/interpretation: S.E.K.; Writing – original draft: A.K.Y. and S.E.K.; Writing – review & editing/critical revision: A.K.Y., M.K., G.D., and S.E.K.

Conflict of Interest: The author(s) have no conflicts of interest to declare.

Funding: This work was supported by the Ankara University Research Foundation (Project Number: FDK-2022-2400 and FYL-2022-2534).

References

Abreu, A. P., Fernandes, B., Vicente, A. A., Teixeira, J., & Dragone, G. (2012). Mixotrophic cultivation of *Chlorella vulgaris* using industrial dairy waste as organic carbon source. *Bioresource Technology, 118*, 61–66. https://doi.org/10.1016/j.biortech.2012.05.055

Acebu, P. I. G., de Luna, M. D. G., Chen, C. Y., Abarca, R. R. M., Chen, J. H., & Chang, J. S. (2022). Bioethanol production from *Chlorella vulgaris* ESP-31 grown in unsterilized swine wastewater. *Bioresource Technology, 352*, 127086. https://doi.org/10.1016/j.biortech.2022.127086

Agwa, O. K., Nwosu, I. G., & Abu, G. O. (2017). Bioethanol production from *Chlorella vulgaris* biomass cultivated with plantain (*Musa paradisiaca*) peels extract. *Advances in Bioscience and Biotechnology, 8*(12), 478–489. https://doi.org/10.4236/abb.2017.812035

Aziz, M. M. A., Kassim, K. A., Shokravi, Z., Jakarni, F. M., Liu, H. Y., Zaini, N., & Shokravi, H. (2020). Two-stage cultivation strategy for simultaneous increases in growth rate and lipid content of microalgae: A review. *Renewable and Sustainable Energy Reviews, 119*, 109621. https://doi.org/10.1016/j.rser.2019.109621

Barzee, T. J., El-Mashad, H. M., Zhang, R., & Pan, Z. (2019). Carrots. *In* Z. Pan, R. Zhang, & H. M. El-Mashad (Eds.), *Integrated processing technologies for food and agricultural by-products* (pp. 297–330). Academic Press. https://doi.org/10.1016/B978-0-12-814138-0.00012-5

Caetano, P. A., do Nascimento, T. C., Fernandes, A. S., Nass, P. P., Vieira, K. R., Junior, M. R. M., & Zepka, L. Q. (2022). Microalgae-based polysaccharides: Insights on production, applications, analysis, and future challenges. *Biocatalysis and Agricultural Biotechnology, 43*, 102491. https://doi.org/10.1016/j.bcab.2022.102491

Camiolo, S., Porru, C., Benítez-Cabello, A., Rodríguez-Gómez, F., Calero-Delgado, B., Porceddu, A., Budroni, M., Mannazzu, I., Jiménez-Díaz, R., & Arroyo-López, F. N. (2017). Genome overview of eight *Candida boidinii* strains isolated from human activities and wild environments. *Standards in Genomic Sciences, 12*, Article 70. https://doi.org/10.1186/s40793-017-0281-z

da Silva Almeida, L. E., & de Assis, S. A. (2024). Application of immobilized β-glucosidase from *Candida boidinii* in the hydrolysis of delignified sugarcane bagasse. *Indian Journal of Microbiology, 64*(2), 650–670. https://doi.org/10.1007/s12088-024-01223-8

de Farias Silva, C. E., & Bertucco, A. (2017). Dilute acid hydrolysis of microalgal biomass for bioethanol production: An accurate kinetic model of biomass solubilization, sugars hydrolysis and nitrogen/ash balance. *Reaction Kinetics, Mechanisms and Catalysis, 122*(2), 1095–1114. https://doi.org/10.1007/s11144-017-1271-2

de Souza, R. B., Silva, R. K., Ferreira, D. S., Junior, S. D. S. L. P., de Barros Pita, W., & de Morais Junior, M. A. (2016). Magnesium ions in yeast: Setting free the metabolism from glucose catabolite repression. *Metallomics, 8*(11), 1193–1203. https://doi.org/10.1039/c6mt00157b

Demiray, E., Karatay, S. E., & Dönmez, G. (2020). Efficient bioethanol production from pomegranate peels by newly isolated *Kluyveromyces marxianus*. *Energy Sources, Part A: Recovery, Utilization, and Environmental Effects, 42*(6), 709–718. https://doi.org/10.1080/15567036.2019.1600621

Dutta, K., Daverey, A., & Lin, J. G. (2014). Evolution retrospective for alternative fuels: First to fourth generation. *Renewable Energy*, *69*, 114–122. https://doi.org/10.1016/j.renene.2014.02.044

El-Souod, A., Ghada, W., Morsy, E. M., Hassan, L. H., & El-Sheekh, M. M. (2021). Efficient saccharification of the microalga *Chlorella vulgaris* and its conversion into ethanol by fermentation. *Iranian Journal of Science and Technology, Transactions A: Science, 45*(3), 767–774. https://doi.org/10.1007/s40995-021-01097-1

Fehér, A., Bedő, S., & Fehér, C. (2021). Comparison of enzymatic and acidic fractionation of corn fiber for glucose-rich hydrolysate and bioethanol production by *Candida boidinii*. *Periodica Polytechnica Chemical Engineering, 65*(3), 320–330. https://doi.org/10.3311/PPch.17431

Grama, B. S., Agathos, S. N., & Jeffryes, C. S. (2016). Balancing photosynthesis and respiration increases microalgal biomass productivity during photoheterotrophy on glycerol. *ACS Sustainable Chemistry & Engineering, 4*(3), 1611–1618. https://doi.org/10.1021/acssuschemeng.5b01544

Jambo, S. A., Abdulla, R., Azhar, S. H. M., Marbawi, H., Gansau, J. A., & Ravindra, P. (2016). A review on third generation bioethanol feedstock. *Renewable and Sustainable Energy Reviews, 65*, 756–769. https://doi.org/10.1016/j.rser.2016.07.064

John, R. P., Anisha, G. S., Nampoothiri, K. M., & Pandey, A. (2011). Micro and macroalgal biomass: A renewable source for bioethanol. *Bioresource Technology, 102*(1), 186–193. https://doi.org/10.1016/j.biortech.2010.06.139

Kim, T. H., & Lee, Y. Y. (2007). Pretreatment of corn stover by soaking in aqueous ammonia at moderate temperatures. In *Applied Biochemistry and Biotechnology: The Twenty-Eighth Symposium Proceedings of the Twenty-Eighth Symposium on Biotechnology for Fuels and Chemicals Held April 30–May 3, 2006, in Nashville, Tennessee* (pp. 81–92). Humana Press. https://doi.org/10.1007/s12010-007-9041-7

Kiran, E. U., Trzcinski, A. P., Ng, W. J., & Liu, Y. (2014). Bioconversion of food waste to energy: A review. *Fuel*, *134*, 389–399. https://doi.org/10.1016/j.fuel.2014.05.074

Kusmiyati, K., Hadiyanto, H., & Fudholi, A. (2022). Treatment updates of microalgae biomass for bioethanol production: A comparative study. *Journal of Cleaner Production, 350*, 135236. https://doi.org/10.1016/j.jclepro.2022.135236

Lavanya, A. K., Sharma, A., Choudhary, S. B., Sharma, H. K., Nain, P. K. S., Singh, S., & Nain, L. (2020). Mesta (*Hibiscus* spp.) – A potential feedstock for bioethanol production. *Energy Sources, Part A: Recovery, Utilization, and Environmental Effects*, *42*(21), 2664–2677. https://doi.org/10.1080/15567036.2019.1618980

Medipally, S. R., Yusoff, F. M., Banerjee, S., & Shariff, M. (2015). Microalgae as sustainable renewable energy feedstock for biofuel production. *BioMed Research International*, *2015*, 1–13. https://doi.org/10.1155/2015/519513

Miller, G. L. (1959). Use of dinitrosalicylic acid reagent for determination of reducing sugar. *Analytical Chemistry, 31*(3), 426–428. https://doi.org/10.1021/ac60147a030

Ngamsirisomsakul, M., Reungsang, A., Liao, Q., & Kongkeitkajorn, M. B. (2019). Enhanced bio-ethanol production from *Chlorella* sp. biomass by hydrothermal pretreatment and enzymatic hydrolysis. *Renewable Energy, 141*, 482–492. https://doi.org/10.1016/j.renene.2019.04.008

Osawa, F., Fujii, T., Nishida, T., Tada, N., Ohnishi, T., Kobayashi, O., & Yoshida, S. (2009). Efficient production of L-lactic acid by Crabtree-negative yeast *Candida boidinii*. *Yeast, 26*(9), 485–496. https://doi.org/10.1002/yea.1702

Panwar, N. L., Kaushik, S. C., & Kothari, S. (2011). Role of renewable energy sources in environmental protection: A review. *Renewable and Sustainable Energy Reviews*, *15*(3), 1513–1524. https://doi.org/10.1016/j.rser.2010.11.037

Park, W. K., Moon, M., Kwak, M. S., Jeon, S., Choi, G. G., Yang, J. W., & Lee, B. (2014). Use of orange peel extract for mixotrophic cultivation of *Chlorella vulgaris*: Increased production of biomass and FAMEs. *Bioresource Technology, 171*, 343–349. https://doi.org/10.1016/j.biortech.2014.08.109

Purewal, S. S., Verma, P., Kaur, P., Sandhu, K. S., Singh, R. S., Kaur, A., & Salar, R. K. (2023). A comparative study on proximate composition, mineral profile, bioactive compounds and antioxidant properties in diverse carrot (*Daucus carota* L.) flour. *Biocatalysis and Agricultural Biotechnology, 47*, 102640. https://doi.org/10.1016/j.bcab.2023.102640

Rees, E. M., & Stewart, G. G. (1997). The effects of increased magnesium and calcium concentrations on yeast fermentation performance in high gravity worts. *Journal of the Institute of Brewing, 103*(5), 287–291. https://doi.org/10.1002/j.2050-0416.1997.tb00958.x

Rippka, R. (1988). Isolation and purification of cyanobacteria. *Methods in Enzymology, 167*, 3–27. https://doi.org/10.1016/0076-6879(88)67004-2

Roca, C., & Olsson, L. (2003). Increasing ethanol productivity during xylose fermentation by cell recycling of recombinant *Saccharomyces cerevisiae*. *Applied Microbiology and Biotechnology, 60*, 560–563. https://doi.org/10.1007/s00253-002-1147-9

Roy, P., Mohanty, A. K., Dick, P., & Misra, M. (2023). A review on the challenges and choices for food waste valorization: Environmental and economic impacts. *ACS Environmental Au, 3*(2), 587–615. https://doi.org/10.1021/acsenvironau.2c00050

Sarkar, D., & Shimizu, K. (2015). An overview on biofuel and biochemical production by photosynthetic microorganisms with understanding of the metabolism and by metabolic engineering together with efficient cultivation and downstream processing. *Bioresources and Bioprocessing, 2*(1), 1–19. https://doi.org/10.1186/s40643-015-0045-9

Selvakumar, P., & Umadevi, K. (2014). Enhanced lipid and fatty acid content under photoheterotrophic condition in the mass cultures of *Tetraselmis gracilis* and *Platymonas convolutae*. *Algal Research, 6*, 180–185. https://doi.org/10.1016/j.algal.2014.10.002

Somda, M., Savadogo, A., Barro, N., Thonart, P., & Traore, A. (2011). Effect of mineral salts in fermentation process using mango residues as carbon source for bioethanol production. *Asian Journal of Industrial Engineering, 3*(1), 1–10. https://doi.org/10.3923/ajie.2011.29.38

Srilatha, K., Bhagawan, D., & Himabindu, V. (2019). Pyrolysis of garden waste: Comparative study of *Leucaena leucocephala* (Subabul leaves) and *Azadirachta indica* (Neem leaves) wastes. In *Waste valorisation and recycling* (pp. 293–306). Springer, Singapore. https://doi.org/10.1007/978-981-13-2784-1_28

McHargue, J. S., & Calfee, R. K. (1931). Effect of manganese, copper and zinc on the growth of yeast. *Plant Physiology, 6*(3), 559. https://doi.org/10.1104/pp.6.3.559

Tandon, P., & Jin, Q. (2017). Microalgae culture enhancement through key microbial approaches. *Renewable and Sustainable Energy Reviews, 80*, 1089–1099. https://doi.org/10.1016/j.rser.2017.05.260

Velazquez-Lucio, J., Rodríguez-Jasso, R. M., Colla, L. M., Sáenz-Galindo, A., Cervantes-Cisneros, D. E., Aguilar, C. N., & Ruiz, H. A. (2018). Microalgal biomass pretreatment for bioethanol production: A review. *Renewable and Sustainable Energy Reviews, 94*, 34–48. https://doi.org/10.18331/BRJ2018.5.1.5

Wistara, N. J., Pelawi, R., & Fatriasari, W. (2016). The effect of lignin content and freeness of pulp on the bioethanol productivity of Jabon wood. *Waste and Biomass Valorization, 7*, 1141–1146. https://doi.org/10.1007/s12649-016-9510-8

Yamaoka, C., Kurita, O., & Kubo, T. (2014). Improved ethanol tolerance of *Saccharomyces cerevisiae* in mixed cultures with *Kluyveromyces lactis* on high-sugar fermentation. *Microbiological Research, 169*(12), 907–914. https://doi.org/10.1016/j.micres.2014.04.007

Yoon, K. Y., Cha, M., Shin, S. R., & Kim, K. S. (2005). Enzymatic production of a soluble-fibre hydrolyzate from carrot pomace and its sugar composition. *Food Chemistry, 92*, 151–157. https://doi.org/10.1016/j.foodchem.2004.07.014

Yu, C. Y., Jiang, B. H., & Duan, K. J. (2013). Production of bioethanol from carrot pomace using the thermotolerant yeast *Kluyveromyces marxianus*. *Energies, 6*(3), 1794–1801. https://doi.org/10.3390/en6031794

Yu, K. L., Chen, W. H., Sheen, H. K., Chang, J. S., Lin, C. S., Ong, H. C., & Ling, T. C. (2020). Bioethanol production from acid pretreated microalgal hydrolysate using microwave-assisted heating wet torrefaction. *Fuel, 279*, 118435. https://doi.org/10.1016/j.fuel.2020.118435

Yücel, H. G., & Aksu, Z. (2015). Ethanol fermentation characteristics of *Pichia stipitis* yeast from sugar beet pulp hydrolysate: Use of new detoxification methods. *Fuel, 158*, 793–799. https://doi.org/10.1016/j.fuel.2015.06.016

Trakya University Journal of Natural Sciences, 27(1), 76–87, 2026
DOI: 10.23902/trkjnat.2025108
www.tujns.org

Research Article

Seasonal changes in river water pollution levels induce oxidative stress and DNA damage in human keratinocytes

Nebiye Pelin Türker*, Pınar Altınoluk Mimiroğlu

Trakya University, Technology Research and Development Centre, Edirne, Türkiye

Cite this article as: Türker, N. P., & Altınoluk Mimiroğlu, P. (2026). Seasonal changes in river water pollution levels induce oxidative stress and DNA damage in human keratinocytes. *Trakya University Journal of Natural Sciences, 27*(1), 76–87. https://doi.org/10.23902/trkjnat.2025108

Abstract

Background: Seasonal heavy metal pollution of river waters poses a significant risk to environmental and human health; yet its biological effects are often insufficiently characterized.

Aims: The aim of this study was to investigate the seasonal variations in river water pollution and to evaluate the associated cytotoxic, oxidative, and genotoxic effects of these waters on human keratinocytes using an integrated *in vitro* approach.

Methods: This study collected river water samples during the four seasons and evaluated their cytotoxic and genotoxic impacts in human keratinocytes using an integrated *in vitro* approach. The cells were exposed to the samples for 24 and 48 h. Cytotoxicity was assessed via the 3-(4,5-dimethylthiazol-2-yl)-2,5 diphenyl tetrazolium bromide assay, elemental accumulation by inductively coupled plasma–mass spectrometry, and oxidative and genotoxic responses by assessing reactive oxygen species (ROS) and 8-hydroxy-2′-deoxyguanosine (8-OHdG) levels.

Results: All samples induced time- and season-dependent cytotoxicity, whereas control cells were unaffected. Autumn-collected samples exhibited the maximal cytotoxicity, with cell mortality ranging from 38.94% to 80.09% at 24 h and increasing to 56.97%–81.03% at 48 h. Spring-collected samples induced the second-highest lethality, with cell death reaching ≤90.03% at 48 h. Enhanced cytotoxicity was associated with elevated cellular levels of Fe, Al, Cr, Ni, Ca, and Sr at 24 h and Ti, Mn, Zn, Cu, and P at 48 h, indicating rapid uptake and delayed accumulation patterns. River water exposure also significantly increased ROS generation ($p < 0.005$) and 8-OHdG

Özet

Dayanak: Nehir sularının mevsimsel ağır metal kirliliği, çevre ve insan sağlığı için önemli bir risk oluşturmaktadır ancak biyolojik etkileri genellikle yeterince tanımlanmamıştır.

Amaçlar: Bu çalışmanın amacı, nehir suyu kirliliğindeki mevsimsel değişimleri araştırmak ve bu suların insan keratinositleri üzerindeki ilişkili sitotoksik, oksidatif ve genotoksik etkilerini bütünleşik bir *in vitro* yaklaşım kullanarak değerlendirmektir.

Yöntemler: Bu çalışmada, dört mevsim boyunca nehir suyu örnekleri toplanmış ve entegre bir *in vitro* yaklaşım kullanılarak insan keratinositlerinde sitotoksik ve genotoksik etkileri değerlendirilmiştir. Hücreler, 24 ve 48 saat boyunca örneklerle temas ettirilmiştir. Sitotoksisite, 3-(4,5-dimetiltiazol-2-il)-2,5-difeniltetrazolyum bromür testi ile, element birikimi indüktif eşleşmiş plazma–kütle spektrometrisi ile ve oksidatif ve genotoksik tepkiler reaktif oksijen türleri (ROS) ve 8-hidroksi-2′-deoksiguanozin (8-OHdG) düzeyleri değerlendirilerek ölçülmüştür.

Bulgular: Tüm numuneler zamana ve mevsime bağlı sitotoksisiteye neden olurken, kontrol hücreleri etkilenmemiştir. Sonbaharda toplanan numuneler maksimum sitotoksisite göstermiş, hücre ölüm oranı 24 saatte %38,94 ile %80,09 arasında değişmiş ve 48 saatte %56,97 ile %81,03'e yükselmiştir. İlkbaharda toplanan örnekler, 48 saatte hücre ölümünün ≤%90,03'e ulaşmasıyla ikinci en yüksek ölüm oranını indükledi. Artan sitotoksisite, 24 saatte Fe, Al, Cr, Ni, Ca ve Sr ve 48 saatte Ti, Mn, Zn, Cu ve P hücre seviyelerindeki artışla ilişkiliydi, bu da hızlı alım ve gecikmiş birikim modellerini gösteriyordu. Nehir suyuna maruz kalma, özellikle sonbahar ve ilkbahar örneklerinde,

Edited by: *Bülent Yorulmaz*
***Corresponding Author:** Nebiye Pelin Türker, **E-mail:** npelinturker@trakya.edu.tr*
***ORCID iDs of the author(s):** NPT. 0000-0001-6060-3557; PAM. 0000-0002-8524-0972*

Received: 28 October 2025, **Accepted:** 31 December 2025, **Epub:** 29 January 2026, **Published:** 24 April 2026

levels, particularly by autumn and spring samples, demonstrating cumulative oxidative DNA damage.

Conclusion: These findings indicate that seasonal river water pollution induces oxidative stress mediated cytotoxicity and genotoxicity in human keratinocytes. The study underscores the necessity of incorporating biological endpoints into routine water quality monitoring to better assess health risks associated with contaminated freshwater systems.

ROS oluşumunu ($p < 0,005$) ve 8-OHdG seviyelerini önemli ölçüde artırarak, kümülatif oksidatif DNA hasarını ortaya koydu.

Sonuç: Bu bulgular, nehir suyunun mevsimsel ağır metal kirliliğinin, insan keratinositlerinde oksidatif stres aracılı sitotoksisite ve genotoksisiteye neden olduğunu göstermektedir. Bu çalışma, kirlenmiş tatlı su sistemleriyle ilişkili sağlık risklerini daha iyi değerlendirmek için rutin su kalitesi izleme protokollerine biyolojik son noktaların dahil edilmesinin gerekliliğini vurgulamaktadır.

Keywords: River water quality, human keratinocyte cells, reactive oxygen species, oxidative DNA damage, seasonal variation

Introduction

Water pollution is a major environmental challenge driven by industrialization, agriculture, environmental factors, insufficient freshwater resources, and inadequate sewage treatment systems. Industrial activities constitute a dominant source of aquatic contamination, particularly effluents released from textile, food processing, pulp and paper, iron, and steel factories; distilleries and tanneries; and nuclear power plants (Chowdhary et al., 2019). These industries discharge wastewater containing volatile organic compounds, toxic chemicals, inorganic pollutants, and hazardous solvents, often without sufficient treatment. They also contaminate surface waters with heavy metals (HMs), the most prevalent being chromium, cadmium, and arsenic (Chen et al., 2019). For example, anthropogenic activities have resulted in extensive hexavalent chromium pollution in the central regions of the Loess Plateau, China (Ge et al., 2020). With accelerating urbanization, the volume and complexity of industrial wastewater discharges continue to increase (Wu et al., 2020).

Agricultural activities represent another significant contributor to water pollution, primarily through runoff containing organic waste, nitrogen-based fertilizers, and pesticides. Cropping systems release pesticides, soil sediments, nitrates, phosphates, salts, and pathogens into aquatic environments, degrading the ecosystem and posing potential risks to human health (Parris, 2011). Such pollution severely affects freshwater ecosystems (Moss, 2008) and poses additional concerns related to food safety and HM accumulation (Lu et al., 2015). In parallel, environmental factors can also influence water quality; elevated levels of trace elements, sodium, and salinity are associated with poor river water quality in regions such as the Loess Plateau (Xiao et al., 2019). In many developing countries, inadequate sewage treatment infrastructure and insufficient investment in water supply systems further exacerbate contamination-associated problems, enhancing the exposure to industrial chemicals, HMs, and algal toxins (Wu et al., 1999).

The impacts of contaminated water on human health are well documented, with polluted drinking and surface waters contributing to gastrointestinal, infectious, and chronic diseases worldwide. The use of water filtration systems or desalinated water in households markedly reduces the incidence of diarrheal diseases compared to untreated municipal water (Yassin et al., 2006). In contrast, the consumption of tap water is associated with an increase in gastrointestinal disorders (Payment et al., 1997). Beyond systemic health effects, recent research emphasizes that water pollution levels exhibit pronounced seasonal and spatial variability, which directly influences the concentrations of contaminants and associated risks. Hammoumi et al. (2024) reported significant seasonal quality fluctuations in the surface water of the Nador Canal; water quality was lower during the summer due to combined natural and anthropogenic factors, including agricultural runoff and industrial discharges. Similarly, in Anambra State, Nigeria, Amaechi et al. (2025) observed elevated levels of Cd, Pb, Zn, and Cu in river water during the dry season, primarily driven by industrial effluents, with a partial dilution of these contaminants occurring during the wet season. At the cell level, exposure to HM-contaminated water induces oxidative stress and inflammatory responses, leading to tissue damage and increasing susceptibility to chronic diseases. Kolawole et al. (2025) demonstrated that cadmium, lead, and arsenic induce a remarkable elevation in oxidative stress biomarkers and inflammatory mediators, underscoring a mechanistic link between environmental contamination and adverse biological outcomes. Water pollution is also associated with dermatological disorders, including melanosis, keratosis, hair loss, scabies, and skin cancer, particularly in populations using contaminated surface waters for drinking purposes. Chronic exposure to arsenic-contaminated water causes severe skin-related health effects (Kazi et al., 2009), while polluted rivers and industrial waters increase the incidence of scabies and skin cancer (Arif et al., 2020; Hanif et al., 2020). Meta-analyses further support the association between polluted aquatic environments and skin conditions such as erythema and pruritus (Fleisher & Kay, 2006; Yau et al., 2009).

Despite this extensive body of epidemiological and chemical evidence, experimental findings directly assessing the effects of river water samples on healthy human skin cells remain limited. A small number of *in vitro* studies have evaluated the biological toxicity of surface or river waters using aquatic organisms or non-human models. For instance, Amaechi et al. (2025) demonstrated season-dependent cytotoxic effects of river water samples on fish-derived cell lines, attributing toxicity to elevated HM loads, while genotoxic endpoints were not examined. Similarly, Hammoumi et al. (2024) assessed seasonal variations in surface water quality and reported reduced biological quality during summer months; however, their evaluation was restricted to physicochemical parameters without cell-based toxicity or DNA

damage analyses. Overall, existing *in vitro* investigations have predominantly focused on non-human models, have been limited to single locations or seasons, and have largely assessed cytotoxicity alone, leaving genotoxic outcomes and human-relevant dermal exposure risks insufficiently characterized. To address this gap, the present study focuses on the Meriç–Ergene River Basin, a region extensively impacted by industrial discharges, agricultural runoff, and urbanization. Water samples were collected from nine strategically selected stations along the Meriç, Ergene, and Tunca rivers to capture spatial variability, hydrological characteristics, and pollution gradients. Using a healthy human keratinocyte line, we evaluated the cytotoxic effects (on cell viability) and genotoxic potential of the collected samples. By integrating spatially distributed environmental sampling with human-relevant *in vitro* assays, this study provides biomonitoring-based evidence that directly links surface water pollution to potential dermal health risks, extending beyond conventional ecological or chemical assessments.

Materials and Methods

Sampling Stations and Transport of Samples

Water samples were collected from three major rivers the Meriç (Maritsa), Ergene, and Tunca rivers located in northwestern Türkiye. The Meriç River forms part of the border between Türkiye and Greece and flows southward into the Aegean Sea, while the Ergene and Tunca rivers are important tributaries draining agricultural and industrial regions before discharging into the Meriç River. At each station, water from underneath the surface was collected, against the flow, and stored in 2 L brown glass bottles. Samples were transported to the laboratory under cold-chain conditions. The sampling station locations are detailed in Table 1. *In situ* measurements of the routine physicochemical parameters of the water at each sampling station, including temperature (°C), pH, and electrical conductivity (µS/cm), were performed at the time of collection with a portable multi-parameter water quality meter calibrated according to the manufacturer's instructions. These parameters were recorded to characterize the prevalent environmental conditions at the time of sampling and support an interpretation of the findings of the subsequent biological and toxicological analyses.

Table 1. Sampling station details.

Rivers	Stations	Locations
Meriç River	Station 1 (M1)	41°39'44"N, 26°33'06"E
	Station 2 (M2)	41°37'32"N, 26°34'48"E
	Station 3 (M3)	41°29'12"N, 26°36'08"E
Ergene River	Station 1 (E1)	41°18'15"N, 27°26'40"E
	Station 2 (E2)	41°20'06"N, 26°55'19"E
	Station 3 (E3)	41°14'45"N, 26°37'04"E
Tunca River	Station 1 (T1)	41°45'34"N, 26°33'32"E
	Station 2 (T2)	41°41'08"N, 26°33'15"E
	Station 3 (T3)	41°40'02"N, 26°33'14"E

Cell Culture

Human keratinocyte cell line (HaCaT) was cultured in Dulbecco's Modified Eagle Medium: Ham's F-12 medium supplemented with 1% L-glutamine, 5% fetal bovine serum, and 1% penicillin/streptomycin. The cells were placed in a cell culture incubator and cultivated at 37 °C under 5% CO_2 and 95% humidity. They were subcultured upon reaching an 80%–90% confluency.

Cytotoxicity Determination via 3-(4,5-dimethylthiazol-2-yl)-2,5 diphenyl tetrazolium bromide (MTT) Assay

The cytotoxic impacts of river water on HaCaT cells were evaluated using the MTT assay. Cells were seeded in a 96-well plate at a density of 2×10^4 cells/well in 180 µL of medium. After incubation for 24 h, the cells were exposed to river water applied at nine concentrations: 100%, 50%, 25%, 12.5%, 6.25%, 3%, 1.5%, 0.75%, and 0.39%, for 24 and 48 h. Then, 20 µL of 5 mg/mL MTT solution (in phosphate-buffered saline) was added to each well. All experiments were conducted in four replicates (n = 4). The plates were incubated for another 2 h, and the formazan crystals formed were dissolved in 100–200 µL of dimethyl sulfoxide. The OD_{570} was measured, and cell viability and mortality were calculated by applying the formulae-formulas:

Viability (%) = (Experimental absorbance/Control absorbance) × 100

Mortality (%) = 100 – Viability (%)

Determination of Cell Elemental Concentrations Employing Inductively Coupled Plasma-Mass Spectrometry (ICP-MS)

HaCaT cells were seeded into 24-well culture plates at a density of 1×10^5 cells/well and incubated at 37 °C for 24 h in a humidified atmosphere containing 5% CO_2. Following cell attachment, the culture medium was replaced with river water samples, to which the cells were exposed for 24 and 48 h. These durations were selected based on the cytotoxicity thresholds determined via the MTT assay to avoid excessive cell death. After exposure, the cells were harvested and acid digested for elemental analyses with 65% ultrapure HNO_3 (trace metal grade), using a controlled combustion/digestion procedure until complete mineralization. Subsequently, the digested samples were diluted to appropriate volumes with ultrapure water before analysis. Cell elemental concentrations were quantified using a 7700 series ICP-MS (Agilent Technologies, Inc., CA, USA). Calibration curves were plotted using certified multi-element standard reference (high-purity) solutions in the range of 0–1000 ppb prepared by serial dilution. Calibration standards were used at five concentrations, covering the samples' expected range. Curve linearity was evaluated, and correlation coefficients (R^2) were verified to ensure acceptable performance levels. Quality control samples were employed to verify calibration validity and signal consistency before proceeding with sample measurements. Calibration standards were measured periodically to ensure analytical accuracy and instrument stability. Data obtained only under stabilized and calibrated conditions were included in the final analysis. Instrument operating parameters, including plasma conditions, nebulizer settings, and acquisition modes,

are detailed in Table 2. All samples were analyzed in triplicate (n = 3), and elemental levels were expressed as mean values. Statistical analyses were employed to identify elements with significant variations between experimental groups. Subsequently, principal component analysis (PCA) was applied to such elements to evaluate the patterns in elemental concentration variations and potential exposure duration-related clustering.

Table 2. ICP-MS parameters.

Instrument parameter	Operating conditions
Plasma gas	Argon, ultrahigh purity, 99.999%
Carrier gas	Helium, ultrahigh purity, 99.999%
Plasma gas pressure	500–700 kPa
Carrier gas pressure	90–130 kPa
Chiller temperature	18 °C
Carrier gas flow rate	1.05 L/min
Radio frequency power	1550 Watt
Radio frequency matching	1.80 V
Cones	Ni sampling cone for the X-lens
Nebulizer pump	0.1 rps

ICP-MS = inductively coupled plasma–mass spectrometry.

Assessment of Reactive Oxygen Species (ROS) Levels

HaCaT cells were seeded in 24-well plates at a density of 1×10^5 cells per well and incubated for 24 hours at 37 °C and under 5% CO_2. Water samples at toxic dosages (ascertained utilizing the MTT assay) were applied to the cells, and incubated for 24–48 h. Experiments were performed in three replicates (n = 3). The ROS levels of these cells were measured spectrophotometrically with a commercial ROS detection kit (Shanghai Sunred Biological Technology Co., Ltd., Shanghai, China); the assay procedure is outlined in Table 3. Statistical significance (Sig.) was evaluated using analysis of variance (ANOVA), followed by Student's t-test for pairwise comparisons. Differences between the mean ROS assay expression values obtained were assessed employing Student's t-test.

Table 3. Protocol for ROS detection using an ELISA kit.

Operation steps	Temperature/time
Standard preparation and reagents	-
Sample preparation	20 min, centrifuge the samples at 2000–3000 rpm
Adding enzyme-labeled antibodies to samples and standards	60 min, 37 °C
Washing process	5 × 100 µL
Adding the chromogenic reagents	10 min, 37 °C
Adding the stop solution	15 min, 50 µL
Measuring optical density values and calculations	Within 10 minutes, 450 nm was detected.

ELISA = Enzyme-Linked Immunosorbent Assay; ROS = reactive oxygen species.

Assessment of Oxidative DNA Damage using 8-Hydroxy-2′-Deoxyguanosine (8-OHdG) as a Biomarker

HaCaT cells were seeded in 24-well plates at a density of 1×10^5 cells per well and incubated for 24 h at 37 °C under 5% CO_2. DNA was extracted from the cells after exposure to toxic doses of contaminated river water for 24 and 48 h. Oxidative DNA damage was assessed utilizing reactions catalyzed by Nuclease P and phosphatase. Oxidative stress-related markers were quantified using liquid chromatography-tandem mass spectrometry (LC-MS/MS) on a Jet Stream 6460 Triple Quadrupole instrument (Agilent Technologies). The analysis parameters are provided in Table 4.

Table 4. Parameters of LC-MS/MS-based oxidative DNA damage analysis.

Mobile phase	A: Ultrapure water containing 5 mM ammonium formate B: Methanol containing 5 mM ammonium formate		
Column	Poroshell EC-C18 (3.0 × 150 mm, 3.5 Micron)		
Column temperature	35 °C		
Injection volume	5 µL		
Flow rate	0.6 mL/min		
Gradient program	**Time (min)**	**A (%)**	**B (%)**
	0.00	95.0	5.0
	0.70	95.0	5.0
	1.70	5.0	95.0
	4.50	5.0	95.0
	5.00	95.0	5.0
	10.00	95.0	5.0

LC-MS/MS = liquid chromatography-tandem mass spectrometry.

Statistical Analysis

Probit analysis was applied to the MTT assay results to determine the 50% lethal dose (LD_{50}), in accordance with the Turkish Standards Institute (TSE) and ISO 10993-5 guidelines. Prior to parametric analyses, the assumption of homogeneity of variances was assessed using Levene's test. When variance homogeneity was satisfied ($p > 0.05$), parametric tests were applied. Comparisons involving more than two groups (e.g., seasonal or station-based differences in cytotoxicity, ROS production, elemental accumulation, and 8-OHdG levels) were evaluated using one-way ANOVA. When significant differences were detected, Tukey's post hoc test was applied to identify pairwise group differences. In cases where the assumption of homogeneity of variances was violated, Welch's ANOVA followed by the Games–Howell post hoc test was used. Comparisons between two groups were performed using Student's t-test or Welch's t-test, as appropriate. PCA was used to explore patterns in ICP-MS-derived elemental profiles. Correlations between 8-OHdG levels were assessed using Pearson's or Spearman's correlation analyses, depending on data

distribution. Statistical analyses were performed using XLSTAT, GraphPad Prism, and SPSS v25.0. A $p < 0.05$ was considered statistically significant.

Results

Physicochemical Characteristics of the River Water Samples

The physicochemical properties of the river water samples, including temperature, pH, and electrical conductivity, measured at the time of sampling, are summarized in Table 5. Pronounced seasonal variations were observed in these parameters across sampling stations, with temperature being minimum during winter (8.0–12.0 °C) and maximum during the summer (27.0–31.0 °C). The pH values remained slightly alkaline, ranging from 7.36 to 8.33, throughout the study period, and exhibited only minor seasonal fluctuations. In contrast, electrical conductivity exhibited pronounced spatial variability, with substantially elevated values recorded at station E (2200–4300 µS/cm) and the least at stations M and T (339–923 µS/cm), likely reflecting differences in hydrological conditions and local anthropogenic influences among the three rivers. Overall, electrical conductivity values were higher during autumn and winter than in spring and summer. These baseline physicochemical characteristics provide essential contextual information for the interpretation of subsequent cell and toxicological findings.

Analysis of Cytotoxicity Results

The cytotoxicities of various river water samples were evaluated, and the findings are presented in Figure 1. The results demonstrated an obvious time-dependent increase in mortality rates among most treatment groups compared to the control (non-exposed) group, which exhibited 0% mortality. The asterisk (*) above the bars indicates statistically significant variations between the two groups. The TSE ISO 10993-5 standard considers a test material to be cytotoxic if it causes >30% cell mortality (<70% viability). A majority of the samples were classified as toxic, based on this guideline. Such cytotoxicity was most pronounced after 48 h of exposure and was particularly severe in the samples collected during Autumn (e.g., T1–T3, M1–M3, and E1–E3), with mortality rates consistently >50%. These findings confirm the marked presence of cytotoxic agents in river water, with the maximum toxicity induced by the Autumn samples at the 48 h time point (Figure 1 and Table 6).

Results of the Intracellular Element Levels Determination

This study provides evidence with robust statistical Sig. that the concentrations of trace elements within cells exposed to river water are highly sensitive to sampling location and exposure duration. PCA demonstrated that, at 24 h and 48 h of exposure, a majority of the total variance was explained by the first PC1, indicating that dataset variability was primarily driven by differences in element accumulation levels among exposure groups. PCA further revealed robust positive correlations among Fe, Al, Ca, Cr, and Ni at 24 h and among Ti, Mn, and P at 48 h. These observations suggest that such elements either originate from a common environmental source or are taken up by cells through shared or closely related biochemical pathways. Moreover, a clear and statistically significant separation of the E group from all others (prominent main effect, $p < 0.001$) confirms that source-specific differences in river water composition are the primary determinants of variations in intracellular element accumulation levels. Extension of exposure duration from 24 to 48 h identified two distinct accumulation dynamics. The absence of statistically significant variations in Fe, Al, Cr, and Ni contents at 24 and 48 h indicates rapid intracellular saturation or cell-regulatory mechanisms achieving equilibrium within the initial 24 h of exposure. In contrast, the Ti, Mn, Zn, Cu, and P contents elevated significantly at 48 h, suggesting that these elements may require prolonged periods of exposure for accumulation or follow slower uptake kinetics. A particularly crucial finding was the pronounced time–season interaction observed with Ca and Sr. Their concentrations increased markedly from 24 to 48 h, with those of Ca and Sr elevating by 1.7–2.58-fold and 1.17–2.10-fold, respectively. Such variability depended on the season, indicating that Ca and Sr accumulation was remarkably

Table 5. Seasonal changes in the physicochemical parameters of river water samples.

	Autumn			Winter			Spring			Summer		
	Temp. (°C)	**pH**	**EC (µS/cm)**	**Temp. (°C)**	**pH**	**EC (µS/cm)**	**Temp. (°C)**	**pH**	**EC (µS/cm)**	**Temp. (°C)**	**pH**	**EC (µS/cm)**
E1	18.0	7.83	3910	10.0	7.81	2410	21.0	7.82	2200	31.0	8.01	2270
E2	18.0	7.90	4300	12.0	7.81	2760	23.0	7.74	2260	30.0	7.99	2330
E3	19.0	7.84	3910	10.0	7.59	2430	21.0	7.68	2250	30.0	8.00	2290
M1	14.0	8.04	526	9.0	8.33	339	23.0	8.23	388	27.5	8.04	493
M2	15.0	8.01	411	8.0	8.27	344	24.0	8.13	382	28.0	8.07	499
M3	17.0	7.79	574	10.0	7.36	536	25.0	7.45	438	27.5	8.06	504
T1	12.0	8.06	900	8.0	8.16	827	22.0	7.78	714	27.0	7.80	834
T2	14.0	7.93	923	8.5	8.13	807	22.0	7.77	712	29.0	7.39	887
T3	14.0	7.65	913	8.0	8.18	822	23.0	7.72	724	28.0	7.87	892

EC = electrical conductivity; Temp. = temperature.

Table 6. Percentage mortality rates after 24 and 48 hours of exposure to river water (n = 4, % mean ± SD).

Ecosystem	Autumn		Winter		Spring		Summer	
	24 h	**48 h**	**24 h**	**48 h**	**24 h**	**48 h**	**24 h**	**48 h**
T1	57.18 ± 0.35	68.34 ± 0.28	0.52 ± 0.42	34.28 ± 0.47	38.69 ± 0.45	19.79 ± 0.45	25.16 ± 0.24	16.17 ± 0.24
T2	60.56 ± 0.45	56.97 ± 0.74	25.62 ± 0.65	39.38 ± 0.66	44.07 ± 0.52	9.26 ± 0.52	26.20 ± 0.36	19.07 ± 0.36
T3	50.01 ± 0.96	64.06 ± 0.96	13.22 ± 0.24	37.15 ± 0.25	46.65 ± 0.68	28.95 ± 0.68	11.33 ± 0.74	37.86 ± 0.74
M1	52.51 ± 0.45	81.03 ± 0.15	25.31 ± 0.74	4.01 ± 0.74	61.73 ± 0.14	2.55 ± 0.14	28.11 ± 0.53	4.89 ± 0.52
M2	38.94 ± 0.75	70.09 ± 0.52	9.03 ± 0.62	5.29 ± 0.63	43.47 ± 0.74	29.01 ± 0.74	25.76 ± 0.45	5.01 ± 0.45
M3	50.79 ± 0.68	71.43 ± 0.58	29.77 ± 0.52	10.93 ± 0.52	51.50 ± 0.63	37.12 ± 0.63	25.31 ± 0.38	19.16 ± 0.38
E1	64.06 ± 0.35	77.2 ± 0.65	28.95 ± 0.54	1.15 ± 0.54	66.14 ± 0.85	90.03 ± 0.85	34.09 ± 0.65	7.99 ± 0.65
E2	80.09 ± 0.54	71.78 ± 0.24	6.47 ± 0.62	20.94 ± 0.62	65.26 ± 0.25	77.74 ± 0.25	19.61 ± 0.75	5.22 ± 0.75
E3	57.30 ± 0.65	77.87 ± 0.45	28.27 ± 0.34	25.91 ± 0.34	84.31 ± 0.78	7.26 ± 0.78	35.36 ± 0.98	18.32 ± 0.98

SD = standard deviation.

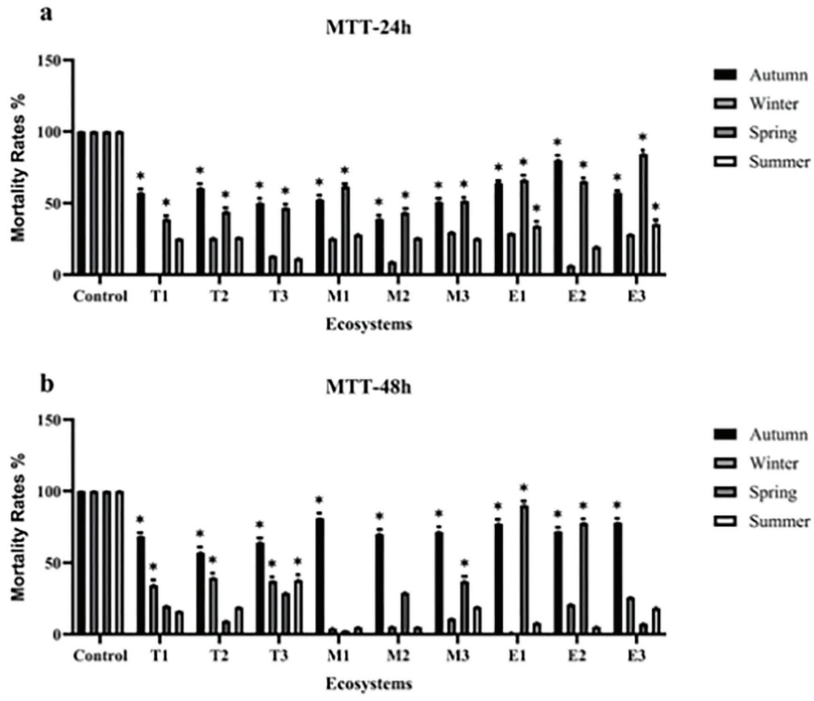

Figure 1. Assessment of river water-induced cytotoxicity in HaCaT cells across ecosystems and seasons: MTT assay results. (a) MTT-24 h results (top panel). The top panel illustrates the viability rates (%) in HaCaT cells after 24 h of exposure to water samples. Exposure to the waters of most river ecosystems—T1–T3, M1–M3, and E1–E3— markedly reduced cell viability compared to the control, with mortality rates clustering between 25% and 75%. (b) MTT-48 h results (Bottom Panel). The bottom panel presents the cell viability after 48 h of exposure. It indicates a time-dependent increase in cytotoxicity, with generally elevated mortality rates observed across ecosystems compared to 24 h. The asterisk symbol (*) indicates that the viability rates between the corresponding groups and seasons differed with statistical Sig. ($p < 0.05$) from the control group.
Key findings: The graph confirms a significant ecosystem–collection time–season interaction, as the E group samples consistently induced the maximum mortality rates, particularly during Autumn and Winter, indicating that the source of water (E) and the season of collection are major determinants of toxicity.
HaCaT = human keratinocyte cell line; MTT = 3-(4,5-dimethylthiazol-2-yl)-2,5 diphenyl tetrazolium bromide; Sig. = significance.

influenced by exposure duration and environmental conditions, positioning these elements as plausible, high-sensitivity biological indicators of seasonal and environmental dynamics. In conclusion, the findings of the combined PCA and variance analyses demonstrate that the river water environments investigated were heterogeneous regarding trace element composition and that cell responses differed prominently depending on the water source. These findings underscore the critical nature of including exposure duration and seasonal variability in environmental pollution risk assessments and toxicological evaluations (Figure 2).

ROS-Mediated Oxidative Stress and DNA Damage Assessed by Measuring 8-OHdG Levels

The differences in ROS levels within the HaCaT cells exposed or not exposed to river water for 24 and 48 h were evaluated using the independent samples t-test, preceded by Levene's test for equal variances. As most groups showed two-tailed Sig. values >0.05, the assumption of equal variances was generally met. The t-test results, specifically the Sig. values, revealed that ROS levels of most treated group cells differed with high Sig.compared to the control group ones (Sig. 0.005). The variations among most samples from the E, M, and T ecosystems across seasons were statistically significant (*). ROS levels induced by only three spring samples, E2-Spring (Sig. = 0.695), M1-Spring (Sig. = 0.251), and T3-Spring (Sig. = 0.070) did not differ with statistical Sig. from the contents of control group cells at the tested time points. These trends suggest that spring-collected samples induced a negligible oxidative stress response in HaCaT cells (Figure 3, Table 7).

As expected, control group cells demonstrated the lowest 8-OHdG levels at both 24 and 48 h of treatment, indicating minimal DNA damage under normal cell culture conditions. In contrast, cells of all groups exposed to river water exhibited markedly elevated 8-OHdG levels compared to the control group cells. Such an increase confirms that pollutants present in river water induced oxidative stress and consequent DNA damage in the HaCaT cells.

The overall trend indicated an increase in DNA damage with prolonged pollutant exposure. As illustrated, cell 8-OHdG levels were higher at 48 h compared to 24 h upon treatment with water collected from several locations, e.g., E1-Winter, E2-Winter, M1-Winter, M2-Spring, and T2-Winter. However, DNA damage

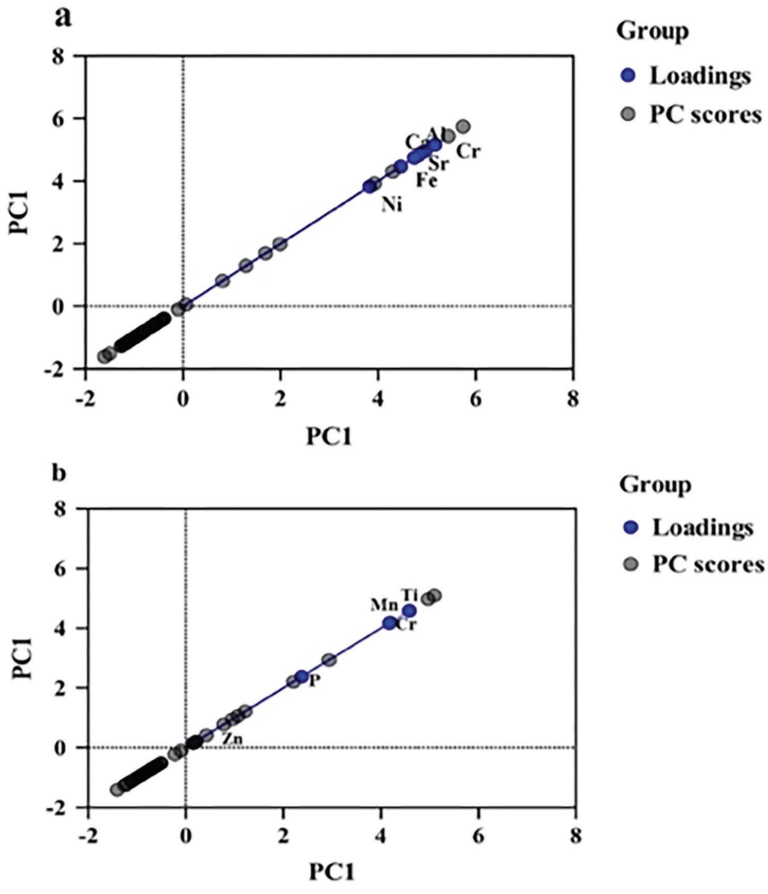

Figure 2. PCA of the intracellular accumulation of elements at 24 and 48 h of exposure to river water. (a) 24 h Exposure: Identification of the Core Accumulation Group and Significant Group Separation: The 24 h PCA biplot demonstrates that Fe, Al, Ca, Cr, and Ni exhibit strong correlations (the Core Accumulation Group) and load heavily onto the PC1 axis. This trend proves that source-derived differences are the dominant factors determining element accumulation. The clear separation of group scores along the PC1 axis confirms that river water exposure resulted in statistically significant variations in element uptake across groups. (b) 48 h Exposure: Impact of Time on Sensitive Element Dynamics: The 48 h PCA biplot indicates an expansion in the element group to include Ti, Mn, and P, which were markedly elevated at 48 h. This observation, combined with the finding that Fe, Al, Cr, and Ni contents did not show statistically significant differences at 24 and 48 h, highlights varying kinetic uptake rates. Critically, the PCA supports Ca and Sr displaying the maximum sensitivity, demonstrating statistically significant and season-dependent fold-changes between their levels at 24 and 48 h, marking them as the biological indicators most reactive to prolonged exposure.
PCA = principal component analysis.

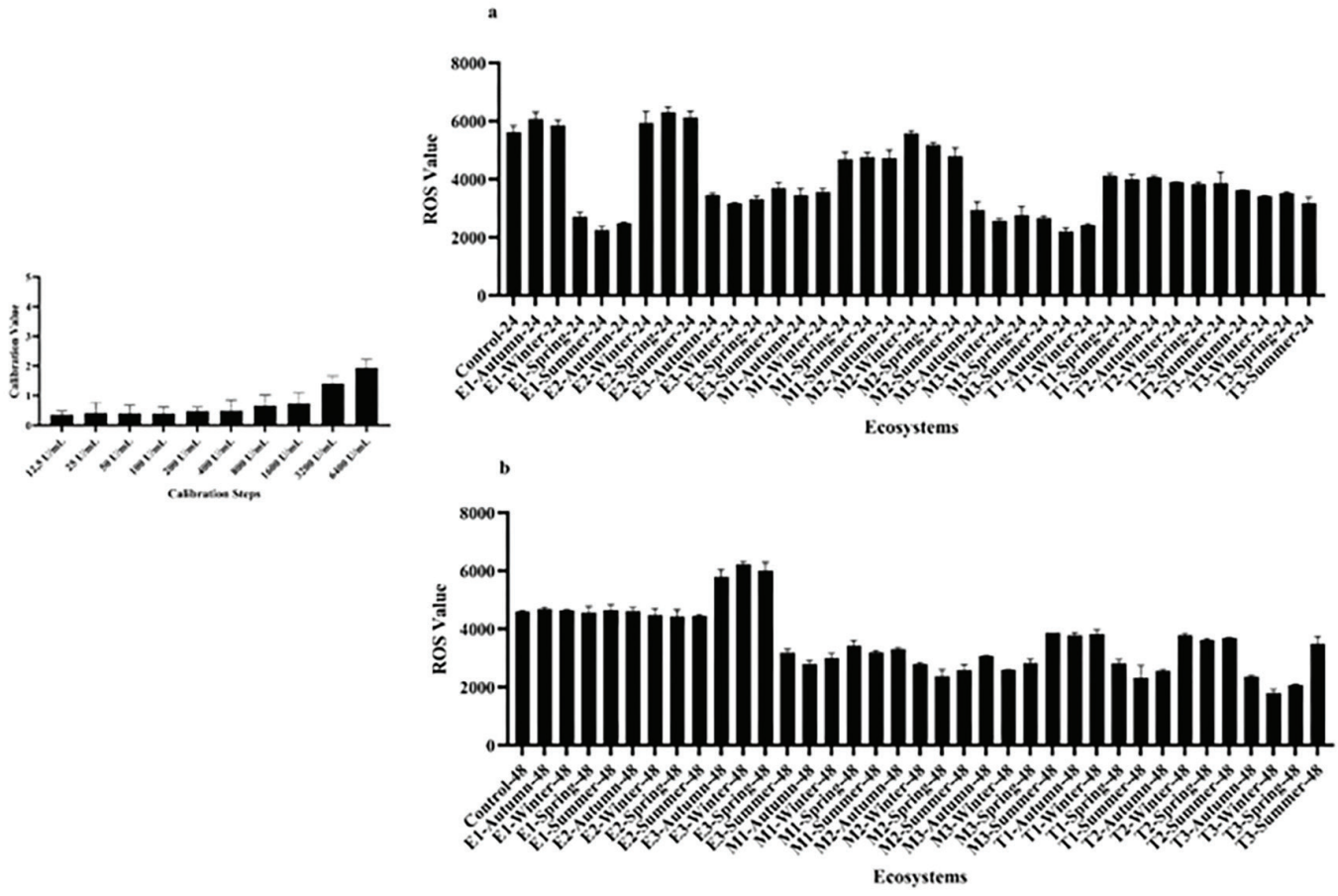

Figure 3. ROS production in HaCaT cells following exposure to river water: Time- and ecosystem-dependent stress.
(a) ROS Production at 24 h (top panel). The top panel presents the ROS contents after 24 h of exposure. It indicates a significant ecosystem–time–season interaction, with particularly severe oxidative stress observed in the E groups (E1, E2, and E3) during all seasons relative to the control as well as the T and M groups. This observation suggests that the water from the E ecosystem induced an immediate and robust oxidative response. (b) ROS Production at 48 h (bottom panel). The bottom panel shows the ROS values after 48 h of exposure to river water. It indicates a temporal moderation of the oxidative response, where the initially high ROS levels observed in the E groups at 24 h either normalized or slightly decreased, but slightly increased in certain M and T groups. The maintenance of moderate ROS levels within most groups at 48 h suggests cell adaptation or establishment of a novel oxidative equilibrium under continuous environmental stress.
HaCaT = human keratinocyte cell line; ROS = reactive oxygen species.

induced by water collected from a few locations declined at 48 h relative to 24 h (e.g., E1-Autumn). This observation suggests activation of DNA repair mechanisms or extensive cell death at 48 h, which reduced the number of viable cells or DNA available for measurement. The T2-Spring group cells exhibited the maximal 8-OHdG levels at 48 h (~18), indicating the most severe DNA damage and suggesting that the pollutants at this location, as well as the collection season exerted the strongest genotoxicity. Conversely, the E1-Autumn group cells showed the highest 8-OHdG contents at 24 h (~13.5), implying a rapid and potent induction of oxidative stress by river water during autumn. In winter group cells, particularly the M2-Winter and T2-Winter group ones, a pronounced elevation in 8-OHdG levels was detected at 48 h (Figure 4). Overall, the severity and duration of oxidative stress–induced DNA damage may vary remarkably depending on exposure time generally increasing at 48 h as well as on the river ecosystem type and seasonal conditions.

Discussion

The present study evaluated the toxicological effects of river water with seasonal variations in HM pollution levels. Cytotoxicity was assessed in the HaCaT human keratinocyte model to assess potential relevance to human health. The pronounced exposure time- and sampling season-dependent impacts observed indicate that river water-induced toxicity is highly dynamic and robustly influenced by seasonal variations in environmental conditions. Similar to previous reports demonstrating region-specific HM accumulation patterns in aquatic ecosystems (Praveen et al., 2016; Shetaia et al., 2023), the findings of the present study suggest that seasonal fluctuations in contaminant inputs critically shape responses in biological systems.

The elevated cytotoxicity induced by autumn- and spring-collected samples is likely linked to elevations in the pollutant loads of river systems caused by surface runoff and leaching. During these

periods, fertilizers, pesticides, and industrial residues are well-recognized contributors to freshwater contamination, and their biological relevance is reflected in the substantial accumulation of multiple elements within cells detected by ICP-MS. Rapid uptake of Fe, Al, Cr, Ni, Ca, and Sr within the first 24 h suggests an early cell response to environmental exposure. In contrast, the delayed accumulation of Ti, Mn, Zn, Cu, and P at 48 h underscores the amplification in toxic effects induced by prolonged exposure.

Among the elements analyzed, Ca and Sr displayed a particularly pronounced time–season interaction. Given the central role of Ca in cell signaling, mitochondrial regulation, and membrane stability, a dysregulation in intracellular Ca accumulation may intensify cytotoxicity-associated pathways. The parallel increase in Sr, which is chemically similar to Ca, may further interfere with Ca-dependent cellular processes. These observations support the notion that Ca and Sr may function as sensitive cell-level indicators of the influence of seasonal environmental variability and pollutant pressure.

The biological relevance of HM accumulation was further substantiated by oxidative stress and genotoxicity endpoints. Significantly elevated ROS levels in most exposed cell groups indicate that oxidative stress represents a key mechanism underlying the observed cytotoxicity. Only a limited number of spring samples failed to induce a marked elevation in ROS production, consistent with their comparatively lower toxic profiles. Increased ROS generation was accompanied by an elevation in 8-OHdG levels, reflecting oxidative DNA damage and cumulative genotoxic impacts with prolonged exposure. These findings align with established evidence indicating that HMs exert genotoxicity through ROS-mediated mechanisms and the disruption of DNA repair pathways (Jadoon & Malik, 2017).

Exposure to HMs such as cadmium, lead, and arsenic results in oxidative stress, mitochondrial dysfunction, and apoptosis in human cells, including keratinocytes (Davodpour et al., 2019; Habibi et al., 2022; Li et al., 2022; Mohamed et al., 2024; Sobhanardakani, 2017, 2019).

Moreover, elevated contents of oxidative DNA damage markers, including 8-OHdG, have been detected in individuals exposed to contaminated water or HMs (Mohod & Dhote, 2013; Szymańska-Chabowska et al., 2009). The results of the present study are therefore consistent with existing toxicological evidence linking exposure to metal-contaminated environments and adverse human health outcomes.

The genotoxic potential of HMs observed in this study is further supported by similar findings made in plant and aquatic organism models, where exposure to HM-contaminated waters has been associated with chromosomal aberrations, micronuclei formation, and DNA fragmentation (Cavusoglu et al., 2010; Chatterjee & Chatterjee, 2000; Doğan et al., 2022; Scalon et al., 2010). Such cross-species consistency reinforces the ecological and biological relevance of the oxidative and genotoxic responses detected in HaCaT cells.

Although cadmium has been recognized as the predominant ecological threat in certain aquatic environments (Shetaia et al., 2023), the present study identified a region-specific contamination profile dominated by Fe, Al, Cr, and Ni. Such a discrepancy highlights that toxicity induced by polluted freshwater cannot be generalized across regions and underscores the necessity of site-specific assessments that consider local anthropogenic activities and environmental conditions.

Overall, the present findings demonstrate that seasonal variations in river water pollution exert significant cytotoxic and genotoxic impacts through oxidative stress-mediated mechanisms. Rather than reiterating contamination levels, these results emphasize the broader implications of sustained and seasonally-modulated pollutant exposure for human health and ecosystem integrity. Consistent with previous calls for comprehensive monitoring of metal-contaminated aquatic systems (Shetaia et al., 2023), this study underscores the importance of continuous, region-specific monitoring strategies and targeted mitigation policies addressing both agricultural and industrial sources of pollution.

Conclusion

This study comprehensively investigates the toxicity levels of river waters sampled at various locations, focusing on their impacts on human skin cells at the physiological and molecular levels. The findings offer valuable insights into the harmful effects of water pollution on human health, specifically highlighting the toxicological risks posed by HM-contaminated water. Our research demonstrates that exposure to HM-polluted river water induces significant levels of oxidative stress, DNA damage, and genotoxicity in human skin cells. Moreover, these effects varied in extent across seasons and exposure durations, underscoring the dynamic nature of water contamination and its impact on biological systems. Among the HMs analyzed, Al, Fe, and Cr were identified as key inducers of DNA damage, suggesting that these metals may serve as potential biomarkers for assessing toxicity in human skin cells. The study emphasizes the need for continuous water quality monitoring, especially in regions affected by industrial and agricultural pollutants, and advocates for further research into the mechanisms underlying HM-induced toxicity. These findings are crucial for developing effective strategies to mitigate the health risks associated with contaminated water and for advancing the protection of public health in the face of growing environmental challenges.

Table 7. Summary of t-test results applied to the ROS levels detected at 24 & 48 h of treatment vs. control. The table summarizes the results of the independent samples t-test comparing the ROS levels in HaCaT cells treated for 24 and 48 h with those of the untreated cells. The groups marked with an asterisk (*) indicate highly statistically significant differences in ROS levels, based on the threshold of $p < 0.005$. Only the E2-Spring, M1-Spring, and T3-Spring samples failed to induce ROS synthesis with statistically significant variations at this threshold.

	Levene's test for equality of variances		**t-test for equal means**		
	F	**Sig.**	**t**	**df**	**Sig. (2-tailed)**
E1-Autumn*	2.408	0.196	-15.724	4	0.000
E1-Winter*	2.616	0.181	15.810	4	0.000
E1-Spring*	0.304	0.610	-17.746	4	0.000
E1-Summer*	0.390	0.566	4.367	4	0.012
E2-Autumn*	1.570	0.278	20.052	4	0.000
E2-Winter*	0.683	0.455	10.046	4	0.001
E2-Spring	0.079	0.792	-0.422	4	0.695
E2-Summer*	2.441	0.193	-10.482	4	0.000
E3-Autumn*	2.176	0.214	10.177	4	0.001
E3-Winter*	1.354	0.309	3.294	4	0.030
E3-Spring*	1.409	0.301	8.280	4	0.001
E3-Summer*	0.412	0.556	-3.029	4	0.039
M1-Autumn*	1.009	0.372	16.756	4	0.000
M1-Winter*	0.324	0.600	19.103	4	0.000
M1-Spring	0.152	0.717	-1.340	4	0.251
M1-Summer*	1.371	0.307	16.610	4	0.000
M2-Autumn*	2.423	0.195	-9.515	4	0.001
M2-Winter*	0.331	0.596	18.793	4	0.000
M2-Spring*	1.411	0.301	5.458	4	0.005
M2-Summer*	0.348	0.587	-4.185	4	0.014
M3-Autumn*	3.385	0.140	-10.082	4	0.001
M3-Winter*	2.833	0.168	-13.119	4	0.000
M3-Spring*	1.111	0.351	-4.856	4	0.008
M3-Summer*	3.908	0.119	-71.920	4	0.000
T1-Autumn*	0.148	0.720	4.113	4	0.015
T1-Winter*	1.888	0.241	17.811	4	0.000
T1-Spring*	0.614	0.477	-4.061	4	0.015
T1-Summer*	1.313	0.316	3.640	4	0.022
T2-Autumn*	0.248	0.645	4.187	4	0.014
T2-Winter*	3.301	0.143	-13.406	4	0.000
T2-Spring*	0.245	0.647	5.010	4	0.007
T2-Summer*	3.800	0.123	-23.763	4	0.000
T3-Autumn*	3.312	0.143	-18.117	4	0.000
T3-Winter*	2.299	0.204	-14.474	4	0.000
T3-Spring	0.635	0.470	2.458	4	0.070
T3-Summer*	0.068	0.807	-15.962	4	0.000

HaCaT = human keratinocyte cell line; ROS = reactive oxygen species; Sig. = significance.

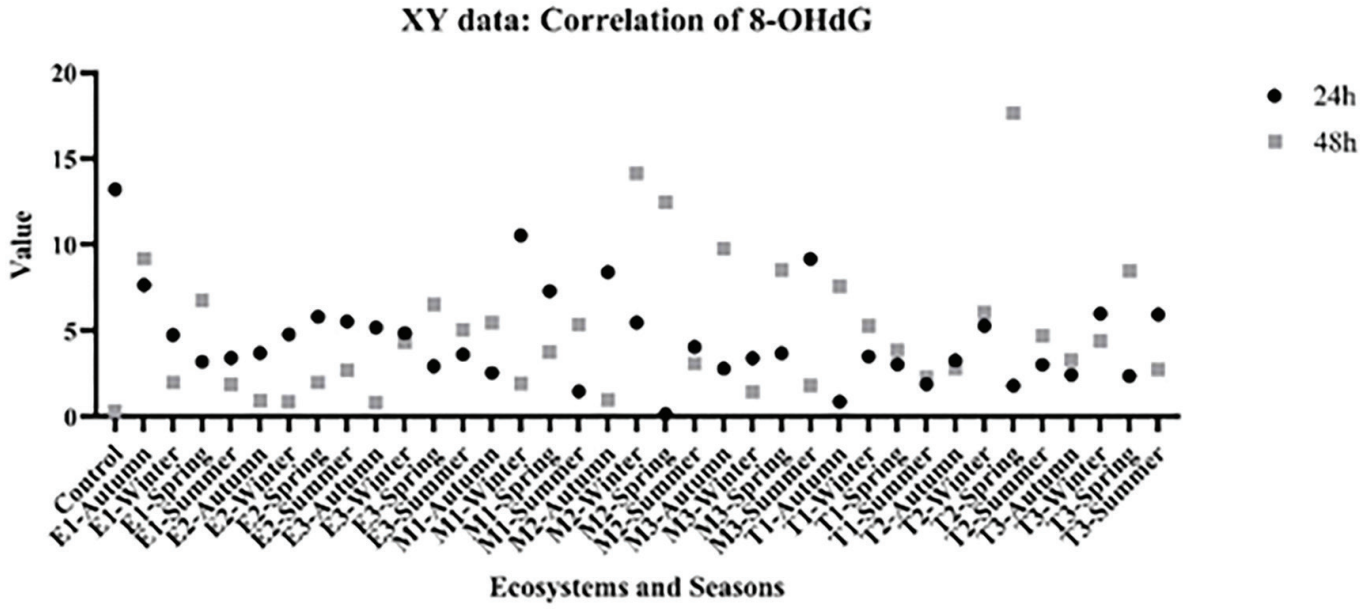

Figure 4. Oxidative DNA damage levels (8-OHdG) in HaCaT cells following river water exposure.
Levels of the oxidative DNA damage marker 8-OHdG in HaCaT cells after 24 h (black circles) and 48 h (grey squares) of exposure to river water samples categorized by ecosystem and season. The values represent arbitrary units, such as ng DNA.
8-OHdG = 8-hydroxy-2'-deoxyguanosine; HaCaT = human keratinocyte cell line.

Ethics

Ethics Committee Approval: Not required.

Data Sharing Statement: All data are available within the study.

Footnotes

Authorship Contributions:

Conceptualization: N.P.T. and P.A.M.; Design/methodology: N.P.T. and P.A.M.; Execution/investigation: N.P.T. and P.A.M.; Resources/materials: N.P.T. and P.A.M.; Data acquisition: N.P.T. and P.A.M.; Data analysis/interpretation: N.P.T. and P.A.M.; Writing – original draft: N.P.T. and P.A.M.; Writing – review & editing/critical revision: N.P.T. and P.A.M.

Conflict of Interest: The author(s) have no conflicts of interest to declare.

Funding: No external funding acquired.

References

Amaechi, M., Onuoha, D. C., & Onwuka, S. U. (2025). Analysis of seasonal variation of heavy metals concentration in selected river in Anambra State resulting from industrial effluents discharge. *Tropical Built Environment Journal, 11*(1). https://www.tbejournal.com/index.php/tbej/article/view/163

Arif, A., Malik, M. F., Liaqat, S., Aslam, A., Mumtaz, K., Afzal, A., & Javed, R. (2020). Water pollution and industries. *Pure and Applied Biology (PAB), 9*(4), 2214–2224. https://doi.org/10.19045/bspab.2020.90237

Cavusoglu, K., Yapar, K., Kinalioglu, K., Turkmen, Z., Cavusoglu, K., & Yalcin, E. (2010). Protective role of Ginkgo biloba on petroleum wastewater-induced toxicity in *Vicia faba* L.(Fabaceae) root tip cells. *Journal of Environmental Biology, 31*(3), 319. https://doi.org/10.19045/bspab.2020.90237

Chatterjee, J., & Chatterjee, C. (2000). Phytotoxicity of cobalt, chromium and copper in cauliflower. *Environmental Pollution, 109*(1), 69–74. https://doi.org/10.1016/s0269-7491(99)00238-9

Chen, B., Wang, M., Duan, M., Ma, X., Hong, J., Xie, F., & Li, X. (2019). In search of key: Protecting human health and the ecosystem from water pollution in China. *Journal of Cleaner Production, 228*, 101–111. https://doi.org/10.1016/j.jclepro.2019.04.228

Chowdhary, P., Bharagava, R. N., Mishra, S., & Khan, N. (2019). Role of industries in water scarcity and its adverse effects on environment and human health. In *Environmental concerns and sustainable development: Volume 1: Air, water and energy resources* (pp. 235–256). Singapore: Springer Singapore. https://doi.org/10.1007/978-981-13-5889-0_12

Davodpour, R., Sobhanardakani, S., Cheraghi, M., Abdi, N., & Lorestani, B. (2019). Honeybees (*Apis mellifera* L.) as a potential bioindicator for detection of toxic and essential elements in the environment (case study: Markazi Province, Iran). *Archives of Environmental Contamination and Toxicology, 77*(3), 344–358. https://doi.org/10.1007/s00244-019-00634-9

Doğan, M., Çavuşoğlu, K., Yalçin, E., & Acar, A. (2022). Comprehensive toxicity screening of Pazarsuyu stream water containing heavy metals and protective role of lycopene. *Scientific Reports, 12*(1), 16615. https://doi.org/10.1038/s41598-022-21081-y

Fleisher, J. M., & Kay, D. (2006). Risk perception bias, self-reporting of illness, and the validity of reported results in an epidemiologic study of recreational water associated illnesses. *Marine Pollution Bulletin, 52*(3), 264–268. https://doi.org/10.1016/j.marpolbul.2005.08.019

Ge, J., Pitman, A. J., Guo, W., Zan, B., & Fu, C. (2020). Impact of revegetation of the Loess Plateau of China on the regional growing season water balance. *Hydrology and Earth System Sciences, 24*(2), 515–533. https://doi.org/10.5194/hess-24-515-2020

Habibi, H., Sobhanardakani, S., Cheraghi, M., Lorestani, B., & Sadr, M. K. (2022). Analysis, sources and health risk assessment of trace elements in street dust collected from the city of Hamedan, west of Iran. *Arabian Journal of Geosciences, 15*(2), 168. https://doi.org/10.1007/s12517-022-09460-1

Hammoumi, D., Al-Aizari, H. S., Alaraidh, I. A., Okla, M. K., Assal, M. E., Al-Aizari, A. R., & Bejjaji, Z. (2024). Seasonal variations and assessment of surface water quality using water quality index (WQI) and principal component analysis (PCA): A case study. *Sustainability, 16*(13), 5644. https://doi.org/10.3390/su16135644

Hanif, M. A., Miah, R., Islam, M. A., & Marzia, S. (2020). Impact of Kapotaksha river water pollution on human health and environment. *Progressive Agriculture, 31*(1), 1–9. https://doi.org/10.3329/pa.v31i1.48300

Jadoon, S., & Malik, A. D. N. A. (2017). DNA damage by heavy metals in animals and human beings: An overview. *Biochem Pharmacol, 6*(3), 1–8. https://doi.org/10.4172/2167-0501.1000235

Kazi, T. G., Arain, M. B., Baig, J. A., Jamali, M. K., Afridi, H. I., Jalbani, N., & Niaz, A. (2009). The correlation of arsenic levels in drinking water with the biological samples of skin disorders. *Science of the Total Environment, 407*(3), 1019–1026. https://doi.org/10.1016/j.scitotenv.2008.10.013

Kolawole, T. A., Palacios, J., Husaini, D. C., & Nwokocha, C. R. (2025). Inflammation and oxidative stress biomarkers in heavy metal toxicity: Bridging the gap to personalized clinical interventions. *Journal of Applied Toxicology.* https://doi.org/10.1002/jat.4874

Li, J. Y., Cui, D. L., Xie, Y. M., Su, J. Z., Zhang, M. Y., Niu, Y. Y., & Xiang, P. (2022). Mechanisms of Cd-induced cytotoxicity in normal human skin keratinocytes: Implication for human health. *International Journal of Molecular Sciences, 23*(19), 11767. https://doi.org/

Lu, Y., Song, S., Wang, R., Liu, Z., Meng, J., Sweetman, A. J., & Wang, T. (2015). Impacts of soil and water pollution on food safety and health risks in China. *Environment International, 77*, 5–15. https://doi.org/

Mohamed, A., Mahathi, P., Nair, N., & DSouza, H. (2024). The toxic effects of lead nitrate on human keratinocytes (HaCaT). *bioRxiv, 2024-11.* https://doi.org/

Mohod, C. V., & Dhote, J. (2013). Review of heavy metals in drinking water and their effect on human health. *International Journal of Innovative Research in Science, Engineering and Technology, 2*(7), 2992–2996. https://doi.org/

Moss, B. (2008). Water pollution by agriculture. *Philosophical Transactions of the Royal Society B: Biological Sciences, 363*(1491), 659–666. https://doi.org/10.1098/rstb.2007.2176

Parris, K. (2011). Impact of agriculture on water pollution in OECD countries: Recent trends and future prospects. *Water Quality Management*, 33–52. https://doi.org/10.1080/07900627.2010.531898

Payment, P., Siemiatycki, J., Richardson, L., Renaud, G., Franco, E., & Prevost, M. (1997). A prospective epidemiological study of gastrointestinal health effects due to the consumption of drinking water. *International Journal of Environmental Health Research, 7*(1), 5–31. https://doi.org/10.1080/09603129773977

Praveen, P. K., Ganguly, S., Kumar, K., & Kumari, K. (2016). Water pollution and its hazardous effects to human health: A review on safety measures for adoption. *International Journal of Science, Environment and Technology, 5*(3), 1559–1563. https://www.researchgate.net/publication/303698187_water_pollution_and_its_hazardous_effects_to_human_health_a_review_on_safety_measures_for_adoption

Scalon, M. C. S., Rechenmacher, C., Siebel, A. M., Kayser, M. L., Rodrigues, M. T., Maluf, S. W., & Silva, L. B. D. (2010). Evaluation of Sinos River water genotoxicity using the comet assay in fish. *Brazilian Journal of Biology, 70*, 1217–1222. https://doi.org/10.1590/s1519-69842010000600011

Shetaia, S. A., Nasr, R. A., El Saeed, R. L., Dar, M. A., Al-Mur, B. A., & Zakaly, H. M. (2023). Assessment of heavy metals contamination of sediments and surface waters of Bitter lake, Suez Canal, Egypt: Ecological risks and human health. *Marine Pollution Bulletin, 192*, 115096. https://doi.org/10.1016/j.marpolbul.2023.115096

Sobhanardakani, S. (2017). Potential health risk assessment of heavy metals via consumption of caviar of Persian sturgeon. *Marine Pollution Bulletin, 123*(1-2), 34–38. https://doi.org/10.1016/j.marpolbul.2017.09.033

Sobhanardakani, S. (2019). Ecological and human health risk assessment of heavy metal content of atmospheric dry deposition, a case study: Kermanshah, Iran. *Biological Trace Element Research, 187*(2), 602–610. https://doi.org/10.1007/s12011-018-1383-1

Szymańska-Chabowska, A., Beck, A., Poręba, R., Andrzejak, R., & Antonowicz-Juchniewicz, J. (2009). Evaluation of DNA damage in people occupationally exposed to arsenic and some heavy metals. *Polish Journal of Environmental Studies, 18*(6). https://www.pjoes.com/pdf-88337-22195?filename=Evaluation%20of%20DNA%20Damage.pdf

Wu, C., Maurer, C., Wang, Y., Xue, S., & Davis, D. L. (1999). Water pollution and human health in China. *Environmental Health Perspectives, 107*(4), 251–256. https://doi.org/10.1289/ehp.99107251

Wu, H., Gai, Z., Guo, Y., Li, Y., Hao, Y., & Lu, Z. N. (2020). Does environmental pollution inhibit urbanization in China? A new perspective through residents' medical and health costs. *Environmental Research, 182*, 109128. https://doi.org/10.1016/j.envres.2020.109128

Xiao, J., Wang, L., Deng, L., & Jin, Z. (2019). Characteristics, sources, water quality and health risk assessment of trace elements in river water and well water in the Chinese Loess Plateau. *Science of the Total Environment, 650*, 2004–2012. https://doi.org/ 10.1016/j.scitotenv.2018.09.322

Yassin, M. M., Amr, S. S. A., & Al-Najar, H. M. (2006). Assessment of microbiological water quality and its relation to human health in Gaza Governorate, Gaza Strip. *Public Health, 120*(12), 1177–1187. https://doi.org/10.1016/j.puhe.2006.07.026

Yau, V., Wade, T. J., de Wilde, C. K., & Colford Jr, J. M. (2009). Skin-related symptoms following exposure to recreational water: A systematic review and meta-analysis. *Water Quality, Exposure and Health, 1*(2), 79–103. https://link.springer.com/article/10.1007/s12403-009-0012-9

Trakya University Journal of Natural Sciences, 27(1), 88–95, 2026
DOI: 10.23902/trkjnat.202598
www.tujns.org

Research Article

Quorum quenching and antimicrobial potential of natural compounds against foodborne biofilm-forming bacteria

Dilvin İpek[1]*, Nükhet N. Demirel Zorba[2], Ji Hyang Kweon[3], Harshad Lade[4]

[1]*Çanakkale Onsekiz Mart University, Ezine Gıda İhtisas Organized Industrial Zone Vocational School, Çanakkale, Türkiye*
[2]*Çanakkale Onsekiz Mart University, Department of Food Engineering, Çanakkale, Türkiye*
[3]*Konkuk University, Department of Environmental Engineering, Seoul, Korea*
[4]*MIT Art, Design and Technology University, School of Bioengineering Sciences and Research, Maharashtra, India*

Cite this article as: İpek, D., Demirel Zorba, N. N., Kweon, J. H., & Lade, H. (2026). Quorum quenching and antimicrobial potential of natural compounds against foodborne biofilm-forming bacteria. *Trakya University Journal of Natural Sciences, 27*(1), 88–95. https://doi.org/10.23902/trkjnat.202598

Abstract

Background: Biofilm formation represents a major challenge for food safety, contributing to persistent contamination, compromised process hygiene, and increased antimicrobial resistance. Because quorum sensing (QS) regulates biofilm development, interference with QS signaling (quorum quenching [QQ]) has emerged as a promising strategy for biofilm control.

Aims: This study aimed to evaluate the biofilm-forming capacity and QS (N-acyl homoserine lactones [AHL] and autoinducer-2 [AI-2]) activity of foodborne bacterial isolates and to assess the antimicrobial and QQ potential of selected natural products under *in vitro* conditions.

Methods: A total of 109 bacterial isolates from dairy processing lines were assessed for biofilm formation using a 96-well microtiter assay. QS activity was detected using indicator microorganisms for AHL and AI-2 signaling. Selected natural products (1 mg/mL) were screened for antimicrobial and QQ activity, with QS inhibition evaluated independently of growth suppression.

Results: A total of 89% of the isolates were classified as strong biofilm producers, with *Bacillus* and *Pseudomonas* species predominating. Plant-derived extracts and natural products, including *Calendula officinalis*, propolis, nisin, and *Hypericum perforatum*, exhibited measurable antimicrobial and antibiofilm activity. Propolis and *C. officinalis* reduced QS-associated biofilm responses independently of growth inhibition, indicating potential QQ activity.

Conclusion: These findings highlight the potential of natural extracts as eco-friendly alternatives to chemical disinfectants in food processing environments.

Özet

Dayanak: Biyofilm oluşumu, gıda güvenliği açısından kalıcı kontaminasyona, proses hijyeninin bozulmasına ve artan antimikrobiyal dirence yol açan önemli bir sorundur. Biyofilm gelişimini düzenleyen quorum sensing (QS) sisteminin engellenmesi (quorum quenching [QQ]), biyofilm kontrolü için umut vadeden bir yaklaşımdır.

Amaçlar: Bu çalışmada, süt ürünleri proses hatlarından izole edilen bakteri izolatlarının biyofilm oluşturma kapasiteleri ile QS'e bağlı (N-asil homoserin laktonu [AHL] ve otoindükleyici-2 [AI-2]) sinyal aktivitelerinin değerlendirilmesi ve seçilmiş doğal ürünlerin *in vitro* koşullarda antimikrobiyal ve QQ potansiyellerinin belirlenmesi amaçlanmıştır.

Yöntemler: Toplam 109 izolatın biyofilm oluşumu 96 kuyucuklu mikroplak yöntemi ile belirlenmiş, QS aktivitesi indikatör mikroorganizmalar kullanılarak saptanmıştır. Doğal ürünler (1 mg/mL) antimikrobiyal ve QQ aktiviteleri açısından tarama düzeyinde incelenmiş, QS inhibisyonu büyüme baskılanmasından bağımsız olarak değerlendirilmiştir.

Bulgular: İzolatların %89'u güçlü biyofilm üreticisi olup, *Bacillus* ve *Pseudomonas* türleri baskın bulunmuştur. *Calendula officinalis*, propolis, nisin ve *Hypericum perforatum* belirgin antimikrobiyal ve antibiyofilm etki göstermiştir. Propolis ve *C. officinalis*, QS ile ilişkili biyofilm yanıtlarını büyüme inhibisyonundan bağımsız olarak azaltmıştır.

Sonuç: Doğal ekstraktlar, gıda işleme ortamlarında kimyasal dezenfektanlara çevre dostu alternatifler sunma potansiyeline sahiptir.

Keywords: Antibiofilm, antimicrobial, dairy processing, food safety, natural compounds, quorum quenching

Edited by: *Hatice Korkmaz Güvenmez*

***Corresponding Author:** Dilvin İpek, **E-mail:** dilvinipek@comu.edu.tr*

***ORCID iDs of the author(s):** Dİ. 0000-0003-2946-5437; NNDZ. 0000-0001-6851-6474; JHK. 0000-0002-4906-9792; HL. 0000-0002-9809-2921*

Received: 20 October 2025, **Accepted:** 9 March 2026, **Epub:** 10 April 2026, **Published:** 24 April 2026

Introduction

Biofilm is a critical contributor to cross-contamination, antimicrobial resistance, biological pollution, energy inefficiency, and economic loss in various environments. Microorganisms use quorum sensing (QS) as a communication mechanism to assess their environment, regulate gene expression, and coordinate phenotypes such as antibiotic production, virulence, motility, sporulation, and biofilm formation. Disruption of QS systems often results in looser, less structured biofilms (Si & Quan, 2017; Suntharalingam & Cvitkovitch, 2005).

Biofilms form on both living and non-living surfaces and are commonly found in hospitals, food processing facilities, and wastewater treatment plants. A range of bacteria—*Staphylococcus*, *Enterococcus*, *Pseudomonas*, *Aeromonas*, *Bacillus*, *Klebsiella*, *Streptococcus*, *Listeria*, *Enterobacter*, *Ochrobacterium*, *Geobacillus*, and *Shigella*—have been implicated in biofilm formation, and many retain active QS systems that enhance their resilience (Lade et al., 2014; İpek, 2017). Analytical profiling of QS signals in biofilm-producing isolates has revealed the presence of both long-chain N-acyl homoserine lactones (AHLs) and autoinducer-2 (AI-2) signaling molecules, indicating that these molecules are actively produced by strong biofilm formers and are therefore relevant to understanding chemical communication within complex microbial communities (İpek, 2023). Such persistent biofilm communities pose a serious threat to food safety and public health. Conventional sanitation in the food industry relies on harsh chemicals—caustic soda, nitric and hydrochloric acids, and chlorine. While effective, these agents carry significant drawbacks: they can cause respiratory and dermatological issues, generate toxic by-products such as trihalomethanes and haloacetic acids, and contaminate soil, water, and air (Hegstad et al., 2010; Huang et al., 2012). Thus, there is growing interest in safer, eco-friendly alternatives for ensuring hygiene in food processing.

Natural compounds, particularly plant-derived extracts, have shown promise both as antimicrobials and QS agents. For instance, essential oils from cassia, tea tree, and red thyme were found to be more effective against *Pseudomonas* and *S. aureus* biofilms than antibiotics like colistin and gentamicin (Kavanaugh & Ribbeck, 2012). Likewise, *Camellia sinensis* extract was shown to inhibit QS signals of *P. aeruginosa* by mimicking autoinducer molecules and binding to their receptors (Mihalik et al., 2008).

Furthermore, pathogenic bacteria embedded in biofilms frequently develop resistance to disinfectants used in food process environments. Resistant strains have been isolated from dairy plants, potable water, wastewater systems, and environmental sediments, highlighting the need for dual-function natural agents that combine antimicrobial and antibiofilm capabilities (Castillo-Juárez et al., 2015; Jeong et al., 2018).

Recent studies continue to support the efficacy of phytochemicals—including flavonoids and phenolic acids—as QS inhibitors and biofilm disruptors (Fydrych et al., 2025; Shariati et al., 2024). Despite growing evidence on the antimicrobial and anti-quorum-sensing properties of plant-derived compounds, biofilm persistence in dairy processing environments remains a major hygienic challenge. Conventional sanitation strategies mainly target planktonic cells and often neglect QS mechanisms that stabilize biofilms. Moreover, comparative evaluation of AHL- and AI-2–mediated signaling inhibition in foodborne isolates is still limited. In this study, we characterized the biofilm-forming and QS profiles of 109 dairy-associated isolates and evaluated the antimicrobial and quorum quenching (QQ) activities of selected natural products under standardized *in vitro* conditions. This integrated approach provides evidence for natural compounds as potential dual-function agents targeting both bacterial growth and QS-regulated biofilm persistence.

Materials and Methods

Bacterial Strains and Culture Conditions

A total of 109 bacterial isolates previously obtained from dairy process lines (İpek & Zorba, 2018) were used in this study. Reference strains *Escherichia coli* ATCC 25922, *P. aeruginosa* ATCC 27853, *S. aureus* ATCC 6538P, and *Micrococcus luteus* ATCC 4698 were included as controls. Isolates were maintained on tryptic soy agar (TSA, Merck, Germany) at –18 °C and cultured in tryptic soy broth (TSB) at 30 °C prior to assays.

For QS assays, the biosensor strains *Chromobacterium violaceum* CV026, *Agrobacterium tumefaciens* A136, and *Vibrio harveyi* BB170 were used. The biosensor cultures were grown in Luria–Bertani broth supplemented with the appropriate antibiotics and incubated at 30 °C for 24 h under standard conditions. For AI-2 assays, *V. harveyi* BB170 was cultivated in Marine Broth (2216; BD Difco, USA) for 24 h, and a 1:5000 dilution was prepared using autoinducer bioassay medium prior to inoculation (İpek, 2017; Lade et al., 2014; Park et al., 2014).

Natural Compounds

The tested agents comprised plant-derived ethanolic extracts (*Calendula officinalis* L., *Hypericum perforatum*, *C. sinensis*, *Panax ginseng*, *Ganoderma lucidum*, *Prunella vulgaris*, *Sambucus nigra*, *Cichorium intybus*, and *Thymus vulgaris*), bee-derived propolis extract, and commercially available natural-origin compounds (nisin, resveratrol, vanillin, curcumin, and apple vinegar). All extracts were prepared at a concentration of 1 mg/mL, with plant materials extracted in 70% ethanol, agitated at 180 rpm for 6 h, and sterilized using 0.2 µm membrane filtration, and then stored at 4 °C until use (Lin et al., 2017).

Biofilm Formation Assay

Biofilm production was evaluated using the 96-well microtiter plate method (Christensen et al., 1985). Overnight cultures adjusted to 10^8 colony-forming unit (CFU)/mL were inoculated into TSB, incubated at 30 °C for 24 h, washed, and stained with 1% crystal violet. The bound dye was solubilized in 96% ethanol, and absorbance was measured at 600 nm (optical density [OD_{600}]).

Isolates were classified as weak, moderate, or strong biofilm producers according to established cut off values (İpek, 2017).

QS Signal Detection

AHL production was determined using *C. violaceum* CV026 (short-chain AHLs) and *A. tumefaciens* A136 (long-chain AHLs with X-gal indicator). Autoinducer-2 (AI-2) activity in Gram-positive isolates was detected by luminescence induction in *V. harveyi* BB170 as described by Sun et al. (2014). Biosensor strains were cultivated under standard conditions prior to assays. AHL production was determined based on pigment or color development in the CV026 and A136 indicator systems. For AI-2 detection, *V. harveyi* BB170 luminescence was measured following incubation with test samples, and signal intensity was quantified using a microplate reader by recording optical density at 600 nm (OD_{600}) together with luminescence values, as previously described (Lade et al., 2014; Park et al., 2014).

Antimicrobial Activity of Natural Compounds

The antimicrobial activity of natural compounds was assessed by the disc diffusion method following European Committee on Antimicrobial Susceptibility Testing (EUCAST, 2014) guidelines. Briefly, bacterial suspensions (10^8 CFU/mL) were inoculated onto Mueller-Hinton agar plates, and sterile discs loaded with 15 µL of extract were applied. Plates were incubated at 30 °C for 24 h, and inhibition zones were measured. No antibiotic was used as a positive control in this study; 70% ethanol was included as the control to evaluate any solvent-related effects on bacterial growth. Sterile water was used as the negative control (<6 mm).

QQ Assays

QQ activity of natural compounds was evaluated using disc diffusion assays for AHL-mediated signaling and microtiter plate–based luminescence assays for AI-2–dependent signaling, as previously described (Truchado et al., 2015; Zhu et al., 2016). For AHL inhibition, sterile discs impregnated with test compounds were placed onto indicator strain–inoculated agar plates and incubated under standard conditions. For AI-2 inhibition, luminescence produced by *V. harveyi* BB170 in the presence of test samples was measured using a microplate reader. Zones showing loss of pigment formation or a significant reduction in luminescence relative to untreated controls were considered indicative of QQ activity. Sterile distilled water was used as the negative control, while 70% ethanol (used as the extraction solvent) was included as the solvent control where applicable.

Minimum Inhibitory Concentration (MIC), Minimum Bactericidal Concentrations (MBC), and Inhibition Ratios

MICs were determined by the broth microdilution method in 96-well microplates using serial two-fold dilutions of the extracts, in accordance with EUCAST guidelines (EUCAST, 2014). Wells were inoculated with standardized bacterial suspensions, and MIC was defined as the lowest concentration showing no visible growth, confirmed by OD_{600} measurements and 2,3,5-triphenyltetrazolium chloride colorimetric assessment. MBCs were determined by subculturing aliquots from non-turbid wells onto agar plates and identifying the lowest concentration yielding no colony growth. Solvent control wells containing 70% ethanol (at the same final concentration used for extract preparation) were included as controls. Sterile water was used as the negative control.

Inhibition ratios (%) were calculated based on optical density values using the following formula:

Inhibition (%) = [(OD_{control} − OD_{treated}) / OD_{control}] × 100

Statistical Analysis

Statistical analysis was performed using Microsoft Excel 2016 (Microsoft, Redmond, WA, USA). All experiments were conducted in triplicate (n = 3) unless otherwise stated. Results are expressed as mean ± standard deviation. Differences between groups were evaluated using one-way analysis of variance, followed by Tukey's post hoc test for multiple comparisons. A p-value of <0.05 was considered statistically significant.

Results

Biofilm Formation by Isolates

Among the 109 bacterial isolates obtained from dairy process lines, 89% (n = 94) were classified as strong biofilm producers, whereas only 9 and 2 isolates showed moderate and weak adherence, respectively. Genera such as *Bacillus* and *Pseudomonas* were dominant among strong producers. *L. innocua*, *B. subtilis*, *B. megaterium*, and *P. fluorescens* displayed moderate adherence, whereas *K. oxytoca* and *B. pumilus* were weak producers. None of the isolates were biofilm-negative. The biofilm-forming capacities of bacterial isolates obtained from dairy industry surfaces, as determined by the 96-well microtiter plate assay, are presented in Table S1. These findings confirm the high prevalence of biofilm-forming bacteria in dairy environments (Figure 1).

QS Signals

Screening with biosensor strains revealed that none of the Gram-negative isolates produced short-chain AHLs detectable by *C. violaceum* CV026. However, most produced medium- or long-chain AHLs, as indicated by pigment formation in *A. tumefaciens* A136 assays; notably, 12 Gram-negative biofilm-forming isolates (22.2%) were identified as medium- and long-chain AHL producers. For Gram-positive isolates, all tested strains induced luminescence in *V. harveyi* BB170, indicating the presence of AI-2 signaling molecules (Figure 2). The presence of AI-2 signaling in Gram-positive bacterial isolates, as detected using *V. harveyi* BB170 as a biosensor strain, is presented in Table S2.

Antimicrobial Activity of Natural Compounds

The antimicrobial activity of natural compounds was tested against selected strong biofilm-forming isolates and reference strains. *C. officinalis*, propolis, nisin, and *H. perforatum* exhibited inhibition zones ranging between 7 and 10 mm, demonstrating moderate antimicrobial activity. In contrast, no inhibition zones

were observed for *C. sinensis*, *P. ginseng*, vanillin, curcumin, *G. lucidum*, *P. vulgaris*, or *S. nigra* extracts (Table 1).

QQ Activity

Several natural compounds exhibited QQ potential. Camellia sinensis extract produced the largest inhibition zone against AHL-mediated signaling, while propolis and apple vinegar also demonstrated inhibitory effects. Interestingly, nisin showed strong inhibition against long-chain AHLs, with a mean zone of 26.5 mm. AI-2 inhibitory activity varied, with propolis and apple vinegar showing inhibition ratios comparable to 70% ethanol, whereas *S. nigra* extract was the least effective (Table 2; Figure 3).

MIC, MBC and Growth Inhibition Profiles of Natural Compounds

MIC and MBC assays confirmed the antimicrobial efficacy of selected natural compounds. *C. officinalis* showed the highest inhibition against *E. coli* ATCC 25922 (72.4%), while propolis demonstrated strong inhibition against *S. lactis* (97.2%). In contrast, *H. perforatum* was generally less effective. Overall, propolis and *C. officinalis* possess both antimicrobial and QQ properties, supporting their potential use in food processing environments (Table 3).

Discussion

The high prevalence of strong biofilm formation among dairy-associated isolates confirms that structured microbial communities remain a persistent risk in food processing environments (Carrascosa et al., 2021; İpek & Zorba, 2018). The predominance of *Bacillus* and *Pseudomonas* species aligns with previous reports describing these genera as recurrent and resilient contaminants in dairy systems (İpek & Zorba, 2018). However, beyond structural persistence, the detection of QS signals emphasizes the regulatory role of microbial communication in maintaining biofilm stability (Suntharalingam & Cvitkovitch, 2005).

The observed differences between AHL- and AI-2–mediated signaling indicate distinct regulatory mechanisms. AHL systems, typically associated with Gram-negative bacteria, are closely linked to biofilm maturation and virulence-related traits (Castillo-

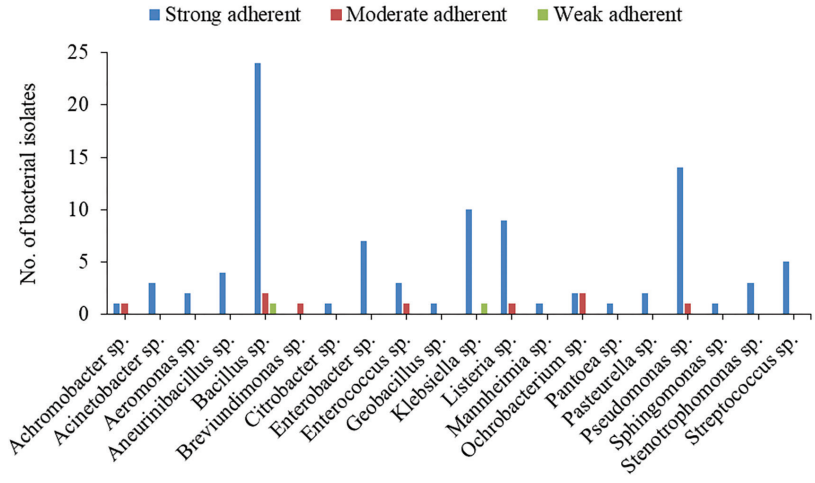

Figure 1. The number of bacterial isolates from different genera capable of forming biofilms.

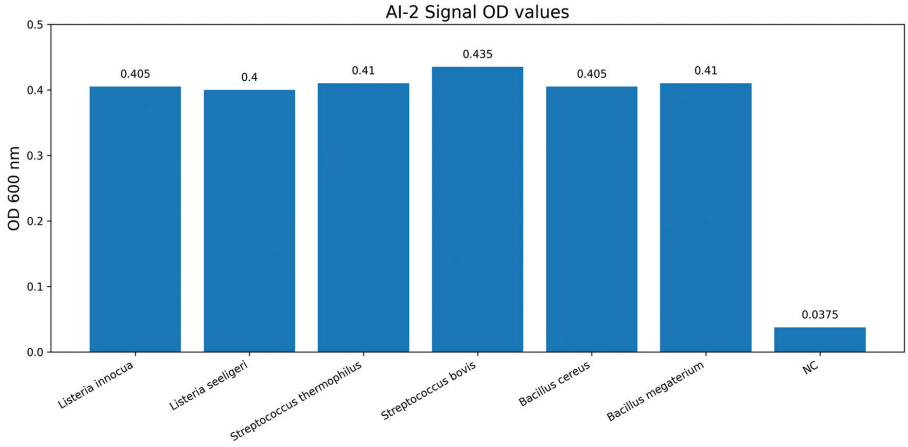

Figure 2. AI-2 signal detection using *Vibrio harveyi* BB170 for Gram-positive bacterial isolates (selected samples).
AI-2 = autoinducer-2; OD = optical density.

Table 1. Antimicrobial effects: inhibition zone values (mm) of natural compounds' extracts (n = 4).

Strains	***Calendula officinalis****	***Propolis****	***Resveratrol****	***Nisin****	***Hypericum perforatum****	***Thymus vulgaris****	***Cichorium intybus****	***Apple vinegar****
Listeria innocua (1)	9.0 (±0.0)	9.0 (±0.0)	10.0 (±0.0)	9.5 (±0.5)	8.5 (±0.5)	7.0 (±0.0)	<6.0	7.5 (±0.5)
Enterobacter cloacae (6)	8.0 (±0.0)	8.0 (±0.0)	7.5 (±0.5)	7.0 (±0.0)	7.0 (±0.0)	8.5 (±0.5)	<6.0	<6.0
Pseudomonas stutzeri (18)	9.0 (±0.0)	9.0 (±0.0)	< 6.0	7.0 (±0.0)	8.0 (±0.0)	<6.0	<6.0	7.0 (±0.0)
Streptococcus lactis (27)	7.0 (±0.0)	9.0 (±0.0)	7.5 (±0.5)	10.0 (±0.0)	9.0 (±0.0)	8.5 (±0.5)	<6.0	<6.0
Bacillus coagulans (32)	8.0 (±0.0)	8.0 (±0.0)	<6.0	7.5 (±0.5)	8.0 (±1.0)	7.0 (±0.0)	<6.0	<6.0
Pseudomonas aeruginosa ATCC 27853	10.0 (±0.0)	7.5 (±0.5)	<6.0	7.0 (±0.0)	7.5 (±0.5)	7.0 (±0.0)	7.0 (±0.0)	<6.0
Staphylococcus aureus ATCC 6538P	9.0 (±0.0)	10.0 (±0.0)	9.0 (±0.0)	9.0 (±1.0)	10.0 (±0.0)	10.0 (±0.0)	8.0 (±0.0)	<6.0
Micrococcus luteus ATCC 4698	9.0 (±0.0)	8.0 (±0.0)	8.0 (±0.0)	8.0 (±0.0)	7.0 (±0.0)	7.0 (±0.0)	<6.0	8.0 (±0.0)
Escherichia coli ATCC 25922	9.0 (±0.0)	8.5 (±0.5)	<6.0	7.0 (±0.0)	7.0 (±0.0)	< 6.0	8.0 (±0.0)	<6.0

*Mean (± standard deviation).

Table 2. AHL QQ Effects: Inhibition zone values (mm) of natural compounds' extracts.

Natural compounds	**Small-chain AHL* (*Chromobacterium violaceum* CV026)**	**Middle/long-chain AHL* (*Agrobacterium tumefaciens* A136)**
Vanillin	11.5 (±0.5)	9.0 (±1.0)
Panax ginseng	11.0 (±1.0)	8.5 (±0.5)
Curcumin	9.0 (±0.0)	8.5 (±0.5)
Camellia sinensis	17.5 (±0.5)	10.0 (±0.0)
Propolis	8.0 (±1.0)	9.0 (±1.0)
Apple vinegar	13.0 (±0.5)	12.0 (±0.5)
Calendula officinalis	7.5 (±0.0)	13.5 (±0.5)
Thymus vulgaris	7.5 (±0.0)	9.5 (±0.5)
Hypericum perforatum	7.0 (±0.0)	8.0 (±0.5)
Resveratrol	8.5 (±1.0)	10.5 (±0.5)
Nisin	6.5 (±0.0)	26.5 (±0.5)
Blank	<6.0	<6.0

*Mean (± standard deviation); [v]alues are expressed as mean ± standard deviation. *Chromobacterium violaceum* CV026 and *Agrobacterium tumefaciens* A136 were used as indicator microorganisms for the detection of short-chain and medium-/long-chain AHLs, respectively.
Inhibition zones of *Cichorium intybus*, *Ganoderma lucidum*, *Prunella vulgaris*, and *Sambucus nigra* were <6 mm in both indicator systems.
AHL = N-acyl homoserine lactone.

Juárez et al., 2015; Si & Quan, 2017). In contrast, AI-2 signaling functions as a broader interspecies communication pathway and is frequently detected in Gram-positive bacteria via LuxS-dependent mechanisms (Sun et al., 2014). The coexistence of both systems in dairy environments may enhance multispecies biofilm coordination and resilience.

The inhibitory profiles of the tested agents differed between signaling systems. *C. officinalis* and propolis reduced both bacterial growth and QS-associated responses, suggesting interference with signal perception or receptor interaction, as previously described for plant-derived phytochemicals (Bouyahya et al., 2022; Shariati et al., 2024; Truchado et al., 2015). In some cases, AHL inhibition occurred without proportional antimicrobial activity, supporting a QQ effect independent of direct bactericidal action.

A notable finding was the pronounced inhibition of long-chain AHL signaling by nisin. Although nisin is primarily recognized for its bactericidal activity against Gram-positive bacteria through membrane pore formation, membrane destabilization may indirectly affect signal diffusion or receptor function, thereby influencing QS responses. While this interaction has not been fully elucidated, it is consistent with reports describing indirect QS modulation via membrane-active compounds (Hegstad et al., 2010).

The differences observed between Gram-negative and Gram-positive isolates likely reflect structural divergence in QS architectures. Gram-negative bacteria mainly rely on LuxI/LuxR-type AHL circuits, whereas Gram-positive species and mixed communities utilize AI-2–mediated communication (Castillo-Juárez et al., 2015; Sun et al., 2014). These regulatory differences may partly explain the strain-dependent variability observed in inhibition responses.

Given the environmental and health-related concerns associated with conventional disinfectants (Hegstad et al., 2010; Huang et al., 2012), natural extracts capable of targeting both microbial growth and communication pathways represent a promising alternative strategy for sustainable biofilm control in dairy processing systems.

This study is limited by its *in vitro* design and single-concentration screening approach, which does not permit dose–response analysis or detailed mechanistic clarification. Future studies should focus

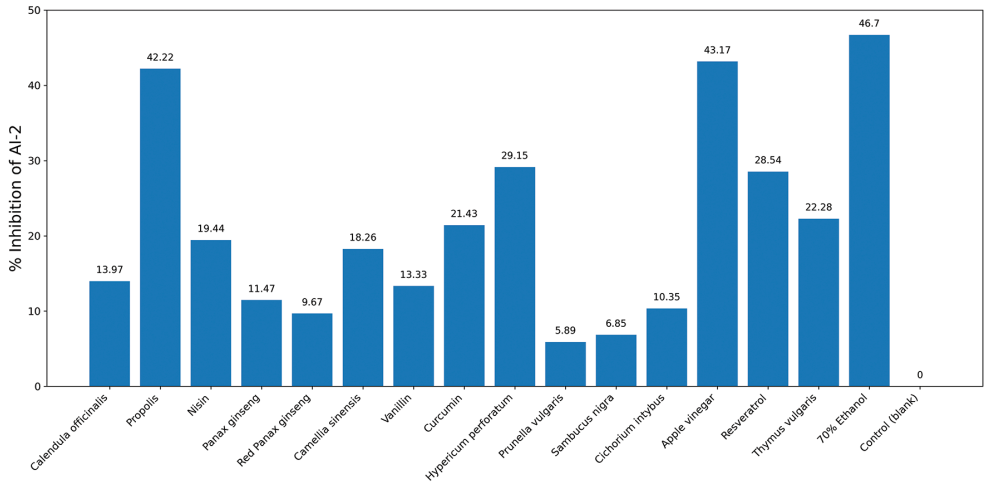

Figure 3. AI-2 signal inhibitory activity of natural compound extracts against the high AI-2–producing isolate Streptococcus bovis.
AI-2 = autoinducer-2.

Table 3. MIC, MBC, and inhibition ratio of natural compounds.

Strains	Comp ound*	MIC and MBC	Inhb.%	Comp ound*	MIC and MBC	Inhb.%	Comp ound*	MIC and MBC	Inhb.%
Listeria innocua (1)	1	500 µg/mL	21.2%	3	500 µg/mL	7.14%	5	500 µg/mL	18.9%
Enterobacter cloacae (6)	1	500 µg/mL	49.4%	3	500 µg/mL	7.5%	5	500 µg/mL	53.04%
Pseudomonas stutzeri (18)	1	500 µg/mL	38.8%	3	500 µg/mL	7.6%	5	500 µg/mL	43.4%
Streptococcus lactis (27)	1	500 µg/mL	33.6%	3	500 µg/mL	6.5%	5	500 µg/mL	48%
Bacillus coagulans (32)	1	500 µg/mL	21.7%	3	500 µg/mL	8.4%	5	500 µg/mL	26.2%
Staphylococcus aureus ATCC 6538 P	1	500 µg/mL	47.7%	3	500 µg/mL	7.6%	5	500 µg/mL	12.5%
Pseudomonas aeruginosa ATCC 27853	1	500 µg/mL	22.6%	3	500 µg/mL	11.7%	5	500 µg/mL	39.2%
Micrococcus luteus ATCC 4698	1	500 µg/mL	24%	3	500 µg/mL	8.9%	5	500 µg/mL	47.5%
Escherichia coli ATCC 25922	1	500 µg/mL	72.4%	3	500 µg/mL	6.5%	5	500 µg/mL	37.2%
L. innocua (1)	2	500 µg/mL	87.7%	4	500 µg/mL	21.6%	6	500 µg/mL	11.8%
E. cloacae (6)	2	500 µg/mL	44.2%	4	500 µg/mL	12.4%	6	500 µg/mL	17.01%
P. stutzeri (18)	2	500 µg/mL	53.6%	4	500 µg/mL	18.8%	6	500 µg/mL	16.5%
S. lactis (27)	2	500 µg/mL	97.2%	4	500 µg/mL	10.2%	6	500 µg/mL	8.5%
B. coagulans (32)	2	500 µg/mL	24.3%	4	500 µg/mL	15.1%	6	500 µg/mL	11.3%
S. aureus ATCC 6538 P	2	500 µg/mL	66.7%	4	500 µg/mL	8.7%	6	500 µg/mL	16.5%
P. aeruginosa ATCC 27853	2	500 µg/mL	28.6%	4	500 µg/mL	18.2%	6	500 µg/mL	10.5%
M. luteus ATCC 4698	2	500 µg/mL	27.5%	4	500 µg/mL	14.1%	6	500 µg/mL	34%
E. coli ATCC 25922	2	500 µg/mL	14.8%	4	500 µg/mL	16.5%	6	500 µg/mL	8.8%

*(1) *Calendula officinalis* L.; (2) Propolis; (3) Resveratrol; (4) *Thymus vulgaris* L.; (5) Nisin; and (6) *Hypericum perforatum* L.
Inhb. = inhibition; MBC = minimum bactericidal concentration; MIC = minimum inhibitory concentration.

on identifying active constituents and validating their efficacy under industrial conditions.

Overall, the results support the potential of selected plant-derived extracts and natural-origin compounds as dual-function agents capable of disrupting both bacterial viability and QS-regulated biofilm persistence in dairy environments.

Conclusion

This study revealed that biofilm formation is widespread among bacterial isolates from dairy process lines, with *Bacillus* and *Pseudomonas* species being the most dominant. Selected plant-derived extracts and natural-origin compounds, particularly *C. officinalis* and propolis, showed strong antimicrobial and QQ activities by inhibiting both AHL- and AI-2-mediated signaling

pathways. These findings highlight the potential of natural products as eco-friendly alternatives to chemical disinfectants for maintaining hygiene and controlling biofilm-associated risks in the food industry.

Future research should focus on identifying the specific active constituents responsible for QQ activity and evaluating their effectiveness under real industrial conditions. Integration of natural products into sanitation protocols could provide sustainable and consumer-acceptable strategies to improve food safety and reduce environmental impact.

Acknowledgements

We would like to thank the research team of the Water Treatment and Membrane Laboratory, Department of Environmental Engineering, Konkuk University, Seoul, Korea, for their valuable cooperation during the QSI study. Special thanks are extended to Harshad Lade for his support through the KU Research Professor Program of Konkuk University.

Ethics

Ethics Committee Approval: Since the article does not contain any studies with human or animal subjects, ethics committee approval was not required.

Data Sharing Statement: All data are available within the study and in the Supplementary Material.

Footnotes

Authorship Contributions: Conceptualization: D.İ., N.N.D.Z., J.H.K., and H.L.; Design/methodology: D.İ., N.N.D.Z., J.H.K., and H.L.; Execution/investigation: D.İ. and N.N.D.Z.; Resources/materials: N.N.D.Z. and J.H.K.; Data acquisition: D.İ. and H.L.; Data analysis/interpretation: D.İ., N.N.D.Z., and H.L.; Writing – original draft: D.İ. and H.L.; Writing – review & editing/critical revision: D.İ., N.N.D.Z., and J.H.K.

Conflict of Interest: The author(s) have no conflicts of interest to declare.

Funding: The study was supported by the Scientific Research Project Commission of Çanakkale Onsekiz Mart University (project numbers: FBA-2014-332 and FBA-2016-908). Additional support was provided by the KU Research Professor Program of Konkuk University.

Supplementary Material: https://d2v96fxpocvxx.cloudfront.net/34c1fd7d-947b-4954-9ae2-39560c57d146/content-images/b920c590-521a-46b8-b1ea-fa0237fcc1df.pdf

References

Bouyahya, A., Chamkhi, I., Balahbib, A., Rebezov, M., Shariati, M. A., Wilairatana, P., Mubarak, M. S., Benali, T., & El Omari, N. (2022). Mechanisms, anti-quorum-sensing actions, and clinical trials of medicinal plant bioactive compounds against bacteria: A comprehensive review. *Molecules, 27*(5), 1484. https://doi.org/10.3390/molecules27051484

Carrascosa, C., Raheem, D., Ramos, F., Saraiva, A., & Raposo, A. (2021). Microbial biofilms in the food industry—A comprehensive review. *International Journal of Environmental Research and Public Health, 18*(4), 2014. https://doi.org/10.3390/ijerph18042014

Castillo-Juárez, I., Maeda, T., Mandujano-Tinoco, E. A., Tomás, M., Pérez-Eretza, B., García-Contreras, S. J., & García-Contreras, R. (2015). Role of quorum sensing in bacterial infections. *World Journal of Clinical Cases, 3*(7), 575–598. https://doi.org/10.12998/wjcc.v3.i7.575

Christensen, G. D., Simpson, W., Younger, J., Baddour, L. M., Barrett, F. F., Melton, D. M., & Beachey, E. H. (1985). Adherence of coagulase-negative staphylococci to plastic tissue culture plates: A quantitative model for the adherence of staphylococci to medical devices. *Journal of Clinical Microbiology, 22*(6), 996–1006. https://doi.org/10.1128/jcm.22.6.996-1006.1985

European Committee on Antimicrobial Susceptibility Testing. (2014). *Breakpoint tables for interpretation of MICs and zone diameters* (Version 4). https://www.eucast.org

Fydrych, D., Jeziurska, J., Wełna, J., & Kwiecińska-Piróg, J. (2025). Potential use of selected natural compounds with anti-biofilm activity. *International Journal of Molecular Sciences, 26*(2), 607. https://doi.org/10.3390/ijms26020607

Hegstad, K., Langsrud, S., Lunestad, B. T., Scheie, A. A., Sunde, M., & Yazdankhah, S. P. (2010). Does the wide use of quaternary ammonium compounds enhance the selection and spread of antimicrobial resistance and thus threaten our health? *Microbial Drug Resistance, 16*(2), 91–104. https://doi.org/10.1089/mdr.2009.0123

Huang, T. P., Tzeng, D. D. S., Wong, A. C., Chen, C. H., Lu, K. M., Lee, Y. H., Tsai, S. F., & Tzeng, K. C. (2012). DNA polymorphisms and biocontrol of *Bacillus* antagonistic to citrus bacterial canker with indication of the interference of phyllosphere biofilms. *PLoS ONE, 7*(7), e42124. https://doi.org/10.1371/journal.pone.0042124

İpek, D. (2017). *Applicability of Ezine cheese process lines disinfection by new disinfectant formulas: Antibiofilm-antiquorum sensing agents* (Doctoral dissertation, Çanakkale Onsekiz Mart University, Turkey).

İpek, D. (2023). Detection and evaluation of quorum sensing signal molecules (AHL and AI-2) in biofilm-forming bacteria isolated from food-related environments. *Trakya University Journal of Natural Sciences, 24*(2), 159–170. https://doi.org/10.23902/trkjnat.1276562

İpek, D., & Zorba, N. N. D. (2018). Microbial load of white cheese process lines after CIP and COP: A case study in Turkey. *LWT–Food Science and Technology, 90*, 505–512. https://doi.org/10.1016/j.lwt.2017.12.062

Jeong, S. H., Lee, H. J., Kim, D. W., & Chung, Y. J. (2018). New biocide for eco-friendly biofilm removal on outdoor stone monuments. *International Biodeterioration & Biodegradation, 131*, 19–28. https://doi.org/10.1016/j.ibiod.2018.03.021

Kavanaugh, N. L., & Ribbeck, K. (2012). Selected antimicrobial essential oils eradicate *Pseudomonas* spp. and *Staphylococcus aureus* biofilms. *Applied and Environmental Microbiology, 78*(11), 4057–4061. https://doi.org/10.1128/AEM.07549-11

Lade, H., Paul, D., & Kweon, J. H. (2014). Isolation and molecular characterization of biofouling bacteria and profiling of quorum sensing signal molecules from membrane bioreactor activated sludge. *International Journal of Molecular Sciences, 15*(2), 2255–2273. https://doi.org/10.3390/ijms15022255

Lin, W. C., Deng, J. S., Huang, S. S., Wu, S. H., Lin, H. Y., & Huang, G. J. (2017). Evaluation of antioxidant, anti-inflammatory and anti-proliferative activities of ethanol extracts from different varieties of *Sanghuang* species. *RSC Advances, 7*(13), 7780–7788. https://doi.org/10.1039/C6RA27198G

Mihalik, K., Chung, D. W., Crixell, S. H., McLean, R. J. C., & Vattem, D. A. (2008). Quorum sensing modulators of *Pseudomonas aeruginosa* characterized in *Camellia sinensis*. *Asian Journal of Traditional Medicine, 3*(12), 23–28. https://www.researchgate.net/publication/298435911_Quorum_sensing_modulators_of_Pseudomonas_aeruginosa_characterized_in_Camellia_sinensis

Park, H., Yeo, S., Ji, Y., Lee, J., Yang, J., Park, S., Shin, H., & Holzapfel, W. (2014). Autoinducer-2 associated inhibition by *Lactobacillus sakei* NR28 reduces virulence of enterohaemorrhagic *Escherichia coli* O157:H7. *Food Control, 45*, 62–69. https://doi.org/10.1016/j.foodcont.2014.04.029

Shariati, A., Noei, M., Askarinia, M., Khoshbayan, A., Farahani, A., & Chegini, Z. (2024). Inhibitory effect of natural compounds on quorum sensing

system in *Pseudomonas aeruginosa*: A helpful promise for managing biofilm community. *Frontiers in Pharmacology, 15*, 1350391. https://doi.org/10.3389/fphar.2024.1350391

Si, X., & Quan, X. (2017). Prevention of multi-species wastewater biofilm formation using vanillin and EPS disruptors through non-microbicidal mechanisms. *International Biodeterioration & Biodegradation, 116*, 211–218. https://doi.org/10.1016/j.ibiod.2016.10.002

Sun, Z., He, X., Brancaccio, V. F., Yuan, J., & Riedel, C. U. (2014). *Bifidobacteria* exhibit LuxS-dependent autoinducer 2 activity and biofilm formation. *PLoS ONE, 9*(2), e88260. https://doi.org/10.1371/journal.pone.0088260

Suntharalingam, P., & Cvitkovitch, D. G. (2005). Quorum sensing in streptococcal biofilm formation. *Trends in Microbiology, 13*(1), 3–6. https://doi.org/10.1016/j.tim.2004.11.009

Truchado, P., Larrosa, M., Castro-Ibáñez, I., & Allende, A. (2015). Plant food extracts and phytochemicals: Their role as quorum sensing inhibitors. *Trends in Food Science & Technology, 43*(2), 189–204. https://doi.org/10.1016/j.tifs.2015.02.009

Zhu, H., Du, M., Fox, L., & Zhu, M. J. (2016). Bactericidal effects of *Cinnamomum cassia* oil against bovine mastitis bacterial pathogens. *Food Control, 66*, 291–299. https://doi.org/10.1016/j.foodcont.2016.02.027

Trakya University Journal of Natural Sciences, 27(1), 96–103, 2026
DOI: 10.23902/trkjnat.202578
www.tujns.org

Research Article

Amylase activity and carbohydrate accumulation in seeds of *Afzelia africana* Sm. and *Gambeya albida* (G. Don) Aubrév. & Pellegr. during desiccation

Blessing Alfred Ngele[1]*, Anobeja Effa[1], Ani Essien Nkang[2]

[1]*University of Calabar, Department of Plant and Ecological Studies, Calabar, Nigeria*
[2]*Arthur Jarvis University, Department of Biological Sciences, Akpabuyo, Nigeria*

Cite this article as: Ngele, B. A., Effa, A., & Nkang, A. E. (2026). Amylase activity and carbohydrate accumulation in seeds of *Afzelia africana* Sm. and *Gambeya albida* (G. Don) Aubrév. & Pellegr. during desiccation. *Trakya University Journal of Natural Sciences, 27*(1), 96–103. https://doi.org/10.23902/trkjnat.202578

Abstract

Background: Desiccation is a critical factor influencing seed viability and storage potential. Among the physiological changes accompanying seed drying are alterations in carbohydrate reserves and the activities of carbohydrate metabolizing enzymes.

Aims: This study investigated changes in reducing sugar and starch content, as well as the activities of α-amylase, β-amylase, and total amylases, in the seeds of two tropical timber species, *Afzelia africana* Sm. and *Gambeya albida* (G. Don) Aubrév. & Pellegr., during progressive desiccation.

Methods: Mature seeds were harvested directly from parent trees and desiccated under ambient conditions for 0, 3, 7, 10, 13, 15, 22, and 35 days. Germination capacity, carbohydrate levels, and amylolytic activities were assessed at each desiccation interval.

Results: Germination in *A. africana* increased gradually with desiccation, whereas seeds of *G. albida* exhibited high initial germination that declined significantly ($p \leq 0.05$) following moisture loss. Reducing sugar levels were consistently higher in *G. albida* than in *A. africana*, while starch content increased in *A. africana* but declined in *G. albida* during later stages of desiccation. Activities of α-amylase, β-amylase and total amylases increased during early desiccation (0–7 days) in both species, followed by a significant ($p \leq 0.05$) decline, with *A. africana* exhibiting higher overall amylolytic activity. These results indicate contrasting carbohydrate metabolic responses to desiccation, consistent with orthodoxlike behavior in *A. africana* and recalcitrant behavior in *G. albida*.

Özet

Dayanak: Kurutma, tohumların canlılığını ve depolama potansiyelini etkileyen kritik bir faktördür. Tohum kurutulmasıyla birlikte meydana gelen fizyolojik değişiklikler arasında karbonhidrat rezervlerinde ve karbonhidrat metabolize eden enzimlerin aktivitelerinde meydana gelen değişiklikler bulunmaktadır.

Amaçlar: Bu çalışmada, iki tropikal ağaç türü olan *Afzelia africana* Sm. ve *Gambeya albida* (G. Don) Aubrév. & Pellegr. türlerinin tohumlarında, aşamalı kurutma sırasında indirgen şeker ve nişasta içeriğindeki değişiklikler ile α-amilaz, β-amilaz ve toplam amilazların aktiviteleri incelenmiştir.

Yöntemler: Olgun tohumlar doğrudan ana ağaçlardan hasat edilmiş ve ortam koşullarında 0, 3, 7, 10, 13, 15, 22 ve 35 gün boyunca kurutulmuştur. Her kurutma aralığında çimlenme kapasitesi, karbonhidrat seviyeleri ve amilolitik aktiviteler değerlendirilmiştir.

Bulgular: *A. africana*'da çimlenme kuruma ile birlikte kademeli olarak artarken, *G. albida* tohumları yüksek bir başlangıç çimlenme oranı sergilemiş, ancak nem kaybının ardından önemli ölçüde ($p \leq$ 0,05) azalmıştır. Azaltıcı şeker seviyeleri *G. albida*'da *A. africana*'ya göre sürekli olarak daha yüksekken, nişasta içeriği *A. africana*'da artmış, ancak *G. albida*'da kurumanın ilerleyen aşamalarında azalmıştır. α-amilaz, β-amilaz ve toplam amilaz aktiviteleri her iki türde de erken kurutma aşamasında (0–7 gün) arttı, ardından önemli ($p \leq 0,05$) bir düşüş gerçekleşti, *A. africana* ise daha yüksek toplam amilolitik aktivite gösterdi. Bu sonuçlar, kurutmaya karşı zıt karbonhidrat metabolik tepkileri olduğunu göstermektedir ve bu,

Edited by: *Cem Vural*
***Corresponding Author:** Blessing Alfred Ngele, **E-mail:** blessingalfredngele@gmail.com*
***ORCID iDs of the author(s):** BAN. 0000-0001-6229-6757; AE. 0009-0000-7648-0432; AEN. 0000-0002-5854-3927*

Received: 18 August 2025, **Accepted:** 3 March 2026, **Epub:** 10 April 2026, **Published:** 24 April 2026

Conclusion: The findings provide physiological insight relevant to seed storage and reforestation strategies for tropical forest species.

A. africana'nın ortodoks benzeri davranışıyla ve *G. albida*'nın dirençli davranışıyla tutarlıdır.

Sonuç: Bulgular, tropikal orman türleri için tohum depolama ve yeniden ağaçlandırma stratejileri ile ilgili fizyolojik bilgiler sağlamaktadır.

Keywords: Seed desiccation tolerance, carbohydrate metabolism, germination response, seed storage behavior

Introduction

Afzelia africana Sm. and *Gambeya albida* (G. Don) Aubrév. & Pellegr. are tropical rainforest timber species. *A. africana*, commonly referred to as African mahogany, is a large deciduous woody species threatened by overexploitation and poor natural regeneration in its native habitats (Padonou et al., 2013). It is a leguminous tree of the family Fabaceae and subfamily Caesalpiniaceae, occurring in both humid and dry forest ecosystems (Umedum et al., 2014). Every part of the plant is valuable. The species produces high quality timber, which is termite resistant but somewhat difficult to work; the seeds contain approximately 31% fat and have potential as a source of oil for both domestic and industrial applications. The seeds are also ground into flour for various culinary uses. The leaves serve as forage and food, while decoctions made from the flowers and roots are traditionally used to treat various ailments. Despite its usefulness, this plant is under threat due to overexploitation, urban expansion, and the degradation of natural forests. It is classified as *Vulnerable* by the International Union for Conservation of Nature (2004). *G. albida*, commonly known as white star apple, is a forest fruit tree belonging to the family Sapotaceae. It possesses significant economic value, particularly due to findings that jams made from its pulp could rival commercial raspberry jams and jellies. Additionally, the seed oil has various applications (Amusa et al., 2003). The fruit is also a rich source of natural antioxidants, contributing to health by combating oxidative stress related diseases (Burits & Bucar, 2000). The timber of *G. albida* is very dense, moderately strong and fairly durable (Etukudo, 2003). The seeds are edible and used locally in soup thickening. The leaves are an excellent fodder and fruit pods are good fuel wood.

Seeds are essential components of plant production systems, serving both direct planting needs and, seedling production and propagation. While certain seeds can be stored without losing viability, others are highly desiccation sensitive and have limited storage potential, restricting their usage in production systems (Hay & Probert, 2013). In the case of *A. africana* and *G. albida*, that both inhabit tropical forests and produces fruits shortly before the onset of the dry season, responses to seed desiccation is important because natural seedling regeneration depends on the moisture content (MC) of the forest floor.

Although some studies have reported that seeds of *A. africana* exhibit desiccation sensitivity under specific conditions (Adelani et al., 2017), available evidence on its seed storage behavior remains inconclusive. Consequently, the present study adopts a physiological perspective, examining MC and germination relationships alongside metabolic responses during progressive drying, rather than assuming a predefined storage classification. In contrast, seeds of *G. albida* have consistently been described as desiccation sensitive, with marked declines in germination observed as seed MC decreases (Adelani et al., 2017). While the general processes regulating responses to desiccation in tropical forest species have been described, the mechanisms governing seed desiccation responses in tropical forest species have not been well documented (Daws et al., 2011). Current studies on other recalcitrant taxa show that desiccation interferes with energy metabolism, osmotic balance, leading to a breakdown of regulatory proteins (Berjak & Pammenter, 2013), while orthodox seeds accumulate protective soluble sugars and carbohydrates to maintain cellular structure (Farrant & Moore, 2011). These varying responses reveal the specific biochemical responses to desiccation and the need for a direct physiological assessment rather than generalizing unrelated taxa (Berjak & Pammenter, 2013).

Although there are suggestions that both *A. africana* and *G. albida* are sensitive to desiccation, there is no published study that has examined how carbohydrate metabolizing enzymes, in particular amylase and reserve carbohydrates (sugar and starch), change during drying in these species. This is a critical gap in knowledge because carbohydrate metabolism plays a major role in the acquisition or loss of desiccation tolerance (Berjak & Pammenter, 2013). Also, without species specific biochemical data, the physiological basis of desiccation sensitivity in these economically and ecologically important species remains unclear. Therefore, this study addresses this gap by investigating amylase activity and carbohydrate accumulation during progressive desiccation of seeds of both species. The research objectives are to quantify changes in MC during specific desiccation intervals; determine the amylase activity in response to desiccation; assess the changes in reducing sugar and starch accumulation during desiccation; and relate these changes to potential desiccation tolerance or sensitivity in both species.

Materials and Methods

Study Area/Experimental Site

The study was conducted in Calabar, the capital city of Cross River State, Nigeria. Laboratory analyses were performed at the Graduate Research Laboratory, Department of Plant and Ecological Studies, Faculty of Biological Sciences, University of Calabar.

Seed Preparation/Desiccation

Mature fruits of *A. africana* and *G. albida*, were harvested directly from the tree stands within Calabar metropolis. The fruits were de-pulped to obtain their seeds. The seeds were desiccated under ambient conditions on a laboratory bench for 0, 3, 7, 10, 13, 15, 22,

and 35 days; with average daytime temperatures of approximately 28 to 32 °C, relative humidity ranging between 60 to 75%, and natural sunlight exposure filtered through the screen house. On each of these sampling dates, twenty seeds of each species were randomly picked and weighed to obtain their fresh weight. Seeds were oven dried at 103 ± 2 °C until constant weight, following standard seed moisture determination protocols (Association of Official Analytical Chemists [AOAC], 2006). The fresh and dry weights obtained were used to calculate the percentage MC of the seed lot. MC was calculated adopting Somrug et al. (2024) as

$$MC\ (\%) = \frac{\text{fresh weight} - \text{dry weight}}{\text{fresh weight}} \times 100$$

Desiccation and Germination Tests

Forty seeds were sown in germination trays at each desiccation level to investigate their germination potentials. The seeds were steeped in water for 12 h before sowing. An equal mixture of smooth sea sand and sawdust was used as the growth medium; 2 kg of the planting medium was weighed into germination trays and laid out in a complete randomized design, replicated three times. The germination of the planted seeds was observed daily, and germination counts were recorded daily. The emergence of radicle through the seed coat was the criterion for germination. The germination records were used in computing the percentage maximum germination (G_{max}) after Ngele et al. (2024) as follows:

$$G_{max}\ (\%) = \frac{\text{number of germinated seeds}}{\text{total number of sown seeds}} \times 100$$

Determination of Reducing Sugars and Starch

The seeds employed for sugar and starch extraction were dried at 60 °C for 24 hours. Sugar and starch concentration in seeds on collection and following desiccation was assayed using the dinitrosalicylic acid (DNS) method (AOAC, 2006) with 1% glucose solution as standard.

Calibration Curve for Sugar

Serial dilutions of the 1% glucose solution were prepared to obtain glucose concentrations of 0, 2, 4, and 6 mg/mL in labeled test tubes. To each of the test tubes were added 1 mL DNS reagent and 2 mL of 1.5% NaOH, and brought to boil for five minutes. The resultant solutions were allowed to cool and the absorbance readings determined spectrophotometrically at 540 nm wavelength. The absorbance readings obtained were plotted against sugar concentration to obtain a calibration curve.

Determination of Reducing Sugars

Reducing sugars were extracted using 80% ethanol. Precisely 0.2 g of dried cotyledonary tissue (dried at 60 °C) from seeds of each species was ground in 5 mL of 80% ethanol. The homogenate was centrifuged at 4000 rpm for 5 minutes. In a test, 0.5 mL of the resulting sugar extract was mixed with 1 mL of DNS reagent and 2 mL of 1.5% NaOH. The mixture was then heated in a water bath for 5 minutes. Reducing sugar content (µmol g^{-1} dry weight) was estimated spectrophotometrically at 540 nm, and concentrations were determined using a standard calibration curve prepared from 1% glucose solution.

Starch Determination

Starch present in the insoluble residue following sugar extraction was solubilized with 1 M NaOH and subsequently neutralized with 1 M acetic acid. The starch content (µmol g^{-1} dry weight) was then determined by acid hydrolysis using 0.5 mL of 1 M HCl, followed by the colorimetric estimation of the resulting reducing sugars.

Determination of Alpha, Beta and Total Amylolytic Activities in Seeds

Enzyme Extraction

The extraction buffer was composed of 50 mM mixed phosphate buffer (prepared from monobasic potassium phosphate [KH_2PO_4], and dibasic potassium phosphate [K_2HPO_4] salts), containing 1% (w/v) polyvinyl polypyrrolidone (PVPP), a phenolic binding agent. The pH was adjusted to 7.0 at 30 °C (Ngele et al., 2024). To prepare the extraction buffer, 2.613 g of K_2HPO_4 was dissolved in 300 mL of distilled water, and 2.042 g of KH_2PO_4 was dissolved in another 300 mL of distilled water. The two solutions were then combined and 6 g of PVPP was added. The buffer was stored refrigerated until used. For enzyme extraction, 0.5 g of cotyledonary seed tissue from each species at specified desiccation intervals was homogenized in 5 mL of cold extraction buffer. The homogenate was first for 5 minutes, and the resulting filtrate was centrifuged again under the same conditions. The final supernatant was kept on ice and served as the crude enzyme extract.

Enzyme Assay

Amylase activity was assessed by measuring the amount of reducing sugars released from soluble starch and expressed as µmol of glucose equivalents g^{-1} dry weight produced in 10 minutes at 25 °C, using 600 µL of crude enzyme extract, following the procedure described by Nkang (2002).

To determine α-amylase activity, β-amylase was selectively inactivated by heating the crude enzyme extract at 70 °C for 30 minutes, a temperature previously reported to preferentially inactivate β-amylase while retaining α-amylase activity in plant tissues (Nkang, 2002). A reaction mixture containing 0.1 mL of 1% (w/v) soluble starch and 600 µL of the heat-treated enzyme extract was incubated at 25 °C for 10 minutes. The reaction was terminated by adding 1 mL of DNS reagent followed by 2 mL of 1.5% sodium hydroxide, and the mixture was boiled for 2 minutes. Absorbance was measured at 540 nm, and α-amylase activity was quantified using a glucose standard curve and expressed on a dry weight basis (µmol reducing sugar released g^{-1} dry weight min^{-1}).

For β-amylase activity, α-amylase was selectively inhibited by incubating the crude enzyme extract with 25 mM ethylenediaminetetraacetic acid (EDTA) at 25 °C for 30 min, as EDTA chelates divalent cations required for α-amylase activity, thereby allowing preferential estimation of β-amylase (Nkang,

2002). A reaction mixture comprising 0.1 mL of 1% soluble starch and 600 µL of the treated enzyme preparation was incubated at 25°C for 10 min. The reaction was stopped by adding 1 mL of DNS reagent and 2 mL of 1.5% sodium hydroxide, followed by boiling for 2 min. The absorbance was read at 540 nm, and β-amylase activity was expressed as µmol reducing sugar released g^{-1} dry weight min^{-1}.

Total amylase activity was assayed using untreated enzyme extract. A reaction mixture containing 2 mL of assay buffer, 600 µL of enzyme extract, and 0.1 mL of 1% soluble starch was incubated at 25 °C for 10 minutes. The reaction was terminated as described above, and absorbance was recorded at 540 nm. Total amylase activity was calculated from the glucose standard curve and expressed on a dry weight basis (µmol reducing sugar released g^{-1} dry weight min^{-1}).

All enzyme assays were conducted in triplicate. While no separate inhibition controls were included, the use of heat treatment and EDTA for selective estimation of α- and β-amylase followed previously validated protocols, and the approach provides comparative rather than absolute measures of enzyme activity during desiccation.

Statistical Analysis

All experiments were conducted using a completely randomized design. Data obtained from MC, germination percentage, carbohydrate concentrations, and amylase activities were based on three independent replicates and are presented as mean ± standard error of the mean. Statistical analyses were performed using the Statistical Package for Social Sciences for Windows, version 20.1.

Differences among desiccation intervals and between species were evaluated using one way analysis of variance (ANOVA). When ANOVA indicated significant treatment effects, mean separation was performed using Duncan's Multiple Range Test (DMRT) at a significance level of $p \leq 0.05$. DMRT was selected because of its sensitivity in detecting treatment wise differences across multiple desiccation intervals, allowing effective discrimination of gradual physiological changes associated with progressive drying. This approach is commonly applied in plant physiological and seed biology studies where treatments represent ordered stress gradients rather than independent categorical factors.

Results

MC and Germinability of *A. africana* and *G. albida* Seeds After Desiccation

The MC levels in seeds of *A. africana* and *G. albida* on collection and following desiccation are presented in Table 1. Seeds of *G. albida* had relatively higher MC on collection (40.04%) compared to *A. africana* (13.81%). MC declined significantly ($p \leq 0.05$) throughout the desiccation period in seeds of *G. albida*. In *A. africana*, MC showed a gradual decline but remained relatively stable during the later desiccation stages (days 15–35). Germination capacity gradually improved with desiccation, reaching its maximum at 15 days (90.00%) when MC was 4.86%.

However, a significant decline in G_{max} ($p \leq 0.05$) was observed at 22 and 35 days of desiccation, coinciding with a further reduction in MC to approximately 4%. In *G. albida* G_{max} was significantly higher ($p \leq 0.05$) on collection (76.67%) but declined gradually with desiccation. No germination occurred after 13 days at MC below 26.7%.

Reducing Sugar Content in Seeds of *A. africana* and *G. albida* During Desiccation

The reducing sugar content in seeds of *A. africana* was lower than that of *G. albida* across the desiccation period (Figure 1). A significant increase ($p \leq 0.05$) in reducing sugars was observed in *A. africana*, peaking at 7 days (3.69 µmol g^{-1} dry weight), after which sugar levels declined.

Overall, *G. albida* seeds maintained consistently higher reducing sugar levels, indicating species specific differences in carbohydrate behavior. Reducing sugar content increased significantly ($p \leq 0.05$) from 0 to 3 days in *G. albida*, with the highest levels at 3 days. Although sugar levels declined afterward, there was a secondary

Table 1. MC and G_{max} of *A. africana* and *G. albida* seeds during desiccation.

Desiccation period (days)	*A. africana*		*G. albida*	
	MC (%)	G_{max} (%)	MC (%)	G_{max} (%)
0	$13.81^{a} \pm 0.62$	$66.28^{bcd} \pm 0.23$	$40.04^{a} \pm 0.34$	$76.67^{a} \pm 3.33$
3	$8.36^{b} \pm 0.24$	$71.67^{abcd} \pm 4.41$	$37.23^{b} \pm 0.18$	$56.67^{b} \pm 3.33$
7	$6.76^{c} \pm 0.08$	$79.67^{ab} \pm 5.78$	$34.77^{c} \pm 0.12$	$15.00^{c} \pm 2.89$
10	$6.36^{c} \pm 0.13$	$77.67^{abc} \pm 8.88$	$32.11^{d} \pm 0.19$	$11.67^{c} \pm 3.33$
13	$5.34^{d} \pm 0.15$	$85.00^{ab} \pm 2.89$	$27.63^{e} \pm 0.14$	$0.00^{d} \pm 0.00$
15	$4.86^{de} \pm 0.06$	$90.00^{a} \pm 5.77$	$25.56^{f} \pm 0.30$	$0.00^{d} \pm 0.00$
22	$4.23^{e} \pm 0.05$	$55.00^{d} \pm 8.66$	$10.31^{g} \pm 0.30$	$0.00^{d} \pm 0.00$
35	$4.03^{e} \pm 0.37$	$60.00^{cd} \pm 5.77$	$9.02^{h} \pm 0.07$	$0.00^{d} \pm 0.00$

Values represent the mean ± standard error of the mean of three replicates. Means within each column for a given species followed by different superscript letters are significantly different at $p \leq 0.05$ according to DMRT. Means sharing at least one common letter are not significantly different.
A. africana = *Afzelia africana*; DMRT = Duncan's Multiple Range Test; *G. albida* = *Gambeya albida*; G_{max} = maximum germination; MC = moisture content.

significant increase ($p \leq 0.05$) at 35 days (3.16 µmol g^{-1} dry weight) suggesting a possible delayed metabolic adjustment to prolonged desiccation.

Starch Content in Seeds of *A. africana* and *G. albida* During Desiccation

Starch content in *A. africana* increased markedly ($p \leq 0.05$) during early desiccation, with maximum concentration at 3 days (5.37 µmol g^{-1} dry weight), followed by a significant decrease ($p \leq 0.05$) between days 7–13 (Figure 2). Starch content then increased steadily ($p \leq 0.05$) from days 15–35. In *G. albida*, starch content increased slightly up to 3 days but not significantly, followed by a significant decline ($p \leq 0.05$) after that. This suggests distinct starch metabolism patterns between both species during desiccation.

Influence of Desiccation on Activities of Amylases in Seeds of *A. africana* and *G. albida*

Alpha-amylase activity in *A. africana* increased significantly ($p \leq 0.05$) from 0 to 3 days of desiccation (Figure 3). Activity then declined significantly ($p \leq 0.05$) between days 7–13, followed by a subsequent increase. In *G. albida*, alpha amylase activity increased significantly during the initial desiccation phase, peaking at 7 days, and subsequently declined. The delayed peak in *G. albida* (7 days) compared with *A. africana* (3 days) shows differences in the timing of enzyme responses in the two species.

Beta amylase activity in seeds of *A. africana* during desiccation followed a similar trend as that of alpha amylase, with significantly ($p \leq 0.05$) higher activity on the 3rd day of desiccation (Figure 4). Similarly, seeds of *G. albida* also demonstrated a significant ($p \leq .05$) increase in beta amylase activity with a peak at the 7th day of desiccation, thereafter activity declined.

Total amylase activity in *A. africana* increased significantly ($p \leq 0.05$), with the highest activity observed at 3 days (21.39 µmol reducing sugar released g^{-1} dry weight min^{-1}) (Figure 5). Activity decreased thereafter but showed slight significant increases ($p \leq 0.05$) between days 15–35. In *G. albida*, total amylase activity increased significantly at 0, 3, and 7 days having values of (2.40 µmol reducing sugar released g^{-1} dry weight min^{-1}, 9.47 µmol reducing sugar released g^{-1} dry weight min^{-1} and 12.72 µmol reducing sugar released g^{-1} dry weight min^{-1} respectively), followed by a significant decline. Generally, *A. africana* exhibited an earlier enzymatic peak, whereas *G. albida* showed delayed and brief increases (Table 2).

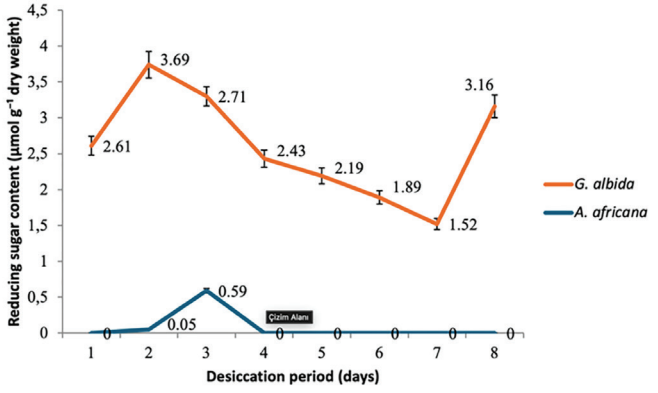

Figure 1. Content of reducing sugar (µmol g-¹ dry weight) in seeds of *A. africana* and *G. albida* during desiccation under ambient conditions; error bars indicate variability at $p \leq 0.05$.
A. africana = Afzelia africana; G. albida = Gambeya albida.

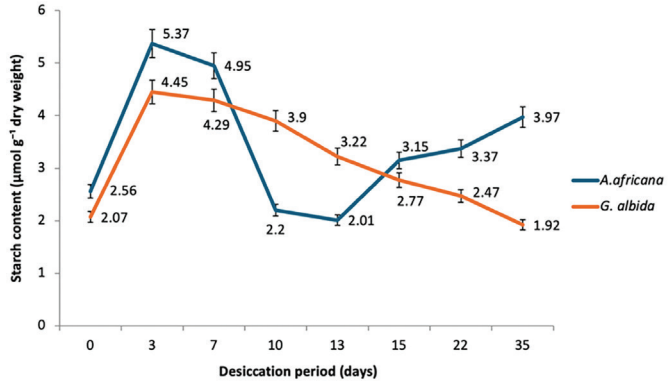

Figure 2. Starch content (µmol g-¹ dry weight) in seeds of *A. africana* and *G. albida* following desiccation; error bars indicate variability at $p \leq 0.05$.
A. africana = Afzelia africana; G. albida = Gambeya albida.

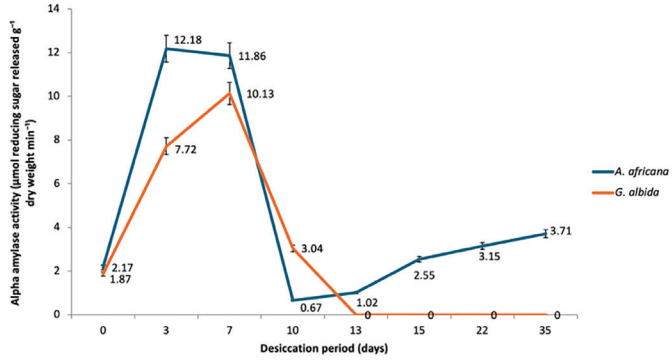

Figure 3. Alpha amylase activity (µmol reducing sugar released g-¹ dry weight min-¹) in seeds of *A. africana* and *G. albida* following desiccation; error bars indicate variability at $p \leq 0.05$.
A. africana = Afzelia africana; G. albida = Gambeya albida.

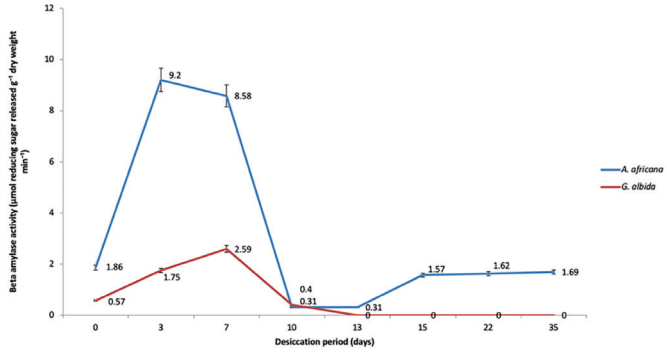

Figure 4. Beta amylase activity (µmol reducing sugar released g^{-1} dry weight min^{-1}) in seeds of *A. africana* and *G. albida* following desiccation; error bars indicate variability at $p \leq 0.05$.
A. africana = Afzelia africana; G. albida = Gambeya albida

Discussion

A. africana seeds exhibited significantly lower MC at collection (13.81%) compared with *G. albida* seeds (40.04%), indicating clear differences in seed water status at maturity. Such contrasts are commonly associated with differences in seed storage behavior. Orthodox seeds typically undergo maturation drying during late development, acquiring tolerance to substantial moisture loss, whereas recalcitrant seeds retain high MC and are sensitive to desiccation (Berjak & Pammenter, 2013; Maia et al., 2011). In the present study, the ability of *A. africana* seeds to retain high germination capacity at low moisture levels supports an orthodox-like response under the conditions tested, whereas the rapid loss of viability in *G. albida* during drying is consistent with recalcitrant behavior.

Reducing sugar content in *A. africana* seeds was relatively low both at collection and following desiccation, whereas *G. albida* maintained consistently higher levels. Previous studies have associated high concentrations of reducing sugars, particularly monosaccharides, with increased desiccation sensitivity, whereas oligosaccharides are more often linked to cellular stabilization during dehydration (Prajith et al., 2014; Whittaker et al., 2004). However, since only reducing sugars were quantified in this study, interpretations are restricted to observed changes in reducing sugar pools rather than specific protective sugars. The higher reducing sugar levels in *G. albida* may therefore reflect limited metabolic regulation during drying rather than an adaptive protective response. Although oligosaccharides such as raffinose have been implicated in desiccation tolerance in other species, these compounds were not directly measured in the present study and are therefore not considered further here.

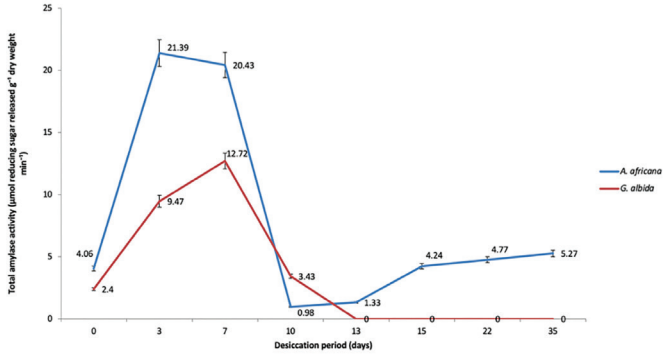

Figure 5. Total amylase activity (µmol reducing sugar released g^{-1} dry weight min^{-1}) in seeds of *A. africana* and *G. albida* following desiccation; error bars indicate variability at $p \leq 0.05$.
A. africana = Afzelia africana; G. albida = Gambeya albida.

The starch metabolism also differed markedly between the two species. Starch content increased during desiccation in *A. africana* but declined in *G. albida*, indicating contrasting patterns of carbohydrate reserve regulation. The accumulation of starch in *A. africana* during drying may reflect a capacity to maintain reserve stability under reduced water availability, whereas starch depletion in *G. albida* coincided with declining germination capacity. Activities of α-, β-, and total amylases increased during early desiccation (0–7 days) in both species, followed by a decline with prolonged drying. *A. africana* exhibited higher and more sustained amylolytic activity, suggesting greater metabolic resilience during dehydration. Similar temporal modulation of amylase activity in orthodox seeds has been reported under varying intensities of desiccation (Lee & Tan, 2020). In contrast, the sharp reduction in amylase activity observed in *G. albida* during the later stages of desiccation may indicate the loss of metabolic integrity, a feature commonly reported in recalcitrant tropical seeds (Nguyen et al., 2023). Although reducing sugars interact with oxidative metabolism in plants, we did not assess reactive oxygen species levels, antioxidant enzymes, or related redox pathways. Consequently, no conclusions are drawn regarding the regulation of oxidative stress during seed desiccation. Such interactions remain important avenues for future investigation.

Overall, this study distinguishes contrasting carbohydrate reserve dynamics and amylolytic responses associated with desiccation tolerance and sensitivity in two tropical tree species. The results provide physiological evidence supporting the suitability of *A. africana* seeds for conventional drying and storage, while highlighting the vulnerability of *G. albida* seeds to moisture loss. These findings are relevant for seed conservation and restoration programs that require speciesspecific handling protocols (Food and Agriculture Organization, 2021).

Although this study offers useful insights, it is limited by the absence of molecular or biochemical markers beyond carbohydrate

Table 2. Summary of key physiological responses during desiccation in *A. africana* and *G. albida.*

Parameter	*A. africana*	*G. albida*
MC trend	Gradual decline; stabilizes after day 15	Rapid decline; no germination after day 13
Peak germination	15 days (90%)	Day 0 (76.7%), then declines to 0%
Peak reducing sugars	Day 7	Day 3; secondary rise at day 35
Peak starch content	Day 3	No significant early rise; declines after day 3
Peak α-amylase	Day 3	Day 7
Peak β-amylase	Day 3	Day 7
Peak total amylase	Day 3	Days 0–7

A. africana = Afzelia africana; G. albida = Gambeya albida; MC = moisture content.

metabolism and the restricted number of species examined. Future studies integrating analyses of specific sugar profiles, enzyme regulation at the molecular level, and controlled environmental conditions would further refine the understanding of desiccation responses in tropical forest seeds.

Conclusion

Based on the findings, it is suggested that *A. africana* seeds may be suitable for conventional drying and storage under conditions similar to those tested in this study, indicating potential for *ex situ* conservation. In contrast, *G. albida* seeds exhibited characteristics consistent with desiccation sensitivity and may therefore require alternative management approaches, such as short term hydrated storage, rapid propagation, or further evaluation for specialized preservation techniques. Future research should incorporate longer term storage trials under controlled environmental conditions to validate storage performance, as well as molecular or ecological investigations to better understand the mechanisms underlying the observed physiological responses.

Ethics

Ethics Committee Approval: This study was conducted in accordance with national and international ethical guidelines for research involving plants. The plant materials (*Afzelia africana* Sm. and Chrysophyllum albidum Linn) were collected from non-protected areas with due consideration for environmental sustainability and without causing harm to endangered or protected species. No human participants or animals were involved in the research; therefore, formal ethical approval was not required. All experimental procedures complied with relevant institutional, national, and international laws and conventions.

Data Sharing Statement: All data are available within the study.

Footnotes

Authorship Contributions: Conceptualization: A.E.N.; Design/methodology: B.A.N.; Execution/investigation: B.A.N. and A.E.N.; Resources/materials: A.E.; Data analysis/interpretation: A.E.; Writing – original draft: B.A.N.; Writing – review & editing/critical revision: A.E.N.

Conflict of Interest: The author(s) have no conflicts of interest to declare.

Funding: No external funding acquired.

References

Adelani, D. O., Aduradola, A. M., & Aiyelagbe, I. O. O. (2017). Storability and pre-sowing treatments of African star apple (*Chrysophyllum albidum* G. Don) *seeds. Journal of Agricultural Science and Environment, 17*(1). https://doi.org/10.51406/jagse.v17i1.1794

Amusa, N. A., Ashaye, O. A., & Oladapo, M. O. (2003). Biodeterioration of African star apple (*Chrysophyllum albidum*) in storage and the effect on its food value. *African Journal of Biotechnology, 2*(2), 56–59. https://doi.org/10.5897/AJB2003.000-1011

Association of Official Analytical Chemists. (2006). *Official methods of analysis* (18th ed.). Association of Official Analytical Chemists.

Berjak, P., & Pammenter, N. W. (2013). Implication of the lack of desiccation tolerance in recalcitrant seeds: A review. *Frontiers in Plant Science, 4*, Article 478. https://doi.org/10.3389/fpls.2013.00478

Burits, M., & Bucar, F. (2000). Antioxidant activity of *Nigella sativa* essential oil. *Phytotherapy Research, 14*(5), 323–328. https://doi.org/10.1002/1099-1573

Daws, M. I., Garwood, N. C., & Pritchard, H. W. (2011). Ecological correlates of seed desiccation tolerance in tropical forest species. *Annals of Botany, 108*(3), 463–473. https://doi.org/10.3732/ajb.91.6.863.

Etukudo, I. (2003). *Ethnobotany: Conventional and traditional uses of plants* (p. 191). Verdicts Press.

Farrant, J. M., & Moore, J. P. (2011). Programming desiccation tolerance: From plants to seeds to resurrection plants. *Plant Science, 180*(3), 397–407. https://doi.org/10.1016/j.pbi.2011.03.018

Food and Agriculture Organization. (2021). *State of the world's forest genetic resources: Conservation and sustainable use*. Food and Agriculture Organization of the United Nations. https://openknowledge.fao.org/server/api/core/bitstreams/1ca65f2b-dfae-44e0-9919-a8428d7ee7b7/content

Hay, F. R., & Probert, R. J. (2013). Advances in seed conservation of wild plant species: A review of recent research. *Conservation Physiology, 1*(1), cot006. https://doi.org/10.1093/conphys/cot006

International Union for Conservation of Nature. (2004). *IUCN Red List of Threatened Species*. https://www.iucnredlist.org

Lee, S. Y., & Tan, T. H. (2020). Regulation of amylase activity in seeds under dehydration stress: Physiological and molecular perspectives. *Journal of Plant Physiology, 255*, 153277. https://doi.org/10.1016/j.jplph.2020.153277

Maia, J., Dekkers, B. J. W., Provart, N. J., Ligterink, W., & Hilhorst, H. W. M. (2011). The re-establishment of desiccation tolerance in germinated *Arabidopsis thaliana* seeds and its associated transcriptome. *PLoS ONE, 6*(12), e29123. https://doi.org/10.1371/journal.pone.0029123

Ngele, B. A., Agba, M. O., Bassey, R. A., & Egeh, A. E. (2024). Effect of irrigation with household detergent on germination, activities of oxidative stress enzymes and chlorophyll content of pod maize. *Pakistan Journal of Agricultural Research, 37*(3), 290–299. https://doi.org/10.17582/journal.pjar/2024/37.3.290.299

Nguyen, T. T., Linh, L. T., & Hoang, N. T. (2023). Metabolic and oxidative responses of recalcitrant seeds during dehydration: Implications for conservation. *Frontiers in Plant Science, 14*, 1123458. https://doi.org/10.3389/fpls.2023.1123458

Nkang, A. (2002). Carbohydrate composition during seed development and germination in two sub-tropical rainforest tree species (*Erythrina caffra* and *Guilfoylia monostylis*). *Journal of Plant Physiology, 159*(5), 473–483. https://doi.org/10.1016/S0176-1617(02)70255-2

Padonou, E. A., Kassa, B., Assogbadjo, A. E., Chakeredza, S., Babatounde, B., & Glele-Kakai, R. (2013). Differences in germination capacity and seedling growth between seed morphotypes of *Afzelia africana* Sm. in Benin (West Africa). *Journal of Horticultural Science and Biotechnology, 88*(6), 679–684. https://doi.org/10.1080/14620316.2013.11513024

Prajith, T. M., Anilkumar, C., Kurup, R., Sabulal, B., & Nabeesa, S. (2014). Comparative analysis of seed development and desiccation aspects of *Saraca asoca* (Roxb.) W. J. de Wilde and *Caesalpinia pulcherrima* (L.) Sw. *Asian Journal of Plant Sciences, 13*(4–8), 164–171. https://doi.org/10.3923/ajps.2014.164.171

Somrug, K., Timsuksai, P., & Jenweerawat, S. (2024). Physiological maturity and harvesting date on seed yield and quality of indigo (*Indigofera suffruticosa* Mill.). *Agricultural Science Digest*. https://doi.org/10.18805/ag.DF-598

Umedum, N. L., Nwosu, C. C., Udeozo, I. P., & Igwemmar, N. C. (2014). Amino acid and heavy metal composition of *Afzelia africana* leaves. *World Journal of Nutrition and Health, 2*(2), 17–20. https://doi.org/10.12691/jnh-2-2-1

Whittaker, A., Martinelli, T., Bochicchio, A., Vazzana, C., & Farant, J. (2004). Comparison of sucrose metabolism during the rehydration of desiccation-tolerant and desiccation-sensitive leaf material of *Sporobolus stapfianus*. *Physiologia Plantarum, 122*(1), 11–20. https://doi.org/10.1111/j.1399-3054.2004.00346.x

Zhang, Z. K., Apse, J. P., & Stanton, R. C. (2000). High glucose inhibits glucose-6-phosphate dehydrogenase via cAMP in aortic endothelial cells. *Journal of Biological Chemistry, 275*(51), 40042–40047. https://doi.org/10.1074/jbc.M005375200

Trakya University Journal of Natural Sciences, 27(1), 104–114, 2026
DOI: 10.23902/trkjnat.2025121
www.tujns.org

Research Article

Interaction between circadian gene *Bmal1* and adipogenic regulator *PPARγ* in UVB-exposed mesenchymal stem cells

Afra Keban, Elçin Tank, Beril Erdem, Esin Akbay Çetin*

Hacettepe University, Faculty of Science, Department of Biology, Ankara, Türkiye

Cite this article as: Keban, A., Tank, E., Erdem, B., & Akbay Çetin, E. (2026). Interaction between circadian gene *Bmal1* and adipogenic regulator *PPARγ* in UVB-exposed mesenchymal stem cells. *Trakya University Journal of Natural Sciences, 27*(1), 104–114. https://doi.org/10.23902/trkjnat.2025121

Abstract

Background: Mesenchymal stem cells (MSCs), including adipose-derived MSCs (ADMSCs) and bone marrow-derived MSCs (BMMSCs), are multipotent cells essential for tissue repair, with strong self-renewal and differentiation abilities. *Bmal1* is a core component of the circadian cycle and plays a regulatory role in stem cell specialization; *PPARγ* links adipogenesis to the circadian rhythm by epigenetically regulating *Bmal1*. Ultraviolet B (UVB) radiation influences circadian processes by modulating the expression of growth factors and cytokines in MSCs.

Aims: This study investigated how UVB affects adipogenesis and circadian-system-related gene transcription in ADMSCs and BMMSCs.

Methods: MSC viability post-exposure was assessed using 3-(4,5-dimethylthiazol-2-yl)-2,5-diphenyltetrazolium bromide analysis. Cells were cultured in adipogenesis medium and stained with Oil Red O at multiple time points. UVB-treated MSCs were maintained under differentiation-inducing conditions for 28 days, and gene expression was evaluated by quantitative real-time polymerase chain reaction (qRT-PCR).

Results: Viability assays identified 25 mJ/cm² as the optimal UVB dose. Flow cytometry confirmed the enhanced expression of MSC markers (CD54, CD90, and CD29) and low expression of hematopoietic markers (CD45, CD106, and MHC class II). Oil Red O staining revealed gradual lipid accumulation, beginning on day 14 and forming mature droplets by day 28. qRT-PCR indicated a significant increase in *PPARγ* expression in adipogenic differentiation groups and *Bmal1* expression post-UVB exposure.

Özet

Dayanak: Yağ dokusundan elde edilen mezenkimal kök hücreler (ADMKH) ve kemik iliğinden elde edilen mezenkimal kök hücreler (KİMKH) dâhil olmak üzere mezenkimal kök hücreler (MKH), güçlü öz yenilenme ve farklılaşma kapasiteleri sayesinde doku onarımında önemli rol oynayan multipotent hücrelerdir. *Bmal1* proteini, günlük hücresel biyolojik süreçleri düzenleyen sirkadiyen döngünün temel bileşenlerinden biridir ve baskılanmasının kök hücrelerin farklılaşma kapasitesini değiştirdiği bilinmektedir. *PPARγ* ise adipojenik farklılaşma ile sirkadiyen ritim arasında bağlantı kurarak *Bmal1*'in epigenetik düzenlenmesinde rol oynamaktadır. Ultraviyole B (UVB) radyasyonunun, MKH'lerde büyüme faktörleri ve sitokin ekspresyonunu etkileyerek sirkadiyen ritim üzerinde etkili olduğu bilinmektedir.

Amaçlar: Bu çalışmada, ADMKH ve KİMKH'lerde UVB ışığının hücre farklılaşması ve sirkadiyen ritim üzerindeki etkileri araştırılmıştır.

Yöntemler: UV ışığına maruz bırakılan MKH'lerin canlılık potansiyelleri MTT analizi ile değerlendirilmiştir. Hücreler adipojenik farklılaşma ortamında kültürlenmiş ve farklı günlerde Oil Red O boyaması yapılmıştır. UVB'ye maruz kalan MKH'ler, farklılaşma ortamında 28 gün boyunca takip edilmiş ve gen ekspresyonundaki değişiklikler kantitatif gerçek zamanlı polimeraz zincir reaksiyonu (qRT-PCR) yöntemiyle analiz edilmiştir.

Bulgular: Sonuç olarak, hücre canlılığı analizleri optimal UVB dozunun 25 mJ/cm² olduğunu göstermiştir. Akış sitometrisi sonuçları, MKH fenotipine özgü belirteçlerin (CD54, CD90, CD29) yüksek düzeyde, hematopoietik belirteçlerin (CD45, CD106, MHC sınıf II) ise düşük düzeyde eksprese edildiğini ortaya koymuştur. Oil Red O

Edited by: *Reşat Ünal*

***Corresponding Author:** Esin Akbay Çetin, **E-mail:** akbayesin@gmail.com*

***ORCID iDs of the author(s):** AK. 0009-0000-1379-0759; ET. 0009-0006-1346-4965; BE. 0000-0002-9820-1147; EAÇ. 0000-0002-0797-8322*

Received: 2 December 2025, **Accepted:** 20 March 2026, **Epub:** 13 April 2026, **Published:** 24 April 2026

Conclusion: Overall, these findings suggest that UVB stimulation at optimal doses enhances the adipogenic differentiation capacity of MSCs while modulating circadian rhythm-associated genes. Moreover, adipogenic differentiation itself appears to contribute to the regulation of the circadian rhythm.

boyaması ile 14. günden itibaren lipit birikimi gözlenmiş, 28. günde ise olgun yağ damlacıkları tespit edilmiştir. qRT-PCR sonuçlarına göre, adipojenik farklılaşma gruplarında *PPARγ* ekspresyonu anlamlı düzeyde artarken, *Bmal1* ekspresyonunun da UVB uygulaması sonrasında arttığı belirlenmiştir.

Sonuç: Elde edilen bulgular, optimal UVB dozunun MKH'lerin adipojenik farklılaşmasını desteklediğini ve sirkadiyen ritmi düzenlediğini göstermektedir. Ayrıca, bu çalışma adipojenik farklılaşmanın sirkadiyen ritim üzerinde düzenleyici bir etkisi olduğunu da ortaya koymaktadır.

Keywords: Mesenchymal stem cell, *Bmal1*, *PPARγ*, ultraviolet light, qRT-PCR

Introduction

Mesenchymal stem cells (MSCs) are multipotent progenitor cells capable of self-renewal and differentiation into multiple mesodermal lineages, including adipocytes, osteoblasts, and chondrocytes (Česnik and Švajger, 2024). In addition, MSCs secrete a wide variety of growth factors and cytokines that contribute to tissue repair and regeneration, making them a commonly used experimental model in regenerative medicine and developmental biology (Pittenger et al., 2019; Vilar et al., 2023). The differentiation fate of MSCs is tightly regulated by mechanisms such as signaling pathways, cell-cycle regulators, microRNAs, transcription factors, and epigenetic modifications (Mens and Ghanbari, 2018). MSCs can be isolated from several tissues, most commonly bone marrow and adipose tissue. Bone marrow-derived MSCs (BMMSCs) exhibit low immunogenicity, multilineage differentiation potential, and robust migratory capacity. Adipose-derived MSCs (ADMSCs) are abundant, easily accessible, and relatively unaffected by donor age. Although MSCs from different tissues share core stem cell characteristics, subtle variations in marker expression and differentiation tendencies render tissue origin a crucial factor in stem cell biology studies (Lotfy et al., 2019; Sachs et al., 2025). For these reasons, MSCs represent an appropriate and physiologically relevant model for investigating molecular mechanisms regulating differentiation and cell-level responses to environmental stimuli.

Circadian rhythm and cell-cycle regulation constitute two fundamental interconnected regulatory systems in eukaryotes, operating from an organismal to the molecular level. Circadian rhythms follow a near-24-hour oscillation pattern of alternating active and inactive phases governed by a core molecular clock comprising transcription–translation feedback loops (Putthanbut et al., 2025; Zeng et al., 2024). Key clock genes include *Bmal1*, *Clock*, *Period* (*Per*), *Cryptochrome* (*Cry*), *RORα/β/γ*, and *Rev-erbα/β* (Göncü & Öztürk, 2019). Of these, Brain and Muscle ARNT-Like 1 (*Bmal1*) functions as a central indispensable regulator of the circadian clock. *Bmal1* heterodimerizes with *Clock*, driving rhythmic transcription of downstream clock-controlled genes. Crucially, evidence indicates that *Bmal1* is essential for maintaining diurnal rhythmicity and plays a critical role in fate determination and differentiation of stem cells. Suppressed or disrupted *Bmal1* expression in stem cells impairs lineage-specific gene activation, alters the metabolic program, and compromises differentiation efficiency (Gao et al., 2022). Therefore, in this study, *Bmal1* was selected as a key molecular link between circadian regulation, cell metabolism, and differentiation.

Adipogenesis was specifically investigated as it is one of the most well-characterized and metabolically sensitive MSC-differentiation pathways. This process is tightly controlled by both circadian clock-associated genes and metabolism-related transcription factors, making it an ideal model for exploring clock–metabolism interactions. Peroxisome proliferator-activated receptor gamma (*PPARγ*) is the master regulator of adipocyte differentiation and governs lipid storage, insulin sensitivity, and glucose metabolism. *PPARγ* activity is influenced by environmental and circadian cues and is modulated through post-translational and epigenetic mechanisms (Montaigne et al., 2021).

Crucially, *PPARγ* represses *Bmal1* transcription in adipocytes, altering cell metabolism, reducing histone acetylation and methylation, and disrupting circadian rhythmicity. *PPARγ* integrates adipogenesis with diurnal clock regulation via this mechanism, establishing a feedback loop between metabolic state, epigenetic modifications, and circadian disruption (Wang et al., 2022). Consequently, adipogenic differentiation provides a biologically relevant context to examine the *Bmal1–PPARγ* interaction under external stimuli. Collectively, these findings suggest the occurrence of such a tightly regulated and bidirectional interconnectivity during adipogenic differentiation (Wang et al., 2022). While *Bmal1* influences metabolic timing and differentiation competence in MSCs (Gao et al., 2022), *PPARγ* is not only a downstream effector of adipogenesis but also an upstream modulator of circadian gene expression through the transcriptional and epigenetic repression of *Bmal1* (Wang et al., 2022). Such a reciprocal regulatory axis positions the *Bmal1–PPARγ* network as a central integrator of circadian rhythm, metabolic state, and cell-differentiation fate (Li et al., 2023a; Montaigne et al., 2021; Takahashi, 2017).

However, the mechanisms by which external stimuli, such as ultraviolet (UV) light modulate this regulatory interplay remain insufficiently understood (Ezati et al., 2023; Liao et al., 2023). UV is a major environmental factor influencing circadian rhythms. Exposure to UV and visible light has been implicated in modulating cell-level metabolism, clock gene expression, and regenerative responses. UVA, ultraviolet B (UVB), and UVC

differ in wavelength: 315–400, 280–315, and 100–280 nm, and bioimpacts (Ezati et al., 2023; Goodenow et al., 2022; Li et al., 2023b; Sani et al., 2024). Controlled UV exposure enhances secretory activity and regenerative potential in MSCs, suggesting a link between UV-induced stress responses and circadian regulation (Liao et al., 2023; Ra et al., 2023).

Therefore, this study aims to investigate how adipogenic differentiation modulates circadian rhythm regulation through a reciprocal interaction between *Bmal1* and *PPARγ* in UV-treated MSCs derived from various tissue sources.

Materials and Methods

Materials

Phosphate-buffered saline (PBS), 0.25% Trypsin-EDTA, 3-(4,5-dimethylthiazol-2-yl) 2,5-diphenyltetrazolium bromide (MTT), 3-isobutyl-1-methylxanthine (IBMX), insulin, and penicillin/streptomycin (P/S) were purchased from Sigma-Aldrich (Merck KGaA, Darmstadt, Germany). Fetal bovine serum (FBS) and Dulbecco's modified Eagle medium/Nutrient Mixture F12 (DMEM/F12) were purchased from Biowest (St. Louis, MO, France). Oil-red O staining solution, RevertAid First Strand cDNA Synthesis Kit, Power SYBR™ Green Master Mix, and culture dishes were obtained from Thermo Fisher Scientific (Waltham, MA, USA). Dexamethasone and indomethacin were purchased from Merck Millipore (St. Louis, MO, France). Xylazine (Rompun®) was bought from Abdi İbrahim İlaç Pazarlama A.Ş. (İstanbul, Türkiye). Ketamine (Ketalar® 50 mg/mL) was obtained from Eczacıbaşı İlaç Pazarlama A.Ş. (Lüleburgaz, Türkiye). All antibodies were purchased from Santa Cruz Biotechnology (Dallas, TX, USA).

MSCs Isolation

MSCs were isolated from three randomly selected 24-week-old male *Wistar albino* rats raised as a single colony. The laboratory was pre-sterilized with UV light for 1 h, and all surgical materials were autoclaved. The animals used were obtained post-approval from the Hacettepe University Animal Ethics Committee (number 2021/05-05; dated June 22, 2021). The rats were anesthetized with xylazine (10 mg/kg) and ketamine (50 mg/kg); lateral and gonadal adipose tissue, femoral, and tibial bones were removed under sterile conditions in a laminar flow cabinet. Adipose tissues were placed in a transport medium containing antibiotics–antimycotics—DMEM/F12 containing 20% FBS and 2% P/S—in a laminar flow cabinet. Tissues were dissected into 4–5 mm-sized pieces and placed in 12-well culture dishes. Then a drop of primary medium was added and incubated for 15 min. Then, after adding enough primary medium to cover the tissue pieces without floating, the incubation was continued (Çetin et al., 2023; Niyaz et al., 2012).

The metaphyzes of the femur and tibia were cut out. The bone marrow was collected using an injector needle, washed with transport medium, and dissected with a scalpel. The tissues were transferred to a medium-containing Falcon tube and centrifuged at 800 rpm for 5 min. The supernatant was removed, and a 1/9 solution of PBS/RBC was added. The tube was kept on ice for 10 min and recentrifuged. The supernatant was collected, suspended three times with 5 mL of medium, and washed by centrifugation. The pellet was suspended with medium in a 6-well culture dish and seeded with 2 mL of medium per well (Sevim et al., 2018).

An equal amount of medium was renewed every day for one week to neutralize the MSC differentiation effect of cytokines. After incubation for a week, changes in cell morphology were examined under an IX70 inverted microscope (Olympus Corporation, Tokyo, Japan). Passaging was performed after the MSCs covered the entire culture dish surface. Based on primary culture and early *in vitro* expansion, $1–5 \times 10^6$ ADMSCs and $0.5–2 \times 10^6$ BMMSCs were obtained between passages 2 and 4, consistent with previous reports (Niyaz et al., 2012), which were used for the experiments.

Characterization and Differentiation Potential of MSCs

MSCs were characterized using flow cytometry. After trypsinization, the MSCs were centrifuged, and fluorescein isothiocyanate-conjugated antibodies were added to the pelleted cells suspended in a wash buffer. The MSCs were then incubated at room temperature for 45 min. For this purpose, antibodies specific to positive and negative markers CD29, CD90, CD54, CD45, CD106, and MHC class II antigens, and isotype controls were used to immunophenotype MSCs.A CytoFLEX LX flow cytometer (Beckman Coulter, IN, USA), and approximately 3×10^5 cells per sample were analyzed. To ensure accurate data interpretation, negative controls, including unstained cells, were employed to define the boundaries of positive signals during the gating process.

For assessing their adipogenic potential, MSCs were seeded at 2×10^4 cells/well in 96-well culture dishes using DMEM/F12 medium supplemented with 10% FBS and 1% (P/S). The cells reached ~80% confluency within 1 day, after which the adipogenic differentiation medium was added. Adipogenesis was induced in the cells of all experimental groups at the same seeding density and at comparable confluency levels; they were cultured for 28 days. Adipogenic medium was prepared by adding 10^{-7} M dexamethasone, 5 µg/mL insulin, 60 µM indomethacin, and 500 µM IBMX to DMEM medium. The medium was changed every two days, and differentiation was examined by Oil Red O staining. Briefly, the medium was removed, and the dish was washed with PBS. Then, 100 µL 10% formalin was added, incubated for 5 min, and washed with distilled water, followed with 60% isopropanol. Oil Red O was added to cover the surface and left aside for 15 min. It was then washed with 60% isopropanol alcohol until the color lightened. Hematoxylin was added to cover the surface and left aside for 10 s. It was washed now with distilled water until the color diminished. The stained wells were covered with PBS and visualized with an Olympus IX70 inverted microscope at X20 magnification. The software ImageJ, version 1.54p (NIH, USA), was used to quantitatively analyze the intensity and distribution of red color in selected images. In brief, three areas from representative sections of each sample were randomly selected. Then, the surface area of

the stained portion was compared to the total matrix area and expressed as a ratio (Zhu et al., 2022).

UV Application and Cell Viability Assay

The ADMSCs and BMMSCs were seeded for 24 h in 96-well culture dishes, the medium was then collected, and then the cells were covered with sterile PBS. UVB at doses of 25, 50, and 100 mJ/cm² were applied for 17, 34, and 68 s, respectively. UV was provided with a Philips PL-S 9W\01 ampoule. PBS was replaced, MTT was added, and incubated at 0, 24, and 48 h to analyze cell viability. The optimum UVB dose was defined as the highest one that preserved cell viability without inducing significant cytotoxicity and was used in all experiments.

For the MTT assay, the culture medium was replaced with a medium-containing MTT/DMEM (serum-free) solution at 1:10 and incubated for 2–4 h under standard conditions. The formazan crystals formed were dissolved by replacing the medium with isopropyl alcohol. OD_{570} nm was measured with an EZ Read 400 ELISA microplate reader (Biochrom Ltd., Cambridge, UK). The viability of the treated groups was calculated as a percentage of the control group.

Quantitative Real-Time Polymerase Chain Reaction (qRT-PCR) Analysis

ADMSCs and BMMSCs were seeded into culture dishes for 24 h. After UVB treatment, adipogenic differentiation medium was added to culture dishes, and the medium was renewed every two days for 28 days. At the end of this period, the expression of *Bmal1* and *PPARγ* genes was quantified by qRT-PCR. First, RNA was isolated from the MSCs using Trizol and converted into cDNA using the RevertAid First Strand cDNA synthesis kit (Thermo Fisher Scientific) and a BIO-RAD T100 Thermal Cycler. *Bmal1* and *PPARγ* expression was quantified using Power SYBR Green PCR Master Mix (Thermo Fisher Scientific) with the 7500 Fast & 7500 RT-PCR Systems (Thermo Fisher Scientific), *β-actin* served as a reference gene. ΔΔCt values were calculated, and data were statistically analyzed. The sequences of all primers used are given in Table 1.

Table 1. Sequences of gene-specific primers.

Primer name	Sequence (5'–3')
Bmal1 forward	TGCCACTGACTACCAAGAAAGT
Bmal1 reverse	AACTTCCGGGACATCGCATT
PPARγ forward	CTGCGTCCCCGCCTTAT
PPARγ reverse	TTCAATCGGATGGTTCTTCG
β-actin forward	GGGTTACGCGCTCCCTCATG
β-actin reverse	CCACGCTCGGTCAGGATCTTC

Statistical Analysis

Statistical analysis was performed using GraphPad Prism 8.02 (GraphPad Software Inc., San Diego, CA, USA). Inter-group differences were analyzed by one-way analysis of variance followed by Dunnett's post hoc test for multiple comparisons. Data are presented as the mean ± standard deviation, and a p-value of <0.05 was considered statistically significant.

Results

MSCs Isolation Results

Rat flank and gonadal adipose, and the femur and tibia marrow tissues were extracted under sterile conditions, and incubated in culture dishes under an appropriate environment. The confluent state of the cells was observed under a microscope on pre-selected days. MSCs had started to adhere to the culture dish within 24 h of addition. On the 6th day, they took the shape and form of colonies (Figure 1a and 1b).

Characterization and Differentiation Potential of MSCs

Flow cytometry was used to characterize the MSCs in the P2–P4 stages. The phenotype positive antigens (≥95%): CD54, CD90, and CD29; and phenotype negative antigens (≤7%): CD45, CD106, and MHC class II on the MSC surface were analyzed (Figure 2).

The potential of ADMSCs and BMMSCs to differentiate into adipogenic cells was demonstrated based on the accumulation of lipid vacuoles via Oil Red O staining performed on days 14, 21, and 28. From the 14th day onward, lipid droplets started to appear. Adipogenesis was most intense on the 28th day, at which the cytoplasm was filled with lipid droplets, and the nucleus was rendered peripheral (Figure 1c and 1d). The lipid contents determined support the qualitative observations. Compared to their respective controls, on days 14, 21, and 28, adipogenesis in ADMSCs and BMMSCs occurred at statistically significant levels in each treatment group ($p \leq 0.0001$) (Figure 3).

UV Application and Cell Viability Assay

An optimization protocol was employed to determine the appropriate UVB dose in MSCs. Cells were treated with 25, 50, and 100 mJ/cm^2 doses for 17, 34, and 68 s, and viability was measured by assaying mitochondrial activity (Figure 4). MTT assay was performed at 0, 24, and 48 h. Cell viability was the highest at 25 mJ/cm². With ADMSCs, viability losses of 40%, 55%, and 40% were observed at 25, 50, and 100 mJ/cm^2 doses at 0 h. At the 24th hour, viability loss was 15% at 100 mJ/cm². At the 48th hour, it is observed that the 100 mJ/cm² dose proliferates rapidly in response to stress. At 50 mJ/cm², viability was 20% less. BMMSCs showed 25% higher viability at 0 h with 25 mJ/cm². At the 24th hour, viability was enhanced by 100%, 150%, and 140% at 25, 50, and 100 mJ/cm². At the 48th hour, cell viability was 50% less than that at 100 mJ/cm². Viability for each hour was compared to the control group.

Gene Expression Analysis

The relative expression levels of genes were analyzed by using qRT-PCR, and *β-actin* as a reference gene (Figure 5). Each treatment group was compared with the control group (C-DMEM). *PPARγ*

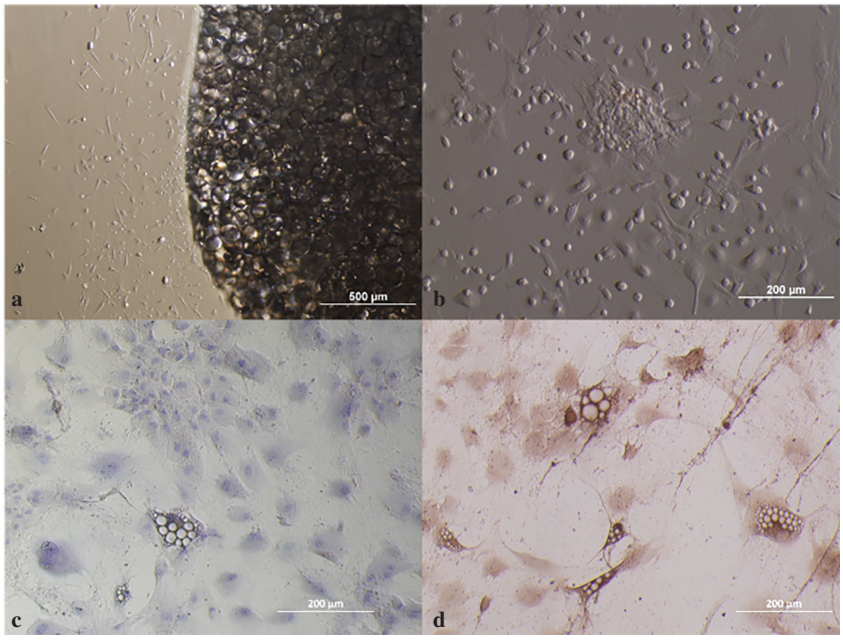

Figure 1. (a) Day 6: Primary isolation of ADMSC; (b) Day 6: Primary isolation of BMMSC; (c) Oil Red O staining of ADMSCs; and (d) BMMSCs were cultured in adipogenic differentiation medium for 28 days.
ADMSC = adipose-derived mesenchymal stem cell; BMMSC = bone marrow mesenchymal stem cell.

expression increased significantly in both adipogenic differentiation control (C-AD DIFF) and UV (UV-AD DIFF) groups (**$p \leq 0.01$ and ***$p \leq 0.001$, respectively) compared to the control group ADMSCs (Figure 5a). A similar trend was seen with BMMSCs for both C-AD DIFF and UV-AD DIFF groups, at $p \leq 0.0001$ (Figure 5b). Additionally, *PPARγ* expression declined in the UV-DMEM group ($p \leq 0.0001$) compared to the control group (Figure 5b). For *Bmal1*, expression level reduced insignificantly in the C-AD DIFF and UV-AD DIFF groups of ADMSCs (Figure 5c), but showed a statistically significant enhancement in BMMSCs of both C-AD DIFF and UV-AD DIFF, at $p \leq 0.05$ and $p \leq 0.01$, respectively (Figure 5d). In addition, *Bmal1* transcription elevated significantly in the ADMSC UV-DMEM group compared to the control ($p \leq 0.05$) (Figure 5c).

Discussion

This study investigated the relationship between adipogenic differentiation and circadian rhythm in UVB-treated MSCs. For this purpose, the cells were first confirmed to be MSCs via characterization and adipogenic differentiation. Then, UVB was applied at three doses to determine the optimum concentration, followed by identifying the day with maximum adipogenic maturity. Then, cell viability, adipogenic differentiation, and the expression of circadian clock-associated genes were analyzed at the molecular level.

Under *in vitro* conditions, the proliferation rate was greater in ADMSCs than in BMMSCs, and ADMSCs more stably maintained stem cell properties, such as self-renewal, proliferation, and differentiation potential after repeated passaging (Christoffers et al., 2024; Zhu et al., 2008). However, BMMSCs demonstrated a markedly higher chondrogenic differentiation capacity (Mohamed-Ahmed et al., 2018), whereas ADMSCs exhibited remarkably greater *in vitro* adipogenic, endothelial differentiation, and angiogenic capacities than BMMSCs in preclinical ischemic injury models (El-Badawy et al., 2016; Yin et al., 2023). Adipose and BMMSCs were chosen for ease of access and adipogenic potential. They are crucial cell sources for regenerative medicine and treating various chronic diseases (Guillamat-Prats, 2021; Lotfy et al., 2023). Differentiation in MSCs starts from the second week, subject to adipogenic differentiation, and completes in the 3rd to 4th week (Mohamed-Ahmed et al., 2018; Ninomiya et al., 2010). In our study, Oil Red O staining performed on day 28 indicated a transformation of MSCs into mature adipocytes.

An appropriate UV dose causes an increase in biomolecules such as growth factors and cytokines in MSCs (Angelina et al., 2025; Yan et al., 2023). Perez et al. (2019) showed that 25 mJ/cm^2 UVB enhanced interleukin -8 release by human MSCs, and that MSCs were more resistant than dermal fibroblasts to UV light. This study identified 25 mJ/cm^2 UVB as the optimum dose at which MSCs could survive. In addition, an earlier study by our group reported the important role of UVA light at 100 mJ/cm^2 in wound healing; it enhances cytokine and growth factor release (Çetin et al., 2023). Another study reported that low-dose UV light did not affect gene expression in human MSCs, but secretory factors and collagen production increased; i.e., the wavelength of UV light and its compatibility with living cells were directly proportional (Wong et al., 2015). Further supporting this correlation, the viability of MSCs treated with 100 mJ/cm^2 UVB declined markedly within the first 24 h, followed by an abnormal increase at the 48th hour. In line with this trend, UV-treated stem cells are effective in wound healing and cell regeneration. UVB light induces a phase shift

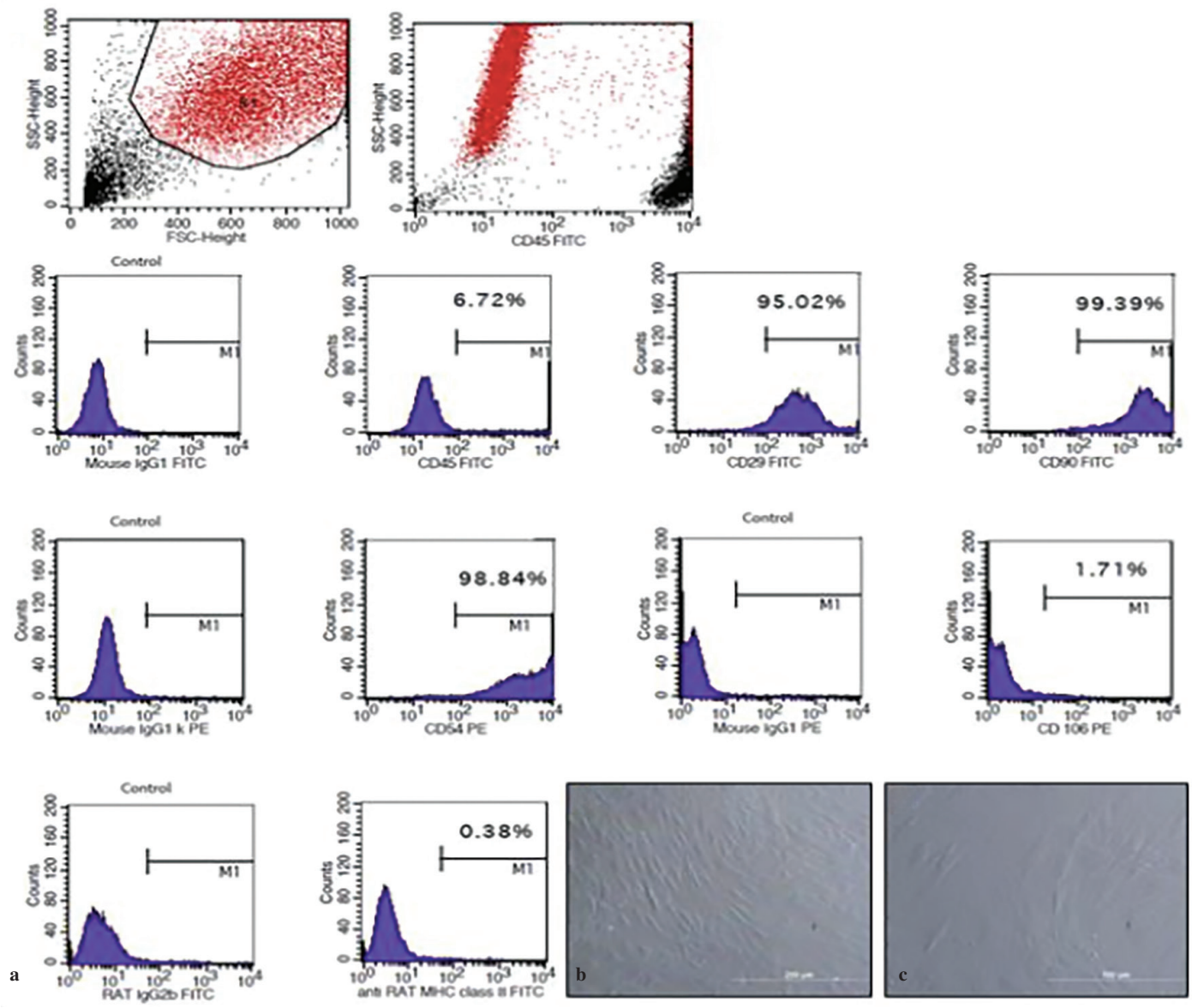

Figure 2. Representative flow cytometry histograms showing expression of MSC surface markers isolated from the P2–P4 population. Most cells (≥95%) were positive for CD54, CD90, and CD29. MSCs were negative for the hematopoietic and immunogenic markers CD45, CD106, and MHC class II, with ≤7% of them expressing these antigens.
CD = cluster of differenti; MHC = major histocompatibility complex; MSC = mesenchymal stem cell.

in the transcription of circadian clock-associated genes such as *Bmal1* and *Per2*, and these changes are associated with sunburn apoptosis, inflammatory responses, and erythema (Lamnis et al., 2024). In this research, UVB was preferred because of its potential to support regenerative processes by enhancing the release of cytokines and growth factors by MSCs. Furthermore, the time point of UV exposure during a 24-hour cycle affects DNA damage and repair through a temporal regulation of the tumor suppressor gene *p53* (Carvalho et al., 2024; Zou et al., 2022). Low levels of DNA repair, especially in the evening when DNA replication is at its peak, render the skin more vulnerable to the harmful effects of UV radiation (Andersen et al., 2023; Su et al., 2024). This process interacts with carcinogenic pathways through receptors directly linked to the circadian rhythm. In contrast, UVB is required for the synthesis of vitamin D3, a compound that affects circadian clock-related genes. Unlike UVB one form of vitamin D3 suppressed *Per2* expression (Lamnis et al., 2024).

Clock gene knock-out reduces cell proliferation and increases apoptosis, whereas *Bmal1* is essential for lineage differentiation (Kaneko et al., 2023; Zhang et al., 2024). Enhanced *Bmal1* expression inhibits adipogenesis, whereas a high *Bmal1* expression pattern was found in mature adipocytes (Lamnis et al., 2024; Xiong et al., 2023). Therefore, the *Bmal1* gene, which plays a central role in stem cell differentiation, was examined in this study. Moreover, *PPARγ* showed circadian expression and was found to be an important peripheral clock activator of the cardiovascular

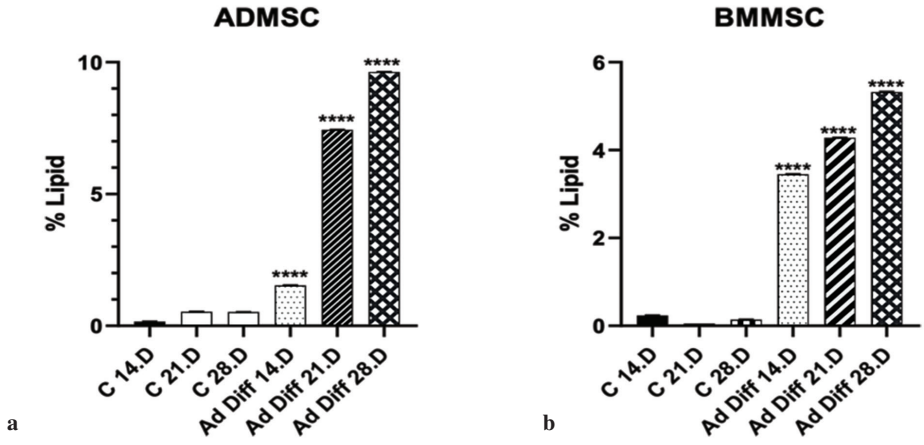

Figure 3. Oil Red O staining indicates the percentage lipid content. It was calculated based on the ratio of the surface area containing oil droplets to the total surface area. (a) % lipid values at days 14, 21, and 28 in ADMSCs and (b) BMMSCs.
AD DIFF = adipogenic differentiation; ADMSCs = adipose-derived mesenchymal stem cells; BMMSCs = bone marrow mesenchymal stem cells; C = control.

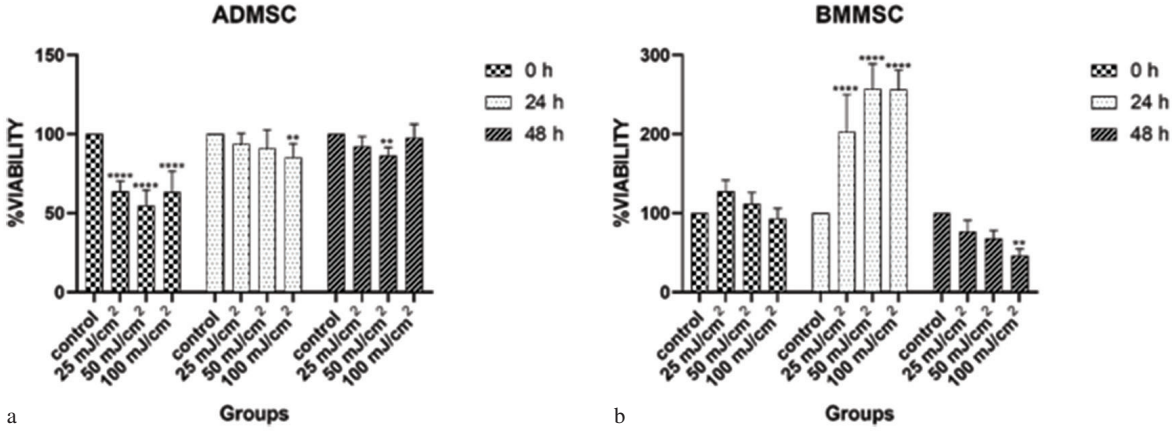

Figure 4. MTT-based cell viability test. Viability at 0, 24, and 48 h in (a) ADMSCs and (b) BMMSCs, graphically presented as MTT results with reference to the control group. UVB was applied at doses of 25, 50, and 100 mJ/cm²; $p \leq 0.05$; $p \leq 0.01$; $p \leq 0.001$; $p \leq 0.0001$.
ADMSCs = adipose-derived mesenchymal stem cells; BMMSCs = bone marrow mesenchymal stem cells; MTT = methyl thiazolyl tetrazolium; UVB = ultraviolet B.

system and metabolism (Ansarin et al., 2023; Li et al., 2025). It has been reported that disruption of *Clock* and *Per2* genes causes a significant decrease in adipogenic differentiation, whereas inhibition of *Clock* or *Per2* leads to an increase in *PPARγ* levels by altering osteocalcin expression (Boucher et al., 2016; Tian et al., 2024). The *Per1* and *Per2* genes have antagonistic effects on *PPARγ* activity, with *Per1* enhancing activity and *Per2* inhibiting recruitment of *PPARγ* to the target promoter (Grimaldi et al., 2010; Zhang et al., 2023). However, the role of *Per2* in adipogenesis depends on a complex regulatory network that interacts with other clock genes, such as *Bmal1* and *REV-ERBα* (Civelek et al., 2023; Gao et al., 2022). Erickson et al. (2024) revealed a relationship between *Per2* expression and the *PPARγ* gene, while Wang et al. (2022) showed that the *PPARγ* gene integrates the obesity and adipocyte clock in a *Bmal1*-dependent manner. In our study, gene expression analysis of *PPARγ* and *Bmal1* statistically showed different expression levels in ADMSCs and BMMSCs. As it is known, circadian clock genes are not found at the same expression level at all times of the day. While *Bmal1* expression increases in the first hours of the day, it is suppressed by the expression of *PER-CRY* genes in the later hours of the day (Li et al., 2023; Mattis et al., 2016). Analyzing MSCs at different times of the day resulted in different *Bmal1* levels. However, our data showed a significant increase between the UV-treated and non-UV-treated groups. The fact that *PPARγ* gene expression was higher in UV-treated groups could mean that UV increased *PPARγ* expression. This could show that UV treatment induced *Bmal1* expression in MSCs.

In vivo, UV exposure may influence circadian rhythm regulation through direct cellular effects and indirect systemic mechanisms involving neuroendocrine signaling, immune responses, and central clock synchronization. Therefore, whole-animal models

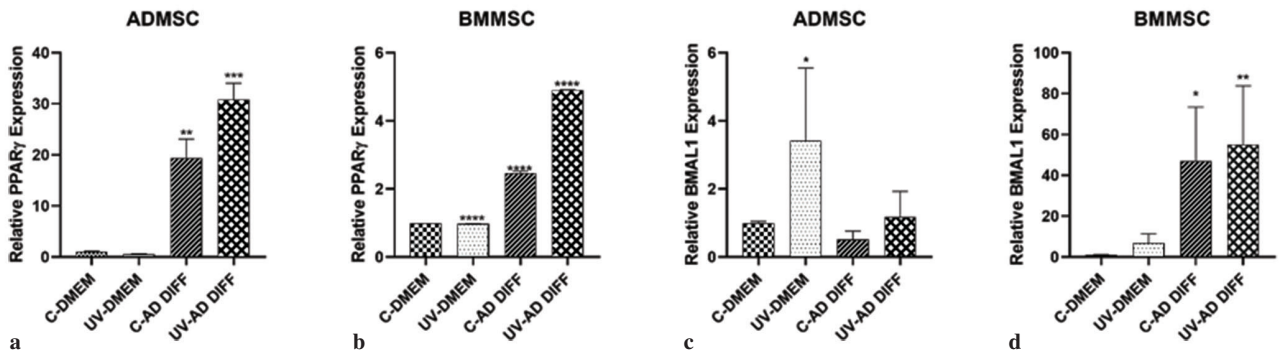

Figure 5. Expression levels of *PPARγ* and *Bmal1*. (a) *PPARγ* expression in ADMSCs; (b) in BMMSCs; (c) *Bmal1* expression in ADMSCs; and (d) in BMMSCs ($p \leq 0.05$; $p \leq 0.01$; $p \leq 0.001$; $p \leq 0.0001$).
AD DIFF = adipogenic differentiation; ADMSCs = adipose-derived mesenchymal stem cells; BMMSCs = bone marrow mesenchymal stem cells; C = control.

could provide valuable insight into tissue-specific and systemic circadian responses to UV exposure. Although the overall direction of UV-induced modulation of circadian clock genes is expected to be consistent with *in vitro* findings, the magnitude and temporal dynamics of these effects may differ *in vivo* due to hormonal regulation, metabolic status, and inter-organ communication. In this context, the *in vitro* MSCs model used in the present study allows precise control of UV dose and exposure timing, enabling the investigation of direct molecular mechanisms underlying UVB-induced regulation of adipogenic differentiation and circadian clock genes. The present findings, therefore, establish a mechanistic foundation that may inform future *in vivo* studies aimed at evaluating the physiological relevance of UV-induced circadian modulation.

Originality of this study lies in its simultaneous evaluation of *Bmal1* and *PPARγ* expression in MSCs obtained from different tissue sources under UV exposure. While previous studies have demonstrated the independent roles of clock genes in determining stem cell fate and adipogenic differentiation, research integrating environmental cues, such as UV irradiation, with circadian-adipogenic gene interactions is limited. In particular, the literature has not sufficiently explored comparative analyses of ADMSCs and BMMSCs in terms of circadian gene sensitivity and adipogenic potential. This study offers a new perspective by demonstrating that UV exposure is associated with coordinated changes in *Bmal1* and *PPARγ* expression patterns in MSC types. These findings suggest a potential regulatory role of light-related environmental stimuli in the circadian mechanism and lineage determination processes of stem cells. Additionally, observing tissue-specific expression differences between ADMSCs and BMMSCs helps us understand the intrinsic heterogeneity in the circadian regulation and adipogenic potential of MSCs. Collectively, these findings expand current knowledge on circadian–metabolic gene interactions in stem cells and suggest that UV-mediated circadian modulation represents a potential regulatory layer influencing the dynamics of adipogenic differentiation.

This study has several strengths that enhance the reliability and interpretability of its findings. First, the simultaneous investigation of circadian clock regulation and adipogenic differentiation provides a comprehensive perspective on stem cell biology, allowing the evaluation of metabolic-temporal interactions within a unified experimental framework. Second, the inclusion of MSCs (ADMSCs and BMMSCs) derived from different tissue sources allows the comparative assessment of tissue-specific variability, contributing to the understanding of intrinsic heterogeneity of the MSCs. Third, the inclusion of UV exposure as an environmental stimulus provides a physiologically relevant modulatory factor, facilitating the investigation of how external cues interact with circadian and differentiation-related molecular pathways. However, several limitations should be considered when interpreting the results. The study was conducted under *in vitro* conditions, which may not fully reflect the complex systemic and microenvironmental effects present *in vivo*. The assessment of circadian genes at specific time points rather than longitudinal rhythmic profiling limits the findings regarding oscillation dynamics. Future studies incorporating time series analysis, functional clock measurements, and *in vivo* validation models will help further elucidate the biological significance of the observed findings.

Conclusion

Within the scope of this study, adipogenic differentiation and expression of circadian rhythm-associated genes were investigated at UVB doses optimal for maintaining the viability of MSCs of two different origins. Studies indicate the relationships between circadian rhythm and UV light, or adipogenic differentiation and circadian rhythm. However, none have addressed the latter in UVB-treated MSCs. In summary, this study demonstrated that the optimum UVB dose induces adipogenesis in MSCs and regulates the circadian rhythm.

The role of *Bmal1* in stabilizing *PPARγ* transcriptional activity and the feedback effect of *PPARγ* on the circadian rhythm are fundamental mechanisms determining the cell's differentiation fate. In this context, the patterns observed reinforce the concept of a coordinated circadian–metabolic regulatory axis in which adipogenic programming and clock gene activity, including *Bmal1*, are dynamically integrated.

These findings provide a mechanistic basis for future studies aiming to evaluate how similar responses would unfold under physiological conditions (*in vivo*) by elucidating how the *Bmal1–PPARγ* interaction is reprogrammed by UVB.

These findings provide a mechanistic basis for future *in vivo* studies aimed at evaluating whether similar UV-induced circadian and differentiation responses occur under physiological conditions.

Acknowledgement

The authors would like to thank the Akbay Lab for their valuable support and contributions to this study. The authors also gratefully acknowledge The Scientific and Technological Research Council of Türkiye (TÜBİTAK) for its financial support.

Ethics

Ethics Committee Approval: The animals used were obtained post-approval from the Hacettepe University Animal Ethics Committee (number 2021/05-05; dated June 22, 2021).

Data Sharing Statement: All data are available within the study.

Footnotes

Authorship Contributions: Conceptualization: A.K. and E.A.Ç.; Design/methodology: A.K. and E.A.Ç.; Execution/investigation: A.K., E.T., B.E., and E.A.Ç.; Resources/materials: A.K. and E.A.Ç.; Data acquisition: A.K., E.T., B.E., and E.A.Ç.; Data analysis/interpretation: A.K., E.T., B.E., and E.A.Ç.; Writing – original draft: A.K., E.T., B.E., and E.A.Ç.; Writing – review & editing/critical revision: A.K., E.T., B.E., and E.A.Ç.

Conflict of Interest: The author(s) have no conflicts of interest to declare.

Funding: This research was supported by the 2209-A University Students Research Projects Support Programme of TÜBİTAK (project no: 1919B012216469). The project was conducted by Afra Keban under the supervision of the corresponding author, Esin Akbay Çetin.

References

Andersen, B., Duan, J., & Karri, S. S. (2023). How and why the circadian clock regulates proliferation of adult epithelial stem cells. *Stem Cells, 41*(4), 319–327. https://doi.org/10.1093/stmcls/sxad013

Angelina, J., Putra, A., Trisnadi, S., Hermansyah, D., Setiawan, E., Sumarawati, T., & Amalina, N. D. (2025). Hypoxia-conditioned mesenchymal stem cells (MSC) exosomes attenuate ultraviolet-B (UVB)-mediated malondialdehyde (MDA) and matrix metalloproteinase-1 (MMP-1) upregulation in collagen loss models. *Medicinski Glasnik, 22*(1). https://doi.org/10.17392/1923-22-01

Ansarin, A., Mahdavi, A. M., Javadivala, Z., Shanehbandi, D., Zarredar, H., & Ansarin, K. (2023). The cross-talk between leptin and circadian rhythm signaling proteins in physiological processes: A systematic review. *Molecular Biology Reports, 50*(12), 10427–10443. https://doi.org/10.1007/s11033-023-08887-3

Boucher, H., Vanneaux, V., Domet, T., Parouchev, A., & Larghero, J. (2016). Circadian clock genes modulate human bone marrow mesenchymal stem cell differentiation, migration and cell cycle. *PLOS ONE, 11*(1), e0146674. https://doi.org/10.1371/journal.pone.0146674

Carvalho, C., Silva, R., Melo, T. M. V. D. P. e, Inga, A., & Saraiva, L. (2024). P53 and the ultraviolet radiation-induced skin response: Finding the light in the darkness of triggered carcinogenesis. *Cancers, 16*(23), 3978. https://doi.org/10.3390/cancers16233978

Česnik, A. B., & Švajger, U. (2024). The issue of heterogeneity of MSC-based advanced therapy medicinal products-a review. *Frontiers in Cell and Developmental Biology, 12*, 1400347. https://doi.org/10.3389/fcell.2024.1400347

Christoffers, S., Seiler, L., Wiebe, E., & Blume, C. (2024). Possibilities and efficiency of MSC co-transfection for gene therapy. *Stem Cell Research & Therapy, 15*(1), 150. https://doi.org/10.1186/s13287-024-03757-6

Civelek, E., Ozturk Civelek, D., Akyel, Y. K., Kaleli Durman, D., & Okyar, A. (2023). Circadian dysfunction in adipose tissue: Chronotherapy in metabolic diseases. *Biology, 12*(8), 1077. https://doi.org/10.3390/biology12081077

Çetin, E. A., Babayiğit, E. H., Özdemir, A. Y., Erfen, Ş., & Onur, M. A. (2023). Investigation of UV-treated mesenchymal stem cells in an *in vitro* wound model. *In Vitro Cellular & Developmental Biology-Animal, 59*(5), 331–345. https://doi.org/10.1007/s11626-023-00772-4

El-Badawy, A., Amer, M., Abdelbaset, R., Sherif, S. N., Abo-Elela, M., Ghallab, Y. H., Abdelhamid, H., Ismail, Y., & El-Badri, N. (2016). Adipose stem cells display higher regenerative capacities and more adaptable electro-kinetic properties compared to bone marrow-derived mesenchymal stromal cells. *Scientific Reports, 6*, 37801. https://doi.org/10.1038/srep37801

Erickson, M. L., Dobias, D., Keleher, M. R., Dabelea, D., Bergman, B. C., Broussard, J. L., & Boyle, K. E. (2024). *In vitro* circadian clock gene expression assessments in mesenchymal stem cells from human infants: A pilot study. *Nutrients, 16*(1), 52. https://doi.org/10.3390/nu16010052

Ezati, P., Khan, A., Priyadarshi, R., Bhattacharya, T., Tammina, S. K., & Rhim, J.-W. (2023). Biopolymer-based UV protection functional films for food packaging. *Food Hydrocolloids, 142*, 108771. https://doi.org/10.1016/j.foodhyd.2023.108771

Gao, W., Li, R., Ye, M., Zhang, L., Zheng, J., Yang, Y., Wei, X., & Zhao, Q. (2022). The circadian clock has roles in mesenchymal stem cell fate decision. *Stem Cell Research & Therapy, 13*(1), 200. https://doi.org/10.1186/s13287-022-02878-0

Goodenow, D., Greer, A. J., Cone, S. J., & Gaddameedhi, S. (2022). Circadian effects on UV-induced damage and mutations. *Mutation Research - Reviews in Mutation Research, 789*, 108413. https://doi.org/10.1016/j.mrrev.2022.108413

Göncü, B., & Öztürk, D. (2019). HT29 hücre hattında sirkadiyen ritme bağlı gen ifadesinin kontrolünde referans gen farklılığının senkronizasyondaki rolü. *Erzincan Üniversitesi Fen Bilimleri Enstitüsü Dergisi, 12*(3), 1370–1380. https://doi.org/10.18185/erzifbed.523088

Grimaldi, B., Bellet, M. M., Katada, S., Astarita, G., Hirayama, J., Amin, R. H., Granneman, J. G., Piomelli, D., Leff, T., & Sassone-Corsi, P. (2010). PER2 controls lipid metabolism by direct regulation of *PPARγ*. *Cell Metabolism, 12*(5), 509–520. https://doi.org/10.1016/j.cmet.2010.10.005

Guillamat-Prats, R. (2021). The role of MSC in wound healing, scarring, and regeneration. *Cells, 10*(7), 1729.

Kaneko, H., Kaitsuka, T., & Tomizawa, K. (2023). Artificial induction of circadian rhythm by combining exogenous BMAL1 expression and polycomb repressive complex 2 inhibition in human induced pluripotent stem cells. *Cellular and Molecular Life Sciences, 80*(8), 200. https://doi.org/10.1007/s00018-023-04847-z

Lamnis, L., Christofi, C., Stark, A., Palm, H., Roemer, K., Vogt, T., & Reichrath, J. (2024). Differential regulation of circadian clock genes by UV-B radiation and 1,25-dihydroxyvitamin D: A pilot study during different stages of skin photocarcinogenesis. *Nutrients, 16*(2), 254. https://doi.org/10.3390/nu16020254

Li, W., Wang, Y., Liu, C., Yu, Y., Xu, L., & Dong, B. (2025). Evaluation of the regulatory effect of the pan-PPAR agonist chiglitazar on the dawn phenomenon. *Diabetes Therapy, 16*(4), 731–748. https://doi.org/10.1007/s13300-025-01708-9

Li, Z., Li, Y., Xu, X., Gu, J., Chen, H., & Gui, Y. (2023a). Exosomes rich in Wnt5 improved circadian rhythm dysfunction via enhanced PPARγ activity in the 6-hydroxydopamine model of Parkinson's disease. *Neuroscience Letters, 802*, 137139. https://doi.org/10.1016/j.neulet.2023.137139

Li, Z., Yan, T., & Fang, X. (2023b). Low-dimensional wide-bandgap semiconductors for UV photodetectors. *Nature Reviews Materials, 8*, 587–603. https://doi.org/10.1038/s41578-023-00583-9

Liao, W., Duan, X., Xie, F., Zheng, D., Yang, P., Wang, X., & Hu, Z. (2023). 3D-bioprinted double-crosslinked angiogenic alginate/chondroitin sulfate patch for diabetic wound healing. *International Journal of Biological Macromolecules, 236*, 123952. https://doi.org/10.1016/j.ijbiomac.2023.123952

Lotfy, A., AboQuella, N. M., & Wang, H. (2023). Mesenchymal stromal/stem cell (MSC)-derived exosomes in clinical trials. *Stem Cell Research & Therapy, 14*(1), 66. https://doi.org/10.1186/s13287-023-03287-7

Lotfy, A., El-Sherbiny, Y. M., Cuthbert, R., Jones, E., & Badawy, A. M. (2019). Comparative study of biological characteristics of mesenchymal stem cells isolated from mouse bone marrow and peripheral blood. *Biomedical Reports, 11*, 165–170. https://doi.org/10.3892/br.2019.1236

Mattis, J., & Sehgal, A. (2016). Circadian rhythms, sleep, and disorders of aging. *Trends in Endocrinology & Metabolism, 27*(4), 192–203. https://doi.org/10.1016/j.tem.2016.02.003

Mens, M. M. J., & Ghanbari, M. (2018). Cell cycle regulation of stem cells by microRNAs. *Stem Cell Reviews and Reports, 14*, 309–322. https://doi.org/10.1007/s12015-018-9808-y

Mohamed-Ahmed, S., Fristad, I., Lie, S. A., Suliman, S., Mustafa, K., Vindenes, H., & Idris, S. B. (2018). Adipose-derived and bone marrow mesenchymal stem cells: A donor-matched comparison. *Stem Cell Research & Therapy, 9*(1), 168. https://doi.org/10.1186/s13287-018-0914-1

Montaigne, D., Butruille, L., & Staels, B. (2021). PPAR control of metabolism and cardiovascular functions. *Nature Reviews Cardiology, 18*(12), 809–823. https://doi.org/10.1038/s41569-021-00569-6

Ninomiya, Y., Sugahara-Yamashita, Y., Nakachi, Y., Tokuzawa, Y., Okazaki, Y., & Nishiyama, M. (2010). Development of a rapid culture method to induce adipocyte differentiation of human bone marrow-derived mesenchymal stem cells. *Biochemical and Biophysical Research Communications, 394*(2), 303–308. https://doi.org/10.1016/j.bbrc.2010.03.001

Niyaz, M., Gürpınar, Ö. A., Günaydın, S., & Onur, M. A. (2012). Isolation, culturing and characterization of rat adipose tissue-derived mesenchymal stem cells: A simple technique. *Turkish Journal of Biology, 36*(6), 658–664. https://doi.org/10.3906/biy-1109-31

Perez, R. L., Brauer, J., Rühle, A., Trinh, T., Sisombath, S., Wuchter, P., Grosu, A. L., Debus, J., Saffrich, R., Huber, P. E., & Nicolay, N. H. (2019). Human mesenchymal stem cells are resistant to UV-B irradiation. *Scientific Reports, 9*(1), 20000. https://doi.org/10.1038/s41598-019-56591-9

Pittenger, M. F., Discher, D. E., Péault, B. M., Phinney, D. G., Hare, J. M., & Caplan, A. I. (2019). Mesenchymal stem cell perspective: Cell biology to clinical progress. *NPJ Regenerative Medicine, 4*, 22. https://doi.org/10.1038/s41536-019-0083-6

Putthanbut, N., Su, P. A. B., Lee, J. Y., & Borlongan, C. V. (2025). Circadian rhythms in stem cells and their therapeutic potential. *Stem Cell Research & Therapy, 16*(1), 85. https://doi.org/10.1186/s13287-025-04178-9

Ra, K., Park, S. C., & Lee, B. C. (2023). Female reproductive aging and oxidative stress: Mesenchymal stem cell conditioned medium as a promising antioxidant. *International Journal of Molecular Sciences, 24*(5), 5053. https://doi.org/10.3390/ijms24055053

Sani, M. A., Khezerlou, A., Tavassoli, M., Abedini, A. H., & McClements, D. J. (2024). Development of sustainable UV-screening food packaging materials: A review of recent advances. *Trends in Food Science & Technology, 145*, 104366. https://doi.org/10.1016/j.tifs.2024.104366

Sevim, H., Kocaefe, Y. Ç., Onur, M. A., Uçkan-Çetinkaya, D., & Gürpınar, Ö. A. (2018). Bone marrow derived mesenchymal stem cells ameliorate inflammatory response in an *in vitro* model of familial hemophagocytic lymphohistiocytosis 2. *Stem Cell Research & Therapy, 9*(1), 198. https://doi.org/10.1186/s13287-018-0941-y

Su, Z., Hu, Q., Li, X., Wang, Z., & Xie, Y. (2024). The influence of circadian rhythms on DNA damage repair in skin photoaging. *International Journal of Molecular Sciences, 25*(20), 10926. https://doi.org/10.3390/ijms252010926

Takahashi, J. S. (2017). Transcriptional architecture of the mammalian circadian clock. *Nature Reviews Genetics, 18*(3), 164–179. https://doi.org/10.1038/nrg.2016.150

Tian, Y., Luan, X., & Yang, K. (2024). Chronotherapy involving rosiglitazone regulates the phenotypic switch of vascular smooth muscle cells by shifting the phase of TNF-α rhythm through triglyceride accumulation in macrophages. *Heliyon, 10*(10), e30708. https://doi.org/10.1016/j.heliyon.2024.e30708

Vilar, A., Hodgson-Garms, M., & Frith, J. E. (2023). Substrate mechanical properties bias MSC paracrine activity and therapeutic potential. *Acta Biomaterialia, 168*, 1–15. https://doi.org/10.1016/j.actbio.2023.06.041

Wang, S., Lin, Y., Gao, L., Yang, Z., Lin, J., Ren, S., Li, F., Chen, J., Wang, Z., Dong, Z., Sun, P., & Wu, B. (2022). PPAR-γ integrates obesity and adipocyte clock through epigenetic regulation of Bmal1. *Theranostics, 12*(4), 1589–1606. https://doi.org/10.7150/thno.69054

Wong, D. Y., Ranganath, T., & Kasko, A. M. (2015). Low-dose, long-wave UV light does not affect gene expression of human mesenchymal stem cells. *PLOS ONE, 10*(9), e0139307. https://doi.org/10.1371/journal.pone.0139307

Xiong, X., Kiperman, T., Li, W., Dhawan, S., Lee, J., Yechoor, V., & Ma, K. (2023). The clock-modulatory activity of nobiletin suppresses adipogenesis via Wnt signaling. *Endocrinology, 164*(8), bqad096. https://doi.org/10.1210/endocr/bqad096

Yan, T., Huang, L., Yan, Y., Zhong, Y., Xie, H., & Wang, X. (2023). MAPK/AP-1 signaling pathway is involved in the protection mechanism of bone marrow mesenchymal stem cells-derived exosomes against ultraviolet-induced photoaging in human dermal fibroblasts. *Skin Pharmacology and Physiology, 36*(2), 98–106. https://doi.org/10.1159/000529551

Yin, X., Lin, L., Fang, F., Zhang, B., & Shen, C. (2023). Mechanisms and optimization strategies of paracrine exosomes from mesenchymal stem cells in ischemic heart disease. *Stem Cells International, 2023*, 6500831. https://doi.org/10.1155/2023/6500831

Zeng, Y., Guo, Z., Wu, M., Chen, F., & Chen, L. (2024). Circadian rhythm regulates the function of immune cells and participates in the development of tumors. *Cell Death Discovery, 10*(1), 199. https://doi.org/10.1038/s41420-024-01960-1

Zhang, L., Zhang, C., Zheng, J., Wang, Y., Wei, X., Yang, Y., & Zhao, Q. (2024). miR-155-5p/Bmal1 modulates the senescence and osteogenic differentiation of mouse BMSCs through the Hippo signaling pathway. *Stem Cell Reviews and Reports, 20*(2), 554–567. https://doi.org/10.1007/s12015-023-10666-3

Zhang, Y., Li, Y., Gao, N., Gong, Y., Shi, W., & Wang, X. (2023). Transcriptome and metabolome analyses reveal perfluorooctanoic acid-induced kidney injury by interfering with PPAR signaling pathway. *International Journal of Molecular Sciences, 24*(14), 11503. https://doi.org/10.3390/ijms241411503

Zhu, Y., Liu, T., Song, K., Fan, X., Ma, X., & Cui, Z. (2008). Adipose-derived stem cell: A better stem cell than BMSC. *Cell Biochemistry and Function, 26*(6), 664–675. https://doi.org/10.1002/cbf.1488

Zhu, Z., Guo, L., Yeltai, N., Xu, H., & Zhang, Y. (2022). Chemokine (C-C motif) ligand 2-enhanced adipogenesis and angiogenesis of human adipose-derived

stem cell and human umbilical vein endothelial cell co-culture system in adipose tissue engineering. *Journal of Tissue Engineering and Regenerative Medicine, 16*(2), 163–176. https://doi.org/10.1002/term.3264

Zou, X., Zou, D., Li, L., Yu, R., Li, X., Du, X., Guo, J., Wang, K., & Liu, W. (2022). Multi-omics analysis of an in vitro photoaging model and protective effect of umbilical cord mesenchymal stem cell-conditioned medium. Stem Cell Research & Therapy, 13, 435. https://doi.org/10.1186/s13287-022-03137-y

Trakya University Journal of Natural Sciences, 27(1), 115–120, 2026
DOI: 10.23902/trkjnat.2025122
www.tujns.org

Research Article

Complete genome characterization of a novel mitovirus from *Morchella* sp.

Hatice Saif[1], Ergin Şahin[2,3], Gülce Ediş[1,4,5,6], Ilgaz Akata[7]*

[1]*Ankara University, Graduate School of Natural and Applied Sciences, Department of Biology, Ankara, Türkiye*
[2]*Dokuz Eylül University, Faculty of Science, Department of Biology, İzmir, Türkiye*
[3]*Dokuz Eylül University, Fauna and Flora Research and Application Center, İzmir, Türkiye*
[4]*Ankara University, Faculty of Agriculture, Department of Fisheries and Aquaculture, Evolutionary Genetics Laboratory (eGL), Ankara, Türkiye*
[5]*AgriGenomics Hub (AgriGx), Animal and Plant Genomics Research Innovation Center, Ankara, Türkiye*
[6]*Biodiversity Research Association (BAD), Ankara, Türkiye*
[7]*Ankara University, Faculty of Science, Department of Biology, Ankara, Türkiye*

Cite this article as: Saif, H., Şahin, E., Ediş, G., & Akata, I. (2026). Complete genome characterization of a novel mitovirus from *Morchella* sp. *Trakya University Journal of Natural Sciences, 27*(1), 115–120. https://doi.org/10.23902/trkjnat.2025122

Abstract

Background: Investigating viral diversity in non-cultivated fungi is essential for achieving a comprehensive understanding of mycoviral evolution and ecology, as current knowledge is largely derived from studies on phytopathogenic and commercially important species.

Aims: This study aimed to identify and characterize mycoviruses associated with wild-collected fungi and to expand existing knowledge on mitovirus diversity in underexplored fungal hosts.

Methods: A specimen assigned to *Morchella* sp. was screened for mycoviruses using molecular detection and genome sequencing. The complete viral genome was sequenced and annotated; bioinformatic techniques were employed to determine organization, nucleotide composition, and coding regions. Sequences were compared using BLASTp, and phylogenetic relationships were inferred based on RNA-dependent RNA polymerase (RdRp) sequences.

Results: A novel mitovirus, designated *Morchella mitovirus 1* (MMV1), was identified. MMV1 possesses a linear RNA genome consisting of 3,167 nucleotides with a G + C content of 41.00% and contains a single open reading frame encoding an RdRp. BLASTp revealed that the MMV1 RdRp shares the highest amino acid sequence identity (40.29%) with *Tuber mitovirus 3*, a member of the *Triamitovirus* genus of the *Mitoviridae* family. Phylogenetic analysis confirmed the placement of MMV1 within *Triamitovirus*.

Conclusion: This study reports the first mitovirus identified from *Morchella* and expands the known genetic diversity and evolutionary

Özet

Dayanak: Kültüre alınmamış mantarlardaki viral çeşitliliğin araştırılması, mikovirüs evrimi ve ekolojisinin kapsamlı biçimde anlaşılması açısından gereklidir; çünkü mevcut bilgiler büyük ölçüde fitopatojenik ve ticari açıdan önemli türler üzerinde yapılan çalışmalardan elde edilmiştir.

Amaçlar: Bu çalışma, doğadan toplanmış mantarlarla ilişkili mikovirüsleri tanımlamayı ve karakterize etmeyi, ayrıca yeterince araştırılmamış mantar konaklarda mitovirüs çeşitliliğine ilişkin mevcut bilgiyi genişletmeyi amaçlamıştır.

Yöntemler: *Morchella* sp. olarak tanımlanan bir örnek, moleküler tespit ve genom dizileme yöntemleri kullanılarak mikovirüsler açısından taranmıştır. Viral genomun tamamı dizilenmiş ve anotasyon yapılmış; organizasyon, nükleotid bileşimi ve kodlama bölgelerini belirlemek için biyoinformatik teknikler uygulanmıştır. Diziler BLASTp kullanılarak karşılaştırılmış ve filogenetik ilişkiler RNA'ya bağımlı RNA polimeraz (RdRp) dizilerine dayanarak çıkarılmıştır.

Bulgular: *Morchella mitovirus 1* (MMV1) olarak adlandırılan yeni bir mitovirüs tanımlanmıştır. MMV1, 3.167 nükleotitten oluşan lineer bir RNA genomuna sahiptir, G + C içeriği %41,00'dır ve RdRp kodlayan tek bir açık okuma çerçevesi içerir. BLASTp analizine göre MMV1'in RdRp'si, *Mitoviridae* familyasının *Triamitovirus* cinsine ait *Tuber mitovirus 3* ile en yüksek amino asit dizi benzerliğini (%40,29) göstermektedir. Filogenetik analiz, MMV1'in *Triamitovirus* içinde konumlandığını doğrulamıştır.

Edited by: *Boris Assyov*

***Corresponding Author:** Ilgaz Akata, **E-mail:** akata@science.ankara.edu.tr*

***ORCID iDs of the author(s):** HS. 0009-0008-4286-4727; EŞ. 0000-0003-1711-738X; GE. 0000-0001-7038-9865; IA. 0000-0002-1731-1302*

Received: 13 January 2026, **Accepted:** 14 April 2026, **Published:** 24 April 2026

landscape of mitoviruses, emphasizing the importance of investigating mycoviruses in non-cultivated fungal hosts.

Sonuç: Bu çalışma, *Morchella* cinsinden tanımlanan ilk mitovirüsü rapor etmekte ve mitovirüslerin bilinen genetik çeşitliliğini ve evrimsel dağılımını genişletmektedir; ayrıca kültüre alınmamış mantar konaklarda mikovirüslerin araştırılmasının önemini vurgulamaktadır.

Keywords: Mycovirus, mitovirus, *Triamitovirus*, *Morchella*, RNA-dependent RNA polymerase

Introduction

Growing interest in mycovirome research is exemplified by numerous recent investigations exploring virus populations across diverse fungal taxa (Akata et al., 2023; Bora et al., 2024; Ferilli et al., 2024; Li et al., 2023; Raco et al., 2023; Rueda-Maíllo et al., 2025; Sahin et al., 2024). This expanding focus is largely driven by improved accessibility and capability of high-throughput sequencing (HTS) platforms. HTS-based approaches have revealed an extensive array of mycoviruses inhabiting phylogenetically varied fungal hosts—spanning early-diverging lineages to more recently evolved clades—each exhibiting distinct ecological adaptations (Hough et al., 2023). Furthermore, HTS screening can detect many unknown viral species, including unclassified groups and novel representatives of established families within the fungal kingdom (Ayllon & Vainio, 2023).

Members of the family *Mitoviridae* are non-encapsidated viruses with uncapped, positive-sense, single-stranded RNA (ribonucleic acid) genomes ranging from 2.1 to 4.9 kb in length (Hillman & Cai, 2013; Koonin et al., 2020). They features a single open reading frame (ORF) that is translated via mitochondrial codon usage and encodes an RNA-dependent RNA polymerase (RdRp) harboring six characteristic conserved motifs (A–F). *Mitoviridae* has been recently expanded to include four new genera: *Kvaramitovirus*, *Triamitovirus*, *Duamitovirus*, and *Unuamitovirus* (International Committee on Taxonomy of Viruses [ICTV], 2024). Although first described in fungi, mitoviruses have since been identified in plants and insects (Bruenn et al., 2015; Nibert et al., 2018; Fonseca et al., 2020). Notably, no mitoviruses have been reported in the fungus *Morchella*. This study isolated and molecularly characterized a novel mitovirus from *Morchella* sp., designated "*Morchella mitovirus 1*" (MMV1).

Based on previous literature, viruses documented within the true morel genus *Morchella* are three endornaviruses, one fusarivirus, one unclassified RNA virus isolated from *M. importuna*, one endornavirus from *M. sextelata*, and two fusariviruses from *M. esculenta* (Gilbert et al., 2019; Lyu et al., 2025; Sahin et al., 2021). Given the ecological and economic importance of *Morchella* and the limited knowledge of its associated virome, further investigation of viruses infecting this genus is warranted. We hypothesized that underexplored *Morchella*-related viromes may include undescribed mitoviruses. Thus, this study aimed to identify and characterize a novel mitovirus from *Morchella* sp. and to determine its genomic and phylogenetic relationships within *Mitoviridae*.

Materials and Methods

Sampling and Molecular Characterization of Fungal Specimens

Fungal specimens were collected during field surveys in northwestern Türkiye. On April 21, 2023, an ascocarp of a *Morchella* specimen (Figure 1a) was collected from the edge of a dirt road in Kaynaklar village, Buca district, İzmir province. The specimen was deposited in the Ankara University Herbarium (ANK) with the accession code ANK Akata & Saif 012, for future reference. Total genomic DNA was isolated from a small piece of the specimen ANK Akata & Saif 012 employing CTAB (Rogers & Bendich, 1994). The nuclear ribosomal internal transcribed spacer (ITS) regions were subsequently amplified by polymerase chain reaction (PCR) using the primers ITS1/ITS4 (Martin & Rygiewicz, 2005). The amplicon was visualized *via* agarose gel electrophoresis, purified with the GeneJET PCR Purification Kit (Thermo Fisher Scientific, MA, USA), and Sanger sequenced utilizing the BigDye™ Direct Cycle Sequencing Kit (Thermo Fisher Scientific, MA, USA). Sequences were resolved on an ABI Prism 3130 Genetic Analyzer (Applied Biosystems, Thermo Fisher Scientific, MA, USA) and compared against the National Center for Biotechnology Information (NCBI) GenBank reference database (https://www.ncbi.nlm.nih.gov/) using BLASTn. The ITS sequence showed 100% query coverages and identities to multiple *Morchella* spp., including *M. esculenta*, *M. elata*, *M. importuna*, *M. conica*, *M. costata*, *M. vulgaris*, and *M. hortensis*. Given the overlap among sequences and the known taxonomic complexity of this genus, the specimen was conservatively retained as *Morchella* sp.

Sample Preparation for HTS

For surface sterilization, the fungal samples were sequentially immersed in 2% NaOCl (2 min) and 70% ethanol (10 s). Following disinfection, all residual chemicals were removed through extensive rinsing with sterile distilled water. The material was then lyophilized and pulverized into a fine, homogeneous powder with a mechanical grinder to facilitate downstream molecular analysis.

Viral dsRNA was isolated from powdered fungal fruiting bodies *via* cellulose-based affinity chromatography, following previously described solid-phase extraction techniques (Darissa et al., 2010; Morris & Dodds, 1979). The protocol was adapted by substituting cellulose CF-11 with Type 101 (Merck, Sigma-Aldrich, Darmstadt, Germany) for column packing. Purified dsRNA extracts were then treated with DNase I (New England Biolabs, MA, USA) and S1 nuclease (Thermo Fisher Scientific,

MA, USA) to degrade any co-extracted DNA. The resulting dsRNA was reverse-transcribed into cDNA using a dN6 primer, 5′-CCTGAATTCGGATCCTCCNNNNNN-3′, and the RevertAid First-Strand cDNA Synthesis Kit (Thermo Fisher Scientific, MA, USA) after initial cleanup with a GeneJet™ PCR purification Kit (Thermo Fisher Scientific, MA, USA). cDNA was amplified by random PCR (rPCR), as described by Darissa et al. (2010). The amplicons were sequenced on an Illumina NovaSeq 6000 system (Novogene, UK).

Bioinformatic Analyses of HTS Data

Bioinformatic processing of quality-filtered reads involved *de novo* assembly in CLC Genomics Workbench 20.0.2 using standard parameters; it generated 106 contigs >1.5 kb in length. All contigs were analyzed utilizing BLASTx against the NCBI non-redundant protein database to screen for viral sequences. It identified a contig 13 of notable length—3,089 nt—assembled from 1,664 reads, exhibiting marked homology to established mitoviruses. BLASTx revealed that it shared 40.29% amino acid identity with *Tuber mitovirus 3*. Such substantial sequence alignment indicates the detection of a novel mitovirus, which we have named MMV1, thereby expanding the diversity of the *Mitoviridae*.

RNA-Ligase-Mediated Rapid Amplification of cDNA Ends

To determine the terminal sequences of the MMV1 genomic RNA, we employed RNA-ligase-mediated rapid amplification of cDNA ends (RLM-RACE). The 3′ termini of the purified viral dsRNA were first ligated to a synthetic adapter oligonucleotide—RLO: 5′p-CATGGTGGCGACCGGTAG-NH2 3′—catalyzed by T4 RNA Ligase 1 (New England Biolabs, MA, USA), via a 6-h incubation at 37°C, followed by a 12-h extension at 12°C to maximize efficiency. Ligated RNAs were subsequently purified with a GeneJET PCR Purification Kit (Thermo Fisher Scientific, MA, USA) prior to downstream amplification.

First-strand cDNA was synthesized using purified RNA, the RevertAid First-Strand cDNA Synthesis Kit (Thermo Fisher Scientific, MA, USA) with the universal RTP primer (5′-CTACCGGTCGCCACCATG-3′), designed to bind an RLO adapter. Following reverse transcription, the 5′ and 3′ termini were PCR-amplified independently employing gene-specific primers in conjunction with RTP. The 5′ end was targeted with a reverse primer: 5′-CCGAAGACTTTGTTTTGTTAACG-3′, and the 3′ end with a forward primer: 5′-TTGGTCGTCTGGATCGTGTAG-3′. Following PCR amplification, the products were cloned into a pGEM-T Easy Vector system (Promega, WI, USA) and Sanger sequenced. The final genome was assembled using Geneious Prime 2020.2.5 (Dotmatics, Bishop's Stortford, UK). Such a comprehensive strategy enabled precise characterization of the terminal regions of the viral genome, yielding essential information about its architecture in a novel mitovirus.

Phylogenetic Analyses of Complete Viral Genome Sequences

A potential ORF within the MMV1 genome was predicted using the ExPASy Translate tool (https://web.expasy.org/translate/), applying the mold mitochondrial genetic code for nucleotide-to-amino acid translation. The resulting putative protein sequences were aligned against reference mitovirus proteins using Clustal Omega to ensure a robust and accurate comparison. Evolutionary relationships were inferred through maximum likelihood phylogeny in MEGA 11, implementing the WAG + G + I + F substitution model (Tamura et al., 2021; Whelan & Goldman, 2001). The phylogenetic framework obtained was statistically validated using 1000 bootstrap replicates to assess node support and ensure confidence in topological conclusions.

Results

The dsRNA segment, which serves as a genome replication intermediate for MMV1, was effectively isolated from the specimen labeled ANK Akata & Saif 012, as represented in Figure 1b. The genomic composition of MMV1 encompassed 3,167 nucleotides and demonstrated a G + C content of 41.00%. The complete sequence of the MMV1 genome has been deposited in GenBank under the accession number PX516901.1. By employing the fungal mitochondrial genetic code, in which "UGA" encodes tryptophan, the MMV1 genome was found to have a single ORF (Figure 1c). The amino acid sequence predicted from this ORF consisted of 802 residues and a calculated molecular weight of 87.59 kDa, as determined by the Protein Molecular Weight calculator tool (bioinformatics.org). The 5′ and the 3′ UTRs (untranslated regions) were 627 and 131 nucleotides long, respectively, depicted in Figure 1d. These UTRs were structurally characterized *via* the RNA Folding Form V2.3 interface of the RNA mfold web server (https://www.unafold.org/mfold/applications/rna-folding-form-v2.php), which demonstrated that both UTRs adopted stem-loop secondary structures exhibiting initial Gibbs free energy (ΔG) values of −9.20 and −7.80 kcal/mol for the 5′ and 3′ UTRs, respectively (Figure 1d).

Analysis using the NCBI Conserved Domains Database (https://www.ncbi.nlm.nih.gov/Structure/cdd/cdd.shtml) indicated that the MMV1-encoded polypeptide included an RdRp domain, which spanned amino acid residues 203–538 (Figure 1d). Subsequent evaluation within the Conserved Domains Database (CDD) framework confirmed this domain to belong to the mitovirus RdRp family (Accession: cl05469; E-value: 6.04e-78). Moreover, comparisons employing the protein Basic Local Alignment Search Tool (BLASTp) demonstrated that the MMV1 RdRp had the highest sequence identity (41.00%) with the corresponding polymerase from *Tuber mitovirus 3*.

To elucidate the evolutionary position of MMV1 among other mitoviruses, phylogeny was reconstructed based on a comparison of RdRp sequences. The resulting tree demonstrated that MMV1 formed a well-supported clade with recognized members of the genus *Triamitovirus*, including *Tuber mitovirus 3* and Geopora sumneriana mitovirus 1 (Figure 2a). Furthermore, multiple sequence alignment of RdRp domains from ten mitoviruses confirmed the presence of six conserved motifs—F, A, B, C, D, and E—arranged sequentially from the N- to C-termini of the MMV1 polymerase. Notably, this suite includes the catalytically essential A, B, and C motifs situated within the palm subdomain (Figure 2b).

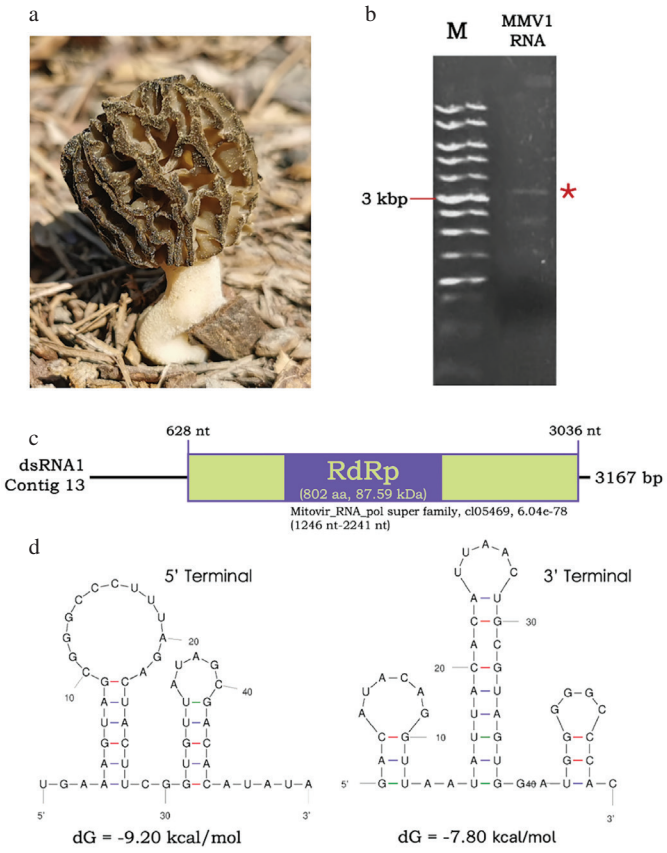

Figure 1. (a) Fruiting body (ascocarp) of *Morchella* specimen ANK Akata & Saif 012. (b) Electrophoretic profile of the double-stranded RNA (dsRNA) segment corresponding to the MMV1 viral genome. (c) Genomic organization of MMV1. The single ORF is represented by a rectangle flanked by UTRs (solid black lines). The region encoding the predicted RNA-dependent RNA polymerase domain is highlighted in purple. (d) Predicted secondary structures for the 5′ and 3′ termini of the MMV1 genome.
MMV1 = Morchella mitovirus 1; ORF = open reading frame; UTRs = untranslated regions.

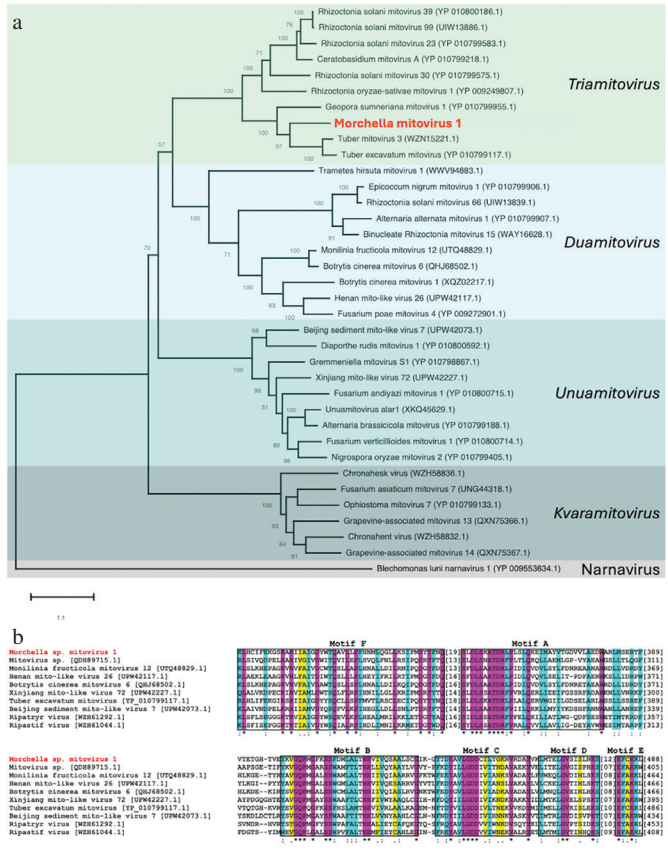

Figure 2. (a) Maximum likelihood phylogenetic tree illustrating the evolutionary relationships between the RNA-dependent RNA polymerase (RdRp) from MMV1 and homologs from other mitoviruses. It was constructed in MEGA 11 with 1000 bootstrap replicates; support values are indicated at branch nodes. The scale bar corresponds to a genetic distance of 0.5. GenBank accession numbers are provided in parentheses. (b) Multiple sequence alignment of the conserved RdRp motifs—F, A, B, C, D, and E, from the N-terminus of the MMV1 genome and those of phylogenetically related mitoviruses. Identical residues are highlighted in magenta, and those with similar biochemical properties are shaded in blue and yellow.
MMV1 = Morchella mitovirus 1.

Discussion

Although morphological characteristics have long served as the primary method for species identification, such an approach has proven inadequate for *Morchella,* as its external features can vary substantially depending on environmental conditions. Thus, species differentiation based solely on morphology often yields unreliable results. The introduction of molecular methods has marked a crucial turning point in *Morchella* taxonomy; however, these alone are also insufficient to fully resolve species boundaries. Although the combined evaluation of morphological and molecular data enhances taxonomic resolution within the *Morchella* group, the ITS region alone is insufficient for accurate species delimitation. This region has been recognized as the universal barcode for fungi since 2012 (Schoch et al., 2012). Nevertheless, pronounced ITS polymorphism among *Morchella* spp. indicates that relying solely on this region may result in misidentifications. Therefore, concatenated analyses that combine multiple gene regions provide more robust and reliable species-level results (Loizides et al., 2022). Indeed, in a study encompassing 45 *Morchella* specimens, a combination of EF1-α, RPB1, RPB2, and ITS regions yielded the greatest resolution in species delimitation, whereas analyses involving only two or three regions produced lower taxonomic accuracy (Sa et al., 2022).

To evaluate the taxonomic position of the current specimen, only the ITS region was sequenced. BLASTn analysis of the obtained sequence showed similarity to those of several *Morchella* spp. Considering the variability and sequence overlap known among species within this genus, as well as the morphological ambiguity observed in the specimen, assigning a specific epithet was not

deemed reliable. Therefore, to avoid potential misidentifications within such a taxonomically complex group, the specimen was conservatively designated as *Morchella* sp.

GenBank contains >4,000 complete, near-complete, and partial mitovirus genomes. A phylogenetic analysis of 2,000 randomly selected mitovirus RdRp sequences revealed distinct lineages that cluster, either branching at the base or apex of the four established mitovirus genera (data not shown). This pattern suggests that these lineages represent novel, yet-to-be-classified genera within *Mitoviridae* and may be evaluated by the ICTV study groups.

The UTRs of mitoviruses display substantial heterogeneity in length and nucleotide sequence, a feature observed even among intra-species isolates. While these genomic segments are hypothesized to serve as binding sites for the translation initiation machinery, specific host-derived molecules—including proteins or non-coding RNAs—that potentially associate with them remain largely uncharacterized. Furthermore, the functional roles of these UTRs and their possible regulation through RNA modifications (epitranscriptomics) that could alter host cellular functions have not been directly experimentally validated. A prevalent hypothesis suggests that their terminal segments function as cis-acting regulatory elements that facilitate recognition and binding by viral RdRp during genomic replication. The application of sophisticated computational approaches, such as deep learning-based comparative genomics, offers a promising avenue for elucidating the properties of these regulatory regions.

The evolutionary dynamics shaping virus–host associations are complex and can originate from multiple distinct processes. Key among these are: 1) codivergence, characterized by topological congruence between the phylogenetic trees of viruses and their hosts; 2) host switching, involving cross-species transmission of a virus to a phylogenetically distant host; and 3) duplication, a process wherein a parasite lineage diversifies within a single host species, resulting in multiple lineages that occupy an identical host range (Göker et al., 2011). In this context, as evolutionary virologists continue to elucidate the sequence diversity of mitoviruses across diverse fungal hosts, they can be better positioned to estimate the evolutionary forces that predominantly govern mitovirus evolution. Following the established species demarcation criteria for *Mitoviridae* (ICTV, 2021), MMV1 constitutes a new species, as its RdRp shares <70% sequence similarity with all known mitoviruses.

MMV1 shared the typical genomic features of *Mitoviridae*, including a linear RNA genome, a single ORF encoding the RdRp, and protein translation based on the fungal mitochondrial genetic code. In addition, the predicted terminal stem-loop structures were consistent with characteristics reported for other mitoviruses. A comparative analysis showed that MMV1 was most closely related to *Tuber mitovirus 3*; however, the relatively low RdRp amino acid identity indicated that it represented a distinct virus. Its phylogenetic placement within *Triamitovirus* further supported such an interpretation. Although the biological impacts of MMV1 on *Morchella* remain unknown, its detection expands the diversity of mitoviruses known to infect wild fungi and underlines the importance of further studies on host–virus interactions and mitovirus evolution in morels.

Conclusion

In conclusion, the genomic features, RdRp sequence similarity, and phylogenetic placement of MMV1 support its assignment to the genus *Triamitovirus* within the family *Mitoviridae*. To our knowledge, this study is the first to report a complete mitovirus genome from a fungal host assigned to *Morchella* sp. Although the findings expand the current dataset on mitoviruses associated with non-cultivated fungi, they should be interpreted with caution as the study is based on a single specimen, and the host could not be identified with confidence at the species level.

Acknowledgements

This study was derived from the MSc thesis of Hatice Saif completed at Ankara University.

Ethics

Ethics Committee Approval: Not required.

Data Sharing Statement: All data are available within the study.

Footnotes

Authorship Contributions:

Conceptualization: E.Ş., G.E., and I.A.; Design/methodology: E.Ş., G.E., and I.A.; Execution/investigation: H.S., E.Ş., and G.E.; Resources/materials: H.S., E.Ş., and G.E.; Data acquisition: H.S., E.Ş., G.E., and I.A.; Data analysis/interpretation: H.S., E.Ş., and G.E.; Writing – original draft: E.Ş., G.E., and I.A.; Writing – review & editing/critical revision: E.Ş. and I.A.

Conflict of Interest: The author(s) have no conflicts of interest to declare.

Funding: This study was funded by Ankara University, Coordinatorship of Scientific Research Projects, under project number FYL-2023-2976.

References

Akata, I., Edis, G., Keskin, E., & Sahin, E. (2023). Diverse partitiviruses hosted by the ectomycorrhizal agaric *Hebeloma mesophaeum* and the natural transmission of a partitivirus between phylogenetically distant, sympatric fungi. *Virology, 581*, 63–70. https://doi.org/10.1016/j.virol.2023.03.002

Ayllon, M. A., & Vainio, E. J. (2023). Mycoviruses as a part of the global virome: Diversity, evolutionary links and lifestyle. *Advances in Virus Research, 115*, 1–86. https://doi.org/10.1016/bs.aivir.2023.02.002

Bora, E., Akata, I., Keskin, E., & Sahin, E. (2024). Molecular characterization and comparative genomic analysis of two *triamitovirus* isolates hosted by the hypogean fungus *Tuber excavatum* Vittad. *Trakya University Journal of Natural Sciences*. Advance online publication. https://doi.org/10.23902/trkjnat.1478899

Bruenn, J. A., Warner, B. E., & Yerramsetty, P. (2015). Widespread mitovirus sequences in plant genomes. *PeerJ, 3*, e876. https://doi.org/10.7717/peerj.876

Darissa, O., Willingmann, P., & Adam, G. (2010). Optimized approaches for the sequence determination of double-stranded RNA templates. *Journal of Virological Methods, 169*, 397–403. https://doi.org/10.1016/j.jviromet.2010.08.013

Ferilli, F., Lione, G., Gonthier, P., Turina, M., & Forgia, M. (2024). First detection of mycoviruses in *Gnomoniopsis castaneae* suggests a putative horizontal gene transfer event between negative-sense and double-strand RNA viruses. *Virology, 594*, 110057. https://doi.org/10.1016/j.virol.2024.110057

Fonseca, P., Ferreira, F., da Silva, F., Oliveira, L. S., Marques, J. T., Goes-Neto, A., Aguiar, E., & Gruber, A. (2020). Characterization of a novel mitovirus of the sand fly *Lutzomyia longipalpis* using genomic and virus–host interaction signatures. *Viruses, 13*(1), 9. https://doi.org/10.3390/v13010009

Gilbert, K. B., Holcomb, E. E., Allscheid, R. L., & Carrington, J. C. (2019). Hiding in plain sight: New virus genomes discovered via a systematic analysis of fungal public transcriptomes. *PLOS ONE, 14*(7), e0219207. https://doi.org/10.1371/journal.pone.0219207

Göker, M., Scheuner, C., Klenk, H. P., Stielow, J. B., & Menzel, W. (2011). Codivergence of mycoviruses with their hosts. *PLOS ONE, 6*(7), e22252. https://doi.org/10.1371/journal.pone.0022252

Hillman, B. I., & Cai, G. (2013). Chapter six - The family Narnaviridae: Simplest of RNA viruses. *Advances in Virus Research, 86*, 149–176. https://doi.org/10.1016/B978-0-12-394315-6.00006-4

Hough, B., Steenkamp, E., Wingfield, B., & Read, D. (2023). Fungal viruses unveiled: A comprehensive review of mycoviruses. *Viruses, 15*(5), 1202. https://doi.org/10.3390/v15051202

International Committee on Taxonomy of Viruses. (2024). *Taxon details: Mitoviridae*. ICTV. https://ictv.global/taxonomy/taxondetails?taxnode_id=202407204&taxon_name=*Mitoviridae*

Koonin, E. V., Dolja, V. V., Krupovic, M., Varsani, A., Wolf, Y. I., et al. (2020). Global organization and proposed megataxonomy of the virus world. *Microbiology and Molecular Biology Reviews, 84*(2), 10-1128. https://doi.org/10.1128/mmbr.00061-19

Li, X., Li, S., Yin, W., Sossah, F. L., Song, B., et al. (2023). Complete genome sequence of a novel mycovirus from *Pleurotus citrinopileatus*. *Archives of Virology, 168*(2), 66. https://doi.org/10.1007/s00705-022-05668-4

Loizides, M., Alvarado, P., Moreau, P.-A., Assyov, B., Halasů, V., Stadler, M., Rinaldi, A., Marques, G., Zervakis, G. I., Borovička, J., Van Vooren, N., Grebenc, T., Richard, F., Taşkin, H., Gube, M., Sammut, C., Agnello, C., Baroni, T. J., Crous, P., Fryssouli, V., Gonou, Z., Guidori, U., Gulden, G., Hansen, K., Kristiansen, R., Læssøe, T., Mateos, J., Miller, A., Moreno, G., Perić, B., Polemis, E., Salom, J. C., Siquier, J. L., Snabl, M., Weholt, Ø., & Bellanger, J.-M. (2022). Has taxonomic vandalism gone too far? A case study, the rise of the pay-to-publish model and the pitfalls of *Morchella* systematics. *Mycological Progress, 21*(1), 7–38. https://doi.org/10.1007/s11557-021-01755-z

Lyu, R., Chen, J., Tang, Q., Hai, D., Wu, T., Xiao, H., Xie, J., & Xiao, Y. (2025). Characterization of a betaendornavirus isolated from the edible fungus *Morchella sextelata*. *Archives of Virology, 170*(4), 1–5. https://doi.org/10.1007/s00705-025-06264-y

Martin, K. J., & Rygiewicz, P. T. (2005). Fungal-specific PCR primers developed for analysis of the ITS region of environmental DNA extracts. *BMC Microbiology, 5*(1), 28. https://doi.org/10.1186/1471-2180-5-28

Morris, T. J., & Dodds, J. A. (1979). Isolation and analysis of double-stranded RNA from virus-infected plant and fungal tissue. *Phytopathology, 69*(8), 854–858. https://doi.org/10.1094/Phyto-69-854

Nibert, M. L., Vong, M., Fugate, K. K., & Debat, H. J. (2018). Evidence for contemporary plant mitoviruses. *Virology, 518*, 14–24. https://doi.org/10.1016/j.virol.2018.02.005

Raco, M., Jung, T., Horta Jung, M., Chi, N. M., Botella, L., & Suzuki, N. (2023). Sequence and phylogenetic analysis of a novel alphaendornavirus, the first virus described from the oomycete plant pathogen *Phytophthora heveae*. *Archives of Virology, 168*(6), 158. https://doi.org/10.1007/s00705-023-05786-7

Rogers, S. O., & Bendich, A. J. (1994). Extraction of total cellular DNA from plants, algae and fungi. In *Plant molecular biology manual* (pp. 183–190). Springer Netherlands.

Rueda-Maíllo, F., Garrido-Jurado, I., Kotta-Loizou, I., & Quesada-Moraga, E. (2025). A mycoviral infection drives virulence and ecological fitness of the entomopathogenic fungus *Beauveria bassiana*. *Journal of Invertebrate Pathology, 209*, 108251. https://doi.org/10.1016/j.jip.2024.108251

Sa, W., Qiao, J., Gao, Q., Li, Z., & Shang, Q. (2022). DNA barcoding and species classification of *Morchella*. *Genes, 13*(10), 1806. https://doi.org/10.3390/genes13101806

Sahin, E., Edis, G., Keskin, E., & Akata, I. (2024). Molecular characterization of the complete genome of a novel ormycovirus infecting the ectomycorrhizal fungus *Hortiboletus rubellus*. *Archives of Virology, 169*(5), 110. https://doi.org/10.1007/s00705-024-06027-1

Sahin, E., Keskin, E., & Akata, I. (2021). The unique genome organization of two novel fusariviruses hosted by the true morel mushroom *Morchella esculenta*. *Virus Research, 302*, 198486. https://doi.org/10.1016/j.virusres.2021.198486

Schoch, C. L., Seifert, K. A., Huhndorf, S., Robert, V., Spouge, J. L., Levesque, C. A., Chen, W., Bolchacova, E., Voigt, K., Crous, P. W., Miller, A. N., Wingfield, M. J., Aime, M. C., An, K.-D., Bai, F. Y., Barreto, R. W., Begerow, D., Bergeron, M. J., Blackwell, M., Boekhout, T., Bogale, M., Boonyuen, N., Burgaz, A. R., Buyck, B., Cai, L., Cai, Q., Cardinali, G., Chaverri, P., Coppins, B. J., Crespo, A., Cubas, P., Cummings, C., Damm, U., de Beer, Z. W., de Hoog, G. S., Del-Prado, R., Dentinger, B., Diéguez-Uribeondo, E., Divakar, P. K., Douglas, B., Dueñas, M., Duong, T. A., Eberhardt, U., Edwards, J. E., Elshahed, M. S., Fliegerová, K., Furtado, M., García, M. A., Ge, Z.-W., Griffith, G. W., Griffiths, K., Groenewald, J. Z., Groenewald, M., Grube, M., Gryzenhout, M., Guo, L.-D., Hagen, F., Hambleton, S., Hamelin, R. C., Hansen, K., Harrold, P., Heller, G., Herrera, C., Hirayama, K., Hirooka, Y., Ho, H.-M., Hoffmann, K., Hofstetter, U., Högnabba, F., Hollingsworth, P. M., Hong, S. B., Hosaka, K., Houbraken, J., Hughes, K., Huhtinen, S., Hyde, K. D., James, T., Johnson, E. M., Johnson, J. E., Johnston, P. R., Jones, E. B. G., Kelly, L. J., Kirk, P. M., Knapp, D. G., Kõljalg, U., Kovács, G. M., Kurtzman, C. P., Landvik, S., Leavitt, S. D., Liggenstoffer, A. S., Liimatainen, K., Lombard, L., Luangsa-Ard, J. J., Lumbsch, H. T., Maganti, H., Maharachchikumbura, S. S. N., Martin, M. P., May, T. W., McTaggart, A. R., Methven, A. S., Meyer, W., Moncalvo, J. M., Mongkolsamrit, S., Nagy, L. G., Nilsson, R. H., Niskanen, T., Nyilasi, I., Okada, G., Okane, I., Olariaga, I., Otte, J., Papp, T., Park, D., Petkovits, T., Pino-Bodas, R., Quaedvlieg, W., Raja, H. A., Redecker, D., Rintoul, T. L., Ruibal, C., Sarmiento-Ramírez, J. M., Schmitt, I., Schüßler, A., Shearer, C., Sotome, K., Stefani, F. O. P., Stenroos, S., Stielow, B., Stockinger, H., Suetrong, S., Suh, S.-O., Sung, G.-H., Suzuki, M., Tanaka, K., Tedersoo, L., Telleria, M. T., Tretter, E., Untereiner, W. A., Urbina, H., Vágvölgyi, C., Vialle, A., Vu, T. D., Walther, G., Wang, Q.-M., Wang, Y., Weir, B. S., Weiß, M., White, M. M., Xu, J., Yahr, R., Yang, Z. L., Yurkov, A., Zamora, J. C., Zhang, N., Zhuang, W.-Y., & Schindel, D. (2012). Nuclear ribosomal internal transcribed spacer (ITS) region as a universal DNA barcode marker for fungi. *Proceedings of the National Academy of Sciences of the United States of America, 109*(16), 6241–6246. https://doi.org/10.1073/pnas.1117018109

Tamura, K., Stecher, G., & Kumar, S. (2021). MEGA11: Molecular evolutionary genetics analysis version 11. *Molecular Biology and Evolution, 38*(7), 3022–3027. https://doi.org/10.1093/molbev/msab120

Whelan, S., & Goldman, N. (2001). A general empirical model of protein evolution derived from multiple protein families using a maximum-likelihood approach. *Molecular Biology and Evolution, 18*(5), 691–699. https://doi.org/10.1093/oxfordjournals.molbev.a003851